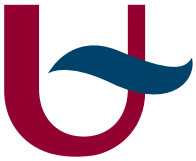

UNIVERSITEIT ANTWERPEN

Faculteit Wetenschappen

Departement Fysica

Static and dynamical properties of finite size two- and three-dimensional Wigner crystals

Structurele en dynamische eigenschappen van eindige twee- en driedimensionale Wignerkristallen

Proefschrift voorgelegd tot het behalen
van de graad van doctor in de wetenschappen
aan de Universiteit Antwerpen te verdedigen door

Sérgio Wlademir da Silva Apolinário

Promotor: Prof. dr. F. M. Peeters
Co-promotor: Prof. dr. B. Partoens

Antwerpen 2008

Acknowledgments

I wish to thank my wife Jamine who came to Antwerpen to stay with me and give me the support I needed to do my PhD. Once more, thank you very much. Also I want to thank my son Arthur for the every day light he gives me.

I am very grateful to my promoter Prof. Dr. F. M. Peeters and co-promoter Prof. Dr. B. Partoens for their very important professional guiding and supporting during my doctoral research.

I would like to thank all the help I had from the present and former members and regular visitors of the CMT group.

My doctoral work was financially supported by the Flemish Scientific Foundation (FWO-VI).

Contents

1

Introduction

1.1 OUTLINE OF THE THESIS

Wigner crystallization was predicted in 1934 and states that a liquid to solid phase transition occurs in a three-dimensional electron gas at low temperature and density due to strong Coulomb repulsion [1]. An appreciable amount of theoretical and experimental works have been devoted to the study of Wigner crystallization. My thesis is motivated by recent experiments on finite size Wigner crystals.

The aim of this thesis is to study in detail the structural properties, the linear dynamics and melting processes of *finite size* Wigner crystals. We considered both two and three dimensional systems. The influence of the inter-particle interaction potential, of the strength and shape (i.e. the symmetry) of the confinement potential, and of the number of particles contained in the system are investigated. Hereby, we aimed at revealing the basic physics of such a system. Where possible we compare our theoretical results with experiment. The outline of the thesis is as follow:

Chapter 1 starts with an introduction about Wigner crystallization. Then we describe the early years when dusty plasma first appeared as a puzzling element in the microprocessor industry and in astrophysics. The first experiment in a dusty plasma where Wigner crystallization was observed is discussed.

Further, more recent experiments are addressed such as the formation of spherically symmetric three dimensional (3D) clouds of charged dust, i.e. the so called Coulomb balls. The experiments involving 2D Wigner crystals formed in dusty plasmas and metallic balls are discussed. Finally we discuss correlated systems of strongly interacting particles such as ions trapped in a linear Paul trap, Wigner crystals in quantum dots and in type II superconductors.

Chapter 2 of this thesis deals with the theoretical model we use to treat our systems. Additionally, technical details about the Monte Carlo simulation, the Newton method and the molecular dynamics simulation in the context of our work is given.

In **chapter 3** we studied the structural and spectral properties of a classical system consisting of a finite number of particles, moving in two dimensions, and interacting through a repulsive logarithmic potential and held together by an anisotropic harmonic potential. Increasing the anisotropy of the confinement potential can drive the system from a two dimensional ($2D$) to a one dimensional ($1D$) configuration through a sequence of structural phase transitions. The latter were classified with respect to the order of their 'phase' transition. Our results on the ground state configurations are compared with recent experiments. The zig-zag transition is investigated in detail.

Chapter 4 Molecular dynamic simulations are performed to investigate the melting process of the above system. We investigated how the eccentricity of the confinement potential affects the melting pattern of such clusters. Our results are compared to the pioneering results of Bedanov and Peeters [2] for the melting process in isotropic clusters. We found that anisotropic systems possess peculiar melting processes which are not homogeneous. Using Lindemann's criterion the melting temperatures are determined as function of the different parameters. In this investigation we also analyzed the sensitivity of our results to the inter-particle interaction potential by considering both a long range (i.e. logarithmic) and a short range (i.e. screened Coulomb) interparticle interaction.

In **chapter 5** we analyze structural and dynamical properties of small size three-dimensional clusters of classical charged particles confined by a spherical parabolic trap. The ground state and the lowest metastable configurations are identified for Coulomb clusters consisting of $N = 4$ to $N = 100$ particles. The eigenmode frequencies are investigated both for clusters with Coulomb and screened Coulomb interparticle interaction. The breathing mode frequency was analytically determined.

In **chapter 6** molecular dynamic simulations are performed to investigate the melting process of small three dimensional clusters (i.e. systems with one and two shells) of classical charged particles trapped in an isotropic parabolic potential. The confined particles interact through a repulsive potential. We identify the presence of magic clusters in those systems and relate their linear dynamics with their structural symmetries. Furthermore, the melting process in those clusters is investigated. The low temperature behavior of systems

composed of two shells and their fine structure are investigated. The influence of the screening of the inter-particle interaction potential on the different properties was investigated in detail. A normal mode analysis is performed and the frequency values are related to the different melting temperatures of the system.

Chapter 7 The structural and dynamical properties of small three dimensional (3D) anisotropically confined Wigner crystals of particles interacting via a Coulombic inter-particle potential are studied. We investigated structural transitions when the system goes from a three-dimensional (3D) to a one-dimensional (1D) configuration. The sequence of transitions are classified as of first and second order. The ground state configurations are analyzed with respect to their symmetry. The results are summarized in a phase diagram where the different configurations are identified. We also investigate the behavior of the symmetry of the ground state configuration for large systems. Ultimately a normal mode analysis was realized and we compare our results with the modes of oscillation of 2D systems.

Chapter 8 The response of the system to temperature was investigated. We found that the system possess inhomogeneous melting, i.e. the melting process is not uniform throughout the cluster. The region of the cluster closest to the center of the cluster has a lower melting temperature than the extremum parts of the cluster that are situated along the $z-$direction. Moreover, the melting temperature of the inner region of the cluster depends on the specific ordered state, i.e. it is large when the cluster is in the multiple ring structure arrangement than when it has a non-symmetric configuration.

1.2 DUST CHARGED PARTICLES AND DUSTY PLASMAS

One important example of strongly correlated systems is dusty plasmas. A dusty plasma is composed of micron size solid objects immersed in a plasma, i.e. a solution formed by electrons, ions, and neutrals. Most often, these small objects or dusty particles are electrically charged. Dusty plasmas appear in many different situations. In space we can find dust in interplanetary space, comets and planetary rings. It also plays an important role in technology, in particular in the fabrication process of silicon-based integrated circuits. In the meantime the study of dusty plasmas became a solid field of investigation. Such a system offers a unique opportunity to investigate physical phenomena relevant to atomic systems such as phase transitions, oscillations, and wave-wave or wave-particle interactions.

1.2.1 Spokes in the Saturn's B ring

The rings of Saturn have puzzled astronomers ever since they were discovered by Galileo in 1610, during the first telescopic observations of the night sky. The puzzles have only increased since Voyagers 1 and 2 imaged the ring system extensively in 1980 and 1981. In the early 1980s images of Saturn's rings taken by Voyager 2 revealed certain features in the B ring (see Fig. 1.1(a)). The spacecraft spotted a pattern of nearly radial "spokes" rotating around the outer portion of Saturn's dense B ring. The spokes found in the B-ring appears only at radial distances between 43,000 kilometers and 57,000 kilometers above Saturn's clouds. As the spacecraft approached Saturn, the spokes appeared dark against a bright ring background. As the Voyager departed, the spokes appeared brighter than the surrounding ring areas. This observation, i.e. that the spoke material scatters sunlight more effectively in the forward direction – indicated that the material is a fine dust.

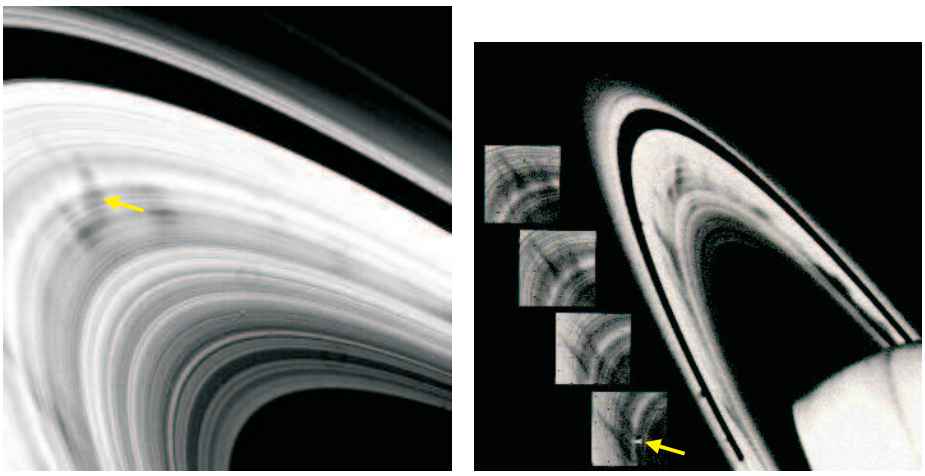

(a) The spoke region is indicated by the yellow arrow.

(b) A sequence of four images taken at roughly 10-minute intervals is shown as inset panels. Eventually a small spoke, pointed by the yellow arrow in the fourth inset image, appears in between several more prominent spokes.

FIG. 1.1: *Picture of Saturn's rings obtained by Voyager 2 on* 22^{th} *of August 1981. Contrast enhancement reveals numerous spokes in the B Ring.*

Perhaps the most interesting aspect of the discovery, is that spokes are not stationary structures. Indeed, they develop remarkably fast, with new spokes forming in as little as five minutes (see Fig. 1.1(b)). It is thought that gravitational forces alone cannot account for the spoke structure, and it has been proposed that electrostatic repulsion between ring particles may play

a role. The leading theory is that spokes are made up by tiny dust charged particles suspended above the main ring by electrostatic repulsion.

While electrostatic charging may create spokes by levitating charged dust particles above the rings, the exact cause of the formation of the spokes is not well understood. The charging process may be caused by bursts of plasma generated in localized regions by micro-meteoroids that sporadically plunge into the rings. The understanding of the generation and dynamics of the spokes may enhance our comprehension on the magnetic field and the planet's magnetosphere, and how these systems interact with the rings and atmosphere. Nevertheless, the recent insertion of the Cassini spacecraft into orbit around Saturn, now with higher spatial and temporal resolution than Voyager's, might contribute to resolve the non understood phenomena involving the Saturn's B ring.

1.2.2 Charged dust and its impact upon the microprocessor's industry

At the same time that Voyager 2 discovered the existence of spokes upon the Saturn's ring, the silicon-based industry was facing its own, but also related to charged dust, intriguing problem. Dust appeared into the fabrication of silicon-based integrated circuits as a "killer" particle. To create an electronic chip requires that multiple layers be added onto a semiconductor wafer, then parts of them etched away. Parts of the wafer which are not wished can be, for example, oxidized by contact with a mono-atomic oxygen gas, and the resulting substance can be somehow removed, e.g. via a vacuum pump. A mono-atomic oxygen plasma can be created by exposing oxygen gas (O_2) to ionizing radiation generated in a parallel-plate arrangement typically powered by 13.56-MHz RF source (for an example of an experimental setup see Fig. 1.2). At the same time, free radicals, i.e. positive ions and electrons, are also generated. Plasma-etched microstructures can be 500 times smaller than the diameter of a human hair. These finer structures make it possible for circuits to become more complex and faster.

Surprisingly a large quantity of chips did not achieve their desirable physical properties due to the presence of wafer's contamination by micron-size particles. This fail in the chip's fabrication represented a considerable loss of profit for the electronic enterprises at that time. Initially the cause was due to contamination from the cleanrooms where the integrated circuits were manufactured. Then, a big effort was directed to improve cleanroom's conditions, but no significant change was obtained. Eventually, in 1989 G. K. Selwyn *et al.* [4] found accidentally that the contamination was happening inside the plasma processing reactors that are used to deposit and etch thin films on the wafers. In an experiment for measuring the concentration of reactive gas a laser light was shone into a plasma used to etch Si wafers. As a result, a non-expected intense bright light was observed from a localized cloud region indicating the

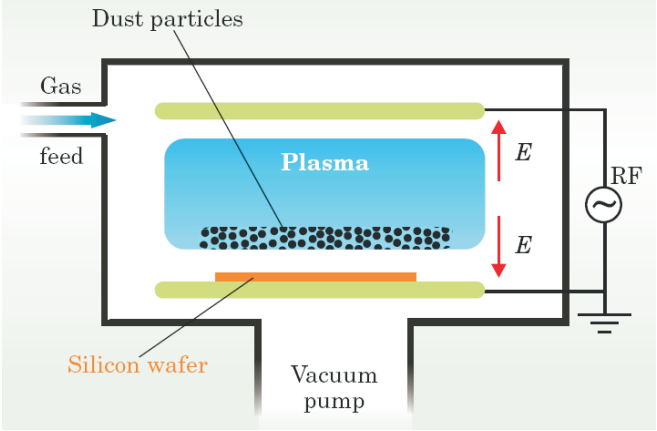

FIG. 1.2: Plasma chamber used for dusty plasma discharge. From Ref. [3].

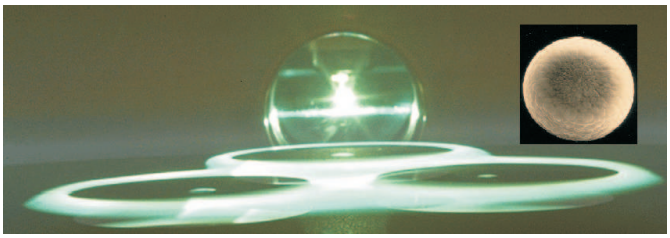

FIG. 1.3: Dust plasma rings encircling silicon wafers in a plasma processing device. Inset shows a typical dust particle of 20μm of diameter generated inside the plasma chamber. From Ref. [4].

presence of micron-sized particles in the plasma (see Fig. 1.3). The plasma environment creates unwanted dust particles. For example, plasma-assisted chemical reactions lead to the formation of SiO_2 particles by coagulation of molecular ions. Due to the need to get rid of free radicals, many machines now use a downstream plasma configuration, where the plasma is formed remotely and channeled to the wafer.

1.3 DUSTY PLASMA GETTING INTO PHYSICS: A RESEARCH FIELD

There are many reasons to study a dusty plasma. Dusty plasma physics is now a solid field of research with many research lines. The leading motivation for the enormous research activity in dusty plasma systems is that they enable to study a vast variety of novel phenomena in condensed matter, like melting,

freezing [5, 6], the glass transition [7, 8], strong-coupling effects, waves and Mach cones in a micro-scale. The main forces acting on the dust are: dust-dust electrostatic interaction, ion drag forces, electrostatic forces due to the electrodes (see Fig. 1.2) and thermophoretic forces. In this section we will give an overview of a few dusty plasma experiments in different conditions.

1.3.1 Dusty plasma crystallization

At first we wish to describe the crystallization process as a consequence of the mutual electrostatic interaction between the charged particles. The simplest situation we can imagine is that of a set of point charges immersed into a neutralizing background. Such a model has been imagined as early as in the 1930s by Eugene Wigner [1] who considered the situation of ions in a "sea" of electrons to study the crystallization order in metals. For simplicity we start by considering the one-component plasma (OCP), i.e. a system formed only by one sort of charged particles. Here the background is only necessary to ensure overall neutrality.

In a OCP system the charged particles interact via a Coulomb potential. Such a system is found in ion clusters confined by Paul- and Penning traps. The thermodynamic phase of an OCP is completely specified by the Coulomb coupling parameter

$$\Gamma \equiv \frac{Q^2}{4\pi\varepsilon_0 b_{WS}} \frac{1}{KT} \tag{1.1}$$

where T is the temperature of the charged particles and Q the charge per particle. As a measure of the interparticle distance the Wigner-Seitz radius $b_{WS} = (3/4\pi n)^{1/3}$ is defined where n is the density of the charged particles.

A OCP system is considered strongly coupled when the interaction energy exceeds the value of the thermal energy, i.e. when $\Gamma > 1$. Numerical simulations [9] showed that a system of charged particles self organize in a crystalline structure corresponding to a body centered cubic (bcc) arrangement when the coupling parameter exceeds a critical value of $\Gamma_c = 168 \pm 2$. For $\Gamma < \Gamma_c$ the particles are in a liquid phase.

In $2D$ systems the crystallization process occurs at the critical value $\Gamma_c = 125$ [9]. The Wigner-Seitz radius is defined as $b_{WS} = (\pi n)^{-1/2}$ and the minimum energy configuration is a hexagonal structure.

Differently from a OCP system the interparticle interaction for the charged dust in a plasma environment is not the pure Coulomb interaction [10]. The presence of free electrons and ions changes the interparticle potential by introducing a shielding effect. The interparticle interaction potential for the dust particles is described by the Debye-Hückel potential (also named Yukawa potential)

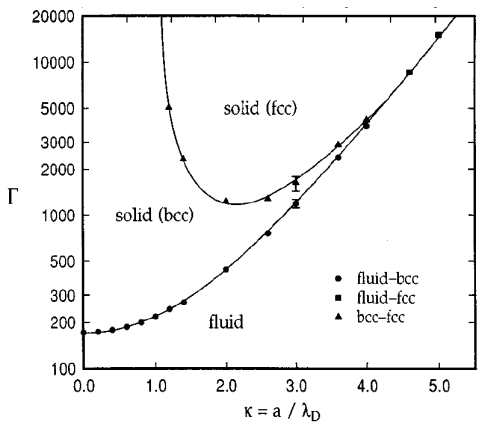

FIG. 1.4: Phase diagram of Yukawa $3D$ systems in the $(\kappa \times \Gamma)$ plane. The melting line increases almost exponentially with the screening strength. In the solid phase two different crystal structures, bcc and fcc are found. From Ref. [11].

$$\phi(r) = \frac{Q}{4\pi\epsilon}\exp\left(-\frac{r}{\lambda_D}\right), \tag{1.2}$$

where λ_D is the Debye shielding length

$$\lambda_D = \left(\frac{1}{\lambda_{D,e}^2} + \frac{1}{\lambda_{D,i}^2}\right)^{-1/2}, \tag{1.3}$$

with $\lambda_{De,i} = \sqrt{\epsilon_0 k T_{e,i}/n_{e,i}e^2}$, where the indices 'e' and 'i' refer to electrons and ions, respectively. Besides the Coulomb coupling parameter a Yukawa system is characterized by a second component, i.e. the screening strength $\kappa = b_{WS}/\lambda_D$, which is the Wigner-Seitz distance b_{WS} in units of the Debye length.

The phase diagram for the $3D$ Yukawa interacting system in $\Gamma - \kappa$ space is shown in Fig. 1.4 [11]. The solid phase itself shows two different crystalline structures: for lower values of κ the bcc structure as in the OCP is found. For stronger screening the fcc structure is obtained. For increasing screening strength the interaction becomes more and more like a hard-sphere potential. The packing density for spheres in the bcc structure is 68% whereas it reaches 74% in the fcc structure (the fcc structure is what one would obtain from stacking oranges into several layers). Thus at higher screening an increased packing density becomes more favorable.

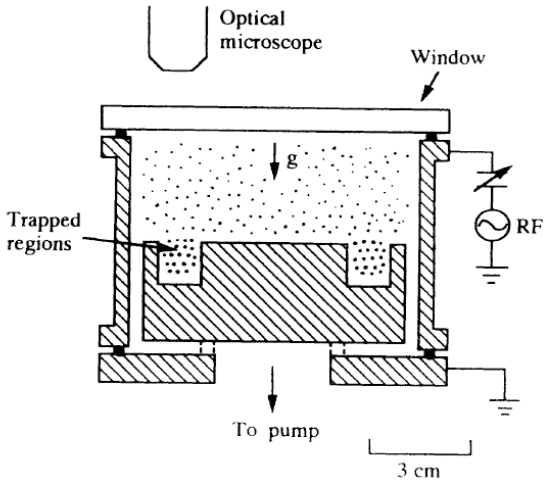

Fig. 1.5: Sketch of the lateral view of the cylindrical discharge system. From Ref. [12].

1.3.2 Complex plasmas in the sheath of an rf discharge

Ref. [12] reported the first direct experimental observation of the Coulomb liquid and crystal phase in a strongly coupled dusty plasma where the dust particles were confined in a $2D$ sheath. The experiment was conducted in a cylindrical symmetric rf plasma system. Fig. 1.5 shows the lateral view of the experimental set-up. The plasma chamber consists of a hollow outer electrode capacitively coupled to a 14 MHz rf power amplifier, a grounded center electrode with a ring-shape groove on the top for particle trapping, and a top glass window for observation. The micrometer-sized SiO_2 particles were generated through gas-phase reaction and aggregation by introducing O_2 and SiH_4 gases into the chamber with a 10 mTorr background argon gas. The particle size and density were controlled by adjusting the gas flow and pressure. Particles could be very well trapped in the toroidal groove. A digital video recording system was used to monitor the image of the particles illuminated by a He-Ne laser through an optical microscope mounted on the top of the chamber. In the solid phase, different colloidal crystals were observed in the groove region. Fig. 1.6 shows the different crystal structures. A hexagonal crystal was observed which has the lowest energy for a 2D infinite system. It is well known that the hexagonal lattice is the most energetically favored structure for infinite 2D systems [10].

The latter experiment is further modified to be able to accommodate one layer of spherically symmetric Wigner crystals. Instead of the large radius groove in the previous experiment, a hollow coaxial cylinder with 3-cm diameter

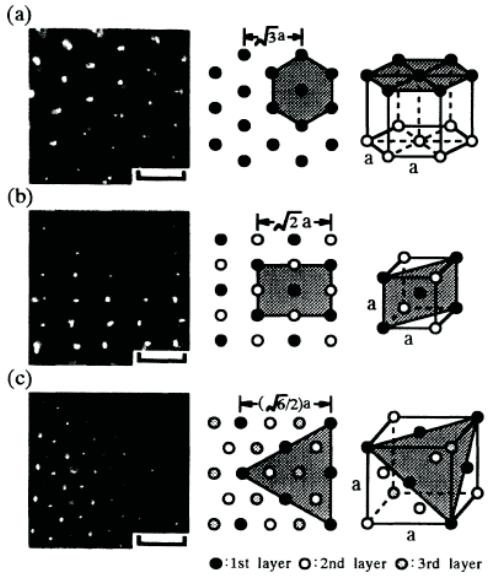

FIG. 1.6: Micrographs and sketches of the different crystal structures. (a) Hexagonal; (b) bcc; (c) fcc. The center column corresponds to the structures in the micrographs. The graded areas in the sketches are normal to the optical axis. The bars in the left pictures correspond to 200μm. From Ref. [12].

and 1.5-cm height is put on the bottom electrode to confine dust particles in weakly ionized glow discharge generated in Ar at a few hundred mTorr using a 14-MHz rf power system [13]. Typical images of the cluster structure are shown in Fig. 1.7 for different particle numbers. For small N, particles are alternately packed in concentric shells with periodically oscillating occupation numbers as N increases which was previously predicted by Bedanov and Peeters [2]. The thermal induced collective excitations are dominated by the intershell angular motion. For large N, the large triangular core surrounded by a few outer circular shells appears and supports vortex-like excitations, which induce uniform and isotropic motion.

In the pioneering work of Prof. A. Piel's group in Kiel (Germany) a dusty plasma system was created in the laboratory by introducing spherical micrometer sized particles into a radio-frequency (rf) discharge. Due to the different polymer composition the physical and chemical properties of the microparticles are very different and can be adjusted for the desired application. Fig. 1.8 shows an electron microscopy image of those microparticles. The density of such particles is typically of 1.5g/cm3. The main characteristic of those particles is that they have: spherical shape, hydrophilic surface, high temperature

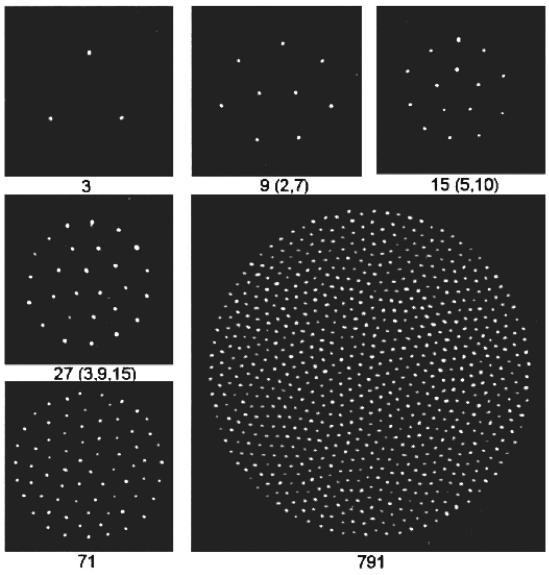

Fig. 1.7: Snapshots of the microimages of typical cluster structures for different number of particles N. For displaying purposes, the scales are not the same for the different pictures. The typical interparticle spacing is between 0.3 and 0.7 mm. From Ref. [13].

resistance usually up to 300 ^oC, superior mechanical stability (pressure stable), and extremely high resistance in all organic solvents.

The experiment was performed in a capacitively coupled parallel plate rf discharge operated in argon at a quite low gas pressure of 1.6 Pa to ensure weak damping (see a scheme in Fig. 1.9). Melamine/formaldehyde microspheres of 9.47 μm diameter ($m = 6.73 \times 10^{-13}$ Kg) are dropped into the plasma. The dust grain acquires a negative charge due to a difference in mobility between the electrons and positive ions. Due to the relative large inertia of the dust it does not follow the oscillation of the electric field rather the dust feels an average electric field. The effective electric potential has a minimum in the centre of the chamber and a maximum close to the electrode plates. As a result the electric field acting on the dust points towards the centre. Oppositely, the gravitational force on the dust particles pushes them into the direction of the lower electrode. Ultimately, the dust particles find their vertical equilibrium position somewhere close to the lower electrode. In such a position the downward gravitational force is compensated by the upward electronic force generated by the electrodes. Depending on the mass of the dust it is levitated a few millimeters above the lower electrode. Close to the lower electrode, the microspheres form a nearly $2D$ horizontal structure.

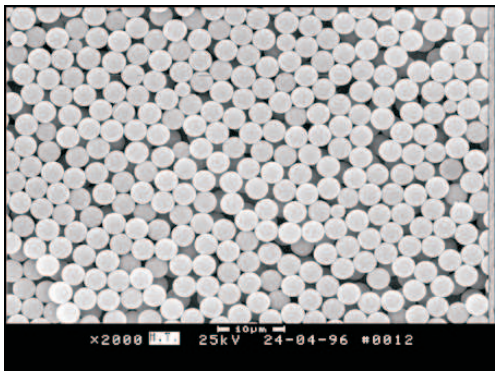

FIG. 1.8: Image of monodisperse particles taken by an electronic microscope. From Ref. [14].

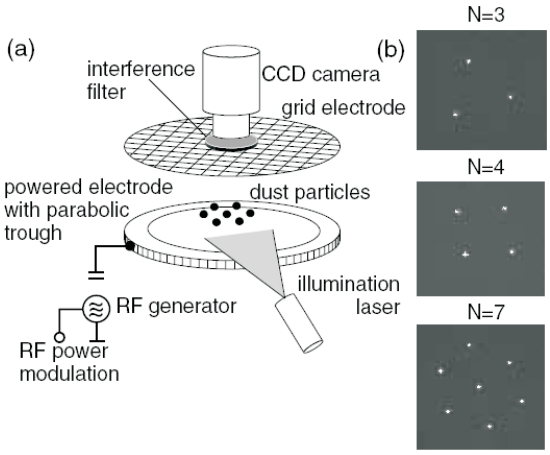

FIG. 1.9: (a) Scheme of the experimental setup; (b) images of the equilibrium of clusters with $N = 3, 4$, and 7 particles. From Ref. [15].

An extended system can be made finite by placing flat metallic barriers on the top of the lower electrode. Those metallic barriers deform the electric field inside the plasma leading to a lateral confinement of the dust. In the inset of Fig. 1.9 we can see the ground state configurations for the finite systems with $N = 3, 4$, and 7 particles. Ultimately the position of those particles can be tracked by using a CCD camera. The motion of the dust particles is damped by a plasma environment which offers a satisfactory precision for the recorded dust trajectory. A scheme of the experimental set up is given in Fig. 1.9.

A normal mode analysis of the clusters was performed by A. Melzer *et al.* Ref. [15]. The normal modes are excited by a pulse modulation of the rf electrode voltage. During the rf power pulse the cluster shrinks in size and is restored to the original size again thus starting oscillations in the cluster. The different normal modes of the cluster are then identified from the trajectories of the particles according to the eigenvectors of the modes. The measured oscillations are shown in Fig. 1.10 for the cluster with $N = 4$ particles. In Fig. 1.10(a), the nonoscillatory ($\omega = 0$) rotation around the center of the potential well is shown for 10 seconds. Additionally, the center-of-mass motion, the breathing, and the antisymmetric modes are shown for 2 seconds in Figs. 1.10(b), (c) and (d), respectively. The breathing mode is obtained as the oscillation of the sum of the radial positions $\sum r_i/N$. The antisymmetric mode is determined from the alternating sum, i.e. $(r_1 - r_2 + r_3 - r_4)/N$ when using the $N = 4$ cluster as an illustrative example. The oscillation frequencies and damping constants are derived by a best fit of a damped harmonic oscillator. The latter obtained normal modes agree with those firstly predicted by Schweigert and Peeters [16].

1.4 DUSTY PLASMA IN THE ABSENCE OF GRAVITATIONAL FORCE

In the previous section we saw that the dust particles, when at equilibrium position self organize in layers close to the lower electrode. The gravitational force pulls particles downwards which are equilibrated by the upward electric field. The picture is different when dusty plasma experiments are realized at the absence of gravity. The weightlessness provided by space vehicles in orbital free fall is ideal to simulate experiments in the absence of gravity. This can be realized in parabolic flights of an airplane. But the prospect of a weightless laboratory environment was so attractive that the first physics experiment on the International Space Station (ISS), begun in February 2001, was a dusty-plasma experiment [17].

A video image of one of the dust structures (Fig. 1.11) shows a variety of features, including a sharply defined void in the center, a stable crystal-like array below the void, and fluid vortices along the horizontal axis and outer edges [17].

It is clear from Fig. 1.11 that in the absence of gravity, we can see different thermodynamic phases at the same temperature, i.e. liquid- and solid-like phenomena can coexist. Charged dust particles in a plasma are affected by their mutual electrostatic interactions and by interaction with gas molecules and ions. Ion drag, which can be the dominant force under weightless conditions, is thought to have caused the void seen in Fig. 1.11 by pushing dust particles out of the center of the plasma chamber's rf discharge.

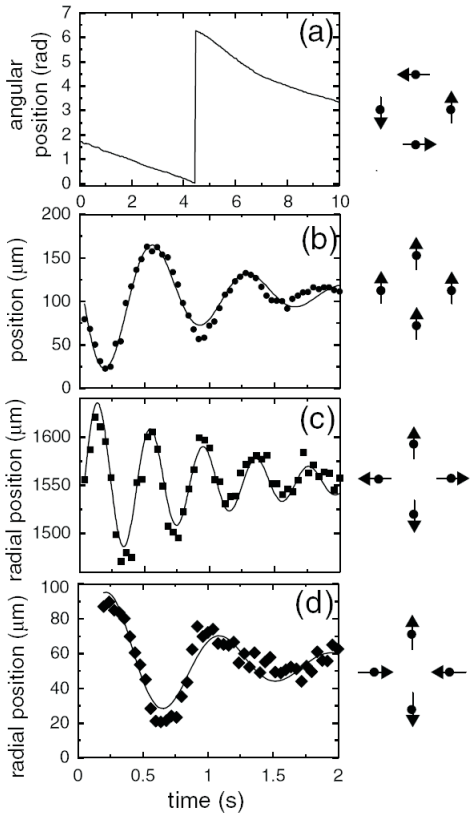

FIG. 1.10: Normal modes of the $N = 4$ cluster. (a) Rotation around the center of the potential well, (b) center-of-mass motion, (c) breathing mode, (d) antisymmetric mode. The symbols denote experimental values and the lines are best fits of damped oscillations to the experimental data. From Ref. [15].

1.5 SPHERICAL DUSTY PLASMA CLOUD: COULOMB BALLS

Recently, a new experimental set up developed by Prof. A. Piel's group allowed the formation of crystalline spherical clouds, called Coulomb balls, which are made up of micrometer colloidal particles in a dusty plasma [18]. Coulomb balls show structural similarities with other strongly coupled systems such as crystallized ion clusters [19, 20], but show differences in structure that are attributed to shielding by the surrounding plasma [21]. Differently from previous experiments [15, 22] the formation of Coulomb balls requires a combination of dielectric walls inside the discharge chamber and an upward temperature gradient. A side view of the plasma reactor is shown in Fig. 1.12(a). The

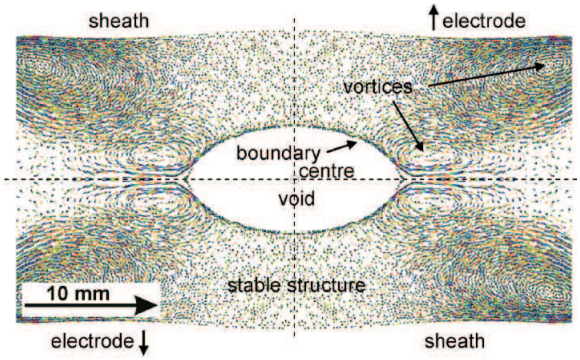

Fig. 1.11: Colour coded trajectories of microparticles of 6.8μm diameter observed over 3 s. The observed original video image, covering approximately a quarter of the field shown here, was mirrored around the main chamber axes to show the full complex plasma structure and dynamics between the electrodes (not shown here). The main structural features are: (1) the microparticle-free void in the centre, (2) the sharp boundary to the complex plasma, (3) the stable and regular structure along the vertical central axis, and (4) the vortices along the horizontal axis and the outer edges. From Ref. [17].

discharge parameter are rf amplitudes of 20-30 V at a frequency of $\omega = 13.56$ MHz and neutral gas pressures of $p_{gas} = 20 - 120$ Pa (argon). At the center of the electrode a glass box with a side length of 30 mm is placed. The upper and lower side of the box are open. Additionally, the lower electrode can be heated to establish a temperature gradient. Particles with a diameter of $d_t = 9.55\mu$m are inserted into the chamber to be used as tracer particles. A manually driven dispenser mounted above the glass box is used to inject the Colomb ball particles. The latter particles have a diameter $d_c = 4.8\mu$m and get negatively charged by collecting electrons from the plasma. The gradient temperature is responsible for an upward thermophoretic force [23] defined as

$$\overrightarrow{F}_{th} = -4.67 n k_B \lambda \left(\frac{d_t}{2}\right)^2 \overrightarrow{\nabla} T, \tag{1.4}$$

where d_t is the diameter of the tracer particles, $\lambda = 1.26 \times 10^{-4}$m (50 Pa, Ar) denotes the mean free path for atom-atom collisions, n the number density, and $\overrightarrow{\nabla} T$ the temperature gradient of the neutral gas.

Finally, the formed Coulomb balls are visualized by means of the video-microscopy set-up shown in Fig. 1.12(b). A laser sheet is used to illuminate a thin slice of the trapped dust cloud whose image is recorded by a CCD camera.

The basic principle involving the confinement of Coulomb balls is summarized in Fig. 1.13. Each particle inside the glass box is affected by the gravitational force $\overrightarrow{F}_g$. The thermophoretic force $\overrightarrow{F}_{th}$ and the vertical component of

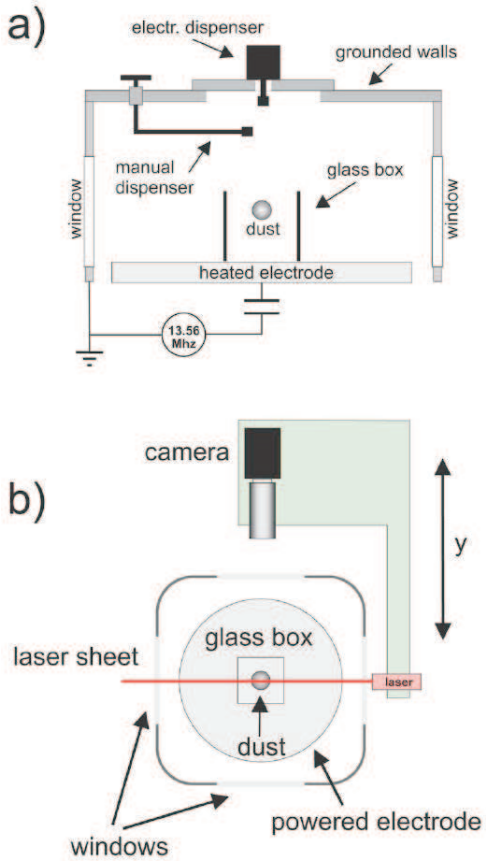

FIG. 1.12: (a) A schematic cross section of the discharge chamber. The powered electrode is located inside the grounded vacuum vessel. The dust particles are confined in a cubic glass box located on top of the electrode. (b) Top view of the video microscopy setup. A vertical laser sheet illuminates a thin slice of the dust cloud. Images are taken at right angle by a CCD camera with a macro lens. From Ref. [18].

the electric field force $\overrightarrow{F}_E$ are directed upward. Due to surface charges on the glass wall and electric fields inside the trap, the negatively charged dust particles are repelled from the glass walls and the electrode toward the bulk plasma. Ultimately, a steady flow of electrons and ions from the bulk plasma onto the glass walls and the electrode causes a downward-directed ion-drag force $\overrightarrow{F}_{ion}$.

In Ref. [24] it was shown that Coulomb balls are not subject to the formation of dust-free regions (voids) and have an unusual structure of nested crystalline shells. Surface shell particles are arranged in patterns with five or six neighbors. Ref. [18] showed that by increasing the temperature of the lower electrode T_{el}

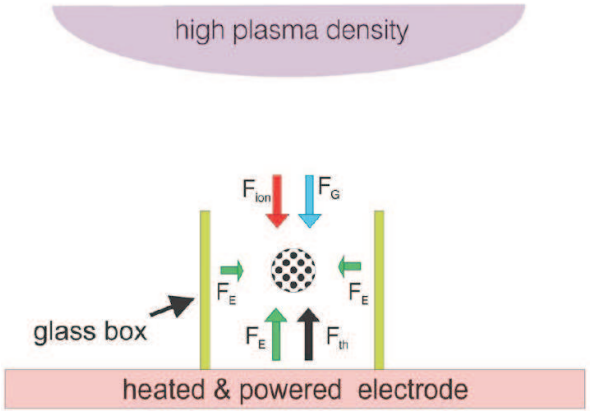

Fig. 1.13: The superposition of gravity (F_g), thermophoretic force (F_{th}), electric field force (F_E), and ion-drag force F_{ion} yields a stable confinement of the Coulomb ball inside the glass box. From Ref. [18].

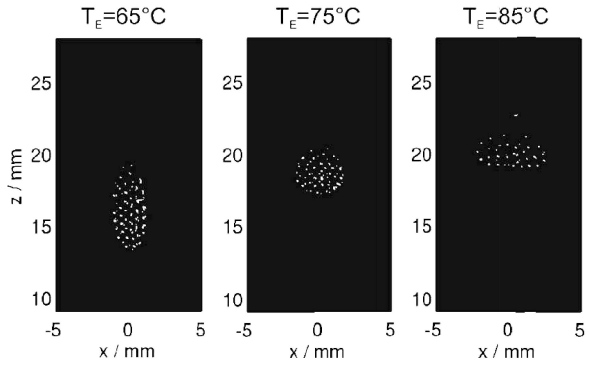

Fig. 1.14: Vertical section through the center of a trapped Coulomb ball at different electrode temperature T_{el}. With increasing temperature the shape of a trapped Coulomb ball merges from prolate to oblate. From Ref. [18].

from 65 to 85^{o}C, the shape of the dust cloud varies from prolate to oblate. At $T_{el} = 75^o$C, the trapped Coulomb ball is mostly spherical (see Fig. 1.14). Moreover, while small systems are in a solid phase, large systems show melting effects Ref. [24].

Coulomb balls are strongly coupled systems with a coupling parameter $\Gamma = Q^2/a\kappa_B T \gg 100$. In such systems, particles interact via a Yukawa type pair potential, $V = (Q^2/r)e^{-r/\lambda_D}$, where λ_D is the Debye shielding length of the plasma. In a recent publication on Coulomb balls by M. Bonitz *et al.* [21] the sensitivity of the structural properties of the cluster to the type of screening

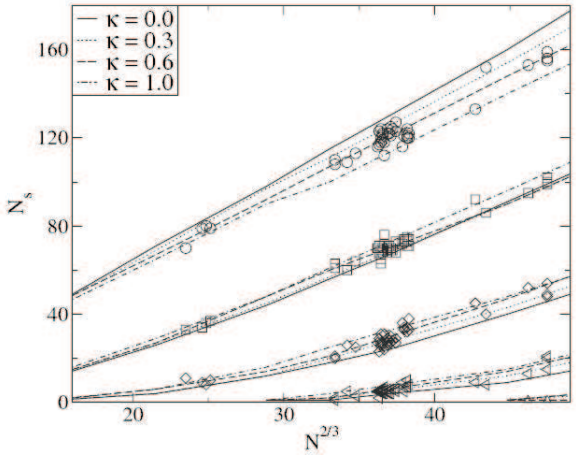

FIG. 1.15: Experimental (symbols) and simulation (lines) results for the shell population of three-dimensional Coulomb clusters at different values of κ (see inset). From Ref. [21].

strength was explored. By means of experiments and computer simulations, they found that the number of shells is independent of the shielding while the shell occupation numbers are sensitive to screening which could be qualitatively explained by using an isotropic Yukawa interparticle interaction potential. A set of systems ranging from $N = 100$ to 500 particles was investigated. The number of particles per shell obtained by experiment and molecular dynamics simulations were compared (see Fig. 1.15). From a best fit to the experimental data, a screening parameter $\kappa = 0.62 \pm 0.23$ was found.

1.6 METALLIC BALLS

Another possibility to construct finite Wigner crystals are by means of the metallic balls experiment. The experiment was developed by Prof. M. Saint Jean and co-authors [25] at Paris (France) and a scheme of the experimental set up is shown in Fig. 1.16. The experimental set-up consists of charged metallic balls on the bottom electrode of a plane horizontal capacitor, the upper electrode being a transparent conducting glass. To get the balls charged, a potential V_e of 1000 volts is applied to this capacitor. And in order to confine the balls, another potential V_c of 2000 volts is applied to a metallic lateral frame intercalated between the two capacitor electrodes. The shape of this lateral frame can be changed which gives the possibility to generate an anisotropic

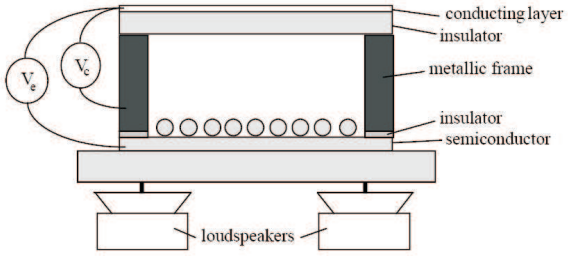

Fig. 1.16: Experimental set-up of the metallic balls experiment. From Ref. [25].

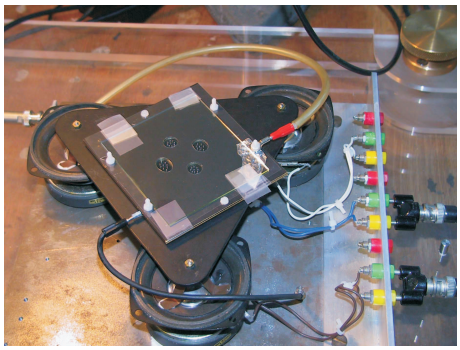

Fig. 1.17: Picture of the metallic balls experimental device where four Wigner crystal cell can be generated simultaneously. Courtesy of Prof. M. Saint Jean.

confinement. The experimental cell is fixed on a plate that leans on three independent loudspeakers. The temperature is simulated by mechanical shaking introduced by the loudspeakers. In this way several mechanical properties could be observed and a melting temperature was determined [26]. A real picture of the experiment is shown in Fig. 1.17.

To obtain the configuration of minimum energy, first the cell is strongly shaken and the system is liquid at this initial stage. Next, a sequence of appropriate annealing introduced by loudspeakers vibrations brings the system to a stable configuration. Throughout the experiment, images of array balls are recorded in real time using a CCD camera onto a VHS videocassette recorder. By analyzing these records and measuring the time spent in each observed configuration, the 'ground state configuration' was retained as the most frequently observed state. The main advantage of this system is that the number of particles is obviously perfectly controlled and that the confining potential can be tuned continuously without difficulty. Moreover, the spatial configuration is directly observed at the macroscopic scale and in real time using a video camera.

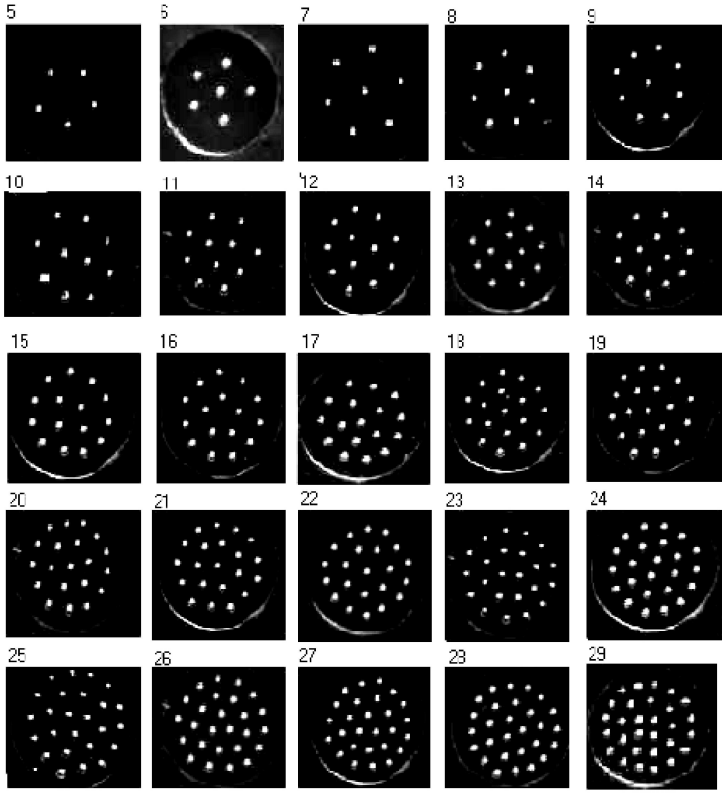

FIG. 1.18: Examples of ground-state configurations observed for $N = 5$ to 29. The diameter of the circular frame is 10mm. From Ref. [25].

For isotropic circular confinement the system of metallic balls at low temperature exhibits self-organized patterns consisting of concentric shells on which the balls are located. Typical configurations are displayed in Fig. 1.18 for systems with several different number of particles. For $N = 3 - 5$, regular polygons are formed. For $N = 6$, a centered pentagon $(1, 5)$ is formed with one particle in the center and 5 particles on a pentagon. States with (1,6), (1,7), (1,8) and (2,8) are obtained when N increases from 7 to 10. Further increasing N to 16 causes an alternate increase of inner and outer shells. As it was widely discussed in the literature [16, 27, 28], this peculiar structure is due to the competition between the ordering into a triangular lattice symmetry, which appears for infinite two-dimensional electrostatic systems, and the circular symmetry imposed by the confining potential.

The configurations shown in Fig. 1.18 were compared to numerical results obtained for systems of particles interacting via a Coulomb [2, 16, 27, 29] and

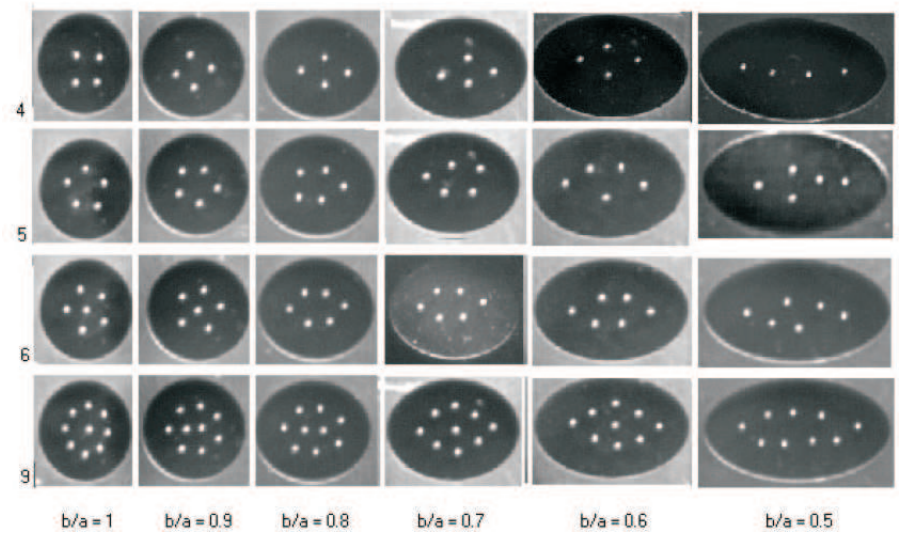

Fig. 1.19: Ground state structures obtained for an elliptic confinement; the asymmetric ration b/a where b and a are the main length of the elliptic frame is varied from 1 to 0.5 for $N = 4, 5, 6$ and 9 particles. From Ref. [30].

logarithmic [27, 28] interparticle pair potential. Such a comparison showed that the observed configurations are in excellent agreement with those calculated for a logarithmic inter-particle interaction potential and a parabolic confinement. Therefore, the metallic ball experiment can be used as a model system particularly well adapted to study the properties of vortices in mesoscopic superconductors [31]. Moreover, Ref. [32] showed that the interaction between two conducting metallic spheres in the metallic ball experiment is well described by a modified Bessel function of second kind. Additionally, it was shown that for typical distances between spheres in system with few particles, the interaction potential can be approximated by a logarithm function, i.e. the asymptotic limit of the second order Bessel function for short distances. In a consecutive work by the same authors [30] the behavior of a finite number of charged metallic balls confined in a mesoscopic elliptic frame was investigated. They investigated the influence of the asymmetry of the confinement potential on the ground state configuration. Elliptic metallic frames with different asymmetric ratios b/a, where 'b' and 'a' are the main length of the lateral elliptic frame, were considered. Fig. 1.19 shows the ground state (GS) configurations obtained for clusters with different number of particles: $N = 4, 5, 6$ and 9 and different values of the asymmetric ratio. In this thesis I present my studies on the effects of the anisotropy of the confinement potential onto the mechanical

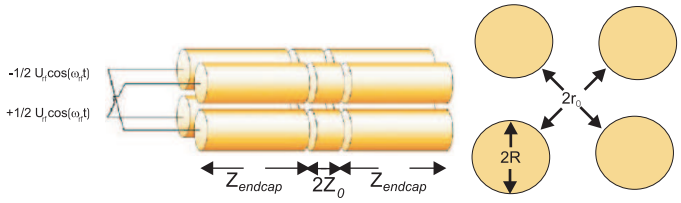

FIG. 1.20: Sketch of the linear Paul trap used in the experiment. Typical values for the experiment are: $r_0 = 3.50$, $R = 4.00$mm, $z_0 = 2.70$, $z_{endcap} = 20.00$mm, and $\omega_{rf} = 2\pi \times 3.88$MHz and an electric field amplitude U_{rf} of about a few hundred volts. From Ref. [33].

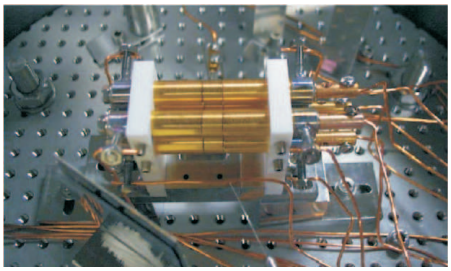

FIG. 1.21: Picture of the actual Paul trap used in the experiment. From Ref. [33].

and static properties of finite size Wigner crystals. I consider systems formed by particles interacting via a logarithmic potential.

1.7 RELATED SYSTEMS

1.7.1 Linear Paul trap

A Linear Paul trap is a quadrupole ion confinement that uses DC and radio frequency (RF) oscillating AC electric fields to trap ions. The 3D quadrupole ion trap was created by Wolfgang Paul who shared the Nobel Prize in Physics in 1989 [34, 35]. Such an ion trap is a fundamental component of a mass spectrometer to analyze ions. Since the first realization of two- and three-dimensional radio frequency traps for charged particles in the 1950's [34, 35], many varieties of such traps have been suggested and constructed. Even though the linear Paul trap in retrospect seems to be one of the most obvious configurations for obtaining three-dimensional confinement.

Fig. 1.20 shows schematically linear Paul trap developed by Prof. M. Drewsen's group at Aarhus (Denmark). A physical picture of the experiment is shown in Fig. 1.21. The ion trap experimental set-up consists, like a standard

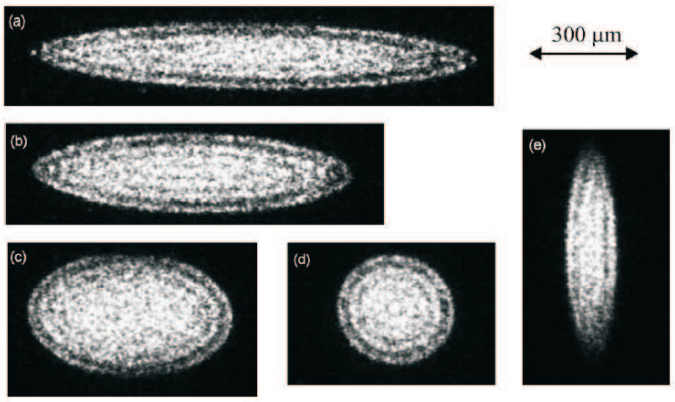

Fig. 1.22: Pictures showing two-dimensional projections of pure $^{24}Mg^{+}$ ion Coulomb crystals containing ~ 500 ions for a series of different axial potentials. The real crystals can be imagined by noting that they have rotational symmetry around the horizontal symmetry axis. In all the pictures, the rf voltage was constant, while the dc voltages U_{dc} on the eight end-pieces was changed from (a) $U_{dc} = 0.01V$ to (e) $10V$. From Ref. [36].

quadrupole mass-filter, of four electrodes mounted such that by applying an rf voltage of the same phase to diagonal electrodes, but with a phase shift of 180^o with respect to the nearest electrodes, generates a near-ideal two-dimensional quadrupole field along the plane perpendicular to the direction defined by the electrode (the z-direction). Each electrode is sub-divided into three parts such that a positive dc voltage leads to static confinement along the trap axis (the z-axis). By appropriate choices of the dc and rf voltages and frequency, both axial and radial confinement can be obtained for given trap dimensions [33]. Defining the parameters:

$$a \equiv \eta \frac{8QU_{dc}}{m\omega_{rf}^2 z_0^2}, \tag{1.5}$$

$$q \equiv \frac{2QU_{rf}}{m\omega_{rf}^2 r_0^2}, \tag{1.6}$$

where m is the mass of the ion, Q is the ion charge, ω_{rf} and U_{rf} are the frequency and amplitude of the rf field, respectively, U_{dc} is the voltage applied to the end-pieces, z_0 and r_0 are the trap dimensions defined in Fig. 1.20, and η is a positive geometric parameter dependent on z_0 and r_0.

It is possible to show that when a and q lie within certain stability regions [37] stable single ion motion exists. The motion is generally complex, but when $q < 0.4$ a single ion not too far from the trap center will feel an effective harmonic potential:

$$\phi(z,r) = \frac{1}{2}m\left(\omega_z^2 z^2 + \omega_r^2 r^2\right) \tag{1.7}$$

where ω_z and ω_r are the oscillation frequencies along the z-axis and in the radial plane, respectively, given by

$$\omega_z = \frac{1}{2}\omega_{rf}\sqrt{a}, \tag{1.8}$$

$$\omega_r = \frac{1}{2}\omega_{rf}\sqrt{\frac{1}{2}(q^2 - a)}. \tag{1.9}$$

The trap shown in Fig. 1.20 has the following dimensions: $r_0 = 3.50$, $z_0 = 2.70$, $z_{endcap} = 20.00$mm and $R = 4.00$mm, which have been chosen for having a nearly perfect radial quadrupole rf field and a near-harmonic dc axial potential over a few mm. The applied rf field is resonantly coupled to the trap electrodes at a frequency $\omega_{rf} = 2\pi \times 3.889$MHz with an amplitude U_{rf} typically about a few hundred volts. With a typical dc voltage of $\backsim$ 1V, Eq. (1.7) gives rise to a potential depth of about $\sim$ 1eV.

In the radial plane, the ions will in addition to the force from the effective potential above, be subjected to a fast oscillating force at the rf frequency, but it can be shown that the amplitude of the corresponding motion (often named micro-motion) always will be much smaller than the distance of the ion from the z-axis when $q < 0.4$ [38].

Due to the combination of the trapping forces and the Coulomb repulsion of ions with the same sign, when cooled to sufficient low temperatures spatial ordered states are formed. The detailed crystal structures depend on the actual trapping potential as well as the quantity of various ion species. Fig. 1.22 shows a $2D$ projection of the $3D$ Wigner crystals formed by $^{24}Mg^{+}$.

1.7.2 Quantum dots

Quantum dots, also called "artificial atoms", where the confinement potential replaces the potential of the nucleus, are fascinating objects. These systems are thought to have vast potential for future technological applications [39]: in memory chips, quantum computation, quantum cryptography, and so on.

Confining a small number of electrons N in a two-dimensional electron gas in semiconductor heterostructures, a number of interesting effects arises from the interplay between confinement and the Coulomb interaction [40]. In quantum dots the confinement potential is usually quite shallow, which results in the possibilities that the strength of the long-range Coulomb inter-particle interaction is going to play an important role.

In a pioneering theoretical work, Bryant [41] investigated the electron correlation effects in quantum dots. He considered a two-electron system in a rectangular box with hard-wall potentials and studied the interplay of kinetic and

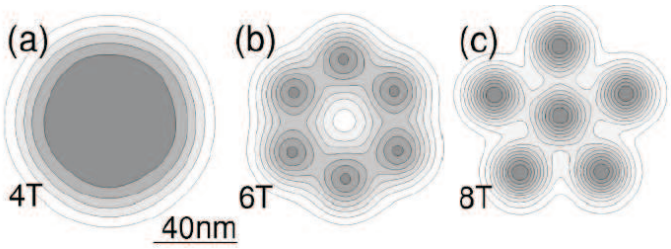

Fig. 1.23: The electron ground state of six electrons in a quantum dot with confinement frequency $\hbar\omega_0 = 3$meV for three magnetic field values. From Ref. [42].

interaction energies as a function of the size of the box. In the infinite-barrier model, the kinetic energy scales with $1/L^2$ where L is the linear dimension of the quantum-well box. While the interaction energy scales as $1/L$ where L is changed without changing the box shape.

For small L (high density system), the electrons behave independently, i.e. as uncorrelated particles, because the Coulomb interaction is insignificant compared to single-particle level spacings. However, when L increases (low density systems) the interactions become important and the level spacings decrease. Electron correlations help to force electrons to form a Wigner crystal. The signature of the Wigner crystal states in a confined system is the degeneracy of the energy levels.

The application of the external magnetic field leads to relative shifts of the energy levels corresponding to different spin-orbital configurations. In consequence, the ground state configuration changes when the magnetic field increases. At a certain, sufficiently high, magnetic field all the electrons have parallel spins and occupy orbitals with successive magnetic quantum numbers. In this state, called a maximum density droplet (MDD), the electron charge distribution still possesses the symmetry of the confinement potential. If, however, the magnetic field increases further, all the occupied energy levels approach the lowest Landau level and become degenerate. Then, the Coulomb interaction leads to a rapid change of the electron distribution. As a result, the confinement-potential symmetry of the electron density is broken and Wigner molecules are formed.

Fig. 1.23 shows an example of the charge density distribution for six electrons in a parabolic dot of energy confinement $\hbar\omega_0 = 3$meV and three different magnetic field values (from Ref. [42]). For a magnetic field of $4.0T$ the charge density well approximates the MDD charge density distribution (see Fig. 1.23(a)). If the magnetic field increases above $5.3T$, the electron system becomes the Wigner molecule with the (0,6) shell structure (see Fig. 1.23(b)). If the magnetic field exceeds $7T$, the Wigner molecule changes its shape into

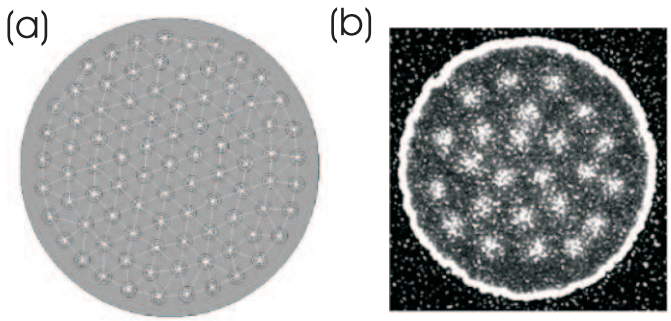

FIG. 1.24: (a) The vortex structure in a superconducting disk with vorticity $L = 104$ (from Ref. [31]) and (b) scanning electron microscope image of vortex pattern in a disk of radius $R = 0.5\mu m$ (from Ref. [43])

the $(1, 5)$ configuration (see the Fig. 1.23(c)), which is the lowest-energy configuration of the classical cluster with six particles [2, 44].

1.7.3 Superconductivity in Type-II superconductors

Superconductor materials are classified as type I and II. In type-II superconductors the coherence length, i.e. the mean free path of cooper pairs, is smaller than the London penetration depth, i.e. the penetration distance of a weak magnetic field. Magnetic field can penetrate type-II superconductors in form of magnetic flux lines called vortices. For such a material a further increase of the external magnetic field leads to a gradual transition from the superconducting to the normal state. On the other hand, superconductor materials that can not be penetrated by magnetic flux lines, and the transition to the normal state occurs abruptly, are called as type-I superconductors. They have in general a very low value for their critical temperature and magnetic field.

The properties of a type-II superconductor change dramatically as it becomes mesoscopic, i.e., can accommodate only a small number of vortices [45]. In a magnetic field, such a superconductor resides in one of a series of discrete states characterized by the vorticity L, i.e. the number of vortices. In mesoscopic superconductors, vortices have stable positions dictated by their mutual interaction and the geometry of the sample. In infinity systems, vortices can arrange themselves in a regular structure known as the vortex lattice, also named the Abrikosov (vortex) lattice. While in finite systems, the sample geometry acts as a kind of confinement potential (since the boundary determines the shielding current pattern and the appearance of vortex images), which makes these systems resemble charged particles confined by some potential. In such samples there is a competition between the triangular Abrikosov

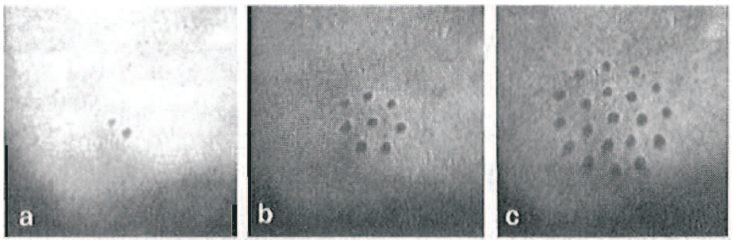

Fig. 1.25: Configuration of (a) 2, (b) 8 and (c) 20 dimples (appearing as dark spots) in an external potential of cylindrical symmetry. From Ref. [46].

distribution of vortices, as being the lowest energy configuration in bulk material and thin films, and the sample boundary which tries to impose its geometry on the vortex distribution. It was shown [31] that vortices form shell structures in superconducting disk and for large radius of the disks the influence of the boundary diminishes and the triangular lattice may reappear (see Fig. 1.24(a)). Concentric shell structures of vortices were recently observed experimentally using the Bitter decoration technique (see Fig. 1.24(b)).

1.7.4 Electrons on the surface of liquid helium

Historically, Wigner first calculated in 1934 that an electron-liquid to electron-solid phase transition should occur in the 3D Fermi system at low temperature. The first experimental indication for Wigner crystallization was obtained by Grimes and Adams [47] for a $2D$ system of a monolayer of electrons trapped on the surface of liquid helium. This electron layer system constitutes a nearly ideal $2D$ Coulomb system since the density of electrons can be varied over several orders of magnitude and the absence of impurities.

The stability of such a localized charge distribution on the surface of liquid helium depends on the applied electric field that pushes the electron towards the helium surface and the number of electrons in the dimple. If one applies a strong electric field perpendicular to the helium surface, the system becomes unstable and the homogeneous electron distribution is destroyed. The electrons become localized in a regular array of pockets, or 'dimples', which constitute a macroscopic analogue of the microscopic Wigner crystal. These many-electron dimples can contain up to 10^7 electrons with a typical diameter of the order of 1 mm. Due to the self-trapping of the electrons the charge in each dimple is fixed and the interaction between individual dimples is dominated by Coulomb repulsion. The arrangement of such dimples at the surface of liquid helium can therefore be considered as a macroscopic two-dimensional Coulomb system. For small number of particles the dimples self-organize in ring configurations as is shown in Fig. 1.25. Oppositely, low electric fields lead to a gradual charge

spread, resulting in the formation of a homogeneous distribution of electrons at the helium surface.

2

Model System and Numerical Approach

In this thesis we investigate the statical and dynamical properties of finite size Wigner crystals. We considered systems of repulsively interacting particles trapped via an external confinement potential. The nature of the interparticle interaction potential depends on the particular system investigated. For a 2D Wigner crystal we consider a logarithmic interparticle interaction potential while that for Coulomb balls and Paul trap systems we assumed respectively, a Yukawa and Coulomb interparticle interaction potential. The experimental facilities to generate external confinement potentials having different shapes, which results in significant changes of the statical and dynamical properties of Wigner crystals, makes us to consider in our model both isotropic and anisotropic confinement potentials. In our model the anisotropy of the confinement potential can be varied continuously and an anisotropy parameter is defined.

The general potential energy form for a system of classical particles interacting repulsively through a potential $\mathrm{V}\left(\mid \mathbf{r}_i - \mathbf{r}_j \mid\right)$ and held together by an anisotropic parabolic confinement potential can be written down as

$$H = \sum_{i=1}^{N} \frac{1}{2} m\omega_0^2 \left(x_i^2 + y_i^2 + \alpha z_i^2\right) + \sum_{i>j}^{N} \mathrm{V}\left(\mid \mathbf{r}_i - \mathbf{r}_j \mid\right), \tag{2.1}$$

where ω_0 is the confinement frequency of a single particle, α the anisotropy parameter of the confinement potential, m the particles' mass, N the total

number of particles, and $\mathbf{r}_i = (x_i, y_i, z_i)$ the coordinate of the ith particle. In the rest of this thesis we will call the potential energy the Hamiltonian since we consider the minimum energy configuration. For classical systems which are described by a Hamiltonian of this form, we are always able to rewrite it in dimensionless form by using appropriate units for the length and the energy.

- Coulomb and screened Coulomb (Yukawa) potentials

  The Hamiltonian of a $3D$ system of particles interacting via a screening Coulomb potential and kept together by an anisotropic parabolic potential is given by Eq. (2.1) with the interparticle interaction potential

$$\mathrm{V}\left(\mathbf{r}_i - \mathbf{r}_j\right) = \frac{q^2}{\epsilon_0} \frac{\exp\left(- \mid \mathbf{r}_i - \mathbf{r}_j \mid /\lambda\right)}{\mid \mathbf{r}_i - \mathbf{r}_j \mid}, \tag{2.2}$$

  where q is the particle charge, ϵ_0 the electric constant, and λ is the screening length of the interparticle interaction potential. The Hamiltonian can be written in the dimensionless form

$$H = \sum_{i=1}^{N} (x_i^2 + y_i^2 + \alpha z_i^2) + \sum_{j>i}^{N} \frac{\exp(-\kappa |\mathbf{r}_i - \mathbf{r}_j|)}{|\mathbf{r}_i - \mathbf{r}_j|}, \tag{2.3}$$

  if we express the coordinates and energy in the following units $r_0 = (q^2/\epsilon\gamma)^{1/3}$ where $\gamma = m\omega_0^2/2$ and $E_0 = \gamma r_0^2$, respectively. The dimensionless inverse screening length, $\kappa = r_0/\lambda$, is a measure of the range of the inter-particle interaction potential. It is clear from Eq. (2.3) that the ground state is a function of the number of charged particles N, the anisotropy parameter α, and the dimensionless screening length κ. The dimensionless Hamiltonian of a pure coulombic system is given by Eq. (2.3) by taking $\kappa = 0$. Although this Hamiltonian is written down for $3D$ systems, it can easily be reduced to $2D$ systems if we omit one of the coordinates.

- Logarithmic potential

  The Hamiltonian of a $2D$ system of particles interacting via an interparticle interacting logarithm potential and kept together by an anisotropic parabolic potential is given by Eq. (2.1) with

$$\mathrm{V}\left(\mathbf{r}_i - \mathbf{r}_j\right) = -\beta \ln\left(\mid \mathbf{r}_i - \mathbf{r}_j \mid\right) \tag{2.4}$$

  for the interparticle interaction potential, where β is a constant related to the potential strength. The Hamiltonian can be written into the dimensionless form

$$H = \sum_{i=1}^{N}(y_i^2 + \alpha z_i^2) - \sum_{j>i}^{N} \ln\left(\mid \mathbf{r}_i - \mathbf{r}_j \mid\right), \tag{2.5}$$

if we express the coordinates and energy in the units $r_0 = (2\beta/m)^{1/2}$ and $E_0 = \beta$, respectively.

Strongly correlated systems at low temperature leads to a wide range of crystal patterns whose structural form depends strongly on the external potential, inter-particle interaction potential and the total number of particles. The study of the static and dynamical properties of these systems requests at first the knowledge of their ground state (GS) and metastable states (MS) configurations. For this purpose we perform Monte Carlo simulation followed by Newton minimization of the hamiltonian. Phase transitions are seen as the temperature of the system is increased. Furthermore, we also performed a normal mode analysis. To simulate the non-zero temperature system we perform Molecular Dynamics simulations. The different thermodynamic phases and the critical temperatures are determined. In what follows we will provide few general remarks about the Hamiltonian of a strong interacting system and its scaling laws. Also we will give a brief overview of the computing techniques, such as Monte Carlo, Newton optimization, normal mode analysis, and Molecular Dynamics simulations that were used in this thesis.

2.1 THE CLASSICAL LIMIT

Quantum dots in a semiconductor environment [40, 48] are created through the application of a lateral confinement potential and by restricting the motion of the electrons in a very narrow quantum well. As a result they usually have the shape of flat disks, with transverse dimensions considerably exceeding their thickness. Our classical 2D model discussed in this thesis is also representative of quantum systems when it is close to the Wigner crystal phase. Before discussing the 2D and 3D classical artificial atoms we want to show that it is not always necessary to solve the full quantum mechanical problem, but that often one can restrict oneself to the classical limit. To do so we will first introduce the full quantum mechanical Hamiltonian which describes N electrons moving in a $2D$ quantum dot with a parabolic confinement and interacting thought a Coulomb potential [51]. It is given by

$$H = -\sum_{i=1}^{N} \frac{\hbar^2}{2m}\nabla^2 + \sum_{i=1}^{N} \frac{1}{2} m\omega_0 r_i^2 + \frac{e^2}{\epsilon} \sum_{i=1}^{N-1} \sum_{j=i+1}^{N} \frac{1}{\mid \mathbf{r}_i - \mathbf{r}_j \mid}, \tag{2.6}$$

with m the effective mass of the electrons, ϵ the dielectric constant of the medium, $\mathbf{r} = (x, y)$ the particles' position and ω_0 is the strength of the confinement frequency.

The Hamiltonian can be expressed in a dimensionless form if we use: $a_0 = \sqrt{\hbar/m\omega_0}$ and $\hbar\omega_0$, respectively as units of length and of energy. The dimensionless Hamiltonian is

$$H = -\frac{1}{2}\sum_{i=1}^{N}\nabla_i^2 + \frac{1}{2}\sum_{i=1}^{N} r_i^2 + \beta^3 \sum_{i=1}^{N-1}\sum_{j=i+1}^{N} \frac{1}{\mid \mathbf{r}_i - \mathbf{r}_j \mid}, \tag{2.7}$$

where the dimensionless electron-coupling constant $\beta = \sqrt{e^4 m/(e^2\hbar^2)/\hbar\omega_0} = a_0/a_B$ with $a_B = \epsilon\hbar^2/(me^2)$ the effective Bohr radius which is a measure of the strength of the electron-electron interaction. The value of the confinement potential ω_0 is large in case of strong confinement. As a result the value of β is small and the system can be treated as a simple quantum problem of non-interacting particles in a harmonic oscillator potential, and the electron-electron interaction can be treated as a perturbation. However, in this thesis we are interested in low density systems and thus in large values of β. Therefore it is interesting to look at the Hamiltonian after the rescaling of the length $r \longrightarrow \beta r$ which is given by

$$H = -\frac{1}{2\beta^2}\sum_{i=1}^{N}\nabla_i^2 + \beta^2\left(\frac{1}{2}\sum_{i=1}^{N} r_i^2 + \sum_{i=1}^{N-1}\sum_{j=i+1}^{N} \frac{1}{\mid \mathbf{r}_i - \mathbf{r}_j \mid}\right). \tag{2.8}$$

Notice that the importance of the kinetic energy term goes to zero for large systems since the energy increases as β^2. This leads to the classical limit in which the particles can be treated as point particles (i.e. close to the Wigner crystallization) and the ground configuration are found by minimizing the hamiltonian

$$H = \frac{1}{2}\sum_{i=1}^{N} r_i^2 + \sum_{i=1}^{N-1}\sum_{j=i+1}^{N} \frac{1}{\mid \mathbf{r}_i - \mathbf{r}_j \mid}. \tag{2.9}$$

2.2 GROUND STATE CONFIGURATION

The stable configuration is a local or global minimum of the potential energy with respect to the position of the particles which in general is a function of the number of particles, and of the interparticle interaction potential. To obtain the minimum energy configuration it is possible to employ the Monte Carlo (MC) simulation technique [52] by throwing randomly a specific number of particles into the confinement potential and let the system relax towards a minimum energy configuration. However, such a method showed a slow convergency

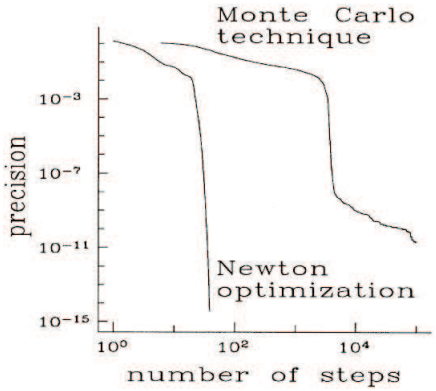

Fig. 2.1: Accuracy of the calculated ground-state energy versus the number of simulation steps, using the Monte Carlo technique, and the present optimized version of the Newton technique for a cluster consisting of $N = 13$ particles. From Ref. [16]

for systems with a relatively large number of particles. To circumvent this problem, we supplement the MC simulation technique by applying the Newton minimization method. As a result one is able to speed up the convergency towards the energy minimum. This procedure was investigated and compared with the ordinary MC method in Ref. [16]. Fig. 2.1 shows the result obtained by both methods. The use of both techniques in conjunction, i.e. Monte Carlo minimization to find roughly the position of the minimum and subsequently the Newton minimization, leads to a considerable increase of the precision and reduction of the needed CPU-time.

2.2.1 Monte Carlo

The Monte Carlo (MC) simulation constitutes a powerful computational tool to calculate the average of physical quantities. Usually one is interested in the value of an average physical quantity. In the classical limit statistical mechanics tells us that the average value of a generic physical quantity $\mathrm{A}(\mathbf{r}^N)$ is given by

$$\langle A \rangle = \frac{\int d\mathbf{r}^N \mathrm{A}(\mathbf{r}^N) \exp\left[-\beta H\left(\mathbf{r}^N\right)\right]}{\int d\mathbf{r}^N \exp\left[-\beta H\left(\mathbf{r}^N\right)\right]}, \tag{2.10}$$

where $\mathbf{r}^N$ and $\mathbf{p}^N$ are respectively the coordinates and momenta of all N particles, and $\beta = 1/K_B T$ where K_B is the Boltzmann's constant.

It might appear that the most straightforward approach would be to compute $\langle A \rangle$ in Eq. (2.10) by numerical quadrature, for instance using Simpson's rule. However, such an approach for most of the physical problems becomes computationally impracticable. The number of points at which the integrand must be evaluated is equal to m^{DN}, where m is the number of equidistant

points along each coordinate, D is the dimensionality of the system and N the total number of particles in the system. For example, if we consider 100 particles in three dimensions and $m = 5$ then we would have to evaluate the integrand in 10^{210} points.

The Monte Carlo algorithm proposed by Metropolis *et al.* [52] is an efficient method to estimate the average value of a given quantity $\langle A \rangle$ shown in Eq. (2.10). Note that the ratio $\exp(-\beta U)/Z$ in Eq. (2.10) is the probability density of finding the system in a configuration around $\mathbf{r}^N$. The Metropolis algorithm uses this latter fact to construct a random walk through the region of space where the integrand of Eq. 2.10 is nonnegligible. In this random walk, a trial move is rejected if it takes you to a relatively improbable region in phase space and it is accepted otherwise. In fact, the result of the Metropolis algorithm, is a stochastic walk through phase space, where only the most probable points, i.e. those with large probability accordingly to the Boltzmann distribution, are visited.

In the approach introduced by Metropolis *et al* [52], the following scheme is proposed:

1. Select a particle at random, and calculate its energy $H\left(\mathbf{r}^N\right)$.
2. Give the particle a random displacement, $r' = r + \Delta r$, and calculate its new energy $H\left(\mathbf{r'}^N\right)$.
3. Accept the move from $\mathbf{r}^N$ to $\mathbf{r'}^N$ with probability

$$acc\left(o \to n\right) = min\left(1, \exp\left\{-\beta\left[H\left(\mathbf{r'}^N\right) - H\left(\mathbf{r}^N\right)\right]\right\}\right) \tag{2.11}$$

Our MC simulation does not involve temperature because it is used to obtain a position close to a stable configuration of the system rather than a specific configuration such as the GS configuration or first lowest energy MS configuration. Moreover, it will be followed by the Newton optimization method. By stable configuration we mean a configuration of minimum energy, i.e. a point in the coordinate space where all first partial derivatives of energy are zero and the dynamical matrix is positive definite.

The input of our MC simulation is a configuration where particles' positions are chosen randomly. One circle in our MC simulation has two steps: 1) we try to move randomly a specific particle, and 2) if the energy of the system decreases the trial move is accepted and the step displacement is increased otherwise the trial move is rejected and the step displacement is decreased. Moreover, we impose a minimum and maximum value of the step displacement. In this way we drive the system configuration to a configuration with low energy.

We try to move particles in sequence and we periodically calculate the percentage of accepted trial moves. If the latter becomes smaller than 10% we stop our simulation.

Our final result from the MC simulation, i.e. a position close to a stable configuration, is used as input for the Newton optimization method. As a result we obtain the exact position of the stable configuration.

This procedure, i.e. Monte Carlo followed by Newton optimization methods, is repeated between 3000 and 100 000 times with different random start configurations depending on the system size. We infer that the GS and lowest energy MS configurations are respectively the configurations with the lowest and second lowest energies among all configurations found. This method of finding minima is not very sensitive to the choice of simulation parameters.

2.2.2 Newton optimization

After n steps in the MC simulation let us suppose that the coordinates of the particles in a cluster are given by $\{r^n_{\alpha,i}; \alpha = x, y; i = 1, ..., N\}$. Then the potential energy in the vicinity of this configuration can be written in the following quadratic form:

$$H = H\left(r^n_{\alpha,i}\right) - \sum_i \sum_\alpha H_{\alpha,i}\left(r_{\alpha,i} - r^n_{\alpha,i}\right) + \frac{1}{2}\sum_{i,j}\sum_{\alpha,\beta} H_{\alpha\beta,ij}\left(r_{\alpha,i} - r^n_{\alpha,i}\right)\left(r_{\beta,j} - r^n_{\beta,j}\right) \tag{2.12}$$

where $H_{\alpha,i} = -\partial H/\partial r_{\alpha,i}$ is the force and $H_{\alpha\beta,ij}$ is the dynamical matrix,

$$H_{\alpha\beta,ij} = \frac{\partial^2 H}{\partial r_{\alpha,i}\partial r_{\beta,j}}. \tag{2.13}$$

The next step in our simulation is based on the condition of minimal total energy, which leads to

$$\sum_j \sum_\beta \left(\eta\delta_{\alpha\beta,ij} + H_{\alpha\beta,ij}\right)\left(r_{\beta,j} - r^n_{\beta,j}\right) = H_{\alpha,i}, \tag{2.14}$$

where $\delta_{\alpha\beta,ij}$ is the unit matrix and the coefficient η is added to assure the stability of the algorithm. It is known that the iteration procedure converges if $\eta + \lambda_{min} > 0$, where λ_{min} is the minimal eigenvalue of the dynamical matrix. The system of linear equations (2.14) is solved using Gauss elimination method [53]. The usual approach guarantees only convergence in the vicinity of the minimum. Therefore, we introduced an empirical damping coefficient η. In the first few iterations, the value for η is set to be large: $\eta = 10 - 100$. If in the next step, the total energy of the system decreases the damping coefficient is reduced, while in the opposite case, the value η is increased. From our experience, we know that such an algorithm for choosing the damping parameter guarantees convergency of the iteration process. We found that about of 10 - 100 steps are needed in order to obtain a relative accuracy $10^{-9} - 10^{-10}$. The exact number of steps depends on the number of particles.

By implementing a large number of different simulations starting from different random initial configurations we are confident that we found the ground state configuration and the first metastable state as long as the number of particles of the system is not too large. Depending on the total number of particles, between several hundred to several thousand random initial configurations were generated.

2.3 EIGENFREQUENCIES AND EIGENVECTORS

After we obtained the GS or MS configuration a normal mode analysis can be performed in order to obtain insight about the linear dynamics of the system. The eigenfrequencies are the square root of the eigenvalues of the dynamical matrix Eq. (2.13). If the system is harmonic, any motion can be expressed as a superposition of normal modes. However, if the system is anharmonic, only at sufficiently low temperatures, where the potential near the minimum can still be well approximated by a harmonic potential, the system behaves harmonically. In the latter case, any small-amplitude motion can still be well described by a sum of normal modes.

For 2D systems confined by a parabolic trap Schweigert and Peeters [16] showed that a large value for the first non-zero frequency indicates that the system configuration forms a magic cluster, i.e. a larger temperature is needed for its first melting process. The eigenvectors of the dynamical matrix gives an indication of the particle trajectory pattern formed during the melting process. In this thesis we have used the normal modes to obtain insight on the relevant melting processes the system can experience as the temperature increases. Moreover, when possible we compared the value of the eigenfrequencies with the different melting temperatures of the systems studied in this thesis.

2.4 MOLECULAR DYNAMICS SIMULATION

We use the Molecular Dynamics (MD) simulation technique for computing the equilibrium properties of the classical systems we investigated. Typical measurements are the average radial or angular particle displacements. Those quantities were computed and together with Lindemann's criterion [54] were used to determine the critical melting temperature of the system. As a MD simulation requests to integrate Newton's equations of motion it naturally follows the trajectories of the particles. This property of the MD method was fundamental in determining the characteristics of the dynamic processes near the melting temperature. This was the mandatory reason why we chose the MD simulation rather than MC simulation when calculating thermodynamic quantities such as melting temperatures.

In many respects Molecular Dynamics simulations are similar to real experiments. A real experiment involves: first the preparation of a material sample that we wish to study. Second, the sample is connected to a measuring instrument (e.g., a thermometer, manometer, or viscosimeter), and finally one measures the property of interest during a certain time interval. If the measurements are subject to statistical noise, then the longer we average, the more accurate our measurement becomes. In a Molecular Dynamics simulation we also have to prepare a sample: we select a model system consisting of N particles and we solve Newton's equations of motion for this system until the properties of the system no longer change with time (equilibrate the system). Finally, after the equilibration we perform the actual measurement.

2.4.1 Integrating the Equation of Motion

The Verlet algorithm [55] is used to integrate the equation of motion and it is considered one of the best algorithms involving MD simulation and has the advantage to be very simple. The Verlet algorithm can be derived from a Taylor expansion of the coordinate of a particle, at a time around t, as follows

$$\mathbf{r}\left(t+\Delta t\right)=\mathbf{r}\left(t\right)+\mathbf{v}(t)\Delta t+\left(1/2\right)\mathbf{a}(t)\Delta t^{2}+\left(1/6\right)\mathbf{b}(t)\Delta t^{3}+O\left(\Delta t^{4}\right), \quad (2.15)$$

similarly

$$\mathbf{r}\left(t-\Delta t\right)=\mathbf{r}\left(t\right)-\mathbf{v}(t)\Delta t+\left(1/2\right)\mathbf{a}(t)\Delta t^{2}-\left(1/6\right)\mathbf{b}(t)\Delta t^{3}+O\left(\Delta t^{4}\right), \quad (2.16)$$

Summing these two equations, we obtain

$$\mathbf{r}\left(t+\Delta t\right)=2\mathbf{r}\left(t\right)-\mathbf{r}\left(t-\Delta t\right)+\mathbf{a}(t)\Delta t^{2}+O\left(\Delta t^{4}\right). \quad (2.17)$$

This is the form of the Verlet algorithm. Since we are integrating Newton's equations, $\mathbf{a}\left(t\right)$ is just the force divided by the mass, and the force is in turn a function of the positions $\mathbf{r}(t)$:

$$\mathbf{a}\left(t\right)=-\left(1/m\right)\nabla V(\mathbf{r}(t)). \quad (2.18)$$

As one can immediately see, the truncation error of the algorithm after a time step Δt is of the order of Δt^4, even if third derivatives do not appear explicitly. This algorithm is at the same time simple to implement, accurate and stable, explaining its large popularity among people performing molecular dynamics simulations.

The Verlet algorithm does not use the velocity to compute the newer position. However, we can derive the velocities from knowledge of the trajectory, using

$$\mathbf{v}(t)=\frac{\mathbf{r}(t+\Delta t)-\mathbf{r}(t-\Delta t)}{2\Delta t}. \quad (2.19)$$

Once the velocity of all particles are known the temperature of the system can be determined by employing the equipartition energy theorem.

Finally that we have computed the new positions, we may discard the positions at time $t - \Delta t$. The current positions become the old positions and the new positions become the current positions.

In our simulation we use the *velocity* Verlet scheme, where positions, velocities and accelerations at time $t + \Delta t$ are obtained from the same quantities at time t in the following way:

$$\begin{aligned}
\mathbf{r}(t + \Delta t) &= \mathbf{r}(t) + \mathbf{v}(t)\Delta t + (1/2)\mathbf{a}(t)\Delta t^2 \\
\mathbf{v}(t + \Delta t/2) &= \mathbf{v}(t) + (1/2)\mathbf{a}(t)\Delta t \\
\mathbf{a}(t + \Delta t) &= -(1/m)\nabla V(\mathbf{r}(t + \Delta t)) \\
\mathbf{v}(t + \Delta t) &= \mathbf{v}(t + \Delta t/2) + (1/2)\mathbf{a}(t + \Delta t)\Delta t
\end{aligned}$$

The latter algorithm is very stable and has the advantage to calculate automatically the velocities of particles.

2.4.2 Molecular Dynamics at Constant Temperature

The term "constant temperature" has to be interpreted from a mechanical statistical point of view. A constant temperature can be set up by bringing the system into contact with a large heat bath. In equilibrium, the probability of finding the system in a given energy state is given by the Boltzmann distribution. For the case of an "ideal gas" consisting of non-interacting atoms in the ground state, all energy is in the form of kinetic energy, and the relationship between kinetic energy and temperature becomes

$$k_B T = m < v_i^2 >, \tag{2.20}$$

where m is the mass of the particle and v_i is the ith component of its velocity. This relation is often used to measure the temperature in a microcanonical and canonical MD simulation. Nevertheless, the condition of constant temperature is not equivalent to the condition that the kinetic energy per particle is constant.

From the relationship between kinetic energy and momentum (Eq. (2.20)) and the Boltzmann distribution, it follows the Maxwell-Boltzmann velocity distribution:

$$P(p) = \left(\frac{\beta}{2\pi m}\right)^{3/2} \exp\left[-\beta p^2/(2m)\right], \tag{2.21}$$

which gives the distribution of the particle velocity in a gas. When the system is in thermal equilibrium with a heat bath the relative variance in the kinetic energy of a given particle can be calculated. It is related to the second and fourth moments of the Maxwell-Boltzmann distribution. For the second moment, $p^2 = \sum_{i=1}^{N} p_i^2$, we have

$$\langle p^2 \rangle = \int d\mathbf{p} p^2 P(p) = \frac{3m}{\beta}, \tag{2.22}$$

while that for the fourth moment, $p^4 = \left(\sum_{i=1}^{N} p_i^2\right)^2$, we can write

$$\langle p^4 \rangle = \int d\mathbf{p} p^4 P(p) = 15 \left(\frac{m}{\beta}\right)^2. \tag{2.23}$$

Finally the relative variance of the kinetic energy is

$$\frac{\sigma_{p^2}^2}{\langle p^2 \rangle^2} \equiv \frac{\langle p^4 \rangle - \langle p^2 \rangle^2}{\langle p^2 \rangle^2} = \frac{15(m/\beta)^2 - (3m/\beta)^2}{(3m/\beta)^2} = \frac{2}{3}. \tag{2.24}$$

Using the assumption that the kinetic energy per particle is a measure of the instantaneous temperature, then we find that, the temperature fluctuates and that its variance is $2/3N$.

2.4.3 The Andersen Thermostat

The constant-temperature MD model proposed by Andersen [56] considers that the system is in contact with a heat bath. The interaction between the system and the heating reservoir is mediated by stochastic impulsive forces that act occasionally on randomly selected particles. Between stochastic collisions, the system evolves at fixed energy according to Newton's laws of motion. The stochastic collisions ensure that all accessible energies are visited according to their Boltzmann weight.

The strength of the coupling of the heat bath is a parameter of the simulation and must be specified. This coupling strength is determined by the frequency of the stochastic collisions ν. If successive collisions are uncorrelated, then the distribution of time intervals between two successive stochastic collisions, $P(t; v)$, is of the Poissom form [57]

$$P(t; v) = v \mathbf{exp}\left[-vt\right] \tag{2.25}$$

where $P(t; v)dt$ is the probability that the next collision will take place in the interval $[t, t + dt]$.

The constant-temperature simulation consists of the following steps:

1. Start with an initial set of positions and momenta $\left\{\mathbf{r}^N(0), \mathbf{p}^N(0)\right\}$ and integrate the equations of motion for a time Δt. In this step the velocity Verlet algorithm can be used.

2. For a given particle, a random number is selected between 0 and 1. If this number is less than the probability that a particle is selected in a time step of length Δt, i.e. $\nu \Delta t$, then that particle's momenta are reset.

3. If particle i has been selected to undergo a collision, its new velocity will be draw from a Maxwell-Boltzmann distribution corresponding to the desired temperature T. All other particles are unaffected by this collision.

2.5 MICROCANONICAL ENSEMBLE

In our simulations we use a microcanonical ensemble. In such an ensemble the total energy is fixed. However, we introduce the temperature via the equipartition theorem of statistical mechanics and this temperature fluctuates around an average value. Nevertheless, the microcanonical MD simulation is less computational costly than the Andersen thermostat method.

In a MD simulation temperature changes are usually achieved by enabling a device in the code which brings the system to a desired temperature by rescaling the velocities. Of course, such a modification means that we are no longer following Newton's equations, and the total energy is no longer conserved. Important data is not collected in this stage: these "controlled temperature" simulations is used only to bring the system from one state to another. In the velocity Verlet algorithm discussed at the previous sub-section, the velocity rescaling is accomplished by replacing the equation

$$\mathbf{v}\left(t+\Delta t/2\right)=\mathbf{v}(t)+\left(1/2\right)\mathbf{a}\left(t\right)\Delta t \tag{2.26}$$

with

$$\mathbf{v}\left(t+\Delta t/2\right)=\sqrt{\frac{T_o}{T(t)}}\mathbf{v}(t)+(1/2)\mathbf{a}(t)\Delta t \tag{2.27}$$

where T_o is the desired temperature, and $T(t)$ the "instantaneous temperature". After this first step, where the temperature of the system is brought to a value close to a desired temperature, a canonical MD simulation can be run by using the Verlet integration algorithm. Although the Newton's equations are obeyed when the Verlet algorithm is been used we first wait until the system reach equilibrium before collecting data.

2.5.1 Measurements

Measurement in a molecular dynamic simulation usually means performing time averages of physical quantities over the system trajectory. To do so, we must first of all be able to express these quantities as a function of the positions and momenta of the particles in the system. For instance, if we are able to express a given instantaneous value of a physical quantity $A(t)$ as:

$$A(t)=f\left(\mathbf{r}_1(t),...,\mathbf{r}_N(t),\mathbf{v}_1(t),...,\mathbf{v}_N(t)\right) \tag{2.28}$$

then we are also able to determine its average value

$$\langle A \rangle = \frac{1}{N_T} \sum_{t=1}^{N_T} A(t) \tag{2.29}$$

where t is an index which runs over the time steps from 1 to the total number of steps N_T.

Typical measurements made in this thesis are:

- Potential energy

  The average value of the potential energy, i.e. the sum of the confinement and the interparticle interaction energies can be obtained by averaging its instantaneous value. A typical expression for the potential energy is shown by Eq. (2.3). In a molecular dynamic code such a computation is usually obtained straightforwardly at the same time as the force computation is made.

- Kinetic energy

  The expression for the instantaneous kinetic energy is very simple

  $$K(t) = \frac{1}{2} \sum_{i=1}^{N} m_i \mid \mathbf{v}_i(t) \mid^2 \tag{2.30}$$

  and its average is not difficult to be computed. An estimate of the temperature is directly obtained from the average kinetic energy by using the equipartition energy theorem.

- Total energy

  In a canonical ensemble, although the total energy $E = K + V$ is a conserved quantity, it is good practice to calculate its instantaneous value at each time step in order to check if the simulation is been performed correctly.

- The melting process in a finite size system is usually not homogeneous. This implies that the whole melting process evolve via consecutive few local melting processes. In order to determine the melting temperature of a specific local melting processes we first, compute the positional displacement related with the specific melting process, and next we use an adaptation of Lindemann's criterion to finite systems [54]. For example, to determine the radial melting temperature of a 2D system of charged particles confined by an isotropic confinement potential we compute the radial averaged displacement, which is defined as

$$\triangle r = \frac{1}{N}\sum_{i=1}^{N}\left\langle r_i^2\right\rangle - \left\langle r_i\right\rangle^2 , \tag{2.31}$$

where r_i is the modulus of the position vector of the i^{th} particle, N is the total number of particles, and $< ... >$ means an average in time.

From Lindemann's criterion [54] we define the radial melting temperature as the temperature at which the radial averaged displacement changes its linear temperature dependence into a very rapid increase.

3

Structure and spectrum of anisotropically confined two-dimensional clusters with logarithmic interaction

Due to strong Coulomb repulsion, an electron gas at low temperature and density undergoes a phase transition to a crystalline state called the Wigner crystal, as predicted theoretically by Eugene Wigner in 1934 [1]. The Wigner crystal is one of the possible ground states of a strongly correlated electron system. Wigner crystallization was first observed in an electron gas confined above the surface of liquid helium by Grimes and Adams [47]. Several theoretical and experimental works have considered the properties of a finite number of particles interacting through a repulsive interparticle interaction potential and kept together by an external confinement potential. Typical experimental realizations of such $2D$ systems include electrons on the surface of liquid helium [47], electrons in quantum dots [40], colloidal suspensions [58] and confined plasma crystals [12]. These systems and their configurations have been observed experimentally, and are important in solid-state physics, plasma physics as well as in atomic physics.

Not only clusters with particles interacting through the Coulomb potential are investigated but also clusters with logarithmic interaction has attracted attention because they correspond with real experimental systems. Vortices in a film of liquid helium interact through a logarithmic potential [59], and also a low concentration of vortices in a type II superconducting $2D$ film interact through a logarithmic potential [60]. The logarithmic interaction between vortices was used to study the stable vortex configurations in a disk shaped

superconductor [31, 61]. Recently, it was shown [25, 30] that the experimental configurations of charged metallic balls on the bottom of a plane horizontal capacitor were better described by a logarithmic interparticle potential [27, 28] than a Coulomb interaction potential [2, 16, 29].

An anisotropic confinement potential is considered in the experiment of Ref. [30] which inspired us to investigate the effect of the symmetry of the confinement on the configuration of the particles. The experimental set-up [30] consists of charged metallic balls on the bottom electrode of a plane horizontal capacitor, the upper electrode being a transparent conducting glass. To get the ball charged, a potential V_e of 1000 volts is applied to this capacitor. And in order to confine the balls, another potential V_c of 2000 volts is applied to a metallic elliptic frame intercalated between the two capacitor electrodes. The experimental cell is fixed on a plate that leans on three independent loudspeakers. Initially the cell is strongly shaken and the system is liquid at this initial stage. Consecutively, a sequence of appropriate annealing introduced by loudspeakers vibrations induces the system to a stable configuration. Throughout the experiment, images of array balls are recorded in real time using a CCD camera onto a VHS videocassette recorder. By analyzing these records and measuring the time spent in each observed configuration, the 'ground state configuration' was retained as the most frequently observed state. It was shown that the asymmetry of the confinement induces various rearrangements of the particles, according to their number and the asymmetry of the potential. These rearrangements consist of a spatial cluster orientation and inter-shell particle exchanges. They also found some metastable configurations and well defined triangular structures. In our model the particles interact through a logarithmic interaction potential as suggested by the experiment. We will show in this chapter that we could reobtain all configurations presented in Ref. [30]. We classified the transitions as first and second order which respectively exhibit a discontinuity in the first and second derivative of the energy as function of the anisotropy of the confinement. Also we show that these transitions affect the eigenfrequencies spectrum of the system. Ref. [62] recently investigated a similar system of logarithmically interact particles but with a circular confinement. Here we will stress the effects due to anisotropy. Previously Ref. [70], considered Coulomb interacting particles in an elliptic confinement potential, but at that time no experimental results were available. Furthermore, here we found an analytical expression for all the eigenfrequencies before the zig-zag transition. This allowed us to find an expression for the anisotropy parameter at which the zig-zag transition occurs as a function of the number of particles in the system.

The chapter is organized as follows. In Sec. II we present our model system. In Sec. III we obtain the ground state properties and structural transitions and compare them with the experimental results of Ref. [30]. The dynamical properties before the zig-zag transition and some eigenfrequency modes which

are independently of the number of particles are investigated in Sec. IV. Finally we present our conclusions in Sec. V.

3.1 MODEL AND NUMERICAL APPROACH

We study a $2D$ model system of N equally charged particles in an elliptic confinement potential and interacting through a repulsive logarithmic potential. The Hamiltonian of the system is given by

$$H = \sum_{i=1}^{N} \frac{1}{2} m(\omega_{0x}^2 x_i^2 + \omega_{0y}^2 y_i^2) - \sum_{i>j}^{N} \beta \ln|\mathbf{r}_\mathrm{i} - \mathbf{r}_\mathrm{j}| \tag{3.1}$$

where m is the mass of the particle, $\mathbf{r}_i = (x_i, y_i)$ is the vector position of the i-th particle, β gives the strength of the interaction and ω_{0x} and ω_{0y} are respectively the confinement frequencies in the x and y directions. These frequencies are related by the expression $w_{0x} = \sqrt{\alpha}\omega_{0y}$ where α is the eccentricity of the elliptic confinement.

We can write the Hamiltonian (6.1) in a dimensionless form if we express the coordinates, energy and temperature in the following units $r_0 = (2\beta)^{\frac{1}{2}} m^{-\frac{1}{2}}$, $E_0 = \beta$ and $T_0 = \beta k_B^{-1}$ where k_B is the Boltzmann constant. The dimensionless Hamiltonian is

$$H = \sum_{i=1}^{N} (\alpha x_i^2 + y_i^2) - \sum_{i>j}^{N} \ln|\mathbf{r}_\mathrm{i} - \mathbf{r}_\mathrm{j}|. \tag{3.2}$$

All the results will be given in dimensionless units. The ground state configuration is the global minimum of the potential energy which is only a function of the number of charged particles N and the eccentricity α. Our numerical method to obtain the ground state configuration is based on the Monte Carlo simulation technique supplemented with the Newton method in order to increase the accuracy of the energy minimum [16]. By starting from different random initial configurations we are able to find all the possible stable (i.e. ground state and metastable) configurations. The eigenfrequencies are the square root of the eigenvalues of the dynamical matrix

$$H_{\alpha\beta,ij} = \left. \frac{\partial^2 H}{\partial r_{\alpha,i} \partial r_{\beta},j} \right|_{r_{\alpha,i}=r_{\alpha,i}^n} \tag{3.3}$$

where $\{r_{\alpha,i}^n; \alpha = x, y; i = 1, ..., N\}$ is the position of the particles in the ground state configuration.

3.2 GROUND STATE CONFIGURATIONS AND STRUCTURAL TRANSITIONS

At low temperature and for circular confinement the observed clusters are self-organized patterns constituted by 'concentric' shells on which the particles are located. Changing eccentricity α from 1 to 0, we can go from a circular potential to a 1D system where the 'concentric' shell arrangements are broken and all particles are aligned along the $x-$axis. In this last limit the particles are infinitely far from each other since the system becomes unbound in the $x-$direction. In this section, we take the system of $N = 6$ particles as an example to present some general properties of the ground state configurations and its configurational transition as a function of the anisotropy parameter α. In particular, we give a detailed overview of first and second order transitions for this system. Next, we will analyze the experimental results of Ref. [30] which focused on small systems with $N = 4, 5, 6$ and 9 particles, large systems with $N = 16$ and 17 particles and systems with some well defined triangular structures.

Changing the eccentricity can induce two types of transitions in the ground state configuration. One of the transitions involves an inter-shell particle exchange which can happen continuously or abruptly, as the eccentricity parameter is varied, characterizing respectively a second and first order transition. The other transition is just a continuous spatial cluster orientation that constitute a second order transition.

We can see these two types of transitions by varying the anisotropy parameter α from 1 to 0 for the $N = 6$ system (see Fig. 3.1). With a decrease of α the ground state configuration passes through a first order transition involving an inter-shell particle exchange from configurations $(1, 5)$ to (6) at $\alpha = 0.88$. These configurations are respectively shown in Figs. 3.2(j) and 3.2(i). Notice that this transition is not continuous in position space as we see in Figs. 3.1(b) and 3.1(c) which show respectively jumps in the coordinates x and y around $\alpha = 0.88$. It is also accompanied by a discontinuity in the eigenfrequencies (see Fig. 3.1(a)).

The variation of elliptic eccentricity α induces also continuous configuration adjustments. These adjustments happen to reduce the system energy. At such continuous transitions one of the eigenfrequencies of the ground state goes to zero. This is the equivalent of the softening of a phonon mode in an infinite crystal structure. For $N = 6$ particles such a softening occurs 5 times over the $\alpha : 0 \to 1$ range. This occurs first at $\alpha = 0.2$. In Fig. 3.2(a) we see that for $\alpha = 0.19$ all particles are aligned along the $x-$axis forming a chain-like structure while for $\alpha = 0.21$ (see Fig. 3.2(b)), just after the transition, the particles are not aligned anymore with the $x-$axis. This transition is called the zig-zag transition and is discussed in further detail in Sec. IV. Initially only the central particles in the line take part in the zig zag transition which can be

verified noticing the different slopes of the y coordinate lines after $\alpha = 0.2$ in Fig. 3.1(c). This behavior was also observed previously for the case of Coulomb interparticle interaction [70] and it is independent of the number of particles in the system. Notice that the oscillation amplitude of each particle decreases when going from the centre of the system to the edge of the line configuration as shown in Fig. 3.2(a) by the length of the eigenvectors.

The eigenfrequency, related with the rotational mode, goes to zero at $\alpha = 0.43$ and 0.84 which is related respectively with the alignment and desalignment of two particles with the $x-$axis as can be seen in Figs. 3.2(d) and 3.2(f) respectively. Also for $\alpha = 0.86$ the rotational mode frequency is zero but now it is related with the alignment of two particles with the $y-$axis as we see in Fig. 3.2(h). Finally, for $\alpha = 1$, the system exhibits a zero frequency rotational mode because of the rotational symmetry of the potential.

The experimental work in Ref. [30] showed ground state configurations for $N = 4, 5, 6$ and 9 and values of α varying from 0.5 to 1. We also present configurations related with these systems in Fig. 3.3. Note that the increase of the confinement asymmetry, i.e. decreasing of α, results in intra and/or inter-shells reorganization of the particles. For a one shell arrangement, illustrated for $N = 4$ and 5 particles, this reorganization is characterized by a particular orientation of the cluster with respect to the major axis of the elliptic confinement. Our results for the ground state configuration for $N = 4$ and 5 are compatible with the experimental ones of Ref. [30] except for the configuration of $N = 5$ at $\alpha = 0.5$ where the configuration found in Ref. [30] corresponds to a saddle point in our model which can be seen in Fig. 3.4(a). This difference with the experimental result may be attributed to the fact that the difference in energy between both states is very small at $\alpha = 0.5$, namely $\Delta E/E < 4.6\%$.

For a two shell structure, the asymmetric confinement can induce shell arrangements in the cluster. The system $N = 6$ is an example in which a two-shell ground state configuration $(1, 5)$ for circular confinement is transformed into a one-shell arrangement (6) when α decreases. This behavior is also observed for $N = 7, 8$ and 9 particles. On the other hand, the experimental paper [30] shows that the increase of the elliptic asymmetry induces, first, a transition from the $(1, 8)$ configuration to the $(2, 7)$ one, followed by another rearrangement which results in a return to the initial configuration $(1, 8)$ for $\alpha = 0.6$. However, in our model, the configuration $(2, 7)$ which can be seen in Fig. 3.4(b) corresponds to a metastable state with energy very close to the energy of the ground state configuration $(1, 8)$. We show the difference of energy between both configurations in Fig. 3.5. The energy difference between both states is very small in the region just around $\alpha = 0.8$ where the configuration $(2, 7)$ was found in the experimental work [30].

Now we turn our attention to larger systems where a well defined triangular structure are found (see Fig. 3.6). These configurations are in good agreement with the results obtained in Ref. [30]. These configurations are analogous to the 'magic numbers structures' discussed in Ref. [16]. Independently if the

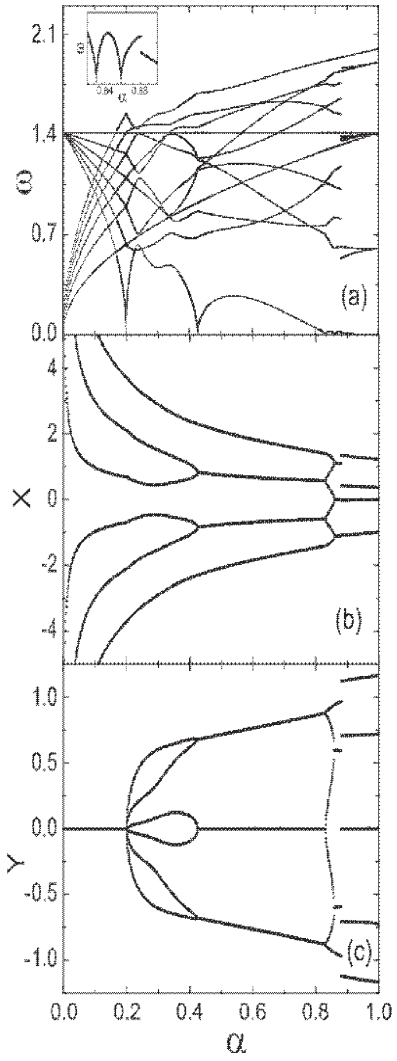

FIG. 3.1: The mode spectrum as a function of the anisotropy parameter for a cluster of $N = 6$ particles. The (b) and (c) are respectively the x and y particles coordinate as a function of α.

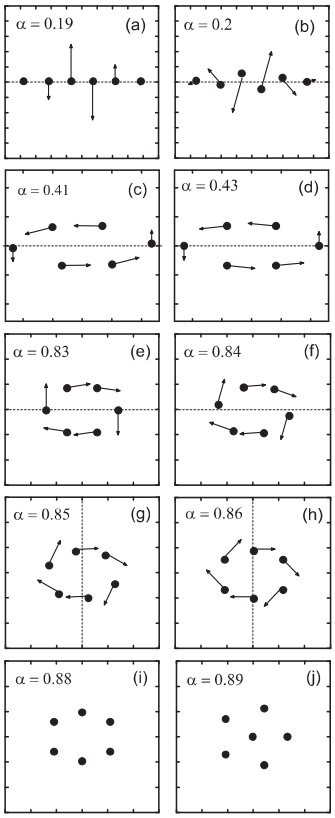

Fig. 3.2: Ground state configurations for different values of the eccentricity parameter α. The eigenvectors corresponding to the lowest normal mode are indicated in (a-h). The scale is different in each figure, but the distance between the ticks is always one length unit.

circular system corresponds to a 'magic number one' the elliptic potential can induce, for some N and α, a triangular array arrangement.

In Ref. [30] an experimental procedure was developed to investigate metastable configurations and they explored the influence of the anisotropy on the metastable states of the system. It was noted that the rules of transition between ground state and metastable configurations appear differently for systems with different number of particles. To illustrate this topic, they considered the cases $N = 16$ ($\alpha = 0.7$) and $N = 17$ ($\alpha = 0.6$) which were also obtained using our theoretical method and they are shown in Fig. 3.7. The configuration of ground state (GS), meta-stable state (MS) and saddle point (SP) are respectively shown in Figs. 3.7(a), 3.7(b) and 3.7(c) for $N = 16$ and Figs. 3.7(d), 3.7(e) and 3.7(f) for $N = 17$. These configurations are classified slightly different in Ref. [30].

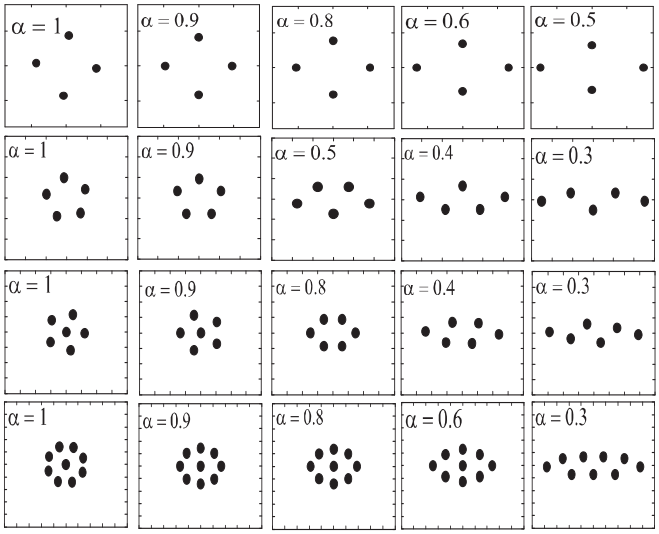

FIG. 3.3: The ground state configurations for different values of N and α which correspond to the experimental results of Ref. [30]. The scale is different in each figure, but the distance between the ticks is always one length unit.

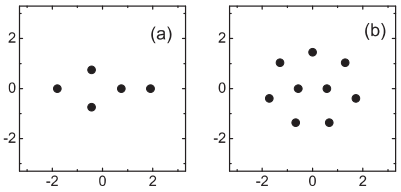

FIG. 3.4: Saddle point configuration for a system with $N = 5$ particles for $\alpha = 0.5$. (b) Metastable state for $N = 9$ and $\alpha = 0.9$.

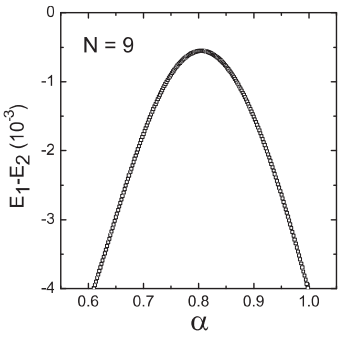

FIG. 3.5: Difference of energy between the ground state energy E_1 with configuration $(8, 1)$ and the meta-stable energy E_2 with configuration $(7, 2)$.

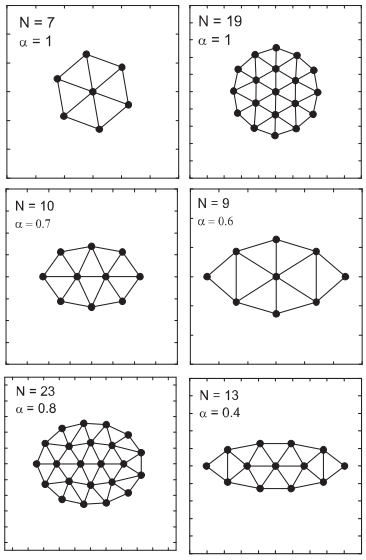

Fig. 3.6: Example of ground state configurations exhibiting a well defined triangular arrangement which is accentuated by the thin lines. The distance between the ticks is one length unit.

There the ground state and first metastable state obtained experimentally correspond respectively to the configurations shown in Figs. 3.7(a) and 3.7(c) for $N = 16$ and in Figs. 3.7(f) and 3.7(d) for $N = 17$. The inner shell of these configurations plays a different transformation rule between the ground and first metastable states. Ref. [30] noted that their ground state and metastable state for the system $N = 16$ and $\alpha = 0.7$ has respectively an inner shell corresponding to the ground state and metastable state configuration of a system with $N = 5$ particles. While for the system with $N = 17$ particles and $\alpha = 0.6$ the opposite situation occurs, i.e. the inner shell of the ground state and metastable state configuration correspond respectively to the metastable and ground state configuration of a system with $N = 5$ particles. We obtained the same rule governing the transition between ground state and the saddle point configuration. We furthermore noted that the shape structure of the outer shell played a different rule in the minimization of the configurational energy. For example, in the case of $N = 16$ the cluster arrangement with a regular outer shell Fig. 3.7(a) has a lower energy than the metastable configuration, Fig. 3.7(b), presenting an irregular outer shell. In contrast, the system with $N = 17$ the configuration of lower energy Fig. 3.7(d), has an irregular outer shell while the cluster with regular outer shell, Fig. 3.7(e), has a larger energy. The energies of the (GS), (MS) and (SP) are respectively $E = -3.59426$, -3.59294 and -3.59175 for $N = 16$ and $E = -4.42750$, -4.42679 and -4.42737 for $N = 17$.

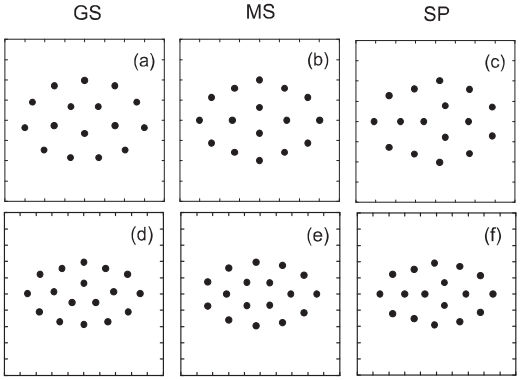

FIG. 3.7: Configurations for $N = 16$ and 17 particles with respectively $\alpha = 0.7$ and 0.6. From left to right the column show the configurations corresponding to the ground state (GS), metastable state (MS) and saddle point (SP). The distance between the ticks is one length unit.

We can see that the relative difference in energy between the configurations with the same number of particles are very small.

3.3 DYNAMICAL PROPERTIES

In this section we investigate in more detail the dependence of the eigenfrequency spectrum on the anisotropy of the confinement potential. The spectrum for the logarithmic interaction system was compared with the behavior of the eigenfrequencies found in Ref. [70] for a Coulomb system. We also investigate the mass mode and breathing mode eigenfrequency.

Before the zig-zag transition we found that a system with $N+1$ particles has the same frequencies as a system with N particle plus two extra frequencies. This is illustrated in Fig. 3.8 where the eigenfrequencies for the system with $N = 6$ and $N = 7$ particles are shown respectively by closed and open dots. We can see that the closed dots completely coincide with the open dots before the zig-zag transition which occurs at $\alpha = 0.167$ for a system with $N = 7$ particles. We found a general expression that fits all eigenfrequencies for a system of N particles before the zig-zag transition. These expressions are:

$$\begin{aligned} \omega &= \sqrt{2 - 2(n-1)\alpha}, \\ \omega &= \sqrt{2n\alpha}, \end{aligned} \tag{3.4}$$

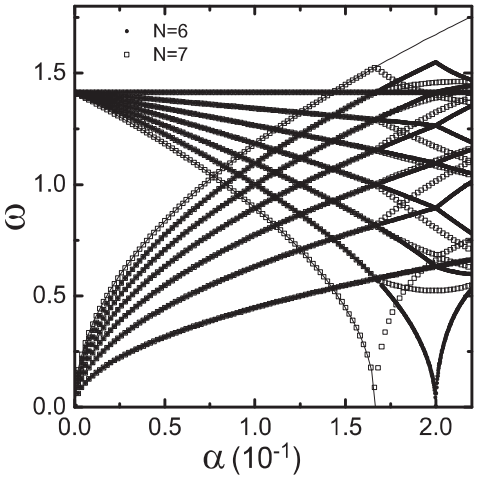

Fig. 3.8: The eigenmode spectrum as a function of the anisotropy parameter for a cluster of $N = 6$ and 7 particles.

with $n = 1, ..., N$. We show the fit for $n = 7$ in Fig. 3.8. The zig-zag transition in a system of N particles occurs when the eigenfrequency given by the expression $\omega = \sqrt{2 - 2(N-1)\alpha}$ becomes zero. From this we can conclude that the zig-zag transition occurs at $\alpha_z = 1/(N-1)$. In Fig. 3.9 we show this expression for α_z which fits perfectly with the numerical obtained zig-zag transition points. A similar power law dependence between the anisotropy parameter α and N was also obtained before for 2D [70] and 3D [64] confined Coulomb clusters, using a numerical fitting procedure.

We also investigated the eigenfrequency of the centre of mass mode in the x and y directions which could be obtained analytically. The Hamiltonian equation of motion yields

$$\dot{v}_{xi} = -2\alpha x_i + \sum_{j_{j\neq i}} \frac{x_i - x_j}{|\overrightarrow{r}_i - \overrightarrow{r}_j|} \tag{3.5}$$

and of course we have the same for $\dot{v}_{yi}$ but with $\alpha = 1$. The displacement of the centre of mass $R_x = \sum_i x_i$ along the $x-$direction satisfies the differential equation

$$\frac{d^2 R_x}{dt^2} = \sum_i \dot{v}_{x_i} = -2\alpha R_x \tag{3.6}$$

and the same for R_y but with $\alpha = 1$. We conclude that the eigenfrequencie of the centre of mass related to the directions x and y are respectively $w_x = \sqrt{2\alpha}$ and $w_y = \sqrt{2}$. These frequencies are independent of the number of charged

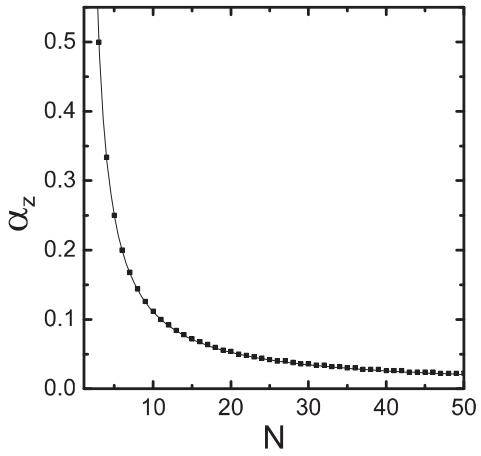

FIG. 3.9: The value of the anisotropy parameter at which the zig-zag transition occurs as a function of the number of particles. The symbols are the results from our simulations and the curve is the expression $\alpha_z = 1/(N-1)$.

particles and the inter-particle potential, which is predicted by the generalized Kohn theorem and is identical for quantum systems [65].

The breathing mode for $\alpha = 1$ is always equal to 2 independently of the number of particles. We can demonstrate this analytically. The mean square radius $R^2 = \sum_i (x_i^2 + y_i^2)$ satisfies the following differential equation

$$\frac{d^2R^2}{dt^2} = 2T - 4\sum_{i=1}^{N}(\alpha x_i^2 + y_i^2) + N(N-1)/2, \tag{3.7}$$

with $T = \sum_i (\dot{x}_i^2 + \dot{y}_i^2)$ the total kinetic energy. In the case $\alpha = 1$ the former equation reduces to

$$\frac{d^2R^2}{dt^2} = 2T - 4R^2 + N(N-1)/2. \tag{3.8}$$

Thus the frequency of the breathing mode in a circular potential is $\omega = 2$ independently of the number of particles.

3.4 SUMMARY AND CONCLUSIONS

The effect of the anisotropy of the confinement potential was investigated in detail for the case of particles interacting through a logarithmic potential. We show that changing the eccentricity of the confinement potential can induce first and second order transitions and that these transitions interfere in the

eigenfrequencies of the system. The first order transition causes a discontinuity in almost all eigenfrequency modes while a second order transition occurs when one specific eigenfrequency becomes zero, i.e. mode softening. Also we saw that the centre of mass mode is independent from the number of particles in the system and that the breathing mode in a circular confinement is always equal to 2.

We noted that the zig-zag transition is initiated by particles located in the centre of the line configuration. The eigenfrequencies before the zig-zag transition for a system of $N + 1$ particles are the same of the eigenfrequencies of a system with N particles plus two new eigenfrequencies. We presented two general expressions depending only on the eccentricity parameter and the number of particles that fit all eigenfrequencies before the zig-zag transition. We obtained an analytical expression for the anisotropy parameter at which the zig-zag transition occurs as a function of the number of particles in the system.

Publication The results in this chapter were published as:

S. W. S. Apolinario, B. Partoens, and F. M. Peeters, *Structure and spectrum of anisotropically confined two-dimensional clusters with logarithmic interaction*, Phys. Rev. E **72**, 046122 (2005).

4

Inhomogeneous melting in anisotropically confined two-dimensional clusters

During the past several years many efforts have been directed to understand static and dynamical properties of mesoscopic devices in which the interacting particles are laterally confined. Typical experimental realizations of such two-dimensional ($2D$) systems include electrons on the surface of liquid helium [47], electrons in quantum dots [40], colloidal particles [58], vortices in mesoscopic shaped superconductors [66, 67], confined plasma crystals [12] and a confined system of metallic balls [25, 30].

The inter-particle interaction ranges from a Coulomb potential, logarithmic interaction, screened Coulomb to dipole interaction. Vortices in a film of liquid helium interact through a logarithmic potential [59], as do a low concentration of vortices in a type II superconducting $2D$ film [60]. The logarithmic interaction between vortices was used to study the stable vortex configurations in a disk shaped superconductor [31, 61]. Recently, it was shown [25, 30] that the configurations of charged metallic balls placed on the bottom of a plane capacitor could be described by a logarithmic interparticle potential.

Historically, Wigner [1] predicted in 1934 that electrons in a three-dimensional Fermi system at low temperature and density undergo an electron-liquid to electron crystal phase transition. Such an electron crystal is called a *Wigner crystal*. No clear observation of such an electron crystal in three-dimensions (3D) has been made up to now. In 1971 Crandall and Williams [68] noted that an analogous phase transition should occur in a classical $2D$ electron system

at sufficiently high density which was first observed by Grimes and Adams [47] in an electron gas confined above the surface of liquid helium. For this kind of system with a circular symmetric interaction potential and in the absence of a corrugated surface, the solid phase with the lowest energy has a triangular lattice structure independent of the electron density [10]. However, a 2D confined system with a finite number of ions or electrons does not crystalize in a triangular lattice (Wigner crystal), but the particles are arranged in a shell structure as was predicted in Ref. [2]. For a large finite cluster the structure is due to the competition between the ordering into a triangular lattice symmetry and the circular symmetry imposed by the confining potential.

Ref. [30] investigated experimentally the effect of the anisotropic confinement on the ground and metastable state of metallic balls trapped by an anisotropic confinement potential. It was shown that the asymmetry of the confinement potential induces various rearrangements of the particles, according to their number and the asymmetry of the potential. They also investigated metastable configurations of the system and well defined triangular structures which are induced by the eccentricity of the confinement potential. This experimental work [30], inspired us [69] to investigate the effect of the symmetry of the confinement on the configurations of the particles. We considered a model of classical charged particles interacting through a logarithmic interaction potential as suggested by the experiment. We reobtained theoretically all configurations observed in Ref. [30]. Many transitions as function of the eccentricity of the confinement potential were found and could be classified as first and second order which respectively exhibit a discontinuity in the first and second derivative of the energy. Also we showed that these transitions affect the eigenmode spectrum of the system. In an earlier work [70] Coulomb interacting particles confined by an elliptic potential were investigated theoretically but at that time no experimental results were available.

Phase transitions in two-dimensional large crystals have mainly been described by changes in the asymptotic behavior of spatial correlation functions. For instance, the Kosterlitz-Thouless-Halperin-Nelson-Young (KTHNY) theory predicts a two-step melting scenario according to which the liquid phase is reached when bond-orientational correlations become short-range [71–76]. This scenario differs considerably from what is generally predicted to occur with small two dimensional clusters in an isotropic trap when the temperature is raised. For the latter system, melting is theoretically predicted to occur via a two step process [2, 16, 77, 78]. At very low temperature, each particle is thermally excited in its local potential. Upon increasing the temperature, first angular rotation becomes possible where orientational order between adjacent shells is lost which is called angular melting. Consecutively for higher temperatures an intrashell melting occurs and at the same time radial diffusion between shells takes place.

In this chapter we investigate how the different melting processes are influenced by the geometry of the confinement potential. Therefore, we study the

melting process in $2D$ model systems of N equally charged particles trapped by an elliptic confinement potential and interacting through a repulsive interparticle potential. We focus on the effect of the eccentricity of the confinement potential on the melting process of the system. We found that the eccentricity of the confinement potential induces different melting processes some of them we found are different from the circular confined system. The dependence of these melting processes on the range of the interparticle potential is studied by considering a logarithmic and screened Coulomb interparticle potential. For sufficient large asymmetry of the confinement we found a temperature induced break up of the sample in different regions which have a different melting temperature.

The chapter is organized as follows. In the next section our model system and the methodology used to find stable configurations is given. In section III we deal with the system of classical particles interacting through a logarithmic interparticle potential. First, we investigate qualitatively the melting processes in relatively small clusters of particles $N = 6$, 12, 13 and 30. These examples concern clusters with distinct number of shells and provide understanding of the main melting processes occurring in anisotropic clusters. Next, the effect on inhomogeneous melting by the size of the cluster is investigated and melting temperatures are obtained. In section IV we investigate how our results depend on the type of interaction considering a cluster with $N = 13$ particles for a screened Coulomb interparticle potential. Finally, in Sec. V we present our conclusions.

4.1 MODEL AND NUMERICAL APPROACH

We study a $2D$ model system of N equally charged particles in an elliptic confinement potential and interacting through a repulsive potential. The potential energy of the system is given by

$$E = \sum_{i=1}^{N} \frac{1}{2} m(\omega_{0x}^2 x_i^2 + \omega_{0y}^2 y_i^2) + \sum_{i>j}^{N} V(|\mathbf{r}_i - \mathbf{r}_j|) \tag{4.1}$$

where m is the mass of the particle, $\mathbf{r}_i = (x_i, y_i)$ is the vector position of the i-th particle, $V(\mathbf{r})$ the repulsive interparticle interaction and ω_{0x} and ω_{0y} are respectively the confinement frequencies in the x and y directions. These frequencies are related by the expression $w_{0x} = \sqrt{\alpha}\omega_{0y}$ where α is the eccentricity of the elliptic confinement. In the present study we consider a logarithmic interparticle interaction $V(\overrightarrow{r}) = -\beta \ln|\overrightarrow{r}|$ and a screened Coulomb potential $V(\overrightarrow{r}) = (q^2/\epsilon)\exp(-|\overrightarrow{r}|/\lambda)/|\overrightarrow{r}|$

We can write the potential energy (6.1) in dimensionless form if we express the coordinates, energy, temperature and time, respectively, in the following units $r_0 = (2\beta/m\omega_{0y}^2)^{1/2}$, $E_0 = \beta$, $T_0 = \beta k_B^{-1}$ where k_B is the Boltzmann

constant and $t_0 = \sqrt{2}/\omega_{0y}$ in case of an logarithmic confinement potential. The dimensionless potential energy is

$$E = \sum_{i=1}^{N}(\alpha x_i^2 + y_i^2) - \sum_{i>j}^{N} \ln|\mathbf{r}_\mathrm{i} - \mathbf{r}_\mathrm{j}|. \tag{4.2}$$

For a screened Coulomb potential this becomes

$$E = \sum_{i=1}^{N}(\alpha x_i^2 + y_i^2) + \sum_{j>i}^{N} \frac{\exp(-\kappa|\mathbf{r}_i - \mathbf{r}_j|)}{|\mathbf{r}_i - \mathbf{r}_j|} \tag{4.3}$$

with respectively for the units of length, energy, temperature and time $r_0 = (q^2/\epsilon\gamma)^{1/3}$ where $\gamma = m\omega_{0y}^2/2$, $E_0 = \gamma r_0^2$, $T_0 = E_0 k_B^{-1}$ and $t_0 = \sqrt{2}/\omega_{0y}$. The dimensionless inverse screening length, $\kappa = r_0/\lambda$, is a measure of the range of the inter-particle interaction potential. All the results will be given in dimensionless units.

The stable configuration is a local or global minimum of the potential energy which is only a function of the number of charged particles N and the eccentricity α (and κ in case of a screened Coulomb interaction). Our numerical method to obtain the stable state configuration is based on the Monte Carlo simulation technique supplemented with the Newton method in order to increase the accuracy of the found energy value [16]. By starting from many different random initial configurations we believe that we were able to find all the possible stable (i.e. ground state and metastable) configurations. These configurations were discussed in our previous chapter and in Ref. [69].

To study the dynamical properties of a small cluster at a specific temperature we implement the molecular dynamic (MD) simulation in three different stages. 1) We use a variant of the velocity Verlet Algorithm [55] which rescales the velocity of the particles to bring the sample to a desired temperature. The rescaling of the velocities in such an algorithm implies that we are no longer following Newton's equations, and no data should be collected in this stage. 2) The last configuration obtained in the previous step serves as initial condition in a subsequent Molecular Dynamics (MD) simulation using the velocity Verlet algorithm which brings the system to a statistical equilibrium state, and 3) the last configuration in the second step is integrated in time using the velocity Verlet algorithm while data are collected. A typical measurement done during this latter stage is the calculation of the averaged displacement of the particles from its equilibrium position [2].

4.2 MELTING TRANSITION FOR SYSTEMS WITH LOGARITHMIC INTERPARTICLE POTENTIAL

In this section we demonstrate how the eccentricity of the confinement potential affects the melting in systems with a logarithmic interparticle potential. Therefore, we consider systems ranging from N=6 up to N=60 particles. These examples involve clusters with distinct number of shells. In the following we show detailed results for four different clusters which contain typical melting processes we observed: system with one shell that encloses no particles, (N=6 particles), systems with one shell but enclosing particles, (N=12 and 13 particles), and a system with two shells, (N=30 particles). Finally, we investigate larger clusters with $N = 40, 50$ and 60 particles. The melting phenomenon for clusters with a different number of particles can be deduced from these results. To acquire insight into the diverse melting processes and their dependence on the eccentricity parameter we show typical particles trajectories performed during a relatively small time interval in a MD simulation. Next, different melting temperatures are obtained quantitatively as function of α by using Lindemann's criterion. We will see that a weak anisotropic system exhibits the same melting processes as in a system with circular confinement potential, i.e. angular melting followed by a radial melting. We show how the melting temperature of these processes change with the eccentricity of the confinement potential. For small and strong anisotropic systems ($\alpha < 0.5$) an inhomogeneous melting process appears untypical for circular systems which we call internal intershell melting.

The small cluster with $N = 6$ particles has one shell configuration $(0, 6)$ for $\alpha \neq 1$ and $(1, 5)$ when $\alpha = 1$ and we will investigate how the eccentricity of the confinement potential influences the melting of such a system. Considering this latter configuration as a starting position in a MD simulation we obtained the trajectory patterns shown in Fig. 4.1 for different values of the eccentricity and temperature. These trajectories were obtained by collecting the position of the particles during a time interval of $\Delta t = 500$. For small anisotropy, for example $\alpha = 0.8$, the system of $N = 6$ particles exhibits the well-known two step melting process like for an isotropic system. The first melting process, called angular melting, occurs at the temperature $T = 0.0082$ (Fig. 4.1(a)). While radial melting, where particles can jump between stable configurations $(0, 6)$ and $(1, 5)$, occurs for a temperature of $T = 0.0181$ (Fig. 4.1(b)). The first consequence of the anisotropic confinement is that decreasing α leads to an increase of the angular melting temperature. For example, for a relatively high temperature $T = 0.0135$ and $\alpha = 0.6$ (Fig. 4.1(c)) the particles are still oscillating around their equilibrium position and no angular melting is observed. For an extremely anisotropic system $\alpha = 0.3$ at low temperature, for example $T = 0.0048$ (Fig. 4.1(d)), particles perform a simple oscillation around their equilibrium position. However, for increasing temperature, particles are first

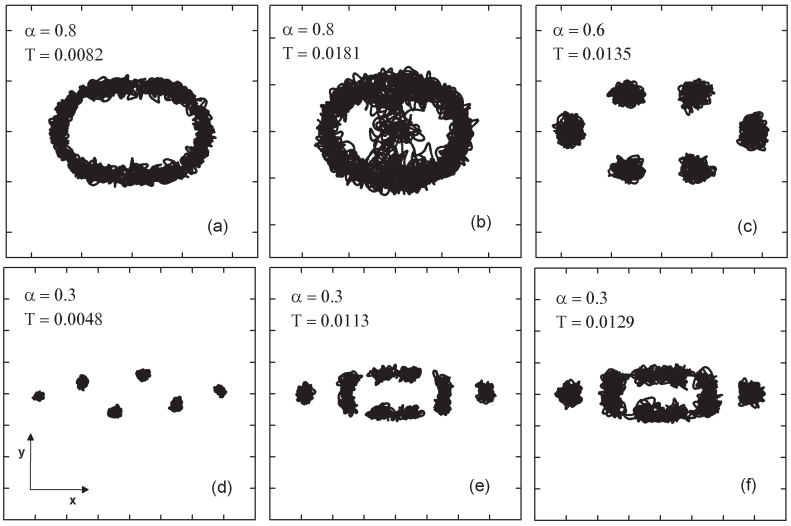

FIG. 4.1: Particle trajectories for a system with $N = 6$ particles, different values of temperature and three eccentricity confinement values $\alpha = 0.8, 0.6$ and 0.3. The scale is different in each figure, but the distance between the ticks is always one length unit.

(Fig. 4.1(e)) able to occupy both degenerated ground state configurations and consecutively in a second step at higher temperature $T = 0.0129$ the four central particles lose their angular orientational order in a dynamic process that we will call *internal intrashell melting*. In contrast, the two particles located in the most extremum position in the cluster have an oscillatory motion around their equilibrium position. Also we can verify from Figs. 4.1(e) and 4.1(f) that increasing the eccentricity of the confinement potential in a system with $N = 6$ particles induces regions in the cluster having a different melting temperature. In order to be able to describe these melting processes quantitatively we distinguish two regions in Fig. 4.1(d). Region 1 holding two particles is placed at the left and right extremum of the cluster while region 2 which is the center of the cluster contains four particles.

In previous work [2] the melting temperature was determined quantitatively by calculating the radial and angular averaged displacement. However, for anisotropic systems with elliptic confinement it is more convenient to calculate the x averaged displacement defined as:

$$u_{x\gamma}^2 = \frac{1}{N_\gamma}\sum_{i=1}^{N_\gamma}(< x_{\gamma i}^2 > - < x_{\gamma i} >^2)/a^2 \tag{4.4}$$

where $\gamma = 1$ and 2 indicates the region number, N_γ is the number of particles in region γ, $x_{\gamma i}$ is the x coordinate of the i^{th} particle of group γ and a is the average distance between the particles. The calculation of the x averaged displacement as function of temperature allowed us to determine the different melting processes quantitatively.

The reason to use the x averaged displacement is that for high anisotropic confinement the system presents regions along the x-direction with distinct dynamical properties. We define the melting temperature as the temperature at which the x averaged displacement changes its linear temperature dependence into a more rapid increase.

Through a MD simulation where we collected data during a time interval of $\Delta t = 10^5$ we obtained the temperature dependence of the x averaged displacement (Fig. 4.2) for the particles in regions 1 (full squares) and 2 (empty squares) for the system with $N = 6$ particles and $\alpha = 0.3$. We can clearly see three melting regions and two plateaux. The first melting process, where the system becomes able to oscillate between both degenerated ground states configurations starts at the temperature $T_1 = 2.46 \times 10^{-3}$. For this latter value of the temperature the x averaged displacement of group two (u_{x2}) changes its initial slope present at low temperatures. A first plateau which presents a dynamical equilibrium is found for the temperature range from $T_2 = 5.73 \times 10^{-3}$ till $T_3 = 11.24 \times 10^{-3}$. For this temperature interval, u_{x2} shows a very small linear increase. The internal angular melting starts to occur at $T_3 = 11.24 \times 10^{-3}$ when u_{x2} shows a sudden increase. A second plateau for u_{x2} occurs for the range of temperatures varying from $T_4 = 17.22 \times 10^{-3}$ till $T_5 = 26.52 \times 10^{-3}$ corresponding to a complete internal angular melting. This melting process is followed by a full melting which happens at temperature $T_5 = 26.52 \times 10^{-3}$ where both x averaged displacement of groups 1 (u_{x1}) and 2 (u_{x2}) diverges.

Let us now look at a larger cluster. Ref. [30] showed that large anisotropic confined systems have a ground state configuration with a regular arrangement for which the packing is close to a hexagonal symmetry. This regular arrangement is induced by the anisotropic confinement. The ground state configuration for $N = 13$ particles and $\alpha = 0.4$ also exhibits a regular structure. We investigate the melting process as a function of the eccentricity of the confinement potential. The melting process for the system with $N = 13$ particles strongly depends on the eccentricity and in particular for $\alpha = 0.4$ the system exhibits a distinct melting pattern. We present in Fig. 4.3 typical trajectory patterns. For an anisotropic confinement of $\alpha = 0.7$ a system with $N = 13$ particles (first row in Fig. 4.3) exhibits intershell melting at a temperature of $T = 0.00244$ (Fig. 4.3(b)). Radial melting occurs at $T = 0.00956$ (Fig. 4.3(d)) where the central particle can jump to the outer shell and a particle in the shell

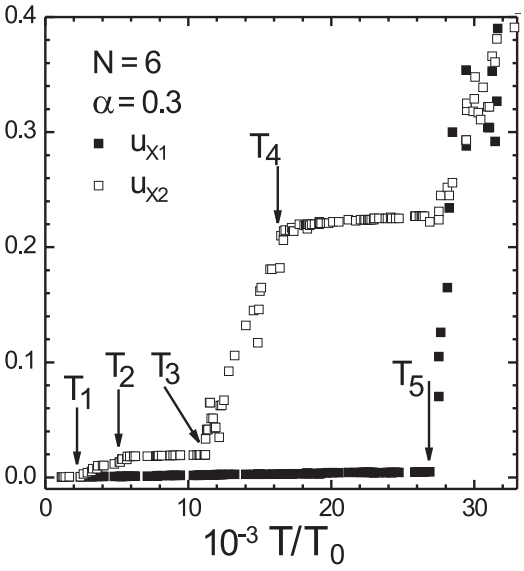

FIG. 4.2: The x averaged displacement for regions 1 (full squares, left and right particles in Fig. 4.1(d)) and 2 (empty squares, center-four particles in Fig.4.1(d)).

can jump to the central area. For a larger temperature ($T = 0.01597$) the two neighbor particles of the central particle are also able to jump to the outer shell and therefore also contribute to the radial melting process (Fig. 4.3(e)). With increasing anisotropy the intershell melting temperature also increases. For a more anisotropic system with $\alpha = 0.6$ (second row in Fig. 4.3) we didn't found intershell melting even for $T = 0.00603$ (Fig. 4.3(g)). For this system intershell and radial melting is found at $T = 0.0091$ and $T = 0.017$, respectively as shown in Figs. 4.3(h) and 4.3(i). If we increase the eccentricity further one can see from the third row of Fig. 4.3 for $\alpha = 0.45$ that intershell melting no longer occurs. Increasing the temperature leads immediately to a full radial melting. Typical trajectories showing the radial melting are displayed in Fig. 4.3(o) and 4.3(p) for the temperatures $T = 0.00956$ and $T = 0.01243$, respectively. A traditional intershell melting, like the one present in a circular confined system, also doesn't appear for the system with eccentricity $\alpha = 0.4$ (fourth row in Fig. 4.3). However a different type of melting process was found, a new internal shell is formed which starts to melt first with increasing temperature, while the particles located at the corners only perform small oscillations (see Fig. 4.3(t)

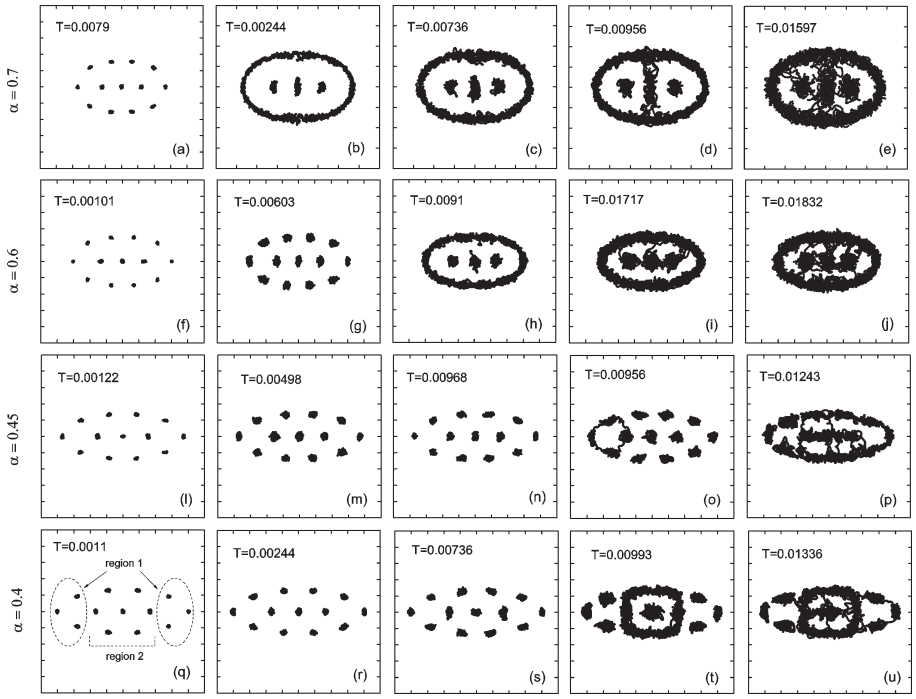

Fig. 4.3: Particle trajectories obtained during a time interval $\Delta t = 500$ for a system with $N = 13$ particles. Each row corresponds to the same value of α and along the column from left to right temperature increases. The distance between the ticks is one length unit.

for $T = 0.0099$). We denote this type of melting as *internal intershell melting* and is a consequence of a temperature induced break up of the system into different regions. For $T = 0.01336$ radial melting is found (Fig. 4.3(u)).

The particle trajectories for increasing temperatures in the last row of Fig. 4.3 show that the dynamical behavior of a cluster with $N = 13$ particles and $\alpha = 0.4$ strongly varies along the x-direction of the cluster. We can distinguish two regions with different dynamic properties in Fig. 4.3(q). Region 1 placed in the extreme left side of the cluster has three particles forming a triangular arrangement; and region 2, which is the center of the cluster, has seven particles with one at the origin of the coordinate system and the six other are placed in the corner of a hexagon around the central particle. The melting temperature for the system with 13 particles and eccentricity $\alpha = 0.4$ and 0.6 was determined by calculating the x averaged displacement. Besides the x averaged displacement of regions 1 and 2 we defined two new expressions: the x averaged displacement of particles of the outer shell, u_{xs}, and the x averaged

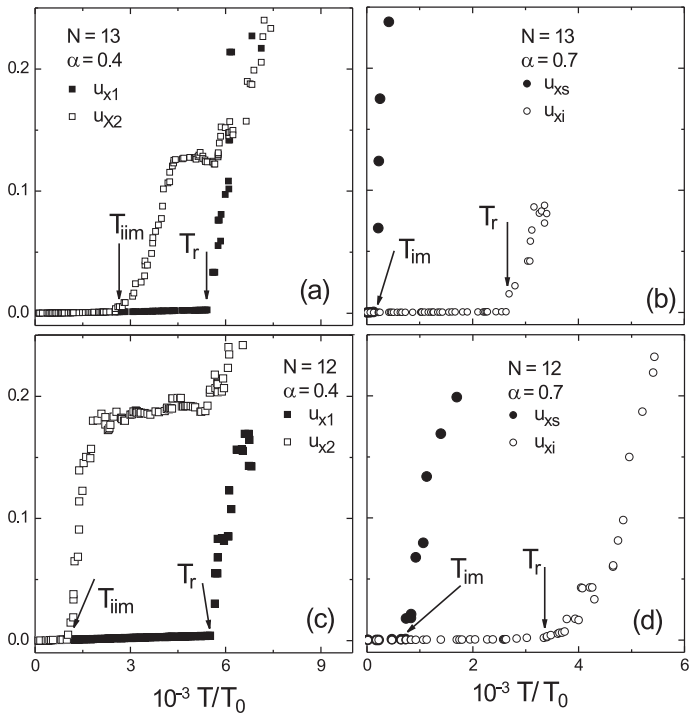

FIG. 4.4: The temperature dependence of the x averaged displacement (Eq. 8.3) for the groups of particles in regions 1 and 2 (see Fig. 4.3(q) and 4.5(a)) of the systems with $N = 12$ and 13 particles and two eccentricity values $\alpha = 0.4$ and $\alpha = 0.7$.

displacement for the particles inside the shell, u_{xi}. With these two latter definitions we can also characterize the critical temperature of the intershell melting process. Fig. 4.4(a) shows the dependence of the x averaged displacement as function of temperature for groups of particles in regions 1 (full squares) and 2 (empty squares) for a system with $N = 13$ particles and eccentricity $\alpha = 0.4$. For increasing temperature, the latter system first exhibits an internal intershell melting at temperature $T_{iim} = 2.65 \times 10^{-3}$ and secondly a radial melting process at temperature $T_r = 5.42 \times 10^{-3}$. For a less anisotropic confinement potential, $\alpha = 0.7$, the system with $N = 13$ particles exhibits an interhell melting process at temperature $T_{im} = 0.13 \times 10^{-3}$ (Fig. 4.4(b)) where the x averaged displacement of particles in the shell diverges. A full melting process is reached at $T_{\rm r} = 2.63 \times 10^{-3}$ when u_{xi} starts to diverge.

It is well known that the so called magic number clusters in systems with circular confinement have a higher intershell melting temperature which is a consequence of a commensurability between particles in different shells. We also investigate the influence of the symmetry on the internal intershell melting process. Differently from the configuration for $N = 13$ particles and $\alpha = 0.4$ the configuration for $N = 12$ particles and $\alpha = 0.4$ is not symmetric with respect to a reflection around $x = 0$. The trajectories for the system with $N = 12$ particles and $\alpha = 0.4$ at the average temperature $T = 0.0004$ and $T = 0.0021$ are shown, respectively, in Figs. 4.5(a) and 4.5(b). The dynamical behavior of the system is not homogeneous along the x-direction. While particles in the center of the cluster exhibit internal intershell melting (Fig. 4.5(b)) the particles at the corners of the cluster oscillate around their equilibrium position. For a quantitative characterization of the different melting processes present in the system we defined two different regions in the cluster shown in Fig. 4.5(a). Region 1 placed on the extreme left side of the cluster has three particles forming a triangular arrangement while region 2 is the center of the cluster and contains 6 particles with five particles forming a pentagon which encloses the 6^{th} particle. The dependency of the x averaged displacement on temperature for the particles in regions 1 (full squares) and 2 (empty squares) for the system with $N = 12$ particles and eccentricity $\alpha = 0.4$ is shown in Fig. 4.4(c). The internal angular and radial melting temperatures for this system are respectively $T_{iim} = 1.12 \times 10^{-3}$ and $T_r = 5.66 \times 10^{-3}$ as indicated in Fig. 4.4(c). At the same eccentricity of $\alpha = 0.4$ the value of the internal intershell melting temperature is higher for the system with $N = 13$ particles ($T_{iim} = 2.65 \times 10^{-3}$) than for the system with $N = 12$ particles showing that the assymmetry of the cluster decreases the stability of the cluster. In order to define the intershell melting temperature for the system with $N = 12$ we also defined the x averaged displacement for the particles in the outer shell, u_{xs}, and for the particles inside the shell, u_{xi}. The intershell melting temperature for the system with $N = 12$ and $\alpha = 0.7$ is $T_{im} = 0.74 \times 10^{-3}$ (Fig. 4.4(d)) which is followed by a radial melting at $T_r = 3.40 \times 10^{-3}$. We also confirmed that the intershell melting temperature increases with increasing anisotropy of the confinement potential. The critical temperature for intershell melting for the system with $N = 13$ particles and eccentricity $\alpha = 0.7, 0.65$ and 0.6 are, respectively, $T_{im} = 0.32 \times 10^{-3}, 0.85 \times 10^{-3}$ and 2.45×10^{-3}. While for the system with $N = 12$ and eccentricity $\alpha = 0.7, 0.65$ and 0.6 the critical temperatures are substantially larger and are respectively, $T_{im} = 0.74 \times 10^{-3}, 1.57 \times 10^{-3}$ and 2.7×10^{-3}.

The angular melting can qualitatively be understood by considering the momentum transfer (i.e. collisions) between nearest neighbors in a shell. At low temperature, the intershell rotational mode dominates the dynamics of the system. Angular melting can occur when a critical kinetic energy value is reached to overcome the barrier and particles move predominantly in the same clockwise or counterclockwise direction. However, when a strong enough

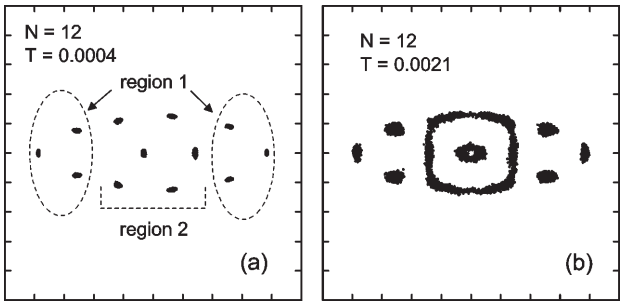

FIG. 4.5: Particle trajectories obtained for a time interval $\Delta t = 500$ for a system with $N = 12$ particles and anisotropy confinement of $\alpha = 0.4$. The distance between the ticks is one length unit.

anisotropic confinement is applied, the shell structure is stretched along the weakest confinement direction and a collision between two particles does not cause the particle at the corner to make a turn. This stops the original angular melting and the oscillations of the particles at the corners become relatively smaller than those of the particles in the middle of the cluster. Under these circumstances, radial melting becomes the first melting process for increasing temperature. For higher anisotropy, the shell structure is restored in the center of the cluster where angular melting becomes possible again.

In order to see if the above physics is also present at larger systems we took $N = 30$ particles for which the ground state configuration has two shells. This will tell us how the number of shells influences the melting processes found previously for systems with one shell. We found that the melting for this latter system is very similar to the melting process for a system with $N = 13$ particles.

We present in Fig. 4.6 the trajectory patterns for the system with $N = 30$ particles and different values of the eccentricity. For an eccentricity parameter of $\alpha = 0.7$ (first row in Fig. 4.6) and increasing temperature the system first exhibits an intershell melting process at an average temperature of $T = 0.00118$ (Fig. 4.6(b)) where the outer shell can rotate, followed by a second intershell melting process at $T = 0.00374$ (Fig. 4.6(c)) involving the second shell in the cluster. Radial melting occurs at $T = 0.00712$ (Fig. 4.6(d)) where the central particle can jump to the second shell. The arrangement of particles inside the outer shell corresponds to the ground state configuration for the smaller system with $N = 13$ particles and eccentricity $\alpha = 0.7$. The melting pattern exhibited by the particles inside the external shell (first row of Fig. 4.6) is very similar to the melting pattern exhibited by the system with $N = 13$ and $\alpha = 0.7$ (first row of Fig. 4.3). For an eccentricity of $\alpha = 0.6$ (second row of Fig. 4.6) an intershell melting process is found at an average temperature of $T = 0.00089$ (Fig. 4.6(f)) for the outer shell. For increasing temperatures we see (Figs. 4.6(g) and 4.6(h)) that the system does not exhibit the previous second intershell melting, instead

a radial melting takes place for the particles inside the outer shell. The set of particles inside the outer shell of this latter system (second row of Fig. 4.6) undergoes a similar melting process like the one found for the system with $N = 13$ particles and $\alpha = 0.45$ (third row of Fig. 4.3). Finally, for a larger anisotropy, $\alpha = 0.25$, the internal intershell melting process is now the first melting process which appears for increasing temperatures (Fig. 4.6(j)) as found previously for systems with a smaller number of particles, $N = 6, 12$ and 13 particles. We can see in (Fig. 4.6(j)) that the three particles in the lateral extremum at both sides of the cluster oscillate around their equilibrium position while a shell involving 17 particles in the center of the cluster is formed. This shell encloses 7 particles which forms a line in the center of the shell and develops an oscillatory motion. For increasing temperature radial melting occurs (Fig. 4.6(l)) at a temperature $T = 0.01076$ where particles inside the shell can jump to the shell and viceversa. We notice that for this melting stage both groups of three particles beside the shell still do not melt and exhibit an oscillatory motion. For a higher temperature of $T = 0.0164$ (Fig. 4.6(m)) the system exhibits full melting involving all particles in the system.

The temperature dependence of the x averaged displacement and the melting temperature for the systems with $N = 30$ particles and $\alpha = 0.7, 0.6$ and 0.25 are shown in Fig. 4.7. For an eccentricity of $\alpha = 0.7$, Fig. 4.7(a) shows the dependence of the x averaged displacement as a function of temperature for the particles inside the external shell and inside the internal shell, u_{xes} and u_{xis} respectively, and for the groups of particles enclosed by the internal shell, u_{xi}. The sudden increase of these quantities determine respectively the following melting temperatures: intershell melting temperatures related to the external and internal shells, T_{ime} and T_{imi} respectively, and the radial melting temperature, T_r. For the latter system, the external and internal shells exhibit an intershell melting process at $T_{ime} = 0.006 \times 10^{-3}$ and $T_{imi} = 1.28 \times 10^{-3}$, respectively for increasing temperatures. A radial melting process occurs at $T_r = 2.41 \times 10^{-3}$. For an eccentricity of $\alpha = 0.6$, the value of the intershell melting temperature associated with the external shell is $T_{ime} = 0.22 \times 10^{-3}$. Now no angular melting related to the internal shell is observed. For this situation both x averaged displacements u_{xis} and u_{xi} simultaneously diverge at the temperature $T_r = 1.64 \times 10^{-3}$. Finally, Fig. 4.7(c) presents the melting temperature for the system with $\alpha = 0.25$. An internal intershell meting occurs at temperature $T_{iim} = 2.02 \times 10^{-3}$. This latter is followed by two radial melting processes: first a melting process involving the particles in the center of the cluster which happen at $T_{r1} = 4.15 \times 10^{-3}$ and second a melting of the group of particles positioned in the edges of the cluster that occurs at the temperature $T_{r2} = 5.56 \times 10^{-3}$.

In order to better understand how internal intershell melting depends on the size of the cluster, we calculated the critical eccentricity parameter, defined as the largest eccentricity for which the internal intershell melting occurs, for the following different systems: $N = 12, 13, 15, 18, 21, 24, 27, 30$ and 33 particles

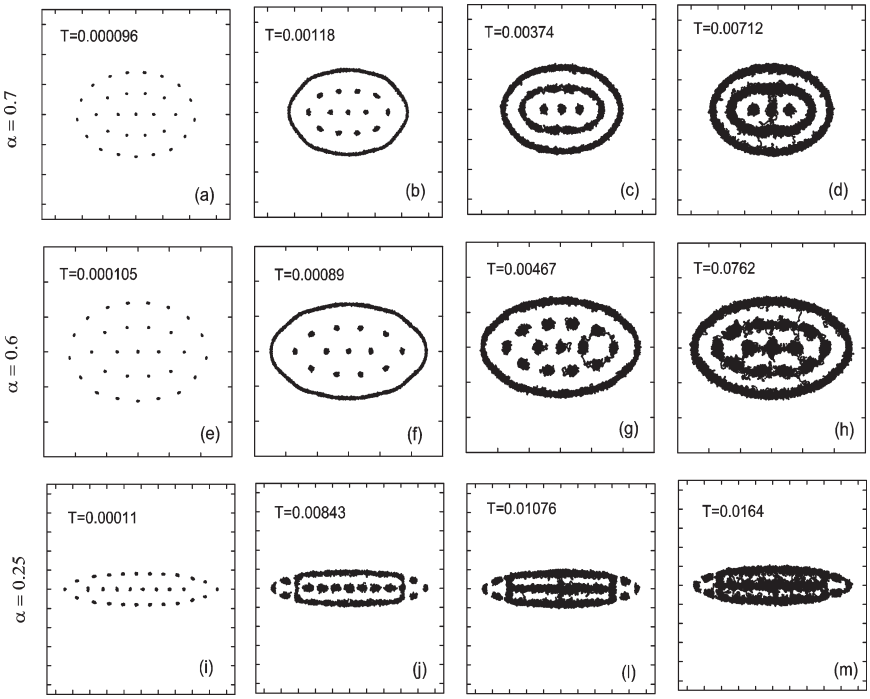

FIG. 4.6: Particle trajectories obtained for a time interval $\Delta t = 500$ for a system with $N = 30$ particles interacting through a logarithmic potential and different values of the eccentricity of the confinement potential. The scale is different in each figure, but the distance between the ticks is always two length unit.

(Fig. 4.8). Transitions between the different melting phases of small systems is continuous (only in the thermodynamic limit do we have a well-defined phase transition). To calculate the critical eccentricity parameter we first calculated the x averaged displacements u_{xs}, u_{x1} and u_{x2} similarly as was previously done for the system of $N = 30$ particles and $\alpha = 0.25$ (Fig. 4.7). Internal intershell melting occurs only if the averages u_{xs}, u_{x1} and u_{x2} increases rapidly over a small temperature range. We determined both the highest value of the eccentricity parameter for which the iim occurs and the lowest value of the eccentricity parameter for which iim no longer occurs. The critical eccentricity parameter was then defined as the geometric average of those values and the error bar as half of their difference. From Fig. 4.8 we notice that the internal intershell melting is always present in small size systems and furthermore that the value of the critical eccentricity decreases as the number of particles increases. Systems with more than 33 particles were found in an undefined dynamic phase between internal intershell melting and inhomogeneous melting.

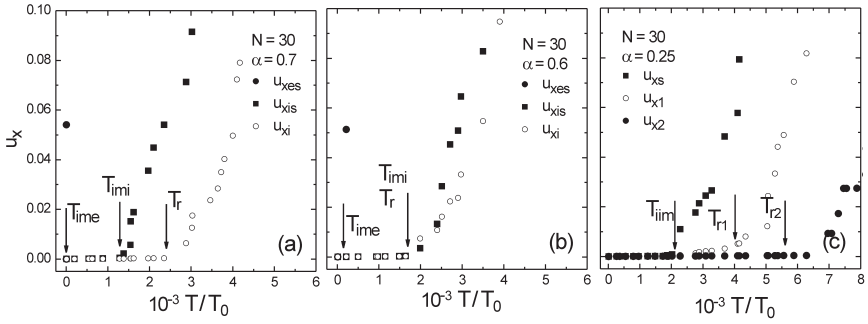

Fig. 4.7: (a), (b) and (c) show the temperature dependence of the x averaged displacement for the system with $N = 30$ particles and value of the eccentricity confinement of $\alpha = 0.7, 0.6$ and 0.25 respectively. In (a) and (b) u_{xes} increase immediately beyond 0.1 for $T > 0$.

Additionally, we investigated larger systems such as $N = 40$, 50 and 60 particles using a qualitative (Fig. 4.9) and quantitative (Fig. 4.10) approach. The first and second columns of Fig. 4.9 show, respectively, the ground state configurations and the melting patterns for the larger systems. Their melting pattern indicates that the set of three particles in the far left and right of the clusters have a higher melting temperature than the center region of the cluster. To confirm this quantitatively we calculated the x-average displacement u_{x2} and u_{x1} (Fig. 4.10) related respectively with the set of three particles placed on the extremum left and right edges of the cluster and the region between these clusters, i.e. the center region. We confirm that inhomogeneous melting pervades for large systems, where the regions at the edges exhibit higher melting temperature contrasting with the dynamic properties found in the rest of the cluster. In other words, u_{x1} and u_{x2} increase rapidly for different values of the temperature. We found (Fig. 4.10) that the melting temperature for clusters with N=40,50 and 60 are $T_{r2} = 10.11 \times 10^{-3}, 9.47 \times 10^{-3}$ and 9.54×10^{-3}, respectively. While the region in the middle of the clusters has lower melting temperatures: $T_{r1} = 3.22 \times 10^{-3}, 4.82 \times 10^{-3}$, and 5.41×10^{-3}, respectively.

4.3 MELTING TRANSITION FOR SYSTEMS WITH SCREENED COULOMB INTERPARTICLE POTENTIAL

In the previous section we found that anisotropic confinement strongly influences the melting process of classical particles interacting through a logarithmic

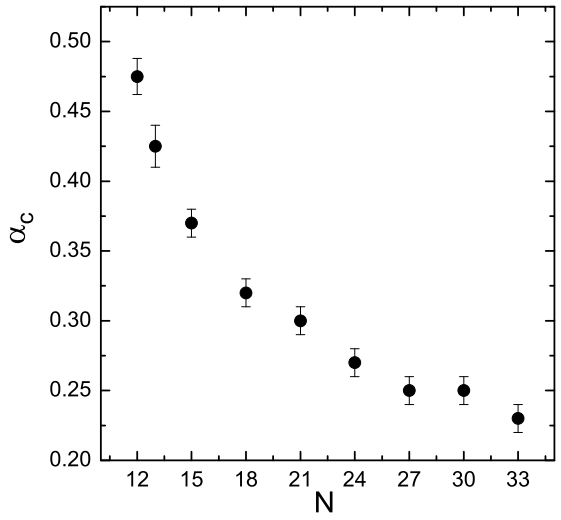

FIG. 4.8: Maximum values of the anisotropy confinement, as function of the number of particles, for which internal intershell melting occurs.

interparticle potential. We saw that new melting processes appear, as for example the internal intershell melting process. Many systems however, for example dusty plasmas, do not interact through a logarithmic potential but through a screened Coulomb interparticle potential. In this section we investigate the dependence of the new melting processes on the range of the interparticle interaction. First, we show the temporal trajectories for the system with $N = 13$ particles and screening parameter $\kappa = 5$. The melting process found for this latter system is compared with the one present for the system with logarithmic interparticle potential for which the typical trajectory patterns were shown in Fig. 4.3. Secondly, we show the relation between the screened Coulomb parameter κ and the eccentricity of the confinement potential α for which internal intershell melting can occur.

The trajectory patterns for the system with $N = 13$ particles, $\kappa = 5$ and different values of the eccentricity of the confinement potential are displayed in Fig. 4.11. For an anisotropic confinement of $\alpha = 0.4$ (first row of Fig. 4.11) the first melting process occurs at $T = 0.00461$ (Fig. 4.11(h)) and it involves only the particles in the left side of the cluster. The reason of such asymmetric melting is due to the short time interval over which this trajectory pattern is shown. The time interval was too short for the system to visit the complete

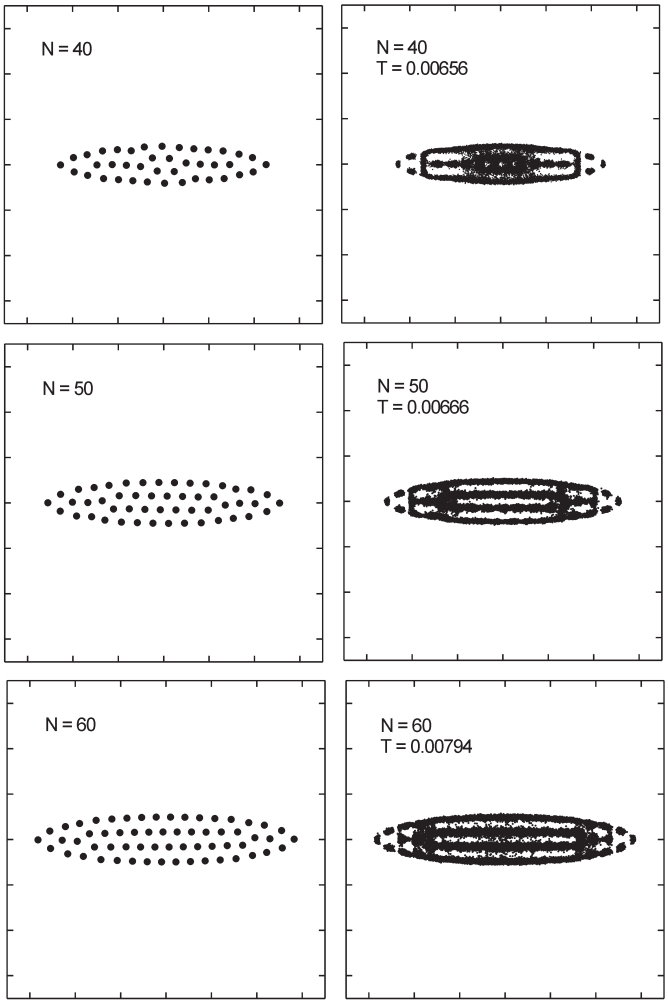

Fig. 4.9: From top to bottom: first column shows the ground state configurations for systems with $\alpha = 0.22$ and $N = 40$, 50 and 60, respectively. Second column exhibit the temporal trajectory of the same systems at some specific temperature. The distance between the ticks is five length units.

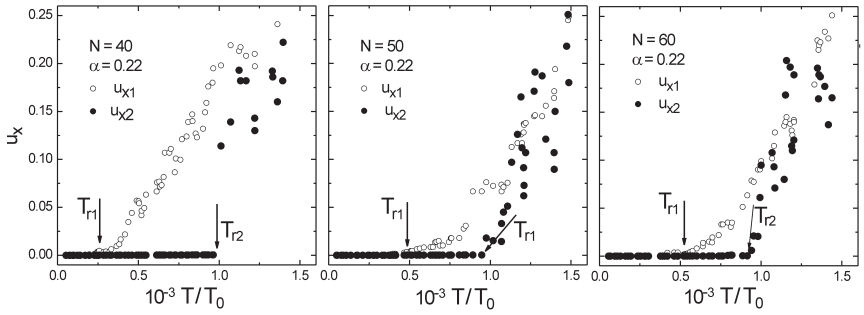

FIG. 4.10: (a), (b) and (c) show respectively the temperature dependence of the x averaged displacement for systems with $N = 40$, 50 and 60 particles and for a value of the eccentricity confinement of $\alpha = 0.22$.

accessible phase space. For higher temperature ($T = 0.00524$), both groups of particles in the left and right sides of the cluster participate in the melting process. Fig. 4.11(j) shows that for $T = 0.01161$ radial melting has set in. This local intershell melting, which involves particles in the lateral areas of the cluster is different from the intershell melting found in the previous system with logarithmic interparticle potential whose trajectory pattern are shown in the first and second rows of Fig. 4.3, respectively, at an anisotropic confinement of $\alpha = 0.7$ and $\alpha = 0.6$. In the latter case the intershell melting involves all particles in the shell while for local intershell melting, particles in the shell start to form two groups of particles which are subjected to independent melting processes. The local intershell melting in the system is a consequence of the short range interaction potential when particles in opposite sides of the shell have its repulsive potential decreased. With increased anisotropy ($\alpha = 0.2$) the radial melting process becomes the first melting process to occur with increasing temperature. This effect of the anisotropic confinement on the melting process was also verified previously for the system with logarithmic interparticle potential (third row of Fig. 4.3). The internal intershell melting process is the first melting process for the system with anisotropy $\alpha = 0.15$ (third row of Fig. 4.11). This phenomenon also occurred for the system with logarithmic interparticle potential but only for an eccentricity of $\alpha = 0.4$.

In the absence of screening, i.e. for $\kappa = 0$, previous studies [2, 29, 79] have shown that the particles arrange themselves in rings. The number of particles on each ring and the number of rings depend on N and were catalogued into a Mendeleev type of table [2, 79]. For small values of κ we still recover this ring structure; the population of each ring can be a function of κ, but for

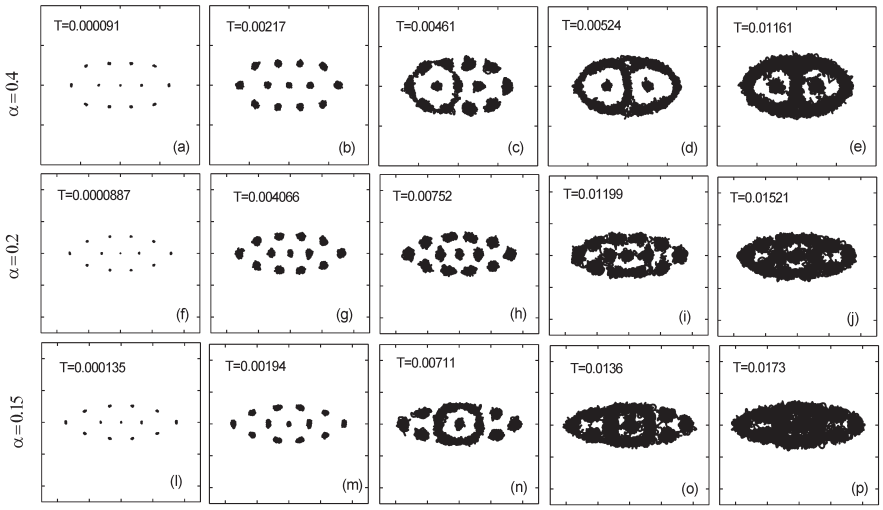

Fig. 4.11: Particle trajectories obtained during a time interval $\Delta t = 500$ for a system with $N = 30$ particles. Each row corresponds to the same value of α and along the column from left to right temperature is increased. The distance between the ticks is one length unit.

sufficiently large screening the particles arrange themselves into a finite size triangular Wigner crystal. Even in a system with anisotropic confinement increasing the screening parameter is able to induce a triangular arrangement of particles. We found that the internal intershell melting also appears for systems with a value of the screening parameter of $\kappa = 0, 1, 2, 10$ and 20. We found that for each of these screening parameters there is a maximum value of the eccentricity parameter α of the confinement for which the internal intershell melting is able to occur, which we call the critical eccentricity α_c. Fig. 4.12 shows that the value of the critical eccentricity α_c decreases with increasing screening parameter κ. This is a consequence of the formation of a triangular arrangement of the particles with increasing screening parameter. Increasing the anisotropic confinement further recovers the arrangement of Fig. 4.3(q) and internal intershell melting becomes possible again.

4.4 SUMMARY AND CONCLUSIONS

The effect of the eccentricity of the confinement potential on the melting process of anisotropically confined particles interacting through a repulsive interparticle

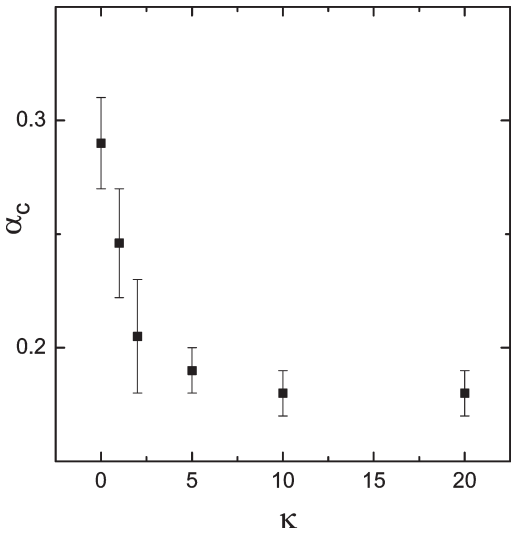

FIG. 4.12: Maximum values of the anisotropy confinement, as function of the screening parameter, for which the internal intershell melting occurs.

potential was investigated. First, a qualitative investigation concerning short time temporal trajectories performed for small and intermediate size systems with $N = 6,\ 12, 13$ and 30 particles and different values of the eccentricity confinement revealed the principal melting properties of anisotropic systems. Angular oscillation substantially influences the dynamic processes in weakly anisotropic confined clusters. At first sight, increasing the anisotropy of the confinement diminishes the importance of angular oscillation on the dynamic of the system. However, for some critical value of the eccentricity, the angular melting process is recovered through a pattern formation called internal inter shell melting. This latter dynamic mechanism can be well understood in terms of the moment transferred between particles belonging to the same shell.

We found that, increasing the anisotropy of the confinement potential drives the system through the following different melting sequences: 1) a similar melting pattern as present in a circular system, i.e., intershell melting followed by radial melting, 2) there is only radial melting, and 3) an angular-like melting appears which we call internal intershell melting since it involves only the particles located in the central region of the cluster. This latter phase transition is followed by radial melting.

The influence of the number of particles on the melting process is as follows. For small systems, for example $N = 12$ and 13 particles both with eccentricity $\alpha = 0.4$, the arrangement of the particles strongly influences the value of the internal intershell melting temperature which reminds us to the dynamic stability found in magic number configurations for isotropically confined systems.

This is a direct consequence of the triangular arrangement on the angular melting process. Furthermore, we found that for larger systems (N=40, 50 and 60 were considered) internal intershell melting is not present anymore but inhomogeneous melting still persists.

We confirmed that inhomogeneous melting is present independently of the range of the interparticle interaction by considering Coulomb and screened Coulomb potentials and should therefore be observed in systems as dust plasmas, colloidal suspensions and metallic balls under anisotropic confinement. In summary, the main message of the chapter is: inhomogeneous melting occurs in anisotropically confined clusters and its appearance in small systems occurs in a distinct form called here internal intershell melting.

Publication The results in this chapter were published as:

S. W. S. Apolinario, B. Partoens, and F. M. Peeters, *Inhomogeneous melting in anisotropically confined two-dimensional clusters*, Phys. Rev. E **74**, 031107 (2006).

5

Structural and dynamical aspects of small three-dimensional spherical Coulomb clusters

It is well known that an infinite Coulomb gas at low temperature self organizes in a body centered cubic lattice. Simulations have shown that the phase transition from order to a liquid state occurs at a well-defined temperature of $T \simeq 1/173$ in units of q^2/a_{WS} (where q is the charge and a_{WS} is the Wigner-Seitz radius, defined as $4/3\pi a_{WS}^3 = 1/\rho$, with ρ the density). The situation is more complex for finite Coulomb crystals as shown by the pioneering works of Schiffer and co-workers. Numerical simulations have shown that the properties of a Coulomb crystal will depend both on the size and shape of the ion plasma, because of the importance of surface effects [86–90]. Finite clouds of ions show ordered structures with a different form of ordering. For instance, with a harmonic (and isotropic) confining potential that is representative for ion traps, cold particles form a cloud with a well-defined surface, constant macroscopic density, with well-defined concentric shells in the interior [86]. The surface layer and each (equally spaced) shell contain ions in a pattern of equilateral triangles. The triangles in the different shells cannot align perfectly; the pattern is reminiscent of the "hexatic" ordering in liquid crystals. Such ordering of trapped ions has been observed both in computer simulations [90] and in the laboratory [91]. Ion clouds can also be confined in rf traps [92]. While the average confining field is a harmonic well - the particle undergo micromotion. The micromotion can also be viewed as due to some effective temperature. As

long as those micromotions are small they do not have any influence on the configurations.

The first experimental investigation of spherical three-dimensional dust plasma crystals consisting of micrometer-sized polymer particles was carried out recently [24]. It was found that small three-dimensional strongly coupled charged particles in a spherical confining potential arrange themselves in a nested shell structure. In a subsequent publication on the same system [21] the sensitivity of the structural properties of the clusters to the type of interparticle forces was explored. By means of experiments, computer simulations, and theoretical analysis, they found that the number of shells are independent of the shielding while the shell occupation numbers are sensitive to screening which could be quantitatively explained by an isotropic Yukawa inter-particle interaction potential. The large size of the dust particles allows direct observation by simple video microscopy because dynamical processes occur on typical frequency scales of a few Hertz, quite unlike strongly coupled colloidal suspensions [93], where particle motion is heavily damped. Therefore, this system is ideally suited for studying the static and dynamics of strongly coupled matter with "atomic resolution". As mentioned by the authors [24] there are many directions of research with dusty plasma, among them the dependence of phase transitions on system size, the formation of bcc order in the bulk of larger crystals, the role of fluctuations close to a phase transition, or the exploration of elastic properties through fundamental types of vibrations.

In this chapter we address the case of small Coulomb clusters confined by a parabolic potential and interacting through a Coulomb or a screened Coulomb potential. Finite size effects are much more pronounced in this case with e.g. the occurrence of magic number configurations. One of the purposes of the present work is to elucidate the structural differences between the ground state (GS) and the lowest energy metastable state (MS). At high temperatures, transitions between different stable states occur. One of the most visited states during the dynamics is, of course, this lowest energy MS. We found that large clusters have a huge number of MS states with energies that are very close to each other. The latter fact strongly dilutes the weight of the lowest energy MS in the dynamics of the system. Here, we will limit ourselves to small clusters. Our investigation will be helpful in understanding the melting processes in small finite size Wigner crystals, both in theoretical [94] and experimental works. In contrast, previous investigations mostly concentrated on systems with a large number of particles ($N > 500$) [19, 24, 89, 95] or on static properties of the GS configurations [96–98]. In our report, the static and dynamic properties of MS for systems ranging from $N = 4$ till 100 particles are presented for the first time. To investigate the microscopic order in the particle configuration, we calculate the spherical Voronoi number associated with a specific polygon around a given particle. In this way we are able to obtain the number of nearest neighbors of each particle belonging to a specific shell. We show that for

the same number of particles, the GS and MS configurations are in many cases structurally different. And we will classify those differences.

We present for the first time the eigenmode frequencies for the ground state and the lowest energy metastable state. All the eigenmode frequencies which are independent on the number of particles are determined analytically. We show that the breathing mode frequency is an upper bound to the eigenmode frequency spectrum in systems interacting through a Coulomb potential. We found an approximate correlation between clusters with maximum (minimum) lowest non-zero eigenfrequency and the peak (minimum) in the second derivative of the binding energy with respect to N indicating the most stable (least stable) clusters. From this analysis, magic clusters are identified.

This chapter of this thesis is organized as follows. In the next section our model system and the methodology used to find stable configurations, eigenmode frequencies and their associated eigenvectors is given. In section III we deal with a system of classical particles interacting through a Coulomb interparticle potential. We investigate the static properties and present a Mendeleev-type table containing information about the structure of the ground state. In addition the lowest energy metastable state configuration is determined and the three lowest non-zero frequencies for the metastable state and the ground state configurations. In section IV we investigate in more detail the dynamics of the previous systems. The eigenfrequencies and eigenvectors are determined both for Coulomb and screened Coulomb interparticle potential. Finally, in section V we present our conclusions.

5.1 MODEL AND NUMERICAL APPROACH

We study a $3D$ model system of N equally charged particles in a parabolic confinement potential and interacting through a repulsive potential. The Hamiltonian of the system is given by

$$H = \sum_{i=1}^{N} \frac{1}{2} m\omega_0 (x_i^2 + y_i^2 + z_i^2) + \sum_{j>i}^{N} \frac{q^2}{\epsilon} \frac{\exp(-|\mathbf{r}_i - \mathbf{r}_j|/\lambda)}{|\mathbf{r}_i - \mathbf{r}_j|}, \tag{5.1}$$

where m is the mass of the particle, $\mathbf{r}_i = (x_i, y_i, z_i)$ is the position of the i-th particle, ω_0 is the frequency characterizing the confinement potential and λ is the screening length of the interparticle interaction potential. We can rewrite the Hamiltonian (6.1) in dimensionless form

$$H = \sum_{i=1}^{N} (x_i^2 + y_i^2 + z_i^2) + \sum_{j>i}^{N} \frac{\exp(-\kappa|\mathbf{r}_i - \mathbf{r}_j|)}{|\mathbf{r}_i - \mathbf{r}_j|}. \tag{5.2}$$

if we express the coordinates, energy, temperature and time, respectively, in the following units $r_0 = (q^2/\epsilon\gamma)^{1/3}$, $E_0 = \gamma r_0^2$, $T_0 = E_0 k_B^{-1}$ and $t_0 = \sqrt{2}/\omega_0$ where

$\gamma = m\omega_0^2/2$. The dimensionless inverse screening length, $\kappa = r_0/\lambda$, is a measure of the range of the inter-particle interaction potential. All the results will be given in dimensionless units. It is clear from Eq. (5.2) that the ground state is only a function of the number of charged particles N and the dimensionless screening length κ. To obtain the stable configurations we use the Monte Carlo simulation technique supplemented with the Newton method in order to speed up the computer program and to increase the accuracy of the found energy value (see Ref. [16] for details). By implementing a large number of different simulations starting from different random initial configurations we are confident that we found the ground state configuration and the first metastable state as long as the number of particles N is not too large. Depending on the total number of particles, between several hundred to several thousand random initial configurations were generated.

The eigenfrequencies are the square root of the eigenvalues of the dynamical matrix

$$H_{\alpha\beta,ij} = \frac{\partial^2 H}{\partial r_{\alpha,i}\partial r_{\beta},j}\Big|_{r_{\alpha,i}=r^n_{\alpha,i}} \tag{5.3}$$

where $\{r^n_{\alpha,i}; \alpha = x, y, z; i = 1, ..., N\}$ are the positions of the particles in a stable configuration.

5.2 FUNDAMENTAL CHARACTERISTICS OF THE GROUND AND FIRST METASTABLE STATES

Any study of Wigner crystals without the knowledge of the details of the particles arrangements must of necessity be of a superficial nature. The particles of which Wigner crystals are composed are arranged in a highly regular way. It is this regularity, together with the attendant symmetry forced by the external confinement potential, that characterise the crystalline state of finite systems. We present in Table 6.1 (see Appendix A), static and dynamic characteristics of the ground state and the lowest energy metastable state for systems of particles interacting through a Coulomb potential and confined by an isotropic parabolic confinement. We considered systems ranging from N=4 up to 100 particles. The main purpose of this table is to compile the most important crystallographic characteristics, which may be of general use to experimentalists and theoreticians. Table 6.1 lists, from left to right, the number of particles in the system, its energy per particle, its configuration, the radius of the shells, the width of the shells, the value of the three non-zero lowest eigenfrequencies, and the number of particles per shell with 'x' nearest neighbors, as obtained by our Voronoi analysis. Except for N=4 to 12 particles, which has only one stable state, Table 6.1 also lists the first metastable state.

The number of shells in the system depends on the total number of particles and in general the number of shells increases with the number of particles. From

the third column of Table 6.1 we can see that the ground state configuration of systems up to 12 particles consists of a single shell. Those configurations in fact form three dimensional regular polygons. From N=13 till 60 the arrangement of particles in the ground state configuration form two shells except for the clusters with N=58 and 59 particles, which respectively have the configurations (1,12,45) and (1,12,46), i.e. they form a two shell configuration with one extra particle in the center. The two shell configuration of the ground state of N=60 particles is unusual since it has less shells than the ground state configuration of the N=58 and 59 systems. This is a consequence of the fact that N=60 has the highly symmetric configuration (12,48) with a commensurate arrangement of the two shells resulting in a higher stability which is expressed in a large lowest (non-zero) eigenfrequency. For $61 < N \leq 100$ we have a three shell configuration as ground state. We can formulate filling rules for the shells when the system is in the ground state. For example, the maximum number of particles accommodated in systems with a single shell is 12 for the ground state configuration. For larger systems, the extra particles form new shells in the system. Initially, for example for the case N=13, the extra particle is placed in the center of the cluster. The number 12 also appears as an upper limit to the number of particles for the inner shell of the two-shell ground state configuration. This can be seen when we go from N=57 to N=58 and N=60 to N=61. Similarly, we observe that 48 is the upper limit for the number of particles in the second shell for systems having two shells as observed for N=60.

From the third column of Table 6.1, i.e. the column listing the configurations, it is clear that the ground state (GS) and metastable (MS) state configurations can differ in the number of shells or in the number of particles in each shell. For example, the system with N=9 particles has the GS configuration with a single shell while its MS configuration has a two shell structure; the system with N=21 particles has a different number of particles in the shell of its GS and MS configurations, respectively, equal to 20 and 19. On the other hand, there are other systems, where the structural difference between GS and MS configurations are not related to a difference in the number of shells or in the number of particles per shell. This is the case for the systems: N=17, 23, 24, 27, 28, 31-33, 35-39, 41-49, 52-54, 57, 59 and all systems larger than N=60 particles with the exception of the systems N=80, 82 and 91. Among the latter systems, some of them have structural differences between the GS and MS configurations due to differences in the number of particles per shell with $'x'$ nearest neighbors. This is the case for the systems: N=23, 59, 73, 74, 76, 77, 83, 86, 87, 90, 97, 99 and 100. The latter fact is documented in the last 5 columns of Table 6.1. For example, for the GS configuration of the N=59 system, the number of particles $N(x)$ in the third shell that has $'x'$ nearest neighbors is $N(3) = 0$, $N(4) = 0$, $N(5) = 12$, $N(6) = 34$ and $N(7) = 0$ and for the MS configuration it is $N(3) = 0$, $N(4) = 0$, $N(5) = 15$, $N(6) = 28$ and $N(7) = 3$. As an example, we show in Figs. 5.1 (a) and (b) the particles on the outermost shell of the GS and MS configurations of the system with

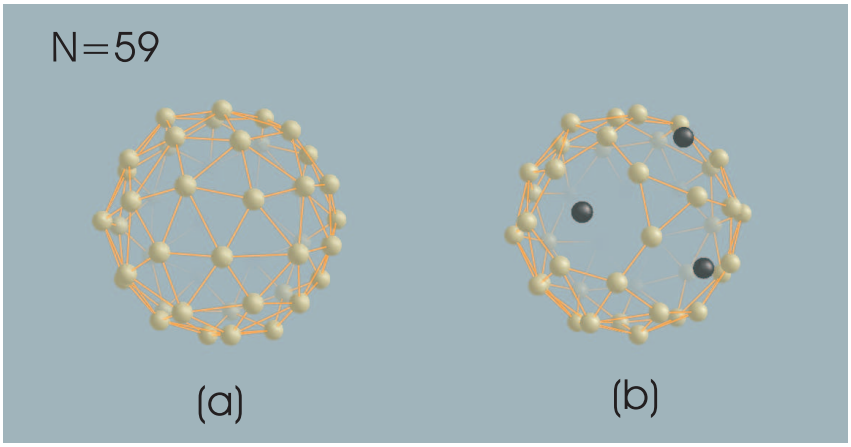

FIG. 5.1: Particle arrangement on the outermost shell for the ground state (a) and lowest energy metastable state (b) configurations of the system with N=59 particles. In order to improve visualization bounds between neighboring particles are drawn except for the 7 coordinated particles in (b) which are drawn in black color.

N=59 particles. From Fig. 5.1 (a) we can clearly identify particles with 5 and 6 nearest neighbors as indicated in Table 6.1. From Fig. 5.1 (b) we can see the three particles, in black color, each having 7 nearest neighbors. We notice that the particles in black are relatively close to each other while the other particles with 5 and 6 nearest neighbors are distributed through the rest of the cluster. While for this latter system the particle packing in the third shell differs in the GS and MS configurations, for the system with $N = 86$ particles, the structural difference is found to occur in the second shell. There, the arrangement of particles for the GS configuration is $N(5) = 12$ and $N(6) = 9$ while for the MS configuration it is $N(4) = 1$, $N(5) = 10$ and $N(6) = 10$.

The present results for the ground state energy and the corresponding configuration agrees with those recently found in Ref. [97]. In the latter work the results for $N = 87$ were missing. In Ref. [98] the metastable configurations were given for $N = 2$ up to $N = 22$. There are a few differences with our results. The $N = 9$ and $N = 19$ clusters were found not to exhibit a metastable state while in our work we found a metastable state.

An interesting concept in the description of a finite size Wigner crystal is that of the width of the shell - in general the bigger the system, the larger the shell width is (see fifth column of Table 6.1). In fact large systems have a more compact internal structure while in small clusters particles accommodate themselves in shells with well defined radius. Without taking this fact into account it would not be possible to understand the basic effects which come into play in different finite size Wigner crystals.

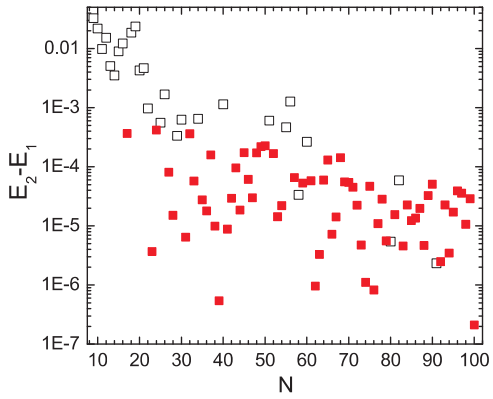

Fig. 5.2: Energy difference between the first metastable state and the ground state as function of the number of particles N when the configurations have different (black open square) or the same (red square) number of particles per shell.

Fig. 5.2 shows the dependence of the energy difference between the first metastable state and the ground state configuration as function of the total number of particles when the configurations have different (black open square) or the same (red square) number of particles per shell. For small systems, $N \leq 56$, the energy difference indicated by the black open squares is larger than those of the red squares except in the case of N=29 particles. It shows that the transition which involves changing the number of particles per shell has higher energy than the one which differs only by the arrangement of particles in the shell. As the number of particles increases the energy difference between both type of configurations diminishes. This is a consequence of the fact that in larger systems the distance between particles belonging to distinct shells is small, since the shell's width is large and then, of course, the energy cost to move one particle from one shell to another will also be small. Note that the overall energy difference $E_2 - E_1$ decreases with increasing system size. Thus for large systems the ground and the lowest energy metastable configurations differ themselves by slight changes in the position of particles belonging to the same shell. The larger the system, the larger are the number of particles in the outer shell and the larger is the width of the shells. Consequently, as shown in Fig. 5.3, which displays the number of metastable states for clusters between N=4 up to 100 particles, a larger system has many more stable configurations than a small one. For $N > 20$ the number of stable states increases exponentially. For N beyond 60 we are not 100% sure that we found all metastable states because of the finite computational time.

Two dimensional systems of repulsive particles most efficiently self organize in a simple lattice of triangles. Such six-fold coordinated triangular lattices [10] can not be wrapped on a sphere surface without the introduction of extra

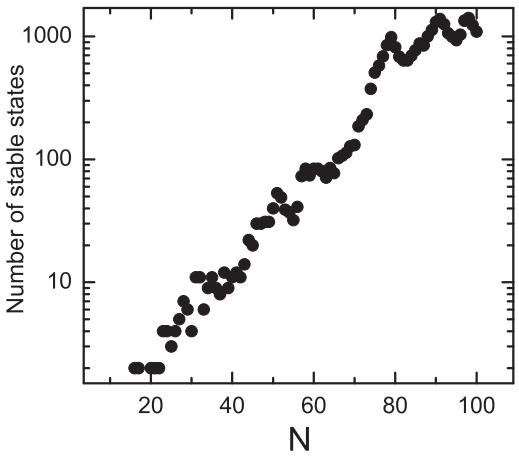

FIG. 5.3: Number of stable states, i.e. the GS and MS state configurations, found for systems ranging from N=4 up to 100 particles.

defects. The topological characteristic of the arrangement of particles on the surface of a sphere can be characterized by their topological or disclination charge, q, which is the departure of their coordination number c from the preferred coordination number 6 ($q = 6 - c$). A classic theorem by Euler [99, 100] shows that the total disclination charge of any triangulation of the sphere must be 12. As the number of particles on the sphere grows, isolated charge $q = 1$ topological defects are predicted to reduce too much strain [101], although it does not contradict Euler's theorem since the total defect charge is still 12. In order to explain the periodic table in terms of rigid spheres, nearly 100 years ago Thomson [102] attempted to determine the minimum energy configuration of repulsive particles laying on the surface of a sphere. Similar problems pervades in a wide range of fields such as multi-electron bubbles in superfluid helium [103], virus morphology [104] and protein s-layers [105, 106].

We determined the number of nearest neighbors for each particle in the outermost shell for systems ranging from N=4 to N=100. Similar results were given in Ref. [97] for $N = 2 \rightarrow 22$ and in Ref. [98] for $N = 2 \rightarrow 160$ which were limited to the ground state configuration. The results are displayed in the last 5 columns of Table 6.1. Figs. 5.4(a) and (b) display respectively for the ground state and the lowest energy metastable state configurations the dependence of $N(x)$ on the total number of particles for the outermost shell. Notice that the MS and GS configurations for systems larger than $N = 11$ particles share the same properties concerning the arrangement of particles on the shell. The number of particles with 5 nearest neighbors saturates around 12 while the number of particles with 6 nearest neighbors increases linearly with the total number of particles. Both the ground state and the metastable state

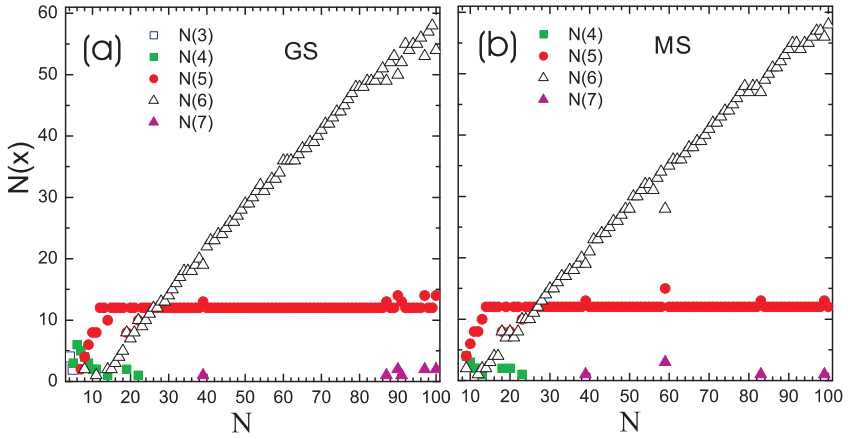

Fig. 5.4: The number of particles in the outermost shell, $N(x)$, having x nearest neighbors in this shell, as function of the total number of particles for the ground state (a) and the lowest energy metastable state (b) configuration.

configuration have in their outer shell a total defect charge equal to 12. For example, the outermost shell of the ground state configuration with $N = 97$ has a total charge defect equal to 12 since the defect charge $q = -2$ associated with the two 7 fold-coordinated defects is canceled by the charge $q = +2$ due to the excess of two defects of 5 fold-coordination. On the other hand, particles with three nearest neighbors are only possible in the ground state configuration of systems with N=4 and 5 particles which do not exhibit any metastable state configuration. It is also seen in both the MS and GS configurations, that mostly in small size systems particles in the outermost shell can have a small number of particles with only 3 or 4 nearest neighbors.

5.3 NORMAL MODES

Here, we discuss the excitation spectrum corresponding to the ground-state configuration of systems of isotropically confined particles interacting both through a Coulomb and screened Coulomb interparticle potential. This spectrum is shown in Fig. 5.5 for the Coulomb interacting system, as function of the number of particles for N ranging from 4 to 100. The eigenfrequency in this figure is in units of $\omega_0/\sqrt{2}$. Notice that there are three eigenfrequencies which are independent of N: (i) for any axial symmetric confinement potential the system as a whole can rotate, which gives a three fold degenerate eigenmode vibration with frequency $\omega = 0$. Fig. 5.6(a) shows the eigenvectors associated with this mode for the system with $N = 12$ particles. (ii) There is a three fold degenerate vibration of the center of mass with frequency $\omega = \sqrt{2} = 1.4142$.

It is an expression of Kohn's theorem for a finite size system. Fig. 5.6(b) displays the eigenvectors associated with this mode for the system with N=12. (iii) The third eigenfrequency corresponds to a vibration of the mean square radius $R^2 = \sum_i (x_i^2 + y_i^2 + z_i^2)$ with frequency $\omega = \sqrt{6} = 2.4495$. This mode is called breathing mode and is illustrated in Fig. 5.6(c) for the system with N=12 particles. Such a mode was also obtained from the cold fluid theory Ref. [107] where there it was referred to as the monopole mode. The breathing mode frequency is the highest frequency mode and is independent of the number of particles (Fig. 5.5). This is in contrast to 2D confined systems of particles interacting through a Coulomb potential where the breathing mode frequency is not the highest frequency mode. The present situation is similar to the case of logarithmic interacting particles [62], confined by a $2D$ parabolic potential where also the breathing mode has the highest frequency. This is not very surprising because the Coulomb interaction of charged particles in a 2D world is logarithmic. In fact Ref. [62] showed that if the Earnshaw's theorem [108] is valid for a given system then the largest radial restoring force will come solely from the external confinement potential. Consequently the breathing mode, which motion of particles is mainly against the confinement potential, will have the largest frequency of oscillation. In this case the addition of particles in the system is only able to enhance slightly the breathing-like modes. In fact we can see (Fig. 5.5) that the value of the second largest frequency increases with the number particle N and then approaches the value of the breathing mode frequency. However as expected by the Earnshaw's theorem the second largest eigenfrequency does not overtake the value of the breathing mode frequency.

Contrary to ion crystals, where particles interact via a pure Coulomb force, the microparticles in dusty plasma are expected to interact through a Yukawa type pair potential. A typical value for the screening parameter is $\kappa = 0.6$ [21]. The eigenfrequency spectrum of the ground state configuration of a Yukawa system with screening parameter $\kappa = 0.6$ and particle number varying from N=4 up to 80 is shown in Fig. 5.7. For screened interaction ($\kappa \neq 0$), the frequency of the rotational and center of mass mode are unaffected since they do not involve a relative particle motion. In contrast, the frequency of the breathing mode will dependent on κ and N and is not necessarily the highest frequency mode. The breathing mode is indicated in Fig. 5.7 (black arrow). We can see that for $N \geq 22$ there starts to appear frequencies with larger values than the breathing mode frequency. With increasing κ, the radial position r_i of the particles in the isotropic confinement well is reduced, the clusters become smaller due to the reduced Coulomb repulsion. With reduced distance, the curvature of the Debye-Hückel potential increases more strongly than the confinement potential force, which in turn leads to the observed increase of the mode frequency (compare Fig. 5, for $\kappa = 0$, and Fig. 7, for $\kappa = 0.6$). As the number of particles increases eventually some of those modes obtain larger frequency than the breathing mode frequency (see Fig. 5.7). We show in

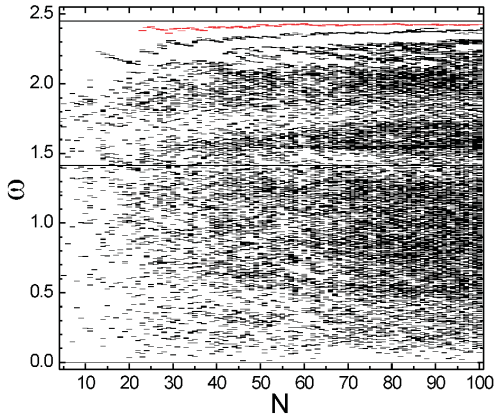

Fig. 5.5: Eigenfrequency in units of $\omega_0/\sqrt{2}$ of the normal modes for the ground state configuration of the pure Coulomb system as function of the particle number N. The second highest frequency is indicated by red ticks.

Figs. 5.8(a) and (b) respectively the eigenvectors of the normal mode of largest eigenfrequencies for the systems with $N = 30$ and 50 particles. These modes are characterized by 1) a radial oscillation of particles in the internal shell, 2) the closest particle in the external shell to a given particle in the internal shell also oscillates radially but out of phase with the oscillation of particles in the internal shell, and 3) the rest of the particles in the external shell have a smaller amplitude of oscillation which is mainly directed tangentially to the shell surface. Such a motion involves a strong change of interparticle distance between some pairs of particles belonging to the internal and external shells, which results in strong restoring forces and thus a high frequency of the mode. Such normal modes were studied experimentally in $2D$ finite screened Coulomb clusters [22]. In that case the mode of highest frequency is also dominated by a strong relative motion of particles and turned out to be no longer the breathing mode frequency.

Following Refs. [16, 79], the value of the center of mass mode can be obtained analytically. The Hamiltonian equation of motion yields

$$\dot{v}_{xi} = -2x_i + \sum_{j_{j\neq i}} (\kappa + \frac{1}{r_{ij}}) \frac{x_{ij}}{r_{ij}^2} e^{-\kappa r_{ij}}, \tag{5.4}$$

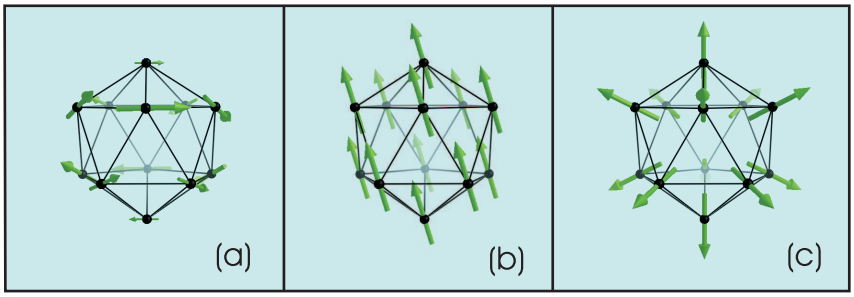

FIG. 5.6: Visualization of the cluster structure and oscillation mode for the system with $N = 12$ particles. (a), (b) and (c) show respectively the eigenvectors of the rotational, center of mass and breathing modes. The arrows represent the eigenvectors, and the arrow's length is proportional to the amplitude of oscillation of the associated particle.

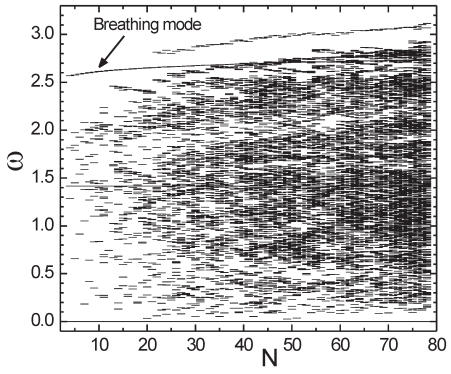

FIG. 5.7: Eigenfrequency (in units of $\omega_0/\sqrt{2}$) of the normal modes for the ground state configuration as function of the total number of particles for a systems of screened Coulomb potential with screening parameter $\kappa = 0.6$.

where $x_{ij} = x_i - x_j$ and $r_{ij} = |\overrightarrow{r}_i - \overrightarrow{r}_j|^2$. We have the same for $\dot{v}_{yi}$ and $\dot{v}_{zi}$. The displacement of the centre of mass $R_x = \sum_i x_i$ along the $x-$direction satisfies the differential equation

$$\frac{d^2 R_x}{dt^2} = \sum_i \dot{v}_{x_i} = -2R_x, \tag{5.5}$$

and the same for R_y and R_z. We conclude that the eigenfrequencies of the center of mass along the directions x, y and z are all equal to $w = \sqrt{2}$. This

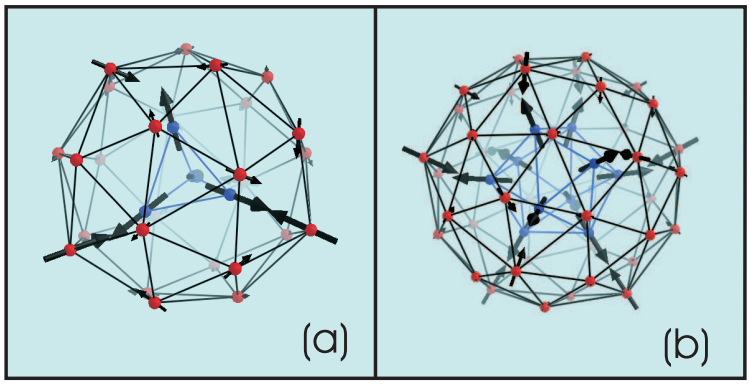

Fig. 5.8: Eigenvectors of the normal mode of largest frequency for the screened Coulomb systems ($\kappa = 0.6$) with N=30 (a) and 50 (b) particles. Particles in the external and internal shells are represented respectively by black and red balls. The arrows represent the eigenvectors of the specific normal mode, and the arrow's length is proportional to the amplitude of oscillation of the associated particle. Bonds are drawn between first neighboring particles to improve visualization.

frequency is independent of the number of charged particles and of the interparticle potential.

The breathing mode frequency can be obtained as follows. The mean square radius $R^2 = \sum_i (x_i^2 + y_i^2 + y_i^2)$ satisfies the following differential equation

$$\frac{d^2R^2}{dt^2} = 2T - \sum_{i=1}^{N}(x_i^2 + y_i^2 + z_i^2) + 2\sum_{j>i}(\kappa + \frac{1}{r_{ij}})e^{-krij}, \tag{5.6}$$

with $T = \sum_i (\dot{x}_i^2 + \dot{y}_i^2 + \dot{z}_i^2)$ the total kinetic energy. For the particular case $\kappa = 0$ the former equation reduces to

$$\frac{d^2R^2}{dt^2} = -6R^2 + 2(T + H), \tag{5.7}$$

where now H is the Hamiltonian for the particular case under study. Thus the frequency of the breathing mode for systems of isotropically confined particles interacting through a Coulomb interparticle potential is $\omega = \sqrt{6}$ and is independent of the number of particles.

Recently, dynamical properties of Coulomb clusters were studied experimentally in which a selective excitation of modes was performed [15, 109]. The experimental technique was applied to 2D clusters and should be extended to 3D [15]. In such systems a normal-mode analysis can become one of the key diagnostics for determining the particle charge and shielding effects. The first step into this direction is the characterization of the normal modes. Beside the three well known oscillation modes, i.e. rotational mode, center of mass

mode and breathing mode, we call to attention the presence of another frequency, shown by the red data in Fig. 5.5, which is slightly smaller than the breathing mode frequency. This normal mode appears for systems having more than a single shell with one particle in the center ($N \geq 23$ particles). In order to characterize this mode we computed the averaged radial deviation of the eigenvectors, which characterizes the radial oscillation of the particles. This quantity is defined as

$$\delta_r = \sum_{i=1}^{N} \frac{\vec{r}_i.\vec{v}_i}{|\vec{r}_i|.|\vec{v}_i|}, \tag{5.8}$$

where $\vec{r}_i$ and $\vec{v}_i$ are respectively the position vector and the eigenvector of the ith particle. Since δ_r is normalized, its maximum (minimum) value is $\delta_r = 1$ (-1) and occurs when the vectors $\vec{r}_i$ and $\vec{v}_i$ are parallel (antiparallel) for all particles. Results are shown in Fig. 5.9, for δ_r computed for the external shell (blue dots) and for the region enclosed by the external shell (red squares). The oscillations of the particles in the center of the cluster are mainly along the radial direction ($\delta_r \approx 1$). Note that the oscillation of particles in the external shell exhibits two different behaviors. For small size systems ($N < 40$), δ_r is small and particles oscillate mainly parallel to the shell while for larger systems ($N > 50$), δ_r is larger and particles oscillate mainly perpendicular to the shell. The simple determination of the direction of oscillation of particles is not enough to provide a satisfactory outline of this oscillation mode. To characterize the oscillation mode it is equally important to know the relative motion between particles as well as their amplitude of oscillation. Note that the value of δ_r has an opposite sign when calculated in the distinct regions. This fact shows that the oscillation performed by particles in the internal region is out of phase to the oscillation of particles on the external shell. The length of the eigenvectors is proportional to the amplitude of oscillation of the particles. The average of the eigenvector's length is shown in the inset of Fig. 5.9 when calculated in the internal region (red squares) and in the external shell (blue dots). We can conclude that particles in the internal region oscillate with larger amplitude than particles on the external shell.

Ref. [16] showed that for 2D systems normal mode analysis is an efficient tool to predict the stability of the cluster. It confirmed the existence of magic clusters in 2D systems: magic clusters were shown to have large values of the first non-zero frequency while non-stable clusters were found to have small values. In order to test if the lowest non-zero eigenfrequencies give similar information concerning the stability of 3D clusters, we computed for the first time the normal modes of 3D isotropic systems. Fig. 5.10 displays the value of the first non-zero frequencies (blue square, left axis) for systems varying from $N = 4$ till 100 particles.

The stability of 3D clusters was investigated previously through the calculation of the second derivative of the binding energy with respect to N in Refs.

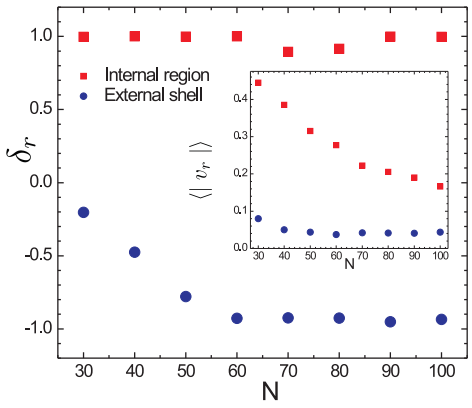

Fig. 5.9: Averaged radial deviation of the eigenvectors δ_r calculated in the internal region of the cluster (red squares) and in the external shell (blue dots) as function of N. In the inset, the average length of the radial component of the eigenvector are displayed for both the internal region (red squares) and the external shell (blue dots).

[98, 110], which is defined [2] by

$$\Delta E = E(N+1) + E(N-1) - 2E(N) \tag{5.9}$$

where $E(N)$ is the ground state energy of a N-particle cluster. The binding energy (red dots, right axis) as function of the total number of particles for systems ranging from $N = 4$ up to 100 particles is shown in Fig. 5.10. The ground state configuration of systems with $N = 4, 6, 10, 12, 19, 32, 38, 56$ [110] and $N = 81, 94$ [98] were classified as magic clusters. We can see that for those systems there is a pronounced peak in the value of $\triangle$E. From Fig. 5.10 we can see that in many situations the maxima and minima in the value of $\triangle$E and those in the first non-zero eigenfrequency coincide for small systems with only a single shell ($N < 22$). Those systems are indicated by arrows on the top of Fig. 5.10(a). On the other hand, such coincidences in the maxima and minima is not that evident for larger systems. Furthermore, also the system with $N = 13$ can be identified as a magic number cluster based on our normal mode analysis. However, it was not classified as magic cluster in Refs. [98, 110]. In fact not all magic clusters can be revealed by the analysis of the binding energy, especially when there are two magic clusters with similar structure but differing only by one single particle. In other words, the energy difference of the system with $N = 13$ particles is negative due to a pronounced decrease of energy found in the magic cluster with $N = 12$ particles.

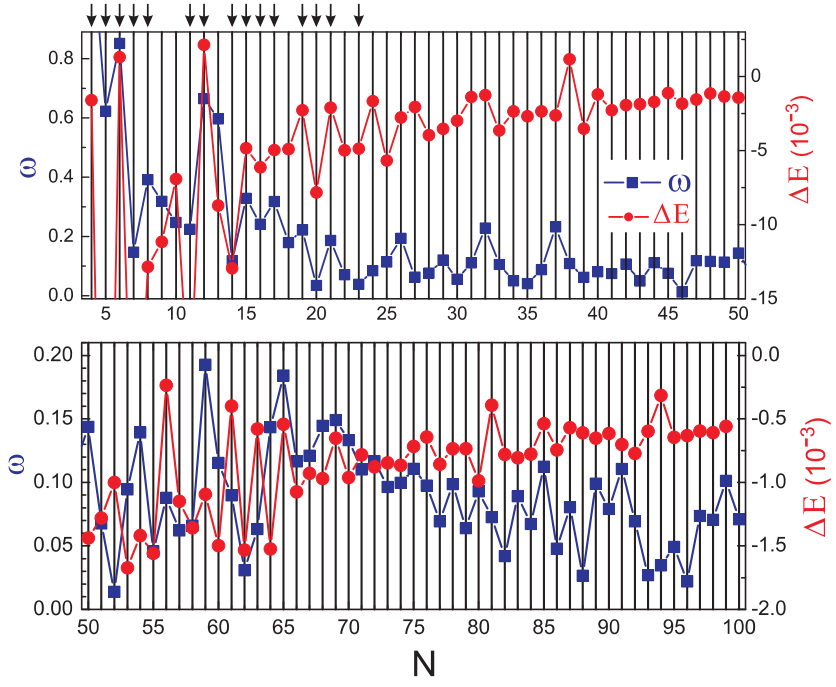

FIG. 5.10: (a) and (b) display the first non-zero frequency (left axis and blue square) and the second derivative of the binding energy (right axis and red circle) as function of the number of particles.

In order to understand why there is correspondence between a peak in $\triangle$E and a high first non-zero eigenfrequency for 3D clusters with a single shell, and no correspondence anymore for larger 3D clusters, it is important to consider typical eigenmodes corresponding to these eigenfrequencies. Figs. 5.11 shows in sequence from (a) to (h) the eigenvectors associated to the lowest non-zero frequency for the systems with $N = 6$, 12, 13, 23, 28, 29, 36 and 60 particles. Those systems were chosen because they have different number of particles in the inner shell. In the external shell the 4-, 5-, and 6-fold particles are represented respectively by gray, black and orange balls. Particles in the inner shell are indicated by red balls. The arrows indicate the direction of oscillation while their lengths are proportional to the amplitude of oscillation of each associated particle. For the systems with $N = 6$ and 12 particles (Figs. 5.11(a) and (b)) we notice that their eigenvectors are mainly directed tangentially to the surface of the shell of the cluster. We call this sort of mode an intra-shell motion. The large value of the eigenfrequencies for the systems with $N = 6$ and 12 particles indicates that these magic clusters have large mechanical resistance against intra-shell diffusion. The eigenfrequency of the system with $N = 13$

particles is $\omega = 0.5966$ which value is comparable to the eigenfrequency of the system with $N = 12$ particles. Fig. 5.11(c) displays the eigenvectors for the first non-zero frequency of the system with $N = 13$ particles, which is similar to the mode of the system with $N = 12$ particles, i.e. an intra-shell motion. This fact is not surprising since the system with $N = 13$ particles has exactly the same arrangement of particles as for the system with $N = 12$ but with one extra particle in the center. This confirms why the system with $N = 13$ particles is also a magic cluster. For small systems, i.e. the ones with only one shell, we found that the normal mode corresponding to the lowest non-zero frequency corresponds to an intra-shell motion. However, for larger clusters the situation is more complex. Figs. 1(d), (e), (f), (g), and (h) display the eigenvectors, respectively, for the systems with $N = 23$, 28, 29, 36 and 60 particles. Notice that particles in the external as well as in the inner shell have oscillation amplitudes different from zero. A careful look to the eigenvectors associated to particles in the inner shell shows that they make a rotational motion while the motion of the particles in the external shell corresponds to an intra-shell diffusion of the particles. Thus the normal mode of lowest frequency for larger systems is a mixed mode, i.e. a combination of rotation and diffusion, respectively played by particles in the inner and external shells.

With this information we can understand why there is a correspondence between a peak in $\triangle$E and a high first non-zero eigenfrequency for 3D clusters with a single shell, and no correspondence anymore for larger 3D clusters. This is not a surprise since in 3D systems the total energy can be reduced via two different processes, i.e. the arrangement of particles in the shells or between shells. The shell of the cluster can be thought of as a quasi 2D system. Then one expects that by a symmetric triangular arrangement of particles in the shell the energy can be reduced. Such arrangement in the shell may increase the resistance of the cluster against intra-shell diffusion but has nothing to do with the resistance against inter-shell motion. With this picture the cluster should then remain with a small first non-zero frequency for the rotation mode, even if the total energy is small due to a more symmetric triangular arrangement in the shell. The fact that the motion corresponding to the first non-zero frequency is a mixed one is the main reason of the disagreement found between the maxima and minima of $\triangle$E and the first non-zero frequency for large systems. This picture is different from the one found in a 2D Wigner crystal since in that situation the normal mode corresponding to the first non-zero frequency is always an inter-shell rotation mode, i.e. there are no mixed modes. Furthermore, magic clusters are the ones where particles arrange themselves in a more triangular arrangement. This arrangement increases the value of the first non-zero frequency and decreases the total energy of 2D systems. That is why in 2D systems the magic clusters were successfully identified both via a normal mode analysis and energy calculations [2, 16]. We can conclude that in 3D systems the energy difference and the normal mode analysis give complementary information.

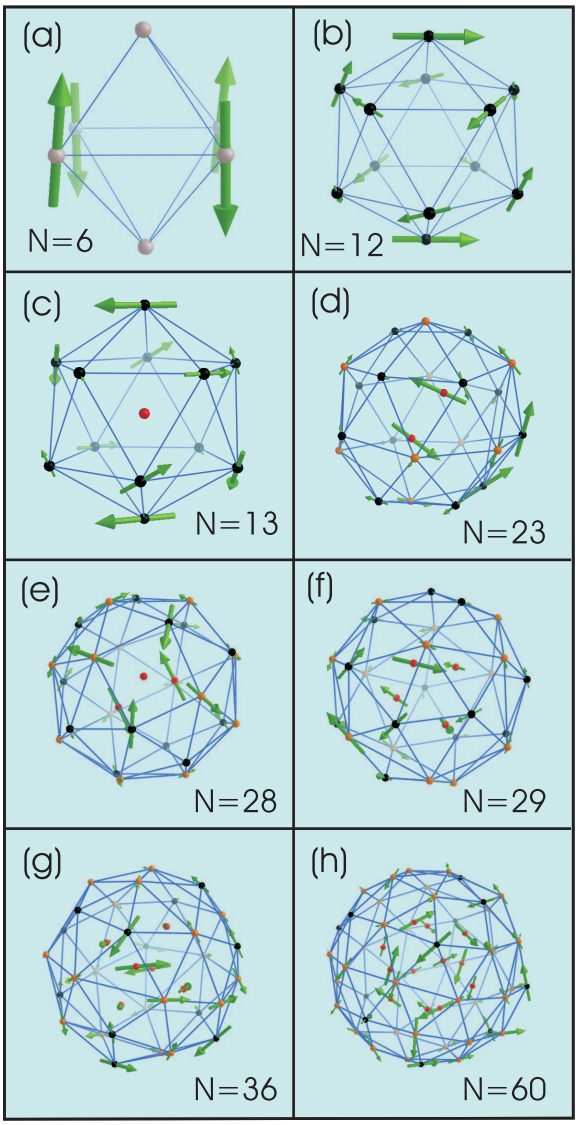

FIG. 5.11: Visualization of the cluster structure and oscillation mode. For the external shell 4-fold, 5-fold, and 6-fold particles are represented, respectively, by gray, black, and orange balls. Particles in the internal shell are represented by red balls. The arrows represent the eigenvectors associated to the lowest non-zero frequency, and the arrow's length is proportional to the amplitude of oscillation of the associated particle.

5.4 SUMMARY AND CONCLUSIONS

We presented the results of a detailed numerical simulation of the configuration of the ground state and the lowest energy metastable state configuration, and the spectrum of normal modes of classical 3D clusters with isotropic parabolic confinement. The confined particles interact through a repulsive potential such as Coulomb or screened Coulomb interparticle potential. For small systems the structural difference between the GS and MS configuration are mostly due to a different number of shells or different number of particles per shell. As the total number of particles increases the energy difference between GS and MS configuration decreases and the structural difference between them are often due to a different arrangement of the same number of particles on the shells.

The eigenmode frequencies are investigated both for Coulomb and screened Coulomb interparticle potential. Both small and larger systems satisfy Euler's theorem and the total topological charge defect is 12. For larger systems the appearance of negative defect charge (seven fold correlation defect) is compensated by an excess of positive charge due to defects with 5 fold coordination number. The breathing and the center of mass mode frequencies are analytically determined and both are independent of the number of particles. The breathing mode has the highest frequency value for the case of a Coulomb interparticle interaction potential system while this is no longer true for systems of confined particles interacting through a Yukawa potential. In fact the breathing mode has the highest frequency both for two and three dimensional parabolic confined systems when the interparticle interacting potential is given by the solution of the Poisson equation. In the present work, the Coulomb interaction is the solution of the Poisson equation while for a two dimensional system its solution is a logarithmic potential. We found a satisfactory relation between the appearance of maximum and minimum in the lowest non-zero eigenfrequency and in the second derivative of the binding energy as function of N for small clusters ($N < 23$) which indicates the most and least stable clusters. Such correspondence is not seen in larger clusters due to the fact that there the normal mode of first non-zero frequency becomes a mixed mode with a rotational and intra-shell motion component.

Publication The results in this chapter were published as:

S. W. Apolinario, B. Partoens, and F. M. Peeters, *Structural and dynamical aspects of small three-dimensional spherical Coulomb clusters*, New J. Phys. **9**, 283 (2007).

6

Melting transitions in isotropically confined three-dimensional small Coulomb clusters

A large number of works is directed towards 2D systems [2, 16, 26]. The melting process in 2D systems was found to happen through two distinct stages. First at low temperature particles of different shells lose their relative angular orientation, which is called intershell melting. Secondly, at higher temperature, particles are able to jump between shells, which is called radial melting. Reference [2] showed that some of the ground state configurations in 2D systems, called magic clusters, exhibit a substantial larger intershell melting temperature. The stability found in magic clusters was due to the existence of commensurability between particles in different shells. The melting process in small 3D isotropic crystals have been much less explored. Ref. [113] investigated only the melting process for clusters with N=30 and 94 particles. They found that for increasing temperature, the system shows two types of diffusion pattern: a first one is diffusion of particles inside the same shell and the second one concerns intershell diffusion. In our investigation we considered clusters having only one shell, i.e. clusters with N=5 till 12 particles and clusters with two shells and those having $N = 19$, 32, 38 and 55 particles were investigated in detail. Differently from previous works we investigated the melting process using the Lindemann's criterion for intrashell, intershell as well as radial displacements. Such analysis allowed us to identify a new melting transition which was not found in Ref. [113], i.e. the intershell melting transition. Furthermore, we found that the melting process at low temperature is much richer than

the usual two step melting process found previously in 2D Coulomb clusters and that temperature can induce also structural transitions which leads to an enhanced symmetry with increasing temperature.

In order to test if our results are still meaningful for other systems such as dusty plasmas and Coulomb balls we extended our investigation to systems with screened Coulomb interacting particles. The linear dynamics of the system is also investigated through a normal mode analysis.

This chapter is organized as follows. In the next section our model system is introduced, the methodology used to find stable configurations and the normal modes are given. In section III we deal with the system of classical particles interacting through a Coulomb interparticle potential. First, we investigate the melting processes in small clusters of particles ranging from $N = 5$ to 13 particles, i.e. clusters with one shell. Subsequently we investigated larger systems and in particular the magic clusters with N= 19, 32, 38 and 56 particles. In section IV we investigate the melting processes which are relevant at very low temperature and in section V systems of screened Coulomb interacting particles are addressed. Finally, in section VI we present our conclusions.

6.1 MODEL AND NUMERICAL APPROACH

We study a $3D$ model system of N equally charged particles in an isotropic confinement potential and interacting through a repulsive potential. The potential energy of the system is given by

$$E = \sum_{i=1}^{N} \frac{1}{2} m\omega_0^2 r_i^2 + \sum_{i>j}^{N} V(|\mathbf{r}_i - \mathbf{r}_j|), \tag{6.1}$$

where m is the mass of the particle, $\mathbf{r}_i = (x_i, y_i, z_i)$ is the vector position of the i-th particle, $V(\mathbf{r})$ is the repulsive interparticle interaction potential and ω_0 is the confinement frequency of a single particle. In the present study we consider a screened Coulomb potential $V(\mathbf{r}) = (q^2/\epsilon)\exp(-|\mathbf{r}|/\lambda)/|\mathbf{r}|$ which reduces to a Coulomb potential for $\lambda \to \infty$. We can write the potential energy (6.1) in dimensionless form

$$E = \sum_{i=1}^{N} r_i^2 + \sum_{j>i}^{N} \frac{\exp(-\kappa|\mathbf{r}_i - \mathbf{r}_j|)}{|\mathbf{r}_i - \mathbf{r}_j|}, \tag{6.2}$$

if we express the coordinates, energy, temperature and time, respectively, in the following units $r_0 = (q^2/\epsilon\gamma)^{1/3}$ where $\gamma = m\omega_0^2/2$, $E_0 = \gamma r_0^2$, $T_0 = E_0 k_B^{-1}$ where k_B is the Boltzmann constant and $t_0 = \sqrt{2}/\omega_0$. The dimensionless inverse screening length, $\kappa = r_0/\lambda$, is a measure of the range of the inter-particle interaction potential. All our numerical results will be given in dimensionless units.

The stable configuration is a local or global minimum of the potential energy which is only a function of the number of charged particles N and the screened Coulomb parameter κ. Our numerical method to obtain the stable state configuration is based on the Monte Carlo simulation technique supplemented with the Newton method in order to increase the accuracy of the found energy value [16]. By starting from many different random initial configurations we are able to find the possible stable states, i.e. ground state and metastable state configurations which we documented in Ref. [112]. The eigenfrequencies are the square root of the eigenvalues of the dynamical matrix

$$H_{\alpha\beta,ij} = \frac{\partial^2 H}{\partial r_{\alpha,i} \partial r_{\beta},j}\Big|_{r_{\alpha,i}=r^n_{\alpha,i}} \tag{6.3}$$

where $\{r^n_{\alpha,i}; \alpha = x, y, z; i = 1, ..., N\}$ is the position of the particles in the ground state configuration.

6.2 MELTING TRANSITION FOR SYSTEMS WITH COULOMB INTER-PARTICLE POTENTIAL

In this section we investigate the characteristics of the melting process in small $3D$ clusters of isotropically confined particles interacting via a Coulombic potential.

In Ref. [110] magic clusters were investigated on the basis of potential energy calculations of the cluster configuration. This was done by calculating the addition energy, which was defined as

$$\Delta(N) = [E(N+1) + E(N-1) - 2E(N)], \tag{6.4}$$

where $E(N)$ is the ground state energy of an N-particle cluster. Mathematically the addition energy corresponds to the second derivative of the potential energy $E(N)$ with respect to the total number of particles N, and as such describes the "curvature" of the energy as function of the number of particles. Physically the addition energy is the amount of energy gained by the formation of two N-particle clusters out of two (N-1)- and (N+1)- particle clusters. From the analysis of the minimum energy and the addition energy of the cluster Ref. [110] found that clusters with $N = 6, 12, 19, 32, 38$ and 56 particles have large mechanical stability. Ref. [98] also identified magic cluster configurations of 3D clusters. They implemented a topological analysis of the relative arrangement of particles in different shells and computed the Voronoi parameter. Furthermore the magic cluster configurations found in both references coincided for small 3D Wigner clusters. However, Refs. [98, 110] do not test directly the stability of 3D clusters. In this section we perform MD simulation to investigate the mechanical stability of $3D$ isotropic Wigner crystals of charged particles interacting through a Coulomb interparticle interaction potential. From this

investigation we were able to identify the correct magic clusters, i.e. those with pronounced mechanical stability.

The main static characteristics of the investigated 3D magic clusters are compiled in Table 6.1. From left to right, Table 6.1 lists the number of particles in the system, its energy per particle, its configuration, the radius of the shells, and the width of the shells. The GS configuration of the systems with less than 13 particles form only one shell. While systems larger than 12 particles form two shells. For example, the third column of Table I shows that the system with N=31 has 4 and 27 particles respectively in the internal and external shells. From the last column of Table 6.1, we notice that the width of the external shell is larger than the width of the internal shell. In fact the external shell is formed by subshells each with a radius very close to each other. On the another hand, particles in small systems organize themselves in a perfect shell with width equal to zero, as we can see for the systems with N=6 and 12 particles. The stability of those subshells are investigated in Sect. IV.

In previous work on 2D systems [54] the melting temperature of the intrashell, intershell and radial melting processes were determined. To do so the Lindemann criterion was used and the averaged displacements were computed. For a 3D system the expression for the square of the radial displacement becomes

$$\triangle r_\gamma = \frac{1}{N_\gamma}\sum_{i=1}^{N_\gamma}\left\langle r_i^2\right\rangle - \left\langle r_i\right\rangle^2, \tag{6.5}$$

where r_i is the modulus of the position vector of the i^{th} particle. Similarly, for the intrashell displacement we defined

$$\triangle \alpha_\gamma = \frac{1}{N_\gamma}\sum_{i=1}^{N_\gamma}\left\langle \alpha_{ij}^2\right\rangle - \left\langle \alpha_{ij}\right\rangle^2, \tag{6.6}$$

where α_{ij} is the angle made by the position vectors of the two first neighboring particles of number i and j belonging to the same shell, and

$$\triangle \alpha_{\gamma\beta} = \frac{1}{N_\gamma}\sum_{i=1}^{N_\gamma}\left\langle \alpha_{ij}^2\right\rangle - \left\langle \alpha_{ij}\right\rangle^2, \tag{6.7}$$

for the intershell displacement, where α_{ij} is the angle made by the position vectors of the two first neighboring particles of number i and j belonging, respectively, to the β^{th} and γ^{th} shells. In both equations N_γ indicates the total number of particles in the γ^{th} shell, and $\langle ...\rangle$ is an average over time. In order to characterize the melting temperature, we made use of a Lindemann-like criterion, which states that, close to the melting process, the respective averaged displacement starts to deviate rapidly from its low temperature linear dependence.

Table 6.1: From left to right: the number of particles in the system (N), its energy per particle (E/N), its configuration (conf.), the radius of the shell (r), and the width of the shell Δ(r).

N	**E/N**	**conf.**	**r**	$\Delta(r)$
6	2.6540390	6	0.9406	0.0000
12	4.8389665	12	1.2700	0.0000
18	6.6788303	1.17	0.0000 1.5353	- 0.0012
19	6.9641459	1,18	0.0000 1.5654	- 0.0122
20	7.2471808	1,19	0.0002 1.5946	- 0.0176
31	10.0795110	4,27	0.7926 1.9399	0.0124 0.1098
32	10.3186788	4,28	0.7935 1.9596	0.0000 0.0882
33	10.5565871	4,29	0.7914 1.9791	0.0215 0.1304
37	11.4787472	6,31	0.9585 2.0947	0.0324 0.1150
38	11.7029516	6,32	0.9549 2.1119	0.0000 0.1166
39	11.9283228	6,33	0.9549 2.1289	0.0348 0.1186
55	15.2847026	12,43	1.2773 2.4618	0.0250 0.1086
56	15.4821444	12,44	1.2770 2.4743	0.0193 0.1110
57	15.6793502	12,45	1.2763 2.4869	0.0210 0.1110

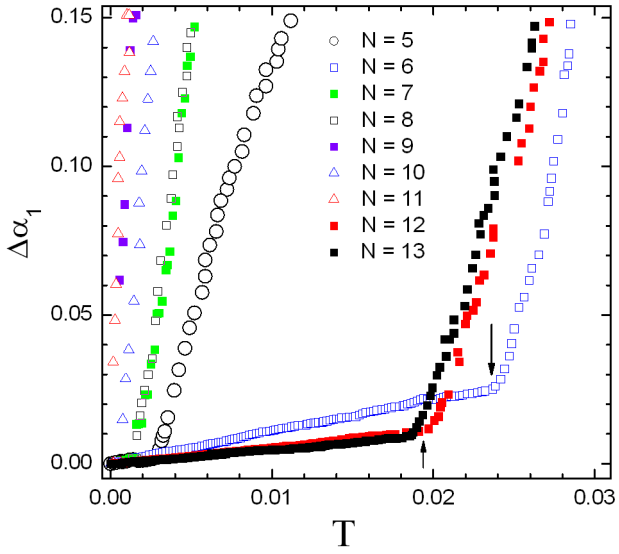

FIG. 6.1: Intrashell displacement for systems ranging from N=5 till 13 particles as function of the temperature.

The dynamics of one-shell systems was investigated by a MD simulation where we collected data during an interval of 10^6 time steps. The intrashell and radial displacements were computed. Fig. 6.1 displays the results obtained for the intrashell displacement as function of temperature for systems varying from N=5 till 13 particles. The intrashell melting temperature of the magic clusters with N=12 and 6 particles are respectively equal to T=0.0195 and 0.0238 (indicated by black arrows in Fig. 6.1). Those critical temperatures are remarkably larger than the melting temperature found in other non-magic clusters. The intrashell melting temperatures of magic clusters with N=12 and 6 particles are respectively about 7 and 8 times larger than the melting temperature T=0.0027 found for the cluster with N=5 particles, which is the non-magic cluster of one shell structure that is most stable against intrashell diffusion. In fact, for increasing temperatures, the intrashell averaged displacement of non-magic clusters of a single shell increases steeply once temperature becomes different from zero. The intrashell melting temperature for systems with N=12 and 13 particles have approximately the same value, i.e. $T = 0.0195$ and 0.0187 respectively. This fact is not a surprise since both systems share the same arrangement of particles on the shell, i.e. particles arrange themselves

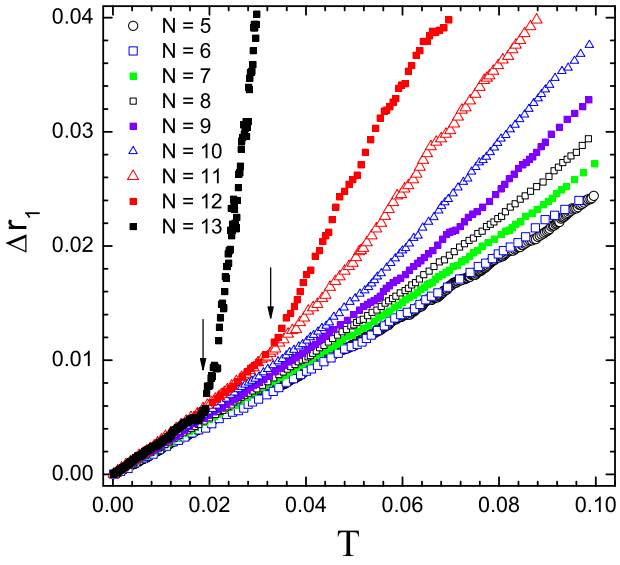

Fig. 6.2: Radial displacement for systems ranging from N=5 till 13 particles as function of the temperature.

in an icosahedral structure. One concludes that the GS configuration of the system with N=13 particles also forms a magic cluster. The latter fact could not be revealed through the addition energy analysis performed in previous works [98, 110].

Fig. 6.2 displays the radial displacement against temperature for the ground state configurations of systems ranging from N=5 till 13 particles. The largest system, i.e. the one with N=13 particles, is formed by one shell with 12 particles which encloses an extra particle sitting in the center. We see that the radial averaged displacement of this system changes its initial linear behavior to a rapid increase at a well defined critical temperature of $T = 0.0194$. From previous experience obtained on $2D$ systems [114] we know that this rapid increase of the radial displacement occurs when the number of jumps of particles from the shell to the cluster's center and vice versa becomes statistically large. This is only possible due to the fact that the system with 13 particles has a MS state with configuration (1,12), i.e. one particle in the center and 12 particles forming a shell. Systems without metastable configurations are expected to expand gradually with increasing temperature. The curves for $\triangle r$ for systems

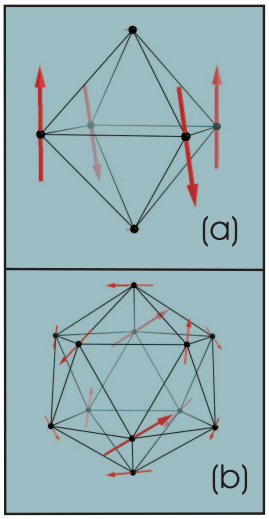

FIG. 6.3: Representation (red arrows) of the oscillation mode of the first non-zero frequency for the systems with (a) N=6 and (b) 12 particles.

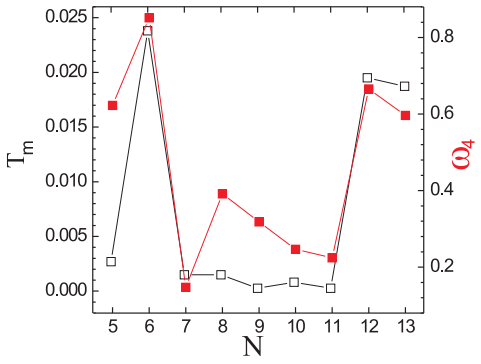

FIG. 6.4: Critical temperature for the first melting process (left axis, black open square) and lowest non-zero frequency (right axis, red square) for systems varying from N=5 till 13 particles.

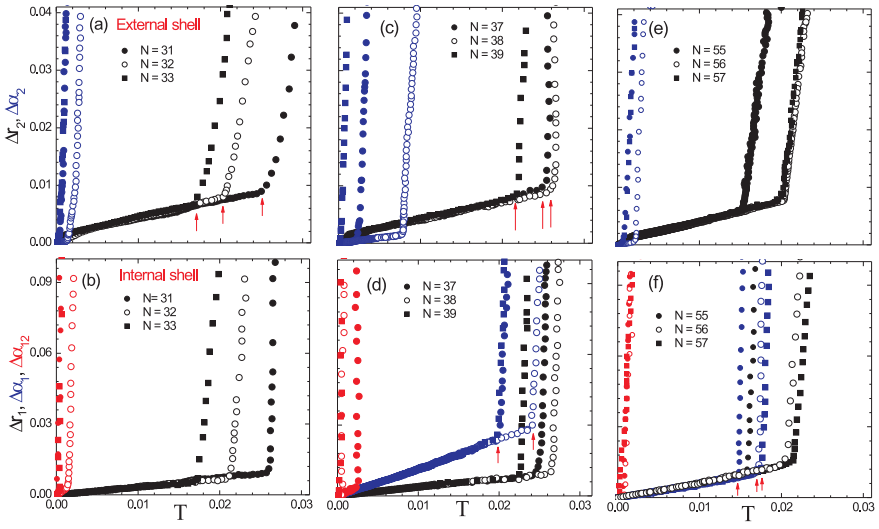

Fig. 6.5: Radial (black color) and intrashell (blue color) displacement computed for the external (upper figures) and internal (lower figures) shell for clusters with different number of particles. The red symbols in the lower figures give the intershell displacement for the different systems.

with N=5, 6, 7, and 8 particles, which do not have metastable states, reflect correctly this statement, i.e. there is no abrupt change in their value. Finally we notice that for increasing temperatures the radial displacements of the clusters N=9, 10, 11 and 12, which respectively have metastable configurations (1,8), (1,9), (1,10) and (1,11), also deviates from their low temperature linear behavior. The larger the system the lower the radial melting temperature is. This can be clearly seen from the cases of N=12 and 13 particles whose radial melting temperature are respectively equal to $T = 0.0326$ and 0.0194 (indicated by black arrows in Fig. 6.2).

At very low temperature the dynamics of the system is ruled by simple harmonic oscillations about a local energy minimum. In this limit the melting process can also be understood through a normal mode analysis. Each mode is defined by an eigenvector and its corresponding eigenfrequency. Figs. 6.3(a) and (b) represent the eigenvectors (red arrows) for the normal mode of the lowest non-zero frequency respectively for the systems with N=6 and 12 particles. The length of the arrows is proportional to the oscillation amplitude of the associated particle. The lowest frequency modes correspond to delocalized motions, in which a large number of particles oscillate with considerable

amplitude. The highest frequency motions are more localized and contribute less to the melting process at low temperature. The first non-zero frequency should then be related with the first melting process that occurs in isotropically Wigner crystals if this melting process occurs at sufficiently low temperature. In other words, if the system has a large melting temperature, it will also have a large first non-zero frequency. The lowest non-zero frequency corresponds in fact to the 4^th mode of oscillation since isotropic clusters always have three modes of rotation which frequencies are equal to zero [112]. Fig. 6.4 displays the critical temperature of the first melting process (left axis) and the values for the first non-zero frequencies (right axis). We notice that the clusters with largest melting temperatures have also a large value for the first non-zero frequency. In particular the magic clusters with N=6 and 12 particles have respectively the frequencies $\omega = 0.8516$ and 0.6654 which are the two largest ones.

For fewer than 12 particles in a 3D system the ground state configuration consists of a single shell. Those configurations in fact are three dimensional regular polygons centered around the origin. For larger systems particle clouds arrange themselves in the form of concentric spherical shells if the confinement potential is isotropic. Those structures are classified by the number of particles per shell and they evolve as follow: for $N = 13$ particles it becomes energetically favorable to have a single particle inside the shell, for $22 < N < 27$ two particles constitute the internal structure, etc. 12 is the maximum number of particles allowed to fill the internal shell which happens for the system with $N = 60$ particles in case of a two shell structure. In the case of ground state configurations consisting of two shells, the inner-shell structures are analogous in shape to those for the corresponding single shell clusters [96]. The latter statement strongly suggests that the knowledge about the dynamics of single shell systems is helpful in the understanding of the dynamics of larger systems.

Now we turn our attention to the investigation of the dynamics of larger systems, i.e. systems with two shells. The main goal of this investigation is trying to elucidate if magic number configurations present commensurability between particles in the same shell or/and in different shells. Such property was found to play an important role into the dynamics of small 2D clusters [2]. Analogously this commensurability in 3D systems should enhance the stability of the cluster leading to an enhanced melting temperature. To do so we compare the results of the intrashell, intershell and radial displacements computed for the N-particle magic cluster with the ones obtained for systems with $N - 1$ and $N + 1$ particles. Fig. 6.5 displays the radial (black data), intrashell (blue data) and intershell (red data) deviations for the magic clusters with N=32, 38 and 56 particles and for their respective neighbors. The radial and intrashell displacements were computed for the external shell (upper figures, i.e. Figs. 6.5(a), (c) and (e)) and internal shell (lower figures, i.e. Figs. 6.5(b), (d) and (f)).

If magic clusters have commensurability between particles belonging to different shells one should expect a large resistance against radial and/or intershell diffusion. Fig. 6.5(a) displays the radial displacement (black symbol) computed for the particles in the external shell for systems with N=31, 32 and 33 particles. Their radial melting temperature are respectively equal to T=0.0249, 0.0206, and 0.0172 (red arrows in Fig. 6.5(a)). Those clusters follow the general behavior that the larger the cluster the lower the radial melting temperature. This is not hard to understand. It is built on the following two facts: 1) the number of metastable states increases with the number of confined particles, and 2) metastable states contribute to a decrease of the melting temperature. Fig. 6.5(e) displays the radial displacement (black symbol) for the external shell particles of the systems with N=55, 56 and 57 particles. Their radial melting temperature are, respectively, equal to T=0.0154, 0.0204, and 0.0199. The radial melting temperature of the magic cluster, i.e. the system with N=56 particles, is only slightly larger than the one of the cluster with N=57 particles. The radial melting temperature found for the external shell of the systems with N=37, 38 and 39 particles are respectively equal to T=0.0255, 0.0265 and 0.0221 and indicated by red arrows in Fig. 6.5(c). The magic cluster with N=38 particles has the largest radial melting temperature. We notice that large resistance against radial diffusion is not a unique property for magic clusters and that such property is only found for the system with N=38 particles. We will see later that particles in the external shell of the system with N=38 particles organize themselves in a particular form. Finally we observe that for a given system the critical temperature of radial melting for the external shell (Figs. 6.5(a), (c) and (e)) and for the internal shell (Figs. 6.5(b), (d) and (f)) have approximately the same values. This fact is, of course, a consequence of the radial diffusion of particles close to the critical temperature. The effect of radial diffusion is expected to be strong in systems with multiple shells.

We have seen (Fig. 6.1) that 6 and 12 particles arrange themselves in a structure carrying special property for their dynamics. This fact naturally led us to formulate the question: if those structures are surrounded by a second shell of particles, in case of large systems, is their stability against melting retained? We found that the answer is positive, i.e. those structures keep their stability properties, as we will demonstrate now. First lets consider the case of 6 particles in the internal shell. Such situation occurs for the GS configuration of systems with N=37, 38 and 39 particles. The internal shell of the non-magic clusters with N=37 and 39 particles have the same intrashell critical temperature of T=0.0197 while that for the cluster with N=38 particles this critical temperature is T=0.0241 (Fig. 6.5(d), red arrows). The value of those critical temperatures are lower than the intrashell melting temperature found for the isolated cluster with N=6 particles, i.e. T=0.0238 (Fig. 6.1). Also here we notice that the cluster with N=38 particles has the largest intrashell critical temperature. Similar picture is valid for the case when an icosahedron forms the internal shell of the systems with N=55, 56 and 57, where the intrashell

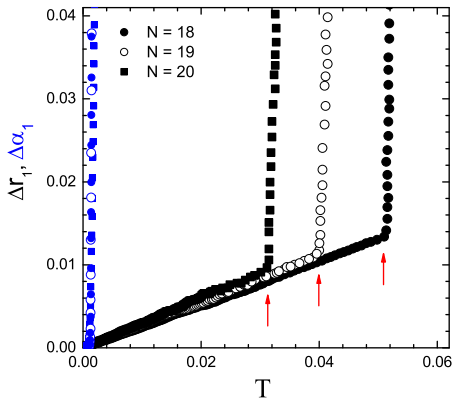

FIG. 6.6: Radial (black color) and intrashell (blue color) displacements computed for the external shell of the systems with $N = 18, 19$, and 20 particles.

melting temperatures in the internal shell are, respectively, equal to T=0.0148, 0.0174 and 0.0177 (see Fig. 6.5(f), red arrows). The lowering of the intrashell critical temperature of the internal shell of large clusters when compared to the ones of isolated clusters with N=6 and 12 particles is easily understood. In larger clusters the icosahedral and octahedral structures are submitted to a fluctuating electric field generated by the thermal induced movement of the external shell particles.

The temperature dependence of the intrashell displacement computed for the external shell and the intershell displacement are shown, respectively, in Figs. 6.5(a) (blue symbol) and 6.5(b) (red symbol) for the systems with N=31, 32 and 33 particles. We notice that for the same system those quantities diverge at the same temperature. For example, the intrashell displacement computed for the external shell (Fig. 6.5(a), blue open circles) and the intrashell displacement (Fig. 6.5(b), red open circles) for the cluster with N=32 particles diverge both at the temperature of T=0.00141. Since those two quantities diverge at the same temperature we can only conclude that the *intrashell melting* on the external shell is the first melting process to occur and that the dynamics of those systems do not show any sign of *intershell melting*. Analogous situation is found for the non-magic clusters N=31, 33, 37, 39, 55 and 57. For those systems the intrashell displacement computed for the external shell and the intershell displacement also have the same critical temperature. This fact can be verified in Figs. 6.5(c) and (d) for the systems with N=37 and 39 particles and in Figs. 6.5(e) and (f) for the systems with N=55 and 57 particles.

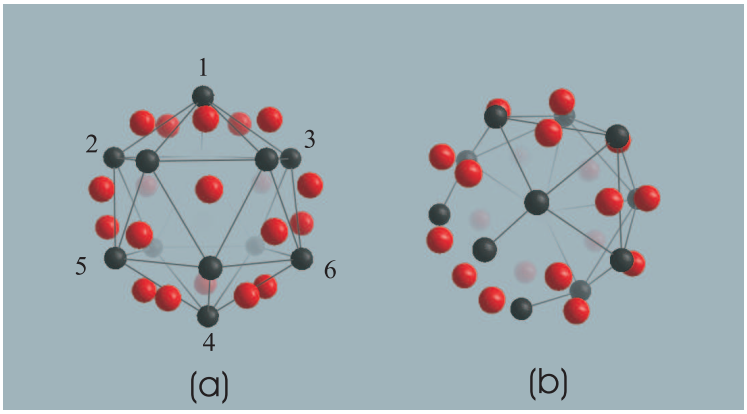

Fig. 6.7: Particle arrangement of 5-fold (black color) and 6-fold (red color) particles on the outermost shell in the ground state of the system with N=38 (a) and 37 (b) particles. In order to improve visualization bounds between first neighboring 5-fold particles are drawn.

The intershell melting plays an important role into the dynamics of the clusters with N=38 and 56 particles as we will now demonstrate. For the system with N=38 particles both the internal and external shells are relatively stable against intrashell melting, i.e. they are locked. The intrashell melting for the system with $N = 38$ particles occurs at the large temperatures of T=0.0241 and T=0.0078, respectively, for the internal (Fig. 6.5(c)) and external (Fig. 6.5(d)) shells. Differently to the large stability found against intrashell melting, this system exhibits low stability against intershell rotation. Fig. 6.5(d) shows that its intershell displacement (red open circles) diverges immediately for increasing temperatures, i.e. at $T = 0.0001$. When temperature is in the range [0.0001, 0.0084], i.e. the interval delimited by the critical temperatures, the dynamics is ruled by the relative motion of shells with respect to each other. The intershell rotation is also the first melting process to appear in the cluster with 56 particles. There the intershell and intrashell melting temperatures are, respectively, equal to T=0.001 and 0.002. The range of temperature in which the intershell rotation is allowed is much larger for the magic cluster with N=38 particles than for the magic cluster with 56 particles.

We have found that the magic clusters with N=6, 12, 13 and 38 particles exhibit large resistance against intrashell diffusion. Furthermore the magic cluster with N=38 particles exhibit intershell melting. A common characteristic in the structure of those magic clusters is that they are composed by octahedral or icosahedral polygons.

The cluster with $N = 19$ particles does not have one of those polygons what makes its dynamics interesting as we will see further. Nevertheless, the system

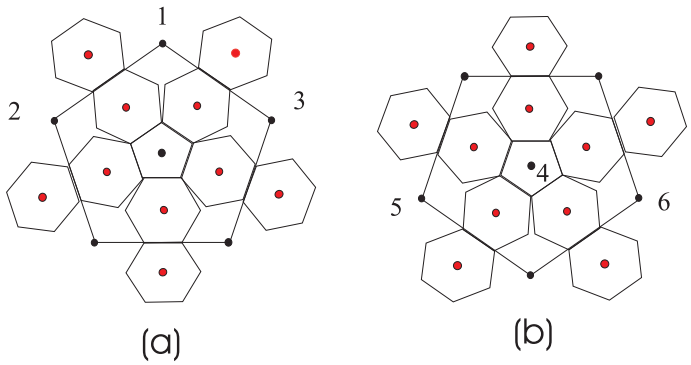

FIG. 6.8: Visualization of the top (a) and bottom (b) of the arrangement of particles in the external shell of the GS configuration of the system with N=38 particles (Fig. 6.7(a)). Particles in black and red are respectively 5- and 6-fold coordinated.

with 19 particles was classified in Refs. [98, 110] as a magic cluster. Fig. 6.6 displays the radial (black symbol) and intrashell (blue symbol) displacements computed for the external shell of N=18, 19 and 20 particles. The radial melting temperature for the clusters with N=18, 19 and 20 particles are, respectively, equal to T=0.051, 0.040 and 0.0315 and indicated in Fig. 6.6 (red arrows). The radial melting temperature follows the usual behavior, i.e. the larger the cluster the lower the melting temperature is. This system also does not present resistance against intrashell diffusion. A rapid increase of intrashell displacements (Fig. 6.6, blue symbols) for the systems with N=18, 19 and 20 occurs immediately for increasing values of the temperature.

The first melting process for systems with one shell was found to occur at relative high temperature if the first non-zero frequency is large. The first melting process for large clusters, i.e. clusters with two shells, is indicated by the red curve in Fig. 6.5. For the systems with N=55, 56 and 57 particles the first melting process occurs almost immediately for increasing temperature while that for the clusters with N=32 and 37 particles have larger values for the critical temperature. Table 6.2 displays the value of the first non-zero frequency and the critical temperature of the first melting process. The systems with relatively large melting temperature and large first non-zero frequency are the ones with N=32, 37 and 56 particles. We notice that those systems are not necessarily the magic clusters. Our results obtained by MD simulations are in accordance with the cluster's stability estimated by the normal mode analysis both for clusters with one and two shells.

From the analysis of the dynamics of one shell systems, i.e. Figs. 6.1 and 6.2, turns out that particles forming an octahedron and icosahedron have a large resistance against intrashell diffusion. We have seen that the system with N=38 particles have also high intrashell critical temperature for both shells.

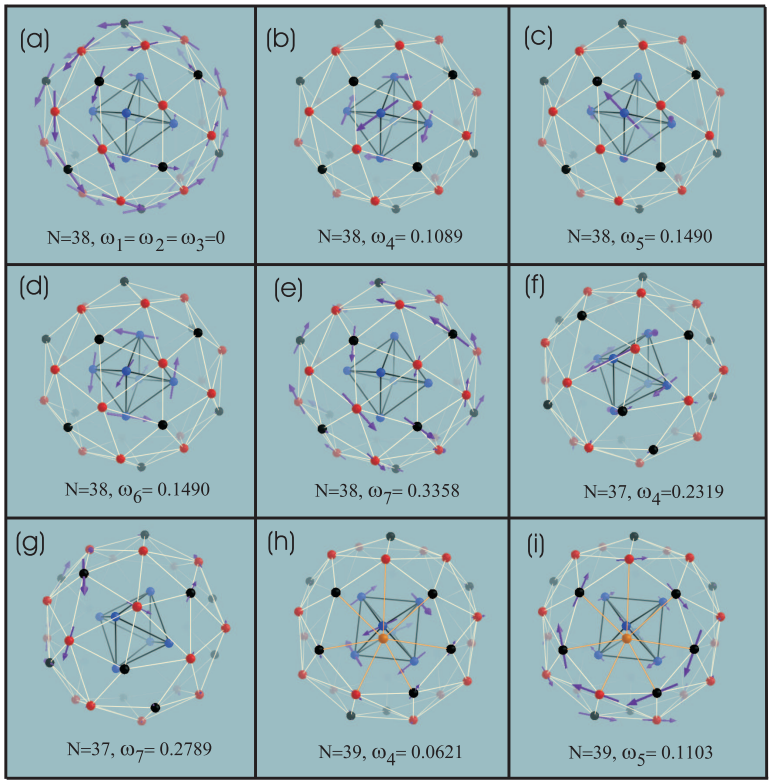

Fig. 6.9: Visualization of the cluster structure and oscillation mode. For the external shell 5-fold, 6-fold and 7-fold particles are represented, respectively, by black, red, and orange balls. Particles in the internal shell are represented by blue balls. The arrows represent the eigenvectors of a specific normal mode, and the arrow's length is proportional to the amplitude of oscillation of the associated particle.

The stability found in the internal shell of the system with N=38 particles is due to its octahedral symmetry. The topological characteristic of the arrangement of particles on the surface of the shell can be characterized by their disclination charge, q, which is the departure of their coordination number c from the preferred coordination number 6 (q=6-c). Particles with 5 and 6 neighbors are respectively called 5-fold and 6-fold particles. Fig. 6.7(a) shows the arrangement of particles in the external shell for the system with N=38 particles. One notices that 5-fold particles (in black color) form an icosahedral structure while the rest of the particles, i.e. 6-fold particles (in blue color), arrange themselves around the corner of the icosahedron. Notice that in the external shell there is no situation where a pair of first neighboring particles is formed by two 5-fold particles. In other words, there is at least one 6-fold particle between any pair

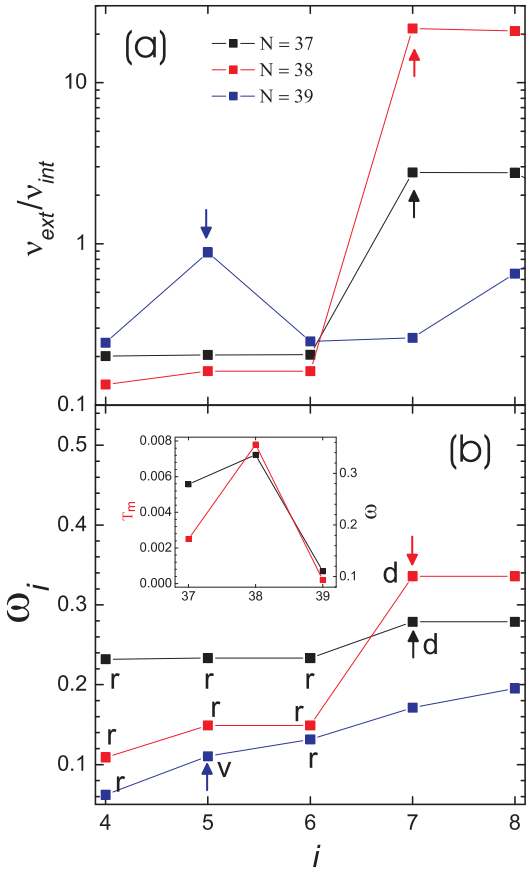

FIG. 6.10: (a) Averaged relative amplitude and (b) eigenfrequencies for the systems with N=37, 38 and 39 particles as function of the mode number i from $i = 4$ till 8. Arrows indicate the respective quantities related to intrashell melting. The letters state for r (rotation), v (vortex) and d (diffusion of particles on the external shell). The insert figure displays the intra-shell melting temperature (red square, left axis) and the frequencies of the mode for intrashell motion (black open square, right axis) for the systems with $N = 37$, 38 and 39 particles.

of 5-fold particles. To improve visualization we display a projection of the top (Fig. 6.8(a)) and bottom (Fig. 6.8(b)) parts of Fig. 6.7. We notice that the relative arrangement of particles in Figs. 6.8(a) and 6.8(b) is equivalent and that the whole structures are rotated with respect to each other by an angle of 72^o. Such icosahedral structure formed by the 5-fold particles in the external shell of the system with N=38 particles is not found for other clusters. As one example we show the arrangement of particles in the external shell of the

Table 6.2: From left to right: the number of particles in the system (N), the temperature of the first melting process (T_m), and the first lowest non-zero frequency ω_4.

N	T_m	ω_4
31	3.12×10^{-4}	0.110
32	1.37×10^{-3}	0.228
33	3.12×10^{-4}	0.106
37	2.30×10^{-3}	0.232
38	4.99×10^{-4}	0.109
39	2.05×10^{-4}	0.062
55	2.36×10^{-4}	0.046
56	8.16×10^{-4}	0.088
57	6.33×10^{-4}	0.062

system with N=37 particles in Fig. 6.7(b). The structure formed by the 5-fold particles is not an icosahedron and two 5-fold particles can form a pair of first neighboring particles.

One of the most interesting results of this paper is the large resistance against intrashell diffusion found in the external shell of the GS configuration of the system with N=38 particles. Next we investigated such mechanical property through a normal mode analysis. To do so we first identify which oscillation modes correspond to diffusion of particles in the external shell. We took into account only the modes of lowest frequencies since delocalized modes are the most important to understand the melting process. 3D isotropic clusters have three degenerated modes of rotation with frequencies equal to zero. We show in Fig. 6.9(a) one of those modes for the GS configuration of the system with $N = 38$ particles. In the external shell the 5- and 6-fold particles are indicated respectively by black and red balls. Particles in the internal shell are indicated by blue balls. The arrows indicate the direction of oscillation while their length is proportional to the amplitude of oscillation of each associated particle. Notice that for this mode particles in the internal and external shells oscillate approximately in parallel. In the sequence Figs. 6.9(b), (c) and (d) display respectively the 4^{th}, 5^{th} and 6^{th} oscillation modes, i.e the first three lowest

non-zero frequencies modes. Notice that those modes are governed mainly by the oscillation of particles in the internal shell characterizing an intershell rotation mode. Differently from the latter oscillation pattern, the 7^{th} mode of the GS configuration of the system with $N = 38$ particles (Fig. 6.9(e)) exhibits an intrashell motion of the external shell. For this mode the amplitude of oscillation of particles is much larger in the external shell than in the internal one.

In order to characterize quantitatively those modes we define the averaged relative amplitude $\Delta v_i = v_{ext}/v_{int}$, where v_{ext} (v_{int}) is the averaged amplitude of oscillation per particle computed in the external (internal) shell for the i^{th} normal mode. The normal mode related to intrashell melting of the external shell is the lowest frequency mode with large value of Δv_i. Fig. 6.10(a) displays Δv_i as function of the mode number i for the systems with N=37 (black open square), 38 (red square) and 39 (blue circle) particles. In agreement with the analysis of Figs. 6.9(b), (c) and (d), the value of the averaged relative amplitude is very small for the first three lowest non-zero frequencies of the system with $N = 38$ particles, i.e. $\Delta v_i < 0.2$ for $i = 4$, 5 and 6 (Fig. 6.10(a), red square). Contrarily, for the 7^{th} mode of the system with $N = 38$ particles the averaged relative amplitude is pronounced larger, i.e. $\Delta v_7 = 21.708$ (Fig. 6.10(a), indicated by red arrow). The latter mode is related to the intrashell melting of the external shell of the system with $N = 38$ particles.

For the systems with $N = 37$ and 39 particles the value of the averaged relative amplitude computed for the 7^{th} and 5^{th} modes are respectively equal to $\Delta v_7 = 2.7698$ (Fig. 6.10(a), black arrow) and $\Delta v_5 = 0.8852$ (Fig. 6.10(a), blue arrow). Those are the modes with an enhanced value for the averaged relative amplitude and therefore must be related to the intra-shell melting temperature on the external shell of those clusters. The eigenvector of the 7^{th} oscillation mode of the system with $N = 37$ particles is shown in Fig. 6.9(g) while that of its rotation mode, i.e. the 4^{th} one, is seen in Fig. 6.9(f). For the system with $N = 39$ particles the 5^{th} mode is shown in Fig. 6.9(i). This mode corresponds to a vortex-like motion where the vortex center sits at the 7-fold particle (orange ball). The mode of first non-zero frequency for the system with N=39 particles (Fig. 6.9(h)) corresponds mainly to an intershell rotation.

Fig. 6.10(b) displays the eigenfrequencies for the systems with $N = 37$ (black open square), 38 (red square) and 39 (blue circle) particles and mode number varying from $i = 4$ till 8. To indicate the motion mode the letters r, v and d are placed beside the data and stands respectively for rotation, vortex and diffusion on the external shell. The frequencies of the modes characterized by intrashell motion are indicated by arrows. From Fig. 6.10(b) we can see that the rotation mode $\omega_6 = 0.1490$ for the system with $N = 38$ particles is substantially smaller than its frequency for the intrashell mode, i.e. $\omega_7 = 0.3358$. The letter fact is in accordance to the values found for the critical temperatures of the system with $N = 38$ particles, i.e. an intershell melting temperature of value $T = 0.0001$ (see Fig. 6.5(d), open red circle) which

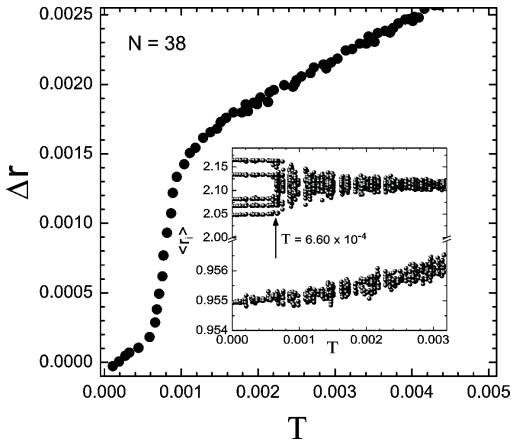

FIG. 6.11: Temperature dependence of the radial displacement for the system with N=38 particles in the low temperature range. In the inset the average radial position of the particles is shown.

is much smaller than the intrashell critical temperature of the external shell $T = 0.0078$ (see Fig. 6.5(c), open blue circle). Furthermore the insert in Fig. 6.10(b) shows the values for the intrashell critical temperature of the external shell (left axis, red square) and the frequency of the intrashell mode (right axis, black open square) for the particle numbers $N = 37$, 38 and 39. We notice a very good agreement between those two data, i.e. the larger the eigenfrequency, the higher the melting temperature is.

6.3 FINE STRUCTURE

Charged particles in 3D clusters, which are confined by a parabolic potential, order themselves in shells, if the number of particles is not too large. Often, such shells have a fine structure, i.e. the shells have a non-zero thickness (see last column of Table I) and closer inspection reveals that the shells consist of a few subshells, i.e. the shell has a non-zero width. In this section we consider the small temperature behavior of such clusters. We present a detailed investigation of the particles motion as a function of temperature before any jumps between shells occur and thus before the radial melting sets in. We found that the detailed behavior depends very crucially on the exact ground state configuration and that temperature induced structural transitions are possible which leads to an enhanced symmetry with increasing temperature.

Fig. 6.11 shows the temperature dependence of the radial displacement computed for the external shell for the magic cluster with N=38 particles. We can see that radial displacement increases rapidly over a small temperature interval

around T=0.0014. These small but rapid increases were never noticed before, probably because one needs rather accurate simulations in a small temperature range and for many temperature steps leading to long calculation times.

Such phenomenon can be understood by investigating the average radial position of each particle as a function of temperature. These results are shown in the inset of Fig. 6.11, where at zero temperature the two-shell structure is clearly seen with the outer shell showing a fine structure resulting in five subshells. However, exactly at the temperature where the jump in the mean square radial deviation occurs for the outer shell, those subshells start to coalesce into a single shell. We can conclude that this jump corresponds to a local melting of the outer shells, forming a single broad shell. This leads to an increased symmetry of the system. Consequently, the transition is a temperature induced structural (phase) transition. It is similar to the structural phase transition which was recently found for certain 2D Coulomb bound clusters [115]. At this jump, the angular order between particles in different shells is destroyed, due to intershell motion, as shown in Figs. 6.5(c) and (d), which displays, respectively, the intrashell and intershell displacements.

The system with 38 particles is a magic configuration, it is interesting to see if the above results are different for a non-magic configuration. We consider first the non-magic cluster with N=33 particles. The radial displacement for the outer shell is shown in Fig. 6.12 and the average position of the particles in its inset. The outer (inner) shell can be divided into seven (two) subshells at zero temperature. With the slightest increase of temperature, the subshells start to form one broad shell. This local radial melting goes hand in hand with the loss of intrashell angular order (see Fig. 6.5(a)).

The radial displacement computed for the external shell of the system with N=57 particles is shown in Fig. 6.13 and in its inset we can see the average radial position for all particles. The outer and inner shells at low temperature are composed of several subshells. For increasing temperature those subshells start to coalesce, but new is that for the outer shell this is a two step process. Indeed, the radial displacement passes through two distinct jumps, respectively, at the temperatures $T = 2.33 \times 10^{-4}$ where the outer shell merges into three subshells and $T = 0.0012$ where finally the particles in the outer shell form a single broad shell. At those critical temperatures the pattern of the average radius changes, as we can see in the inset of Fig. 6.13. Furthermore, the orientational order between the first and second shells is already lost at the low critical temperature of $T = 2.33 \times 10^{-4}$ (see Fig. 6.5(e,f)).

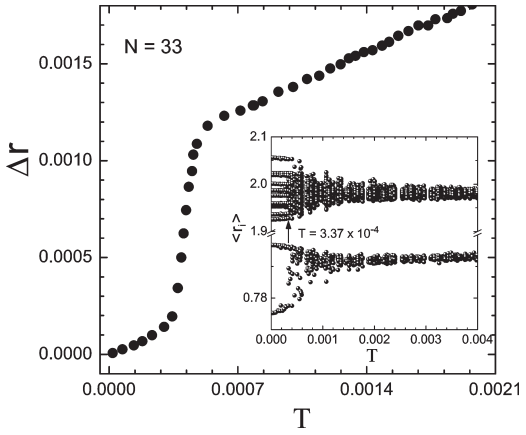

Fig. 6.12: The same as Fig. 6.11 but now for N=33 particles.

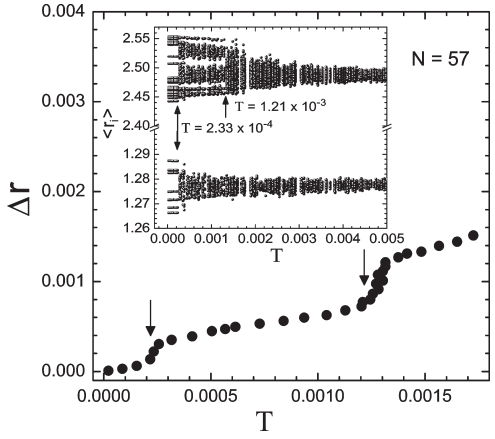

Fig. 6.13: The same as Fig. 6.11 but now for N=57 particles.

6.4 MELTING TRANSITION FOR SYSTEMS WITH A SCREENED COULOMB INTERPARTICLE POTENTIAL

In the previous sections we have investigated melting processes for isotropically confined Wigner crystals of particles interacting through a pure Coulomb potential. The dynamics of the systems was investigated over the whole temperature range. At high temperatures melting can develop through three processes, i.e. intrashell, intershell and radial melting. While that for larger clusters and at low temperatures a local transition sets in the external and internal shells which brings the system to a more symmetric configuration. However,

many systems, for example dusty plasmas, does not interact through a pure Coulomb potential but rather through a screened Coulomb interparticle potential. In this section we investigate the dependence of the melting processes on the range of the interparticle interaction. First, we investigate the melting process for magic clusters with N=6 and 12 particles and interacting though a screened Coulomb potential with screening parameter $\kappa = 1$. This value of the screening parameter is typically found in experiments [21]. The characteristics of the melting process found for those systems will be compared with the one present in systems of particles interacting through a Coulomb potential. Finally, the effect of screening of the interparticle interaction potential in larger clusters, i.e. systems with N=38 and 39 particles, is addressed.

The temperature dependence of the intrashell displacement for the systems with $N = 6$ and 12 particles and $\kappa = 1$ are displayed in Fig. 6.14 (blue symbols). For the sake of comparison the results for the Coulomb case are also displayed. We note that there is no significant change in the behavior of the intrashell melting when the Coulomb potential is screened. The intrashell melting temperatures for the systems with $\kappa = 1$ and 0 have approximately the same values, i.e. $T = 0.0238$ and 0.0196, respectively for N=6 and 12 particles. The radius of the GS configuration decreases with increasing screening parameter. For the Coulomb ($\kappa = 1$ screened Coulomb) case, the radius of the GS configurations are r=0.9406 (0.8165) and 1.27 (1.0646) respectively for the systems with N=6 and 12 particles, respectively. Although the radius of the cluster is reduced by increasing the value of κ the relative angle between the position vectors of the particles in the GS configuration remains the same. In fact, particles in both GS configurations, i.e. for $\kappa = 0$ and 1, arrange themselves in the corners of an icosahedron.

Fig. 6.14 also displays the radial displacement against temperature for the GS configuration of the systems with N=6 and 12 particles and screening parameter $\kappa = 1$ (black data). The radial displacement for the Coulomb system was also added to the figure. We can see that the radial melting temperature also does not depend strongly on the screening parameter. The radial melting temperature for the system with N=12 particles is approximately $T = 0.0326$ and 0.0332, respectively, for $\kappa = 0$ and 1. Before the critical temperature we notice a slight difference in the linear behavior of the radial displacement. Actually, the radial displacement has a different slope for different values of κ which was not the case for the intrashell displacement.

Now we analyze the effect of the screening of the interparticle interaction potential into the dynamics of large clusters. The screening parameter κ can induce structural phase transitions of first and/or second order. At those transitions discontinuities in first and seconde derivatives of the energy with respect to the screening parameter are found [70, 116]. This phenomenon can appear both in the GS and MS configurations and so the energy difference between those states is a good quantity to identify such structural phase transitions.

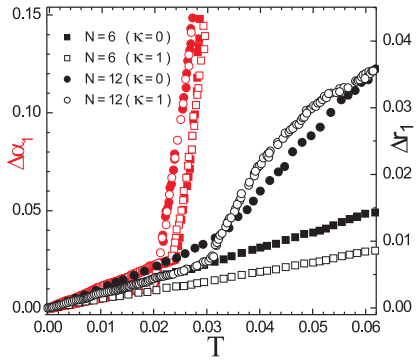

Fig. 6.14: Temperature dependence of the intrashell (red symbols) and radial (black symbols) displacements for the magic clusters with N=6 and 12 particles and screening parameter $\kappa = 1$ and 0.

Second order structural phase transitions can be identified through the computation of the first non-zero frequency. At the point where the second order transition occurs the first non-zero frequency becomes equal to zero [132]. Fig. 6.15 displays the energy difference $E_2 - E_1$ (right axis) between the lowest energy MS and the GS configurations against the screening parameter κ for the systems with $N = 38$ (blue squares) and $N = 39$ (red squares) particles. We notice that the behavior of the energy difference strongly depends on the cluster size. The energy difference for the system with N=38 particles increases smoothly with κ. The latter fact indicates that the screening parameter κ does not induce a first order structural phase transition neither in the GS nor in the MS configurations of the system. In addition, Fig. 6.15 also displays the first non-zero frequency ω_4 (left axis) for the system with $N = 38$ (open circles) and $N = 39$ (closed circles) particles. From the first non-zero frequency of the system with $N = 38$ particles one can see that there is no second order structural phase transition since the first non-zero frequency does not go to zero. Actually, for a value of the screening parameter inside the interval $0 \leq \kappa \leq 1$ the GS and MS configurations of the clusters with $N = 38$ particles keep the shell arrangement $(6, 32)$. Differently, the energy difference $E_2 - E_1$ of the system with $N = 39$ particles has many peaks which indicates that the GS or the MS configurations pass through a first order structural phase transition. In fact, we found that for its GS configuration the shell arrangements are (6,33) and (7,32) respectively, for $\kappa = 0$ and $0 < \kappa \leq 1$ while that for the MS configuration the shell arrangements are (6,33), (7,32) and (8,31) respectively,

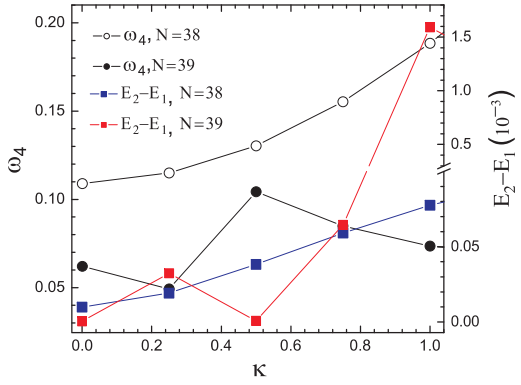

FIG. 6.15: For the systems with N=38 and 39 particles: first non-zero frequency ω_4 (left axis), and the energy difference $E_2 - E_1$ between the lowest energy MS and the GS configuration (right axis) as function the screening parameter κ.

for $\kappa = 0$, $0.25 \leq \kappa \leq 0.75$ and $1 \leq \kappa \leq 2$. Such structural phase transition might influence the melting behavior of the GS configuration. The latter will be discussed now for the systems with $N = 38$ and 39 particles with $\kappa = 1$.

Fig. 6.16 displays the intrashell (blue data) and radial (black data) displacements for the internal and external shells of the systems with $N = 38$ particles and screening parameter $\kappa = 1$. The shell's occupation for the system with N=38 particles and $\kappa = 1$ is (6,32). The critical temperatures for the intrashell melting are $T = 0.01378$ (Fig. 6.16, red arrow) and 0.0084 (Fig. 6.16, green arrow), respectively, for the internal and external shells. For the case of a pure Coulomb interparticle potential (Figs. 6.5(c) and (d)) the corresponding critical temperatures are $T = 0.0241$ and 0.0078. Those critical temperature are comparable in magnitude and it is clear that the screening of the interparticle interaction potential does not alter the main dynamical properties of the magic cluster with N=38 particles, i.e. a large intrashell melting temperature both in the internal and external shells.

Fig. 6.17 displays the intrashell (blue data) and radial (black data) displacements for the internal and external shells of the systems with $N = 39$ particles and screening parameter $\kappa = 1$. The shell's arrangement for the system with N=39 particles and $\kappa = 1$ is (7,32). The intrashell melting temperature for the internal shell (Fig. 6.17, closed circles) is $T = 0.0028$. This latter value is much lower than the one found for the case of a pure Coulomb interparticle potential, i.e. $T = 0.0197$ (Fig. 6.5(d)). For the case of $\kappa = 1$ the internal shell becomes less stable since seven particles do not make a magic arrangement. Oppositely, the stability of the external shell is enhanced and the intrashell melting temperature goes from $T = 0.0003$ ($\kappa = 0$) to 0.0069 ($\kappa = 1$). In fact, particles in the external shell of the system with $N = 39$ particles and $\kappa = 1$

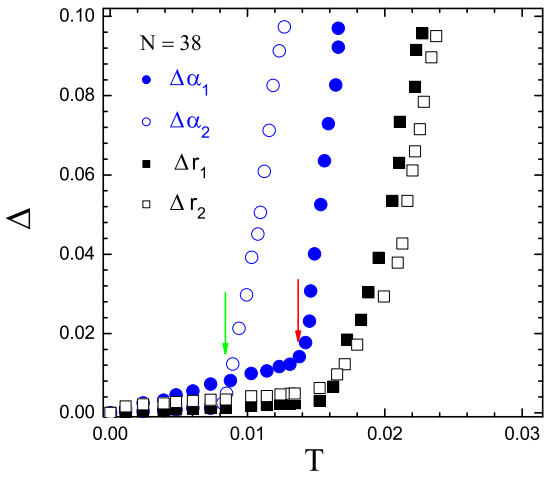

Fig. 6.16: Temperature dependence of the intrashell and radial displacements computed for the internal and external shells of the magic cluster with N=38 particles and screening parameter $\kappa = 1$.

arrange themselves in a magic configuration similar to the one shown in Fig. 6.7(a).

6.5 SUMMARY AND CONCLUSIONS

We investigated the melting process of small 3D isotropically confined Wigner crystals of charged particles interacting through Coulomb or screened Coulomb potentials. The stability of the clusters was investigated by MD simulations where the Lindemann's criterion was used. We found that the GS configuration of the systems with N=6, 12, 13 and 38 particles have large mechanical stability and are therefore identified as the true magic clusters. The common characteristic of magic clusters is that they are formed by one of the highly regular structures, i.e. an octahedron or icosahedron. For the system with N=38 particles each 5-fold coordinated particle sits in one of the corners of an icosahedron and are surrounded by 6-fold coordinated particles.

We found that, due to the existence of MS configurations, the solid-liquid transition is rather sharp even in small size systems, i.e. systems with N=12 and 13 particles. Oppositely, the radial melting transition in smaller clusters, as for example with N=5 till 8 particles, evolves continuously over a wide

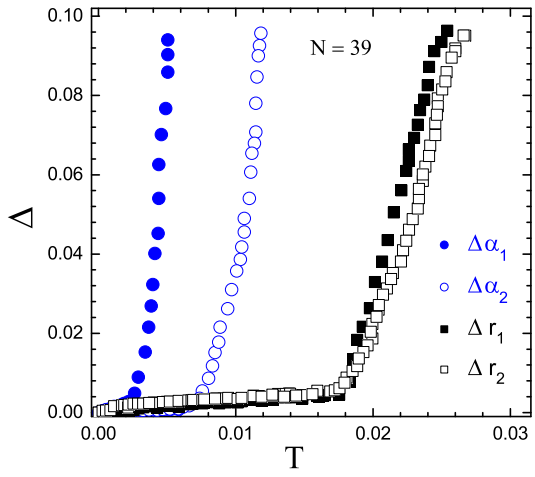

FIG. 6.17: The same as Fig. 6.16 but now for N=39 particles.

temperature interval. Systems with 6 and 12 particles have large intrashell melting temperature. Furthermore the resistance against intrashell diffusion in icosahedral and octahedral structures is found to remain large even when those structures form the inner shell of larger clusters.

We found that small size effects, i.e. the cluster's symmetry, plays an important role into the dynamics of small Wigner crystals. The melting transition can evolve through three different processes which strongly depend on the arrangement of particles on the shells of the GS configuration. The solid-liquid transition in non-magic clusters occurs through two steps: first at low temperature the non-magic cluster passes through an intrashell melting and then at higher temperature through a radial melting. Differently, pronounced resistance against intrashell diffusion is found in magic cluster with $N = 38$ particles which gives the system the possibility to undergo an intermediate melting process, the so called intershell melting. This melting process was never studied before in 3D clusters.

The dynamics of systems with two shells where the external shell is formed by a set of subshells with slightly different radius was investigated in the small temperature range. It was shown that the radial order of those subshells in such a shell is maintained until the angular order between the different shells is lost. At this temperature, a jump in the mean square radial displacement is observed. This corresponds to a local melting of the shell resulting in larger

radial fluctuations. This structural transition was not noticed before in $3D$ clusters. After this transition the symmetry of the cluster is increased and the particles in the broadened shell can interchange their positions. Such melting process is characteristic of the low temperature dynamics and does not affect the stability of magic clusters.

The effect of screening of the inter-particle interaction on the melting process was also investigated. The different critical melting temperatures for the systems with N=6, 12, 38 and 39 particles and $\kappa = 1$ were determined. This value of the screening parameter is typical for experiments in dusty plasmas. We show that the effect of screening does not modify significantly the main characteristics of the dynamics found in the magic clusters as long as the configuration of the cluster is not modified. Furthermore, by changing the screening of the interparticle interaction potential one can induce structural phase transitions, i.e. where the configuration of the shell structure is modified, that enhances or decreases the stability of the shells of non-magic clusters.

A normal mode analysis was performed and we found good agreement between the values of the eigenfrequencies and those of the critical temperatures obtained by MD simulation. From the normal mode analysis it turned out that: 1) the oscillation mode associated to the first non-zero frequency has a strong character of intershell rotation in case of a two shell configuration; 2) normal modes of the type intrashell motion has large eigenfrequencies if the system is a magic cluster, and 3) the 5^{th} mode of the system with $N = 39$ particles presented a vortex-like motion around a 7-fold particle on its external shell.

Publication The results in this chapter were published as:

S. W. S. Apolinario and F. M. Peeters, *Melting transitions in isotropically confined three-dimensional small Coulomb clusters*, Phys. Rev. E. **76** 031107 (2007).

7

Multiple rings in a 3D anisotropic Wigner crystal: structural and dynamical properties

Recent developments of experiments in spherically confined dust plasma have motivated two of our most recent works [112, 132]. Ref. [112] presented a detailed numerical simulation of the configuration of the ground state and the lowest energy metastable state, and of the spectrum of normal modes of classical 3D clusters with isotropic parabolic confinement. The confined particles were considered to interact through a repulsive potential such as Coulomb or screened Coulomb interparticle potential. We found that both small and larger systems satisfy Euler's theorem and the total topological charge defect is 12. The breathing and the center of mass mode frequencies were analytically determined. The breathing mode was found to have the highest frequency for the case of a Coulomb interparticle interaction potential. Furthermore we found a relation between the appearance of maximum and minimum in the lowest non-zero eigenfrequency and in the second derivative of the binding energy as function of N for small clusters ($N < 23$) from which we determine the most stable and least stable clusters. A thermodynamic investigation of such a system was given in Ref. [132]. It was found that the ground state (GS) configuration of systems with N=6, 12, 13 and 38 particles have large mechanical stability and were therefore identified as magic clusters. The common characteristic of magic clusters is that they are formed by one of the highly regular crystal structures, i.e. an octahedron or icosahedron.

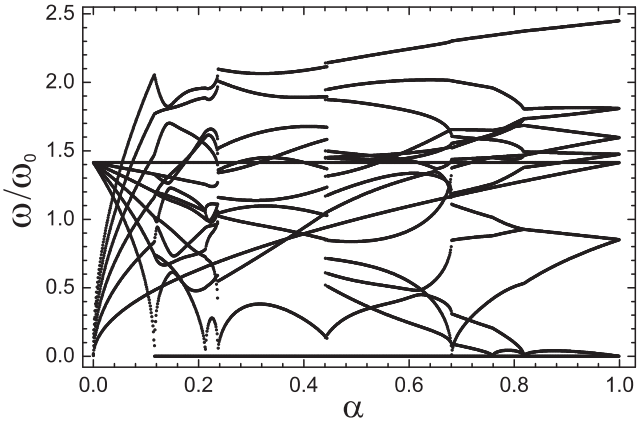

FIG. 7.1: Normal mode frequencies for the system with $N = 6$ particles as function of the anisotropy parameter.

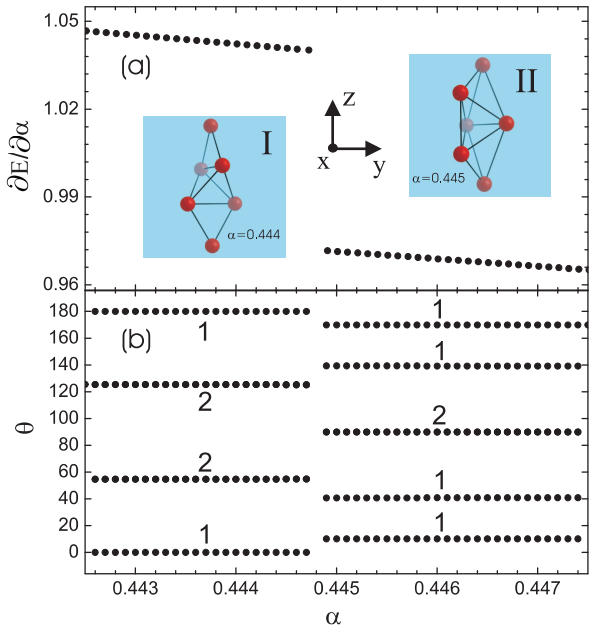

FIG. 7.2: (a) First derivative of the energy E with respect to the anisotropy parameter α; the insets I and II display respectively the GS configuration for $\alpha = 0.444$ and 0.445, i.e. the GS configuration just before and after the critical anisotropy parameter of $\alpha = 0.4445$. (b) The spherical coordinate θ of each particle as function of the anisotropy parameter α.

In any real experimental system the confinement potential will have an asymmetric component. Therefore, in this chapter we study the dynamical and statical properties of anisotropically confined Wigner crystals. Such an investigation is an extension of our previous work [112] and has relation to previous work on anisotropic confined $2D$ clusters [69, 133]. Additionally, our study complements previous investigations of structural phase transitions arising between a $2D$ to a $3D$ classical artificial atom [135]. The latter reference showed that the development from a ring structure into a shell configuration passes necessarily though a layered structure which is intermediated by structural transitions of first and second order. We shall demonstrate that anisotropic finite $3D$ Wigner crystals form in fact a hybrid element in the sense that they exhibit physical properties inherent of both 2D and 3D systems. Toward this objective we determine the lowest energy configurations and perform a normal mode analysis where we give special attention to delocalized modes, i.e. the normal mode oscillations with very low frequencies.

The present chapter is organized as follows. In Sect. II we present our theoretical model. In Sect. III we give our results for the statical properties of the ground state configurations, which is divided in four subsections: (A).: we investigate the structural phase transitions of first and second order which take place in a small system with N=6 particles when the anisotropy parameter is varied; (B).: a larger system with N=18 particles is investigated and we introduce the fraction of degenerate frequencies η as a quantity to characterize highly symmetric clusters. (C).: we generalize our results by presenting a phase diagram for systems with N=4 to 25 particles; and (D).: larger systems are investigated, i.e. systems with $N = 50, 60$ and 70 particles. A normal mode analysis of multiple ring structures is discussed in Sect. IV. Finally, in Sect. V we present our conclusions.

7.1 THEORETICAL MODEL

We study a $3D$ model system of N equally charged particles in an anisotropic confinement potential and interacting through a repulsive potential. The potential energy of the system is given by

$$E = \sum_{i=1}^{N} \frac{1}{2} m\omega_0^2 \left(x_i^2 + y_i^2 + \alpha z_i^2\right) + \sum_{i>j}^{N} \frac{q^2}{\epsilon_0 \left|\mathbf{r}_i - \mathbf{r}_j\right|}, \tag{7.1}$$

where ϵ_0 and q are respectively the electric constant and the particle charge, $\mathbf{r}_i = (x_i, y_i, z_i)$ is the coordinate of the i^{th} particle, N is the total number of particles, ω_0 is the confinement frequency of a single particle, and α is the anisotropy parameter of the confinement potential. We can write the potential energy (8.1) in dimensionless form

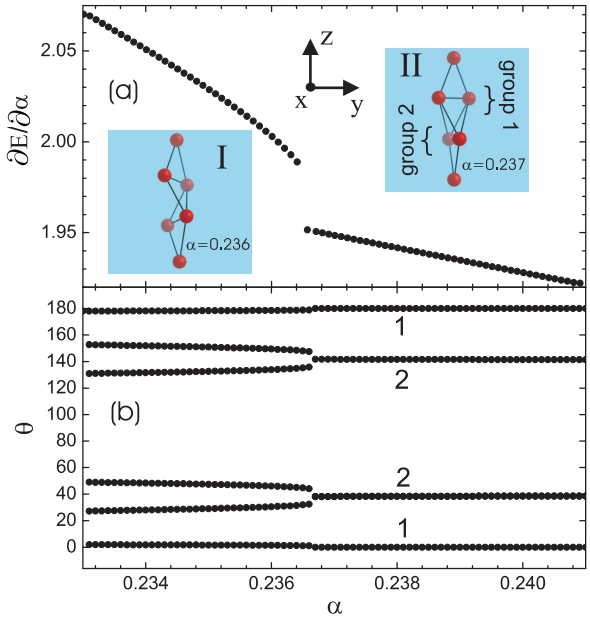

FIG. 7.3: The same as Fig. 7.2 but for smaller values of the anisotropy parameter, i.e. for $0.233 < \alpha < 0.241$.

$$E = \sum_{i=1}^{N} \left(x_i^2 + y_i^2 + \alpha z_i^2 \right) + \sum_{i>j}^{N} \frac{1}{|\mathbf{r}_i - \mathbf{r}_j|}, \tag{7.2}$$

if we express the coordinate and energy in the following units: $r_0 = (q^2/\gamma\epsilon_0)^{1/3}$, where $\gamma = m\omega_0/2$ and $E_0 = q^2/\epsilon_0 r_0$. All our numerical results will be given in dimensionless units.

Intuitively, we expect interesting behavior as a function of α which governs the anisotropy of the confinement potential. This can be seen as follows: for $\alpha = 0$ we have an unbounded system in one direction, i.e. a wire-like configuration as discussed in Ref. [134], while for $\alpha = 1$ the system consists of an isotropic 3D Wigner crystal. This implies that, as a function of α structural transitions (e.g., configurational changes) have to take place. We found that the ground state configuration shows a surprisingly complex behavior as a function of α.

To obtain the stable configurations we use the Monte Carlo simulation technique supplemented with the Newton method in order to speed up the computer program and to increase the accuracy of the found energy value (see Ref. [16] for details). By implementing a large number of different simulations starting from different random initial configurations we are confident that we found the ground state configuration as long as the number of particles N is not too

large, i.e. roughly $N < 60$. Depending on the total number of particles, between several hundred to several thousand random initial configurations were generated.

The eigenfrequencies are the square root of the eigenvalues of the dynamical matrix

$$H_{\alpha\beta,ij} = \frac{\partial^2 H}{\partial r_{\alpha,i} \partial r_{\beta},j}\Big|_{r_{\alpha,i}=r^n_{\alpha,i}} \tag{7.3}$$

where $\{r^n_{\alpha,i}; \alpha = x, y, z; i = 1, ..., N\}$ are the positions of the particles in a stable configuration.

7.2 RESULTS

7.2.1 N=6

The influence of the anisotropy parameter α of the confinement potential to the ground state (GS) configuration is investigated in this subsection for a small system. In order to avoid a complicate analysis but still acquire satisfactory knowledge of mechanical processes [116] induced by the anisotropy parameter we first investigate a relatively small system, i.e. the system with $N = 6$ particles. It is already known for some time [110] that for $\alpha = 1$, i.e. for an isotropic confinement potential, the GS configuration of the system with $N = 6$ particles form a magic cluster. Magic clusters present an enhanced mechanical stability which is reflected in a large value of the lowest non-zero eigenfrequency and a pronounced value of the addition energy, which is defined as $\Delta E = E(N + 1) + E(N - 1) - 2E(N)$ where $E(N)$ is the GS configuration of the system with N particles [16, 112, 118, 132].

Fig. 7.1 shows the eigenfrequency spectrum for the system with $N = 6$ particles as function of the anisotropy parameter. For $\alpha = 1$, i.e. for the isotropic case, we see that the normal modes are highly degenerate. Of the total of 18 normal modes present in the $3D$ system with $N = 6$ confined particles we found only seven different values for the eigenfrequencies. However, with decreasing value of the anisotropy parameter α the degeneracy is lifted (see Fig. 7.1). Notice that at $\alpha = 0.4445$ the eigenfrequencies undergo a discontinuity. Such discontinuity is found to be a consequence of a structural phase transition, i.e. a configurational change of the GS configuration, induced by the anisotropy parameter. We show the GS configurations for $\alpha = 0.444$ and 0.445, respectively in the insets I and II of Fig. 7.2(a). We notice that for $\alpha = 0.445$ the GS configuration still exhibits a shell structure while for $\alpha = 0.444$ this is no longer true. In order to know the nature of the structural transition we calculate the first derivative of the energy with respect to the anisotropy parameter (see Fig. 7.2(a)). The derivative of the energy is discontinuous at the critical point $\alpha = 0.4445$ which characterizes a structural phase transition

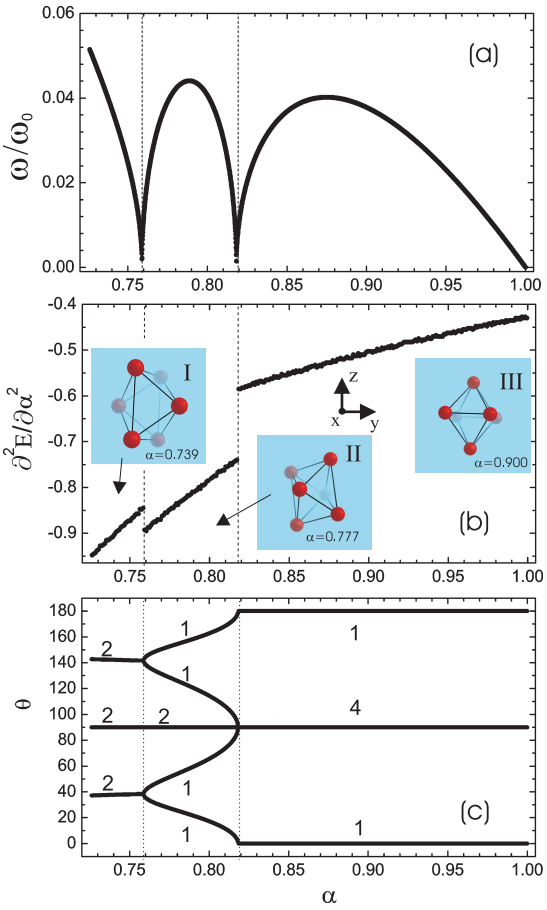

FIG. 7.4: (a) Lowest energy eigenfrequency for the system with $N = 6$ particles as function of the anisotropy parameter. (b) Second derivative of the energy with respect to the anisotropy parameter α; the insets I, II and III display, respectively the GS configurations for $\alpha = 0.739$, 0.777 and 0.900. (c) The spherical coordinate θ of each particle as function of the anisotropy parameter α.

of first order. The distribution of particles along the z-direction is found to be strongly dependent on the anisotropy parameter near this structural transition. Fig. 7.2(b) displays the usual spherical coordinate θ of each particles as function of the anisotropy parameter. The number written near each line indicate how many particles have the same value for the spherical coordinate. Clearly we see also a pronounced jump in the values of θ for all particles at the critical anisotropy parameter.

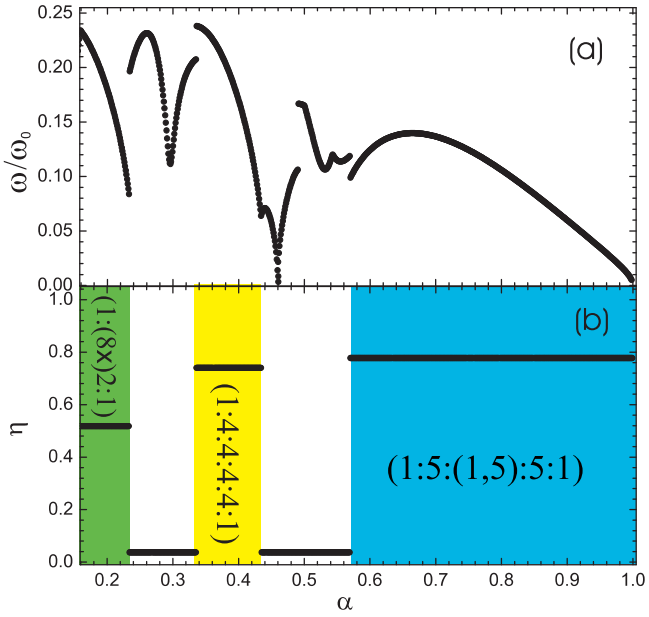

Fig. 7.5: (a) Lowest energy normal mode frequency for the system with N=18 particles as function of the anisotropy parameter α. (b) The fraction of degenerate frequencies η in the system as function of α. The regions of multiple ring structures are indicated by blue and yellow areas and correspond respectively to the configurations $(1:5:(1,5):5:1)$ and $(1:4:4:4:4:1)$. The region corresponding to a degenerate multiple ring structure of the type $(1:(8\times)2:1)$ is indicated by the green area.

Even for a highly asymmetric confinement potential the system is able to undergo a first order phase transition at $\alpha = 0.2365$. But in this case the GS configuration has almost a one dimensional structure and the change in the particle's position is much smaller. Fig. 7.3(a) displays the first derivative of the energy with respect to the anisotropy parameter. We can see that the first derivative of the energy is discontinuous at the critical anisotropy parameter of $\alpha = 0.2365$. The GS configuration just before the transition, i.e. for $\alpha = 0.237$ (see inset II of Fig. 7.3), is equivalent to the configuration found previously when $\alpha = 0.444$ (see inset I of Fig. 7.2). Particles in such a configuration arrange themselves in the following way: 1) the top and bottom particles are aligned along the z-axis, 2) the other four particles form two groups as indicated in the inset II of Fig. 7.3(a) where particles belonging to the same group have the same value of the z-coordinate, and 3) the difference in the usual azimuthal angle of any two particles belonging to distinct groups is always 90^o. This type of configuration also appears in larger clusters as we will see later and they have a specific eigenfrequency distribution. This configuration has the arrangement

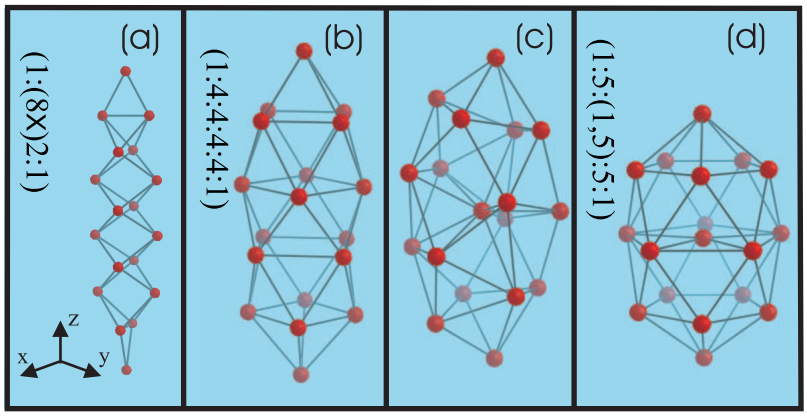

FIG. 7.6: (a), (b), (c) and (d) are the ground state configurations for the system with $N = 18$ particles and anisotropy parameter respectively equal to $\alpha = 0.2, 0.4, 0.5$ and 0.7.

(1:2:2:1) where we account for the particles' distribution along the z-direction. For decreasing values of α, i.e. for $\alpha < 0.237$ (see inset I of Fig. 7.3(a)), the cluster symmetry is broken and the four particles in the most inner region of the cluster obtain different values for their spherical coordinate θ. Such change in the distribution of particles along the z-direction is documented in Fig. 7.3(b), which displays the spherical coordinate θ of each particle as function of α. The number written near each line indicates the number of particles with the same value of the spherical coordinate θ for a given α. We can see in Fig. 7.3(b) that for $\alpha < 0.2365$ there are six distinct lines where each one is associated to one particle while for $\alpha > 0.2365$, i.e. after the transition point, the number of different lines is reduced and the two most inner curves become associated to two particles.

The anisotropy parameter also drives the system to undergo second order transitions. Such second order phase transitions happen when the critical anisotropy parameter reaches $\alpha = 0.818, 0.759, 0.682, 0.212$ and 0.116. Those second order transitions are found to involve a continuous change in the particle's position and in the eigenfrequencies of the system. Fig. 7.4(a) shows the lowest non-zero frequency as function of the anisotropy parameter in the slightly anisotropic regime, i.e for $\alpha > 0.7$. We can see that at the critical values of the anisotropy parameter of $\alpha = 0.818$ and 0.759 the eigenfrequency spectrum exhibits a softening of the lowest-energy mode. For such transition the first derivative of the energy with respect to the anisotropy parameter remains continuous while its second derivative exhibits a discontinuity at the two critical values $\alpha = 0.818$ and 0.759 as we see in Fig. 7.4(b). To help us

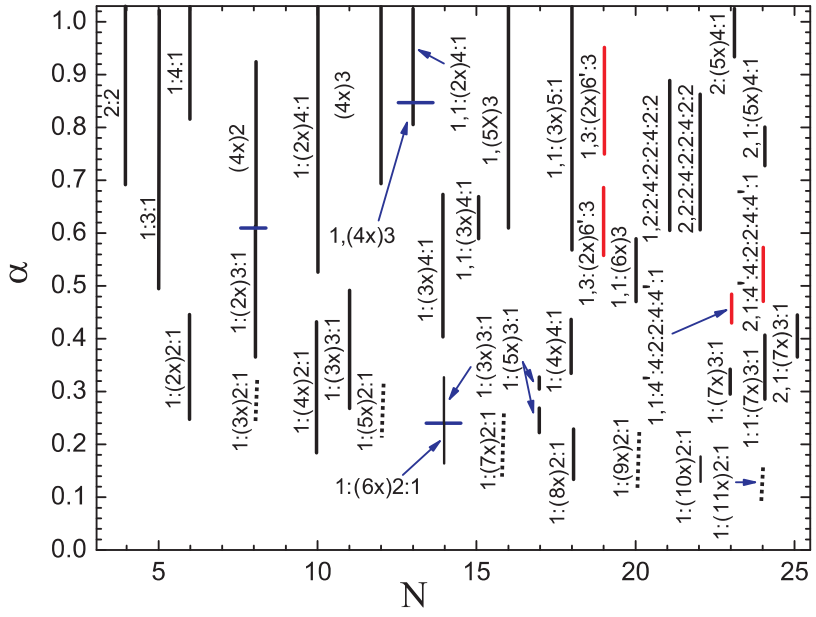

Fig. 7.7: Phase diagram: The vertical lines indicate the values of α where the GS configuration is a multiple ring structure along the z-direction. The numbers beside these lines give the particles' GS arrangement.

in understanding the effects of the second order phase transition on the structure of the cluster we display in the insets I, II and III of Fig. 7.4(b) the GS configurations found respectively for the cases of $\alpha = 0.739, 0.777$ and 0.9.

Before any phase transition takes place, i.e. for $\alpha > 0.818$, the ground state configuration of the system remains the same and corresponds to an octahedron structure, where its main axis points to the z-direction (see for example the inset III in Fig. 7.4(b)). Between the two critical values of the anisotropy parameter, i.e. for $0.759 < \alpha < 0.818$, we can see that the main axis of the icosahedron deviates from the z-direction (see inset II of Fig. 7.4(b)). Finally for $\alpha < 0.759$ the icosahedron reaches another orientation and its main axis lays on the xy plain. Such change in the orientation of the icosahedron can be better followed from the dependence of the spherical coordinate θ to the anisotropy parameter (see Fig. 7.4(c)).

7.2.2 N=18

The GS configuration for the system with six particles form a structure with only one shell. The eigenfrequency spectrum and the structural phase transitions of larger clusters are expected to present a more complex behavior. Now

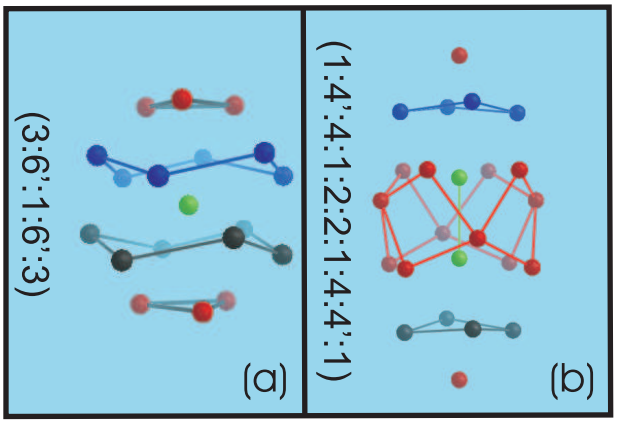

FIG. 7.8: Fine structure for systems with $N = 19$ and $\alpha = 0.9$ (a) and $N = 24$ and $\alpha = 0.5$ (b). Particles in blue and black colors form rings with non-zero width. The other particles in the external (inside the external) shell are in red (green) color.

we turn our attention to larger systems and we start our investigation by considering the system with $N = 18$ particles having the GS configuration (1,17) when $\alpha = 1$ which is different from the simple shell structure, i.e. it has one extra particle in the center. The first non-zero frequency gives us an indication of the structural phase transition undergone by the system as α is changed. Fig. 7.5(a) displays the first non-zero frequency for the system with $N = 18$ particles and anisotropy parameter varying from $\alpha = 0.15$ to 1. We notice that there are several discontinuities in the lowest non-zero frequency and they correspond to first order structural transitions, i.e. at $\alpha = 0.570, 0.491, 0.336$ and 0.234. A second order transition occurs at $\alpha = 0.459$, i.e. when a mode softening occurs. Such first and second order structural phase transitions can drive the system to configurations of higher symmetry. The eigenfrequency spectrum must be sensitive to the symmetry of the cluster. Most importantly, the number of degenerate frequencies increases for highly symmetric clusters. We defined for a given value of α and particle number N the fraction of degenerate frequencies η which is the ratio between the number of degenerate frequencies and the total number of frequencies, i.e. the $3N$ frequencies of any given system of N particles. Fig. 7.5(b) displays η as function of the anisotropy parameter α for the system with $N = 18$ particles. We notice in Fig. 7.5(b) three regions of α with relatively large $\eta-$value. Those regions are indicated by the blue, yellow and green areas and correspond respectively to the ranges $0.57 \leq \alpha \leq 1$, $0.336 \leq \alpha \leq 0.434$ and $0.159 \leq \alpha \leq 0.233$. The values of η at those regions are respectively equal to $\eta = 0.777$, 0.740 and 0.518. Oppositely, the blank areas correspond to the situation of highly non-symmetric clusters with very low values of η.

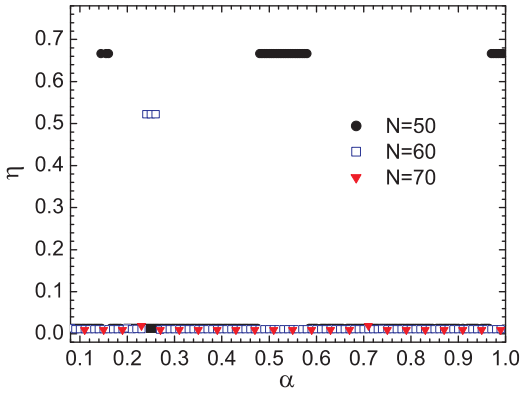

Fig. 7.9: Fraction of degenerate frequencies η for the GS configuration of the systems with $N = 50$, 60 and 70 particles as function of the anisotropy parameter.

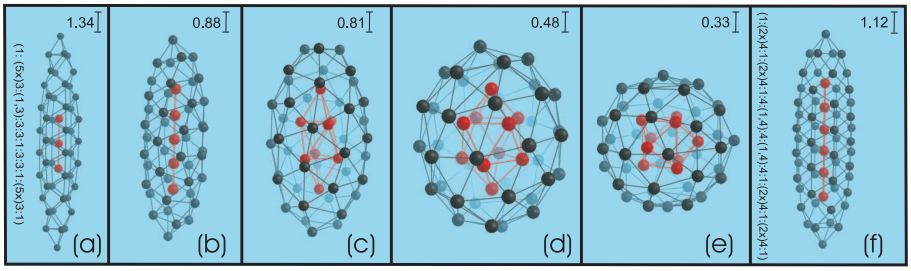

Fig. 7.10: From (a) to (e) the GS configurations for systems with $N = 50$ particles and anisotropy parameter $\alpha = 0.15, 0.3, 0.5, 0.8$ and 0.98, respectively. (f) GS configuration for the system with $N = 60$ particles and $\alpha = 0.25$. Black (red) balls correspond to particles in the external (inside the external) shell. The length unit is indicated on the top right of each figure.

Fig. 7.6(d) shows the GS configuration for the system with $N = 18$ particles and anisotropy parameter equal to $\alpha = 0.7$. Such configuration is representative for the region of α indicated by the blue area in Fig. 7.5(b). We can describe this configuration as follows (see Fig. 7.6(d)): at the extremes of the cluster there are two isolated particles located along the z-axis, one particle in the center and three rings formed by five particles in each ring. Furthermore those rings are parallel to each other and perpendicular to the z-axis. We use the following notation for such an arrangement (1:5:(1,5):5:1). The different ring-like layers are separated by " : " while the notation for the ring configurations are as previously used for $2D$ systems. Such multiple ring structure is also found for other ranges of the anisotropy parameter. For example, in the yellow region

of Fig. 7.5(b) the multiple ring structure has the arrangement (1:4:4:4:4:1). Differently from the first case, this configuration does not have a particle in the center and is formed by two particles sitting in the extrema of the cluster, and a sequence of four rings with four particles in each ring (see for example Fig. 7.6(b) for $\alpha = 0.4$). We observe that those rings have a square shape and are rotated with respect to each other by an angle of 45^o. Fig. 7.6(c) shows the GS configuration for $N = 18$ particles and $\alpha = 0.5$, i.e. a non-symmetric configuration which is representative for the second blank area in Fig. 7.5(b). Ultimately, the GS configuration goes to a degenerate multiple ring structure when $0.159 \leq \alpha \leq 0.233$ (green region). A typical configuration found in this region is shown in Fig. 7.6(a) for $\alpha = 0.2$. This arrangement is similar to the one shown in the inset I of Fig. 7.2(a) but now there is a sequence of 8 sets of 2 particles. Such arrangement can be referred by the term $(1:2:2:2:2:2:2:2:2:1)$ or shortly $(1:(8\times)2:1)$ where $(8\times)$ indicates that there are eight sets holding each two particles.

7.2.3 Phase diagram and fine structure

Such multiple and degenerate multiple rings can be thought as configurations that are intermediate between a two and three dimensional configuration. We can say that the multiple ring configuration is a three dimensional structure formed by smaller two dimensional parts. Such configuration is not unique to the system with $N = 18$ particles but it is also present in other systems. We computed the fraction of degenerate frequencies η for all systems ranging from $N = 5$ till 25 particles in order to identify the regions of the anisotropy parameter where the systems exhibits GS configuration with multiple and/or degenerate multiple ring structures. The result of this investigation is summarized in Fig. 7.7 in the form of a phase diagram. For each given number of particles N the vertical lines indicate the range of α where the system has highly symmetric configurations and beside each vertical line the related particle arrangement is written. The phase diagram shown in Fig. 7.7 can be divided in two areas, that is, the upper one (roughly $\alpha > 0.5$) where the multiple rings accommodate about 4, 5 and 6 particles; and the lower part (roughly $\alpha < 0.5$) where we find the degenerate multiple rings and multiple rings with 3 particles per ring. We noticed that the degenerate multiple ring structures for the systems with an *odd* number of sets with two particles, i.e. systems with $N = 8, 12, 16, 20$ and 24 particles, were not revealed via the computation of η, although it appeared for systems with an *even* number of sets of two particles, i.e., systems with $N = 6, 10, 14, 18$ and 22 particles. Alternatively, those configurations were obtained by computing the distribution of particles along the z-direction and the first non-zero frequency which determined the critical values of α where the system passes through phase transitions. The values of the anisotropy parameter where the degenerate multiple rings occur for the

system with $N = 8, 12, 16, 20$ and 24 are indicated in Fig. 7.7 by vertical dotted lines. We notice that only for $N = 7$ and 9 particles there are no regions of the anisotropy parameter where high symmetric configurations can be found. The increase of the number of particles leads to the formation of multiple rings configurations where the width of the rings along the z-direction is relatively large. Analogous fine structures in $2D$ systems were reported in Ref. [137]. In $3D$ systems we find that fine structure occurs for systems with $N = 19, 23$ and 24 particles and anisotropy parameter indicated by vertical red lines in Fig. 7.7. Examples of such a *fine structure* is shown in Fig. 7.8(a) for N=19 and $\alpha = 0.9$ and Fig. 7.8(b) for N=24 and $\alpha = 0.5$. In both cases particles in blue and black colors form rings with non-zero width along the z-direction. Other particles, i.e. in the external (inside the external) shell, are represented by red (green) balls. We name the arrangement of Fig. 7.8(a) and (b) respectively by (3:6':1:6':3) and (1:4':4:1:2:2:1:4:4':1) where the accents refers to rings with non-zero width. The formation of fine structure reduces the inter-particle interaction energy of the system. This phenomenon is similar to the zig-zag transition induced by the increasing of the particle number [69].

7.2.4 N=50, 60 and 70

In order to obtain insight about the particle distribution along the z-direction in large clusters we investigated systems with $N = 50, 60$ and 70 particles. In particular we wish to answer if the GS configuration of large clusters form symmetric clusters, i.e. multiple or degenerate multiple ring structures. The fraction of degenerate frequencies η as function of α is shown in Fig. 7.9 for the systems with $N = 50$ (circle), 60 (square) and 70 (triangle) particles. For the system with $N = 50$ particles we can find three distinct regions of the anisotropy parameter, i.e. $0.15 \leq \alpha \leq 0.16$, $0.48 \leq \alpha \leq 0.58$ and $0.98 \leq \alpha \leq 1.0$, where the value of the fraction of degenerate frequencies is relatively large, i.e. $\eta = 0.66$. For other values of the anisotropy parameter the fraction of degenerate frequencies becomes very small, i.e. $\eta = 0.02$. The GS configurations for the system with $N = 50$ particles and anisotropy parameters $\alpha = 0.15, 0.3, 0.5, 0.8$ and 0.98 are shown in Figs. 7.10(a), (b), (c), (d) and (e), respectively. Black (red) balls represent particles in the external (inside the external) shell. Fig. 7.10(a) displays a multiple ring structure with particle arrangement $(1 : (5\times)3 : (1, 3) : 3 : 3 : 1 : 3 : 3 : 1 : (5\times)3 : 1)$ while Fig. 7.10(b) does not present any symmetry pattern with respect to rotation around the z-direction. The other three GS configurations shown in Figs. 7.10(c), (d) and (e) exhibit a multiple ring structure for the internal shell (see red balls) with particle arrangement (1:3:3:1), (1:4:4:1) and (3:3:3), respectively. However, we can notice that the external shell for those GS configurations are not multiple rings.

The fraction of degenerate frequencies for the system with $N = 60$ particles and $\alpha = 0.25$ is relatively large, that is, $\eta = 0.52$ (Fig. 7.9) and its GS configuration corresponds to a multiple ring structure of arrangement $(1 : (2\times)4 : 1 : (2\times)4 : 1 : 4 : (1,4) : 4 : (1,4) : 4 : 1 : (2\times)4 : 1 : (2\times)4 : 1)$ which is shown in Fig. 7.10(f). In contrary, the value of the frequencies for the system with $N = 70$ particles is small ($\eta = 0.02$) throughout all the range of the anisotropy parameter and this system does not present multiple ring structure.

By decreasing the anisotropy parameter α one extends the cluster along the z-direction. In fact we can see for the system with $N = 50$ particles that the length scale shown in the top right of each GS configuration in Fig. 7.10 decreases from Figs. 7.10(a) to (e). The increase of the particle density forces the formation of a triangular arrangement of particles on the external shell in order to reduce the inter-particle interaction energy. Such a triangular arrangement of particles constitutes the preferable configuration, i.e. the configuration of lowest energy, in a $2D$ infinity system of repulsively interacting particles.

As a result, multiple ring structure of the whole cluster is not formed in large systems under slight anisotropic confinement. Nevertheless, particles in the internal shell are still able to self organize in multiple rings for the system with $N = 50$ particles. In contrast, this is not seen for systems with $N = 60$ and 70 particles. This indicates that the formation of multiple ring structure of the internal shell is gradually lost as the number of particles increases. In other words, for large systems in the presence of a confinement potential, the GS becomes a non-symmetric configuration. This is also supported by the fact that the increase of the number particles leads to the formation of a bcc arrangement which is the preferable particle arrangement for a $3D$ infinite system. In the limit of a large number of particles the shell structure becomes only well defined at the border of the cluster. However, for partial multiple ring configurations, that is, multiple ring uniquely present in the internal shell, the fraction of degenerate frequencies is no longer a good symmetry indicator. In other words, it does not always differentiate clusters with multiple rings in the internal shell from ordinary non-symmetric configurations, although such an indicator works properly for multiple ring structures as we saw for the clusters with N=50 and 60 particles, and anisotropy parameter $\alpha = 0.15$ and 0.25, respectively.

7.3 NORMAL MODES

The two dimensional character of the *dynamics* in a multiple ring structure, that is, oscillations in the plane of the rings, becomes visible via a normal mode analysis. Moreover, the low energy modes can suggest melting behavior [132, 133]. We display in Fig. 7.11 the eigenvectors associated to the first nine lowest

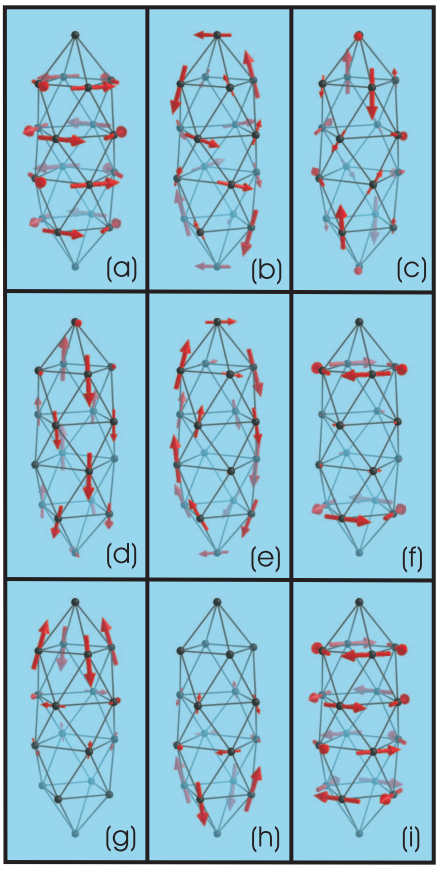

Fig. 7.11: From (a) to (i) we display the first nine lowest energy eigenvectors oscillation modes for the system with $N = 18$ particles and $\alpha = 0.4$. The direction and length of the vectors indicate respectively the direction and amplitude of oscillation of each particle in the cluster.

eigenfrequencies of the system with N=18 particles and anisotropy parameter $\alpha = 0.4$. The rotation mode around the z-axis which has frequency equal to zero is shown in Fig. 7.11(a). The eigenvectors shown in Figs. 7.11(b) and (c) are degenerate and have a frequency equal to $\omega = 0.16985$. We notice that for this mode particles' oscillations correspond to two dimensional dynamics. It is well known that the rotation mode in an isotropically confined system is three fold degenerate and has frequency equal to zero. If the confinement potential is anisotropic some of those degenerate modes obtain a frequency different from zero. Such a mode is seen in Figs. 7.11(d) and (e), which display two fold

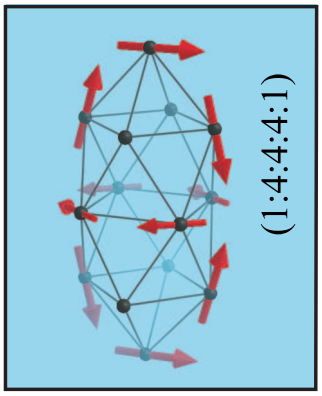

FIG. 7.12: Eigenvector associated to the 4^{th} frequency $\omega = 0.3786$ for the system with $N = 14$ particles and anisotropy parameter $\alpha = 0.5$. This mode corresponds to a vortex/ant-vortex motion.

degenerate rotation modes of non-zero frequency $\omega = 0.32651$. Such oscillation corresponds to a rotation mode around a given axis in the xy plain.

The oscillation mode shown in Fig. 7.11(f) is an inter-ring rotation mode and has frequency $\omega = 0.38892$. Notice that the amplitude of oscillation in the two external rings is much larger than the one in the two most internal rings. In what concerns the direction of oscillation we can see that the two upper rings oscillate out of phase with respect to the two lower rings. The 7^{th} and 8^{th} modes (see Figs. 7.11(g) and (h)) are degenerate and have frequency equal to $\omega = 0.39401$. We can see that the amplitude of oscillations is much larger for those particles close to the extreme of the cluster. The latter fact is indicative for the appearance of inhomogeneous melting.[133] Finally, Fig. 7.11(f) displays the eigenvector associated to the frequency $\omega = 0.61093$. This oscillation mode corresponds to an inter-ring motion around the z-axis. We notice that the two most external (internal) rings oscillate clock-wise (anti-clock wise). The inter-ring rotation modes shown in Figs. 7.11(f) and (i) indicates that the low temperature dynamics in multiple ring structure must have a strong two dimensional behavior.

Such inter-ring oscillation modes are not only found for $N = 18$ and $\alpha = 0.4$, but we also found it for all multiple ring configurations that we presented in Fig. 7.7. Nevertheless some of the configurations exhibit normal modes that correspond to a vortex/anti-vortex excitation around axes perpendicular to the z-direction, see for example Fig. 7.12 for $N = 14$ particles and anisotropy parameter $\alpha = 0.28$. In such situations, full $3D$ melting is expected. Interestingly, vortex/ant-vortex motion appears for multiple ring structure of systems with a relatively small number of particles, i.e. $N = 14$ particles, while that in

$2D$ clusters vortex/ant-vortex motion typically appears for large systems, i.e. roughly $N > 40$ particles [16, 136].

7.4 CONCLUSION

In summary we have investigated a $3D$ system of equally charged particles confined anisotropically by an external confinement potential. We assumed that the particles interact via a Coulombic interparticle interaction potential. Our theoretical model is applicable for systems such as dusty plasma and colloids. It is expected that the found behavior is qualitatively the same for other isotropic interaction potentials as e.g. a screened Coulomb potential. We found that the anisotropy parameter α can drive the system to undergo first and second order structural phase transitions. Those transitions are found to affect the distribution of particles along the z-direction and the eigenfrequency spectrum.

The system was found to self organize in three different general structures, i.e. multiple rings, degenerate multiple rings and non-symmetric structures, if the number of particles is small, typically $N \leq 25$ particles. For larger systems, i.e. $N \geq 50$, multiple ring structures were found in the external shell only if the anisotropy parameter was smaller than $\alpha \leq 0.2$, or in the internal shell for more isotropic confinements, roughly $\alpha \geq 0.4$. A fine structure was formed in small clusters upon increasing the particle number. Our results on the structure of the GS configurations as function of the anisotropy parameter were summarized in a phase diagram.

For a multiple ring structure the GS configuration is found to exhibit inter-ring and vortex/anti-vortex modes of oscillation. The latter modes are delocalized and therefore must be of relevance for the melting process. Furthermore, those modes indicate that low temperature dynamics in multiple ring structures must have a strong $2D$ behavior. Next to it we found that for the multiple ring configurations the eigenfrequency spectrum becomes highly degenerate. Oppositely, non-symmetric systems are found to have a low degenerate eigenfrequency spectrum. For the latter case the pattern of oscillation of the eigenvectors become much more complex and therefore it is impossible to give general trends as function of the anisotropy parameter.

Finally, we notice that the identified multiple ring structure is relevant for the physics of small Coulomb crystals due to the fact that they constitute a hybrid system built up by blocks of $2D$ structures forming piled rings along the z-direction. We expect that the melting process of such a system will follow from the interplay between the dynamics of both a $2D$ and $3D$ isotropically confined Coulomb clusters.

Publication The results in this chapter were published as:

S. W. S. Apolinario, B. Partoens, and F. M. Peeters, *Multiple rings in a 3D anisotropic Wigner crystal: structural and dynamical properties*, Phys. Rev. B **77**, 035321 (2008).

8

Melting of anisotropically confined Coulomb balls

8.1 INTRODUCTION

The effect of the anisotropy of the confinement on the structural properties of $3D$ systems of equally charged particles was investigated in Ref. [138]. The system was found to self organize in three different general structures, i.e. multiple rings, degenerate multiple rings and non-symmetric structures, if the number of particles is small, typically $N \leq 25$ particles. For larger systems, i.e. $N \geq 50$, multiple ring structures were found in the external shell only if the anisotropy parameter was smaller than $\alpha \leq 0.2$, or in the internal shell for more isotropic confinements, roughly $\alpha \geq 0.4$. Our results on the structure of the GS configurations as function of the anisotropy parameter were summarized in a phase diagram.

In this chapter we investigate the dynamical properties of *anisotropically* confined Wigner crystals which is an extension of our previous works [112, 132, 138] on isotropic Wigner balls. We investigate the homogeneity of the melting process and the effect of the different ordered states, i.e. degenerate multiple rings, multiples rings and non-symmetric structures, on the melting process of the system.

The chapter is organized as follows. In the next section our model system is introduced, the methodology used to find stable configurations and the molecular dynamics (MD) simulation approach. In section III we investigate the

melting process of small clusters, i.e. systems ranging from $N = 10$ to 18 particles. In section IV we investigate the melting process of larger clusters, i.e. systems with $N = 30$ and 40 particles. Finally, in section V we present our conclusions.

8.2 THEORETICAL MODEL

We study a $3D$ model system of N equally charged particles in an anisotropic confinement potential and interacting through a repulsive potential. The potential energy of the system is given by

$$E = \sum_{i=1}^{N} \frac{1}{2} m\omega_0^2 \left(x_i^2 + y_i^2 + \alpha z_i^2\right) + \sum_{i>j}^{N} \frac{q^2}{\epsilon_0 \left|\mathbf{r}_i - \mathbf{r}_j\right|}, \tag{8.1}$$

where ϵ_0 and q are respectively the dielectric constant and the particle charge, $\mathbf{r}_i = (x_i, y_i, z_i)$ is the coordinate of the i^{th} particle, N is the total number of particles, ω_0 is the confinement frequency, and α is the anisotropy parameter of the confinement potential. We can write the potential energy (8.1) in dimensionless form

$$E = \sum_{i=1}^{N} \left(x_i^2 + y_i^2 + \alpha z_i^2\right) + \sum_{i>j}^{N} \frac{1}{\left|\mathbf{r}_i - \mathbf{r}_j\right|}, \tag{8.2}$$

if we express the coordinate and energy in the following units: $r_0 = (q^2/\gamma\epsilon_0)^{1/3}$ and $E_0 = q^2/\epsilon_0 r_0$, where $\gamma = m\omega_0/2$, and the temperature unit is given by $T_0 = E_0\kappa_B^{-1}$, where κ_B is the Boltzmann constant and $t_0 = \sqrt{2}/\omega_0$. All our numerical results will be given in dimensionless units.

The stable configuration is a local or global minimum of the potential energy which is only a function of the number of charged particles N and the eccentricity α of the confinement potential. Our numerical method to obtain the stable state configuration is based on the Monte Carlo simulation technique supplemented with the Newton method in order to increase the accuracy of the found energy value [16]. By starting from a large number of different random initial configurations we believe that we were able to find all the possible stable (i.e. ground state and metastable) configurations. The configurational properties of anisotropically confined systems were discussed in details in our previous paper [138].

To study the dynamical properties of a small cluster at a specific temperature we use, first: a variant of the velocity Verlet Algorithm [55] which rescales the velocity of the particles to bring the sample to a desired temperature, and second: we implement the molecular dynamics (MD) simulation using the velocity Verlet algorithm [55]. A typical measurement done during this latter

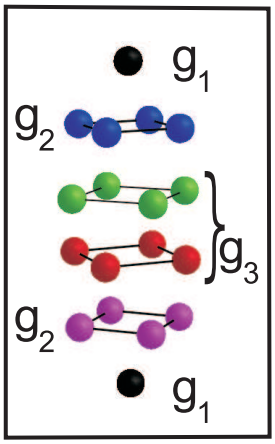

Fig. 8.1: Ground state configuration for the system with $N = 18$ particles and anisotropy parameter $\alpha = 0.4$. This configuration corresponds to a multiple ring structure with arrangement $(1 : (4\times)4 : 1)$, i.e. four parallel rings having each four particles plus two isolated particles (black balls) situated in the extremities of the cluster along the z direction. The cluster is divided in three groups, i.e. groups 1 (g_1), 2 (g_2) and 3 (g_3).

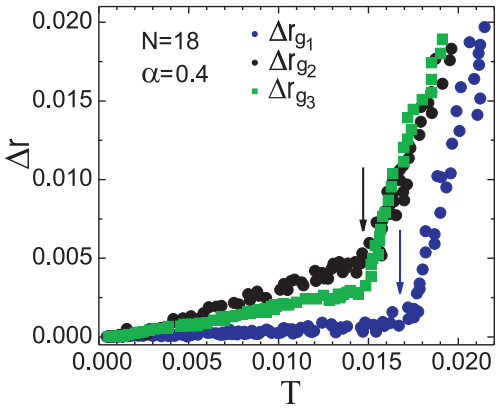

Fig. 8.2: Radial averaged displacement computed for the group 1 (Δr_{g_1}), group 2 (Δr_{g_2}), and group 3 (Δr_{g_3}) of the system with $N = 18$ particles and anisotropy parameter $\alpha = 0.4$.

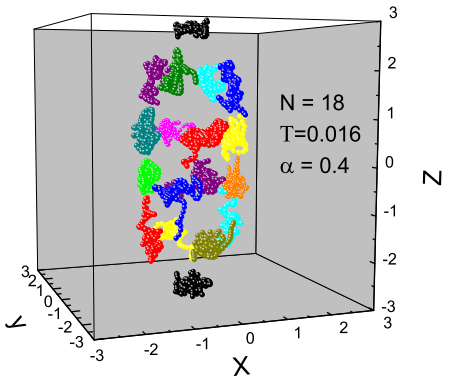

FIG. 8.3: Particles trajectories obtained during a time interval of 400 time steps for a system with $N = 18$ particles, anisotropy parameter $\alpha = 0.4$ and at a temperature of $T = 0.016$. Different colors were used to distinguish between trajectories of neighboring particles.

stage is the calculation of the averaged displacement of the particles from its equilibrium position [2, 69].

8.3 SMALL SYSTEMS

The GS configuration of a three dimensional anisotropic Wigner crystal has three different ordered states [138], i.e. multiple rings, degenerate multiple rings and non-symmetric configurations. The system with $N = 18$ particles is one of the most representatives among the systems from $N = 4$ up to 25 particles, since it has the three different structural phases as function of α.

The GS configuration of the cluster with $N = 18$ particles and anisotropy parameter $\alpha = 0.4$ is shown in Fig. 8.1. Such a GS configuration forms a multiple ring structure of arrangement $(1 : (4\times)4 : 1)$, i.e. it has two particles situated in the extremities of the cluster along the z direction and a sequence of four rings each having four particles. Particles belonging to the same ring are represented by balls of the same color. Bounds between balls are drawn only for enhancing the visualization of the cluster.

The multiple ring structure can be thought as a three dimensional system formed by blocks of two dimensional structures, i.e. the rings, plus two isolated particles. In order to determine the melting temperature of the different block

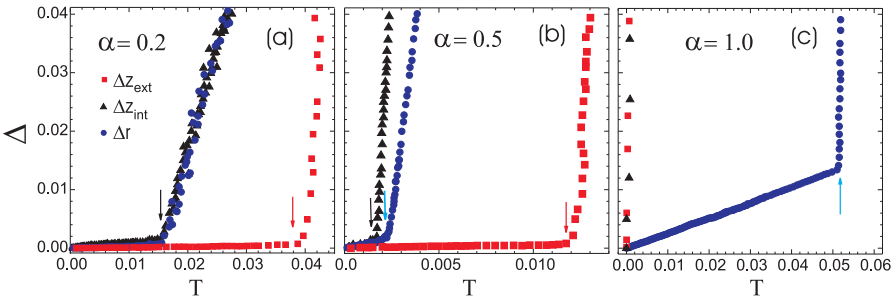

Fig. 8.4: Temperature dependence of the z averaged displacements computed for the external and internal groups, i.e. Δz_{ext} (red squares) and Δz_{in} (black triangles), respectively, and the radial averaged displacement Δr (blue circles). (a), (b) and (c) correspond to the system with $N = 18$ particles and anisotropy parameter equal to $\alpha = 0.2$, 0.5 and 1.0, respectively.

structures we computed the radial averaged displacement (defined in Eq. (8.3)). Such a quantity was computed for three different groups of particles, i.e. the groups 1, 2 and 3 which are respectively represented by the symbols g_1, g_2 and g_3 in Fig. 8.1. Group g_1 comprises the two particles (represented by black balls) situated in the extremities of the cluster along the z direction. The third group g_3 consists of the two most internal rings, i.e. the rings formed by the green and red balls (see Fig. 8.1). The second group g_2 is formed by the two other rings, i.e. the rings formed by the violet and blue balls. It is clear from Fig. 8.1 that the cluster is symmetric with respect to the $z = 0$ plane. All particles belonging to the same group have the same distance from the $z = 0$ plane. As a result, the two different structures belonging to the same group have the same dynamical properties.

The radial averaged displacement Δr is defined as follows:

$$\Delta r_\gamma^2 = \frac{1}{N_\gamma} \sum_{i=1}^{N_\gamma} (< r_{\gamma i}^2 > - < r_{\gamma i} >^2)/a^2 \tag{8.3}$$

where γ can assume the values $\gamma = 1, 2$ and 3, which indicates respectively the groups 1, 2 and 3, N_γ is the number of particles in group γ, $r_{\gamma i}$ is the modulus of the vector position of the i^{th} particle of group γ and a is the average distance between particles. The calculation of the radial averaged displacement as function of temperature allowed us to determine the different melting processes quantitatively. In order to characterize the melting temperature, we made use of a Lindemann-like criterion, which states that, close to the melting process, the respective averaged displacement starts to deviate rapidly from its low temperature linear dependence. We define the melting temperature as the temperature at which the radial averaged displacement changes its linear

temperature dependence into a more rapid increase. Such a fact is also related to previous investigation in $2D$ anisotropic Wigner crystals [69, 133].

Fig. 8.2 shows the temperature dependence of the radial averaged displacement calculated for the different groups of particles belonging to the system with $N = 18$ particles and anisotropy parameter $\alpha = 0.4$. The radial averaged displacements Δr_{g_2} (black circle) and Δr_{g_3} (green square) computed respectively for the groups g_2 and g_3 increase rapidly at the same melting temperature, i.e. $T = 0.015$ (Fig. 8.2, black arrow). The melting temperature for the group g_1 is slightly larger, i.e. $T = 0.017$ (Fig. 8.2, blue arrow).

The particle trajectory obtained during a time interval of 400 time steps in a MD simulation at a temperature of $T = 0.016$ for the system with $N = 18$ particles and anisotropy parameter $\alpha = 0.4$ is shown in Fig. 8.3. It is apparent from Fig. 8.3 that the dynamical property of the group g_1 is different from that of the groups g_2 and g_3. While the two particles belonging to the group g_1 (Fig. 8.3, black balls) remain oscillating around their equilibrium position, particles of the groups g_2 and g_3 do not have a localized trajectory around their equilibrium positions, rather, we can see that at the temperature of $T = 0.016$ particles belonging to one ring are already able to jump to a position in the neighboring ring.

The latter results, i.e. Figs. 8.2 and 8.3, showed that the melting process for the system with $N = 18$ particles and anisotropy confinement $\alpha = 0.4$ is inhomogeneous. In other words, the melting process does not involve all particles, i.e. the center of the cluster (regions g_2 and g_3) melts first than the extremities of the cluster, i.e. group g_1, for increasing temperature. Such a picture is different from the one we found for small isotropic systems [132]. In the latter, the first melting process is an intrashell melting, i.e. a low temperature melting process involving all particles of the cluster.

In this chapter we want to characterize the melting process of anisotropic systems. Towards this objective we will calculate the z averaged displacement. Such a quantity is defined analogously to the definition given for the radial averaged displacement (Eq. 8.3) but replacing r by z.

Moreover, for any given system we will define two groups of particles: the external group g_{ext}, i.e. the group formed by the set of two particles most distant from the center of the cluster, i.e. with the largest modulus of the z coordinate of the position vector; and the internal group g_{in}. For the case of the GS configuration shown in Fig. 8.2, the external group g_{ext} would correspond to the group g_1, while the internal group g_{in} would correspond to the sum of the groups g_2 and g_3. The corresponding melting temperatures for the z averaged displacement in the internal and external groups, will be indicated by T_{ext} and T_{in}, respectively.

The z averaged displacement will be computed for the internal and external groups. The melting process is considered inhomogeneous if the following condition is satisfied: the value of the critical temperature of the external group

$T_{\rm ext}$ is larger than $T_{\rm in}$, and $T_{\rm ext}$ is larger than $T_{\rm m}$, where $T_{\rm m}$ is the melting temperature of the system which is given by the calculation of the radial averaged displacement.

Figs. 8.4(a), (b) and (c) show the temperature dependence of the z averaged displacement for the internal Δz_{in} (red squares) and external Δz_{ext} (black triangles) groups and the radial averaged displacement Δr (blue circles) for the whole system with $N = 18$ particles and anisotropy parameters respectively equal to $\alpha = 0.2$, 0.5 and 1.0. The melting temperature for the isotropic system ($\alpha = 1$) is equal to $T_{\rm m} = 0.051$ (Fig. 8.4(c), blue arrow). We can see that the z averaged displacements calculated in the internal and external groups increase very rapidly immediately when $T \neq 0$ (see blue squares and black triangles in Fig. 8.4(c)). The latter result shows that the melting process is homogeneous. The very rapid increase of the z averaged displacement near $T \approx 0$ is due to the intrashell melting process which occurs at very low temperatures [132].

From Fig. 8.4(a) we can see that the radial averaged displacement Δr and the z averaged displacement calculated for the internal group $\Delta z_{\rm in}$ increase rapidly at the same temperature $T = 0.016$ (see Fig. 8.4(a), black arrow). The critical temperature for the external group has a larger value, i.e. $T = 0.038$ (see Fig. 8.4(a), red arrow). Such a situation indicates that for an anisotropy parameter of $\alpha = 0.2$ the melting process of the system with $N = 18$ particles is inhomogeneous. Analogously, from Fig. 8.4(b) we can see that the melting process for an anisotropy parameter of $\alpha = 0.5$ is also inhomogeneous. For this latter case, the melting temperatures of the system $T_{\rm m} = 0.0023$ (Fig. 8.4(b), blue arrow), and of the internal group $T_{\rm in} = 0.0018$ (Fig. 8.4(b), black arrow) are both smaller than the critical temperature of the external group $T_{\rm ext} = 0.012$ (Fig. 8.4(b), red arrow), i.e. the melting process does not involve all particles.

Fig. 8.5 shows the melting temperature $T_{\rm m}$ (blue circles) and the critical temperatures for the internal $T_{\rm in}$ (black triangles) and external $T_{\rm ext}$ (red square) groups for different size systems and as function of the anisotropy parameter. In each figure the region of α corresponding to non-symmetric configurations are left in blank while the regions of α corresponding to degenerate multiple rings or multiple ring structures are colored. Moreover, the symmetric arrangement of particles, i.e. multiple rings and degenerate multiple rings, are indicated for each system.

The critical temperatures for the system with $N = 18$ particles and different values of the anisotropy parameter are shown in Fig. 8.5(f). We can see from Fig. 8.5(f) that for $\alpha > 0.7$ the melting process becomes homogeneous, i.e. $T_{\rm m} > T_{\rm ext}$, while that for $\alpha < 0.7$ the melting process becomes inhomogeneous, i.e. $T_{\rm m} < T_{\rm ext}$. Moreover, Fig. 8.5(f) also reveals that the decrease of the melting temperature is not monotonic with decrease of the value of α. In fact, we notice (see red arrows in Fig. 8.5(f)) that for values of the anisotropy parameter where the GS configuration corresponds to a symmetric arrangement, i.e. multiple rings or degenerate multiple rings, the melting temperature $T_{\rm m}$

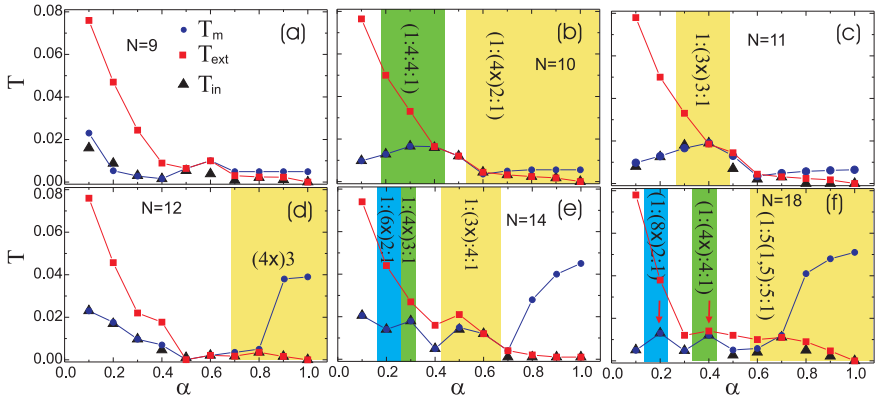

FIG. 8.5: The critical temperature of the system $T_{\rm m}$ (blue circles), the critical temperature of the external $T_{\rm ext}$ and internal $T_{\rm in}$ group of particles are shown for systems with different number of particles N as a function of the anisotropy parameter α. In each figure the region of α corresponding to non-symmetric configurations are left in blank. The regions of α corresponding to degenerate multiple rings or multiple ring structures are colored as blue, green and yellow and the symmetric arrangements are indicated.

of the system is enhanced. For example, for the anisotropy parameter $\alpha = 0.4$ whose GS configuration corresponds to a multiple ring structure of arrangement $(1 : (4\times)4 : 1)$ the melting temperature is $T_{\rm m} = 0.016$, while that for a non symmetric structure at the anisotropy parameters of $\alpha = 0.3$ and 0.5 the melting temperature are respectively $T_{\rm m} = 0.003$ and 0.0035. Nevertheless, we can see that the melting temperature of the system initially decreases with decreasing anisotropy parameter. For instance, for $\alpha = 1.0$ the melting temperature is $T_{\rm m} = 0.051$ and its value decreases to $T_{\rm m} = 0.048$, 0.040, 0.011 and 0.006 for $\alpha = 0.9$, 0.8, 0.7 and 0.6, respectively. Isotropic systems have large melting temperature due to the large value of the potential barrier between shells. If the temperature of the system is small, particles will remain trapped to one of the shells and will not have enough kinetic energy to overcome the potential barrier between shells. However, as the anisotropy parameter decreases the cluster gradually obtain a more prolate shape. In a prolate cluster the distance between particles belonging to the different elliptic shells are smaller than the ones in a spherical cluster. As a result, prolate clusters have lower barrier potentials between shells than spherical clusters. This is the reason that the melting temperature of slightly anisotropic systems is reduced when decreasing the value of the anisotropy parameter.

The GS configuration for the system with $N = 9$ particles does not have high symmetric arrangements. We calculated the critical temperature of this

system for different values of the anisotropy parameter (see Fig. 8.5(a)). One notices that initially the melting temperature of the system $T_{\rm m}$ decreases as the anisotropy parameter decreases. Moreover, the system with $N = 9$ particles also presents inhomogeneous melting for very anisotropic confinements, i.e. $\alpha < 0.5$. For example, for $\alpha = 0.1$ the melting temperature of the system is $T_{\rm m} = 0.023$ while the critical temperature of the external group is much larger, i.e. $T_{\rm ext} = 0.079$.

The systems with $N = 10, 11$ and 14 particles have regions of the anisotropy parameter α where the GS configurations correspond to a high symmetric arrangement. Those regions are indicated by the colored areas in Figs. 8.5(b), (c) and (e), respectively. In all cases we can find an increase of the melting temperature when the system is in the multiple ring or degenerate multiple ring configuration. Moreover, for very anisotropic confinements the critical temperature of the external group $T_{\rm ext}$ (red square) is substantially larger than the melting temperature of the system $T_{\rm m}$ (blue circles). For example, for the system with $N = 10, 11, 12$ and 14 and $\alpha = 0.1$ (see respectively Figs. 8.5(b), (c), (d) and (e)) the melting temperatures are much lower, i.e. $T_{\rm m} = 0.010, 0.0094, 0.022$ and 0.02 respectively, than the critical temperature of the external groups, i.e. $T_{\rm ext} = 0.079, 0.078, 0.079$ and 0.075, respectively.

8.4 LARGE SYSTEMS: N=30 AND 40

The melting process of small isotropically confined Wigner crystals consists of two steps as the temperature of the system increases [132]: first, at low temperature, intershell melting takes place, and when temperature is further increased, finally radical melting occurs. The increase of the number of particles leads to the formation and growth of a body centered cubic particle arrangement in the internal region of the cluster. As a result, the two melting steps typically found in small clusters gives place to a melting process ruled by the dynamics found in the bulk of the cluster [64].

In the last section we showed that inhomogeneous melting is typical for highly anisotropic clusters, i.e. roughly for anisotropy parameter $\alpha \leq 0.5$. In this section we investigate how the inhomogeneous melting process responds to an increase of the cluster size. As an example we consider systems with $N = 30$ and 40 particles.

The distinct critical temperatures for the system with $N = 30$ particles and anisotropy parameter varying from $\alpha = 0.1$ to 1.0 in steps of $\Delta\alpha = 0.1$ are shown in Fig. 8.6(a). From Fig. 8.6(a) we can clearly see that the melting process is inhomogeneous (homogeneous) when $\alpha < 0.5$ ($\alpha > 0.5$), i.e. for $\alpha < 0.5$ ($\alpha > 0.5$) we have that $T_{\rm m} < T_{\rm ext}$ ($T_{\rm m} > T_{\rm ext}$). Analogously, we find the same picture for the system with $N = 40$ particles (see Fig. 8.6(b)). In the latter case, the critical value of the anisotropy parameter, i.e. the value of

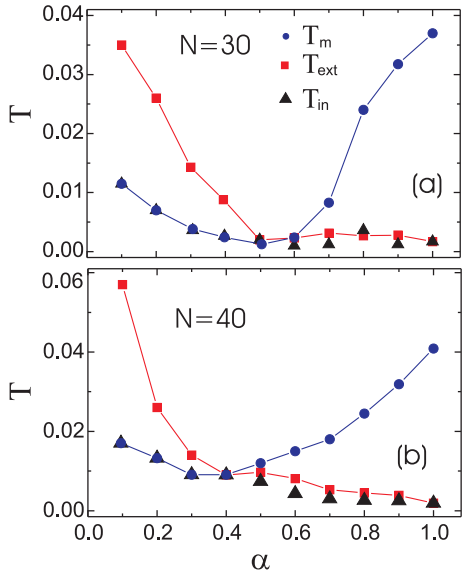

FIG. 8.6: (a) and (b) display the critical melting temperatures as function of the anisotropy parameter, respectively for systems with $N = 30$ and 40 particles.

α which separates the inhomogeneous from the homogeneous melting regimes, is equal to $\alpha = 0.4$. We found that this is a general trend, namely the critical α-value decreases with increasing N.

8.5 CONCLUSIONS

Using MD simulation we investigated the melting processes of a finite size $3D$ system of equally charged particles confined by an external anisotropic confinement potential. We assumed that the particles interact via a Coulombic interparticle interaction potential. Our theoretical model is applicable for systems such as dusty plasmas and colloids. It is expected that the found physical behavior is qualitatively the same for other isotropic interaction potentials as e.g. a screened Coulomb potential.

We found that the melting of the system becomes inhomogeneous, i.e. the melting process is not uniform throughout the cluster, as the anisotropy parameter decreases. The region of the system closest to the center of the cluster has lower melting temperature than the extremum parts of the cluster. Additionally, the melting temperature of the cluster depends on the specific ordered state, i.e. it is larger when the cluster is in the multiple ring or degenerate

multiple ring configuration. Moreover, inhomogeneous melting was verified to happen both for small and large systems.

Publication The results in this chapter were submitted for publication:

S. W. S. Apolinario and F. M. Peeters, *Melting of anisotropically confined Coulomb balls*, submitted.

9

Summary

The aim of this thesis was to study the statical and dynamical properties of finite size Wigner crystals in two and three dimensions. The properties of finite size Wigner crystals are strongly influenced by finite size effects, i.e. the number of particles, the shape of the confinement potential and the interparticle interaction potential. We found that the latter fact leads to the formation of distinct structures, i.e. magic clusters, multiple ring and degenerate multiple ring structures; and distinct melting processes, i.e. internal inter-shell and inhomogeneous melting processes. In order to understand the complexity of the structural and dynamical properties of those systems we performed very detailed simulations.

We started by investigating the effect of the *anisotropy* of the confinement potential on the statical properties of a $2D$ system of charged particles interacting via a logarithmic potential. Such an interparticle interaction potential was found to be relevant for $2D$ systems of metallic charged balls. We show that changing the eccentricity of the confinement potential can induce first and second order structural phase transitions and that these transitions are reflected in the eigenfrequencies of the system. The first order transition causes a discontinuity in almost all eigenfrequency modes while a second order transition occurs when one specific eigenfrequency becomes zero, i.e. mode softening. Also we saw that the centre of mass mode is independent from the number of particles in the system and that the breathing mode in a circular confinement

is always equal to $2\sqrt{\omega_0}$ but depends on the eccentricity of the confinement potential.

We noted that for very anisotropic confinement the zig-zag transition is initiated by particles located in the centre of the line configuration. We presented two general expressions depending only on the eccentricity parameter and the number of particles that fit all eigenfrequencies before the zig-zag transition. Moreover, we obtained an analytical expression for the critical anisotropy parameter at which the zig-zag transition occurs as a function of the number of particles in the system.

The melting process of an anisotropic confined $2D$ finite size Wigner crystal was investigated in Chapter 4. We found that, increasing the anisotropy of the confinement potential drives the system through the following different melting sequences: 1) a similar melting pattern as present in a circular system, i.e., intershell melting followed by radial melting, 2) there is only radial melting, and 3) an angular-like melting appears which we call *internal intershell melting* since it involves only particles located in the central region of the cluster. This latter phase transition is followed by radial melting.

We found that the melting process of anisotropically confined clusters is inhomogeneous. Moreover, the appearance of inhomogeneous melting in small systems occurs in a distinct form called here internal intershell melting. While that for larger systems internal intershell melting is not present but inhomogeneous melting still persists. Finally, we verified that inhomogeneous melting is present independently of the range of the interparticle interaction potential and should therefore be observed in systems as dust plasmas, colloidal suspensions and metallic balls.

In Chapter 5 we presented the results of a detailed numerical simulation of the configuration of the ground state (GS) and the lowest energy metastable (MS) state configuration, and the spectrum of normal modes of classical 3D clusters with isotropic parabolic confinement. The confined particles interact through a repulsive potential such as Coulomb or screened Coulomb interparticle potential. We found that for small systems the structural difference between the GS and MS configuration are mostly due to a different number of shells or different number of particles per shell. As the total number of particles increases the energy difference between the GS and MS configuration decreases and the structural difference between them are often due to a different arrangement of the same number of particles on the shells.

The eigenmode frequencies are investigated both for Coulomb and screened Coulomb interparticle potential. Both small and larger systems satisfy Euler's theorem and the total topological charge defect is 12. For larger systems the appearance of negative defect charge (seven fold correlation defect) is compensated by an excess of positive charge due to defects with 5 fold coordination number. The breathing mode has the highest frequency value for the case of a Coulomb interparticle interaction potential system while this is no longer true for systems of confined particles interacting through a Yukawa potential. We

found a satisfactory relation between the appearance of maximum and minimum in the lowest non-zero eigenfrequency and in the second derivative of the binding energy as function of N for small clusters ($N < 23$) which indicates respectively the most and least stable clusters. Such correspondence is not seen in larger clusters due to the fact that there the normal mode of first non-zero frequency becomes a mixed mode with a rotational and intra-shell motion component.

In Chapter 6 we investigated the melting process of small 3D isotropically confined Wigner crystals of charged particles interacting through Coulomb or screened Coulomb potentials. We found that the GS configuration of the systems with N=6, 12, 13 and 38 particles have large mechanical stability and are therefore identified as the true magic clusters. The common characteristic of magic clusters is that they are formed by one of the highly regular structures, i.e. an octahedron or icosahedron. For the system with N=38 particles each 5-fold coordinated particle sits in one of the corners of an icosahedron and are surrounded by 6-fold coordinated particles.

We found that small size effects, i.e. the cluster's symmetry, plays an important role into the dynamics of small Wigner crystals. The melting transition can evolve through three different processes which strongly depend on the arrangement of particles on the shells of the GS configuration. The solid-liquid transition in non-magic clusters occurs through two steps: first at low temperature the non-magic cluster passes through an intrashell melting and then at higher temperature through a radial melting. Differently, pronounced resistance against intrashell diffusion is found in the magic cluster with $N = 38$ particles which gives the system the possibility to undergo an intermediate melting process, the so called intershell melting. This melting process was never studied before in 3D clusters.

The effect of screening of the inter-particle interaction on the melting process was also investigated. The different critical melting temperatures for the systems with N=6, 12, 38 and 39 particles and $\kappa = 1$ were determined. This value of the screening parameter is typical for experiments in dusty plasmas. We show that the effect of screening does not modify significantly the main characteristics of the dynamics found in the magic clusters as long as the configuration of the cluster is not modified.

A normal mode analysis was performed and we found good agreement between the values of the eigenfrequencies and those of the critical temperatures obtained by MD simulation. From the normal mode analysis it turned out that: 1) the oscillation mode associated to the first non-zero frequency has a strong character of intershell rotation in case of a two shell configuration; 2) normal modes of the type intrashell motion has large eigenfrequencies if the system is a magic cluster, and 3) the 5^{th} mode of the system with $N = 39$ particles presented a vortex-like motion around a 7-fold particle on its external shell.

Next we investigated a $3D$ system of equally charged particles confined anisotropically by an external confinement potential. We assumed that the

particles interact via a Coulombic interparticle interaction potential. Our theoretical model is applicable for systems such as dusty plasma and colloids. It is expected that the found behavior is qualitatively the same for other isotropic interaction potentials as e.g. a screened Coulomb potential. We found that the anisotropy parameter α can drive the system to undergo first and second order structural phase transitions. Those transitions are found to affect the distribution of particles along the z-direction and the eigenfrequency spectrum.

The system was found to self organize in three different general structures, i.e. multiple rings, degenerate multiple rings and non-symmetric structures, if the number of particles is small, typically $N \leq 25$ particles. For larger systems, i.e. $N \geq 50$, multiple ring structures were found in the external shell only if the anisotropy parameter was smaller than $\alpha \leq 0.2$, or in the internal shell for more isotropic confinements, roughly $\alpha \geq 0.4$. A fine structure was formed in small clusters upon increasing the particle number. Our results on the structure of the GS configurations as function of the anisotropy parameter were summarized in a phase diagram.

For a multiple ring structure the GS configuration is found to exhibit inter-ring and vortex/anti-vortex modes of oscillation. The latter modes are delocalized and therefore must be of relevance for the melting process. Furthermore, those modes indicate that low temperature dynamics in multiple ring structures must have a strong $2D$ behavior. Next to it we found that for the multiple ring configurations the eigenfrequency spectrum becomes highly degenerate.

Finally, we notice that the identified multiple ring structure is relevant for the physics of small Coulomb crystals due to the fact that they constitute a hybrid system built up by blocks of $2D$ structures forming piled rings along the z-direction.

In Chapter 8 we investigated through a MD simulation the melting processes of a $3D$ system of equally charged particles confined anisotropically by an external confinement potential. We assumed that the particles interact via a Coulombic interparticle interaction potential.

We found that the melting of the system becomes inhomogeneous, i.e. the melting process is not uniform throughout the cluster, as the anisotropy parameter decreases. The region of the system closest to the center of the cluster has lower melting temperature than the extremum parts of the cluster that are situated along the z direction. Moreover, the melting temperature of the cluster depends on the specific ordered state, i.e. it is larger when the cluster is in the multiple ring or degenerate multiple ring structures. Moreover, inhomogeneous melting was verified to happen both for small and large systems. It is expected that the found physical behavior is qualitatively the same for other isotropic interaction potentials as e.g. a screened Coulomb potential.

10

Samenvatting

Het doel van deze thesis is het bestuderen van de statische en dynamische eigenschappen van Wignerkristallen met een eindige grootte in twee en drie dimensies. De eigenschappen van eindige Wignerkristallen worden sterk beïnvloed door eindigheidseffecten, zoals bv. het aantal deeltjes, de vorm van de opsluitinspotentiaal en de deeltjes-deeltjes interactiepotentiaal. We vonden dat dit resulteert in de vorming van verschillende structuren, zoals magische clusters en structuren opgebouwd uit verschillende ringen, en het voorkomen van verschillende smeltprocessen, bv. interne inter-shell en inhomogene smeltprocessen. Om deze complexheid in structurele en dynamische eigenschappen van deze systemen te begrijpen hebben we zeer gedetailleerde simulaties uitgevoerd.

Ten eerste hebben we het effect van de *anisotropie* van de opsluitingspotentiaal op de statische eigenschappen van een $2D$ systeem bestaande uit geladen deeltjes en interagerend met een logaritmische potentiaal bestudeerd. Zo'n interactiepotentiaal is relevant voor een $2D$ systeem van geladen metalen ballen. We tonen aan dat het veranderen van de excentriciteit van de potentiaal eerste en tweede orde structurele faseovergangen kan veroorzaken en dat deze overgangen zichtbaar zijn in de eigenfrequenties van het systeem. De eerste orde overgang veroorzaakt een discontinuïteit in bijna alle eigenfrequenties. De tweede orde overgang komt voor wanneer één specifieke eigenfrequentie nul

wordt ('mode softening'). We observeerden ook dat de massacentrummode onafhankelijk is van het aantal deeltjes in het systeem, maar afhankelijk van de excentriciteit, en dat de 'breathing' mode in een cirkelvormige opsluiting steeds gelijk is aan $2\sqrt{\omega_0}$.

We hebben eveneens gevonden dat voor een sterk anisotrope opsluiting de zigzag overgang geïnitieerd wordt door deeltjes die zich in het centrum van de lijnconfiguratie bevinden. We vonden twee algemene uitdrukkingen, die enkel afhangen van de excentriciteit en het aantal deeltjes, die alle eigenfrequenties opleveren tot aan de zigzag overgang. Eveneens hebben we een analytische uitdrukking bekomen voor de kritische anisotropieparameter, waarbij de zigzag overgang optreedt, als functie van het aantal deeltjes van het systeem.

In hoofdstuk 4 werd het smeltproces van een eindig $2D$ Wignerkristal in een anisotrope opsluitingspotentiaal onderzocht. We vonden dat bij een toename van de anisotropie van de opsluitingspotentiaal het systeem de volgende smeltsequentie doorloopt: 1) een gelijkaardig smeltpatroon als in het geval van een cirkelvormig systeem (intershell gevolgd door radieel smelten), 2) enkel radieel smelten en 3) een angulair smeltproces, dat we *intern intershell smelten* noemen, aangezien het enkel voorkomt bij deeltjes die zich in het centraal gebied van de cluster bevinden. Deze laatste fase wordt gevolgd door een radieel smelten.

We vonden dat het smeltproces van clusters in een anisotrope opsluitingspotentiaal niet homogeen is. Meer nog, het niet homogeen smelten gebeurt voor kleine systemen in de vorm van het intern intershell smelten. Voor grotere systemen komt het intern intershell smelten niet voor, maar wel nog steeds niet homogeen smelten. Uiteindelijk verifieerden we dat het niet homogeen smelten voorkomt onafhankelijk van de dracht van de interactiepotentiaal tussen de deeltjes, zodat dit zowel in systemen van 'dusty' plasma's, colloïdale suspensies en metalen ballen geobserveerd zou kunnen worden.

In hoodstuk 5 worden de resultaten besproken van de numerieke simulatie van de grondtoestandsconfiguratie (GS) en de laagste metastabiele toestanden (MS) van klassieke 3D clusters met isotrope parabolische opsluiting, en het spectrum van de normale modes van deze clusters. De opgesloten deeltjes interageren d.m.v. een repulsieve potentiaal zoals de Coulomb of de afgeschermde Coulomb potentiaal. We vonden dat, voor kleine systemen, de structurele verschillen tussen de GS en de MS configuratie voornamelijk te wijten zijn aan een verschillend aantal schillen of een verschillend aantal deeltjes per schil. Als het totaal aantal deeltjes toeneemtt, vermindert het energieverschil tussen de GS en de MS configuratie en de structurele verschillen ontstaan vaak door een verschillende ordening van hetzelfde aantal deeltjes in de schillen.

De eigenmode frequenties zijn onderzocht voor zowel de Coulomb als de afgeschermde Coulomb potentiaal. Zowel kleine als grotere systemen voldoen aan Eulers theorema en het totale topologische ladingsdefect is 12. Voor grote systemen wordt de verschijning van een negatief geladen defect (een deeltje met zeven buren) gecompenseerd door een overschot aan positieve lading door

defecten met vijfvoudig cordinatie getal. De 'breathing' mode heeft de hoogste frequentiewaarde in het geval van de Coulomb interactiepotentiaal, terwijl dit niet langer het geval is voor systemen van opgesloten deeltjes die interageren d.m.v. een Yukawa-potentiaal. We vonden een goede relatie tussen het verschijnen van maximum en minimum in de laagste eigenfrequentie verschillend van 0 en voor de tweede afgeleide van de bindingsenergie als functie van N voor kleine clusters ($N < 23$) wat wijst op respectievelijk de meest en minst stabiele clusters. Zulke overeenkomsten zijn niet zichtbaar in grote clusters door het feit dat daar de normale mode van de eerste van nul verschillende eigenfrequentie een gemixte mode wordt met een rotationele en een intra-schil bewegingsmode.

In hoofdstuk 6 hebben we het smeltproces onderzocht van kleine 3D, isotrope Wignerkristallen van geladen deeltjes die interageren d.m.v. een Coulomb- of afgeschermde Coulomb-potentiaal. We vonden dat de grondtoestandsconfiguratie van de systemen met N=6, 12, 13 en 38 deeltjes een grote mechanische stabiliteit hebben en daarom werden ze geïdentificeerd als magische clusters. De gemeenschappelijke eigenschap van magische clusters is dat ze gevormd worden door een van de uiterst geordende structuren, namelijk een octaëder of icosaëder. Voor het systeem met N=38 deeltjes zit elk vijfvoudig gecoördineerd deeltje op een van de hoeken van een icosaëder en wordt omringd door zesvoudig gecoördineerde deeltjes.

We vonden dat effecten door de kleine afmetingen, namelijk de clustersymmetrie, een belangrijke rol speelt in de dynamica van kleine Wignerkristallen. De smeltovergang kan evolueren door drie verschillende processen welke sterk afhangen van de ordening van de deeltjes op de schillen van de GS-configuratie. De vaste-stof/vloeistof-overgang in niet-magische clusters gebeurt in twee stappen: bij lage temperatuur doorloopt de niet-magische cluster eerst een intraschil smeltproces en vervolgens, bij hogere temperaturen, een radieel smeltproces. In tegenstelling hiermee vindt men een uitgesproken weerstand tegen een intraschil diffusie bij de magische cluster met N=38 deeltjes wat het systeem de mogelijkheid geeft om een tussenliggend smeltproces te ondergaan, het zogenaamde interschil smeltproces. Dit smeltproces was nog nooit eerder bestudeerd in 3D clusters.

De invloed van afscherming van de interdeeltjes potentiaal op het smeltproces werd ook onderzocht. De verschillende kritieke smelttemperaturen voor de systemen met N=6, 12, 38 en 39 deeltjes en $\kappa = 1$ werden bepaald. Deze waarde voor de afschermparameter is typisch voor experimenten in 'dusty' plasmas. We tonen dat het effect van de afscherming de belangrijkste eigenschappen van de dynamica aanwezig in de magische clusters niet sterk benvloed zolang de configuratie van de cluster niet verandert.

Een analyse van de eigentrillingen is uitgevoerd waarbij we een goede overeenkomst vonden tussen de eigenfrequenties en de kritische temperaturen verkregen door MD simulaties. Uit deze analyse kan besloten worden dat: 1) de oscillatie-mode corresponderend met de eerste frequentie verschillend van nul heeft een sterk inter-schil rotatie karakter in het geval een configuratie met twee

schillen; 2) eigentrillingen van het type intraschil-beweging hebben grote eigenfrequenties als het systeem een magische cluster is, en 3) de 5^{de} oscillatie-mode van een systeem met $N = 39$ deeltjes is een vortex-achtige beweging rond een 7-voudig deeltje op zijn buitenste schil.

Vervolgens hebben we het $3D$ systeem onderzocht van gelijk geladen deeltjes die worden opgesloten door een externe anisotrope opsluitingspotentiaal. Hierbij namen we aan dat de elektronen interageerden via de Coulomb potentiaal. Ons theoretisch model is toepasbaar op 'dusty' plasma's en coloïdale systemen. Verwacht wordt dat het verkregen gedrag kwalitatief overeenkomt met dat van andere isotrope interactie-potentialen, zoals bijvoorbeeld een afgeschermde Coulomb potentiaal. We vonden dat door de anisotropieparameter α te variëren we het systeem een eerste en tweede orde structurele faseovergang kunnen laten ondergaan. Deze faseovergangen beïnvloeden hierbij de distributie van de deeltjes langs de z-as alsook het spectrum van eigenfrequenties.

Het systeem organiseerde zich in drie verschillende types structuren, d.i. meerdere ringen, ontaarde meerdere ringen en niet-symmetrische structuren, als het aantal deeltjes klein is, typisch $N \leq 25$. Voor grotere systemen, typisch $N \geq 50$, kon de structuur van meerdere ringen in de buitenste schillen enkel teruggevonden worden als de anisotropieparameter voldoende klein was $\alpha \leq 0.2$, en in het gebied daarbinnen voor meer isotrope opsluitingspotentialen, benaderend $\alpha \geq 0.4$. Bij toenemend deeltjesaantal werden kleinere structuren in de vorm van clusters gevormd. Onze resultaten van de structuur van de GS configuraties als functie van de anisotropieparameter zijn samengevat in een fasediagram.

Voor de structuur van meerdere ringen vonden we in de GS configuraties inter-ring en vortex/anti-vortex oscillatiemodes. Deze laatste zijn niet gelocaliseerd en zullen daarom belangrijk zijn in het smeltproces. Verder duiden deze oscillaties erop dat voor lage temperaturen de dynamica van het systeem een sterk $2D$ gedrag vertoont. Alsook vonden we dat de configuraties van deze meerdere ring structuren een spectrum van eigenfrequenties heeft dat in hoge graad ontaard is.

Als laatste merken we op dat het onderzoeken van de structuur van meerdere ringen relevant is om het gedrag te begrijpen van kleine Coulomb kristallen doordat deze een hybride systeem vormen, opgebouwd uit opeengestapelde $2D$ ringen langs de z-as.

In hoofdstuk 8 onderzochten we, aan de hand van moleculaire dynamica simulaties, het smeltproces van een $3D$ systeem van gelijk geladen deeltjes opgesloten door een anisotrope opsluitingspotentiaal. Hierbij namen we aan dat de deeltjes interageerden via de Coulomb interactie-potentiaal.

We vonden dat het smelten van het systeem inhomogeen wordt, d.i. het smeltproces is niet uniform doorheen de cluster, als de anisotropieparameter verkleint. Het gebied van het systeem rond het centrum van de cluster heeft een lagere smeltemperatuur dan de verder verwijderde delen langs de z-as van de cluster. Eveneens hangt de smelttemperatuur van de cluster af van de toestand

of structuur waarin deze is, d.i. deze is hoger wanneer de cluster de structuur van meerdere of ontaarde meerdere ringen heeft. Alsook werd dit inhomogeen smeltgedrag gevonden in zowel grote als kleine systemen. Verwacht wordt dat het verkregen gedrag kwalitatief overeenkomt met dat van andere isotrope interactie-potentialen zoals bijvoorbeeld een afgeschermde Coulomb potentiaal.

Appendix A

Table 0.1: From left to right: the number of particles in the system, its energy per particle, its configuration, the radius of the shell (r), the width of the shell ($\Delta(r)$), the value of the three non-zero lowest eigenfrequencies (f_i, $i = 1, 2, 3$), and the number of particles per shell with x nearest neighbors where x varies from 3 to 7.

N	**E/N**	**conf.**	**r**	$\Delta(r)$	f_1	f_2	f_3	**N(3)**	**N(4)**	**N(5)**	**N(6)**	**N(7)**
2	0.7500000	2	0.5000	0.0000	1.4142	1.4142	1.4142	-	-	-	-	-
3	1.3103707	3	0.6609	0.0000	1.4142	1.4142	1.4142	-	-	-	-	-
4	1.7858262	4	0.7715	0.0000	1.2247	1.2247	1.4142	4	**-**	**-**	**-**	**-**
5	2.2451872	5	0.8651	0.0181	0.6226	0.6226	1.3954	2	3	**-**	**-**	**-**
6	2.6540390	6	0.9406	0.0000	0.8517	0.8517	0.8517	-	6	-	-	-
7	3.0641858	7	1.0106	0.0277	0.1472	0.1472	0.9726	-	5	2	-	-
8	3.4434094	8	1.0714	0.0000	0.3916	0.3916	0.5842	**-**	4	4	**-**	**-**
9	3.8097820	9	1.1269	0.0126	0.3185	0.3185	0.7584	**-**	3	6	**-**	**-**
	3.8425262	1,8	0.0000	-	0.2235	0.3348	0.3348	-	-	-	-	-
			1.2004	0.0000				-	4	4	-	-
10	4.1649900	10	1.1783	0.0131	0.2467	0.2467	0.7600	-	2	8	-	-
	4.1869791	1,9	0.0000	-	0.2719	0.2719	0.5719	-	-	-	-	-
			1.2453	0.0060				**-**	3	6	**-**	**-**
11	4.5132754	11	1.2265	0.0353	0.2243	0.2409	0.5546	**-**	2	8	1	**-**
	4.5231515	1,10	0.0000	-	0.2116	0.2116	0.6566	-	-	-	-	-
			1.2878	0.0070				-	2	8	-	-
12	4.8389665	12	1.2700	0.0000	0.6655	0.6655	0.6655	-	-	12	-	-
	4.8543111	1,11	0.0178	-	0.1992	0.2149	0.4765	-	-	-	-	-
			1.3286	0.0166				**-**	2	8	1	**-**
13	5.1667983	1,12	0.0000	-	0.5966	0.5966	0.5966	-	-	-	-	-
			1.3659	0.0000				-	-	12	-	-
	5.1718595	13	1.3130	0.0333	0.1311	0.1915	0.3391	-	1	10	2	-

Table 0.1 – Continued

N	E	conf.	r	$\Delta(r)$	f_1	f_2	f_3	N(3)	N(4)	N(5)	N(6)	N(7)
14	5.4859154	1,13	0.0071	-	0.1176	0.1703	0.3059	-	-	-	-	-
			1.4033	0.0195				-	1	10	2	-
	5.4894163	14	1.3527	0.0000	0.3624	0.3624	0.4466	-	-	12	2	-
15	5.7920942	1,14	0.0000	-	0.3289	0.3289	0.4074	-	-	-	-	-
			1.4383	0.0154				-	-	12	2	-
	5.8011249	15	1.3906	0.0000	0.2582	0.2688	0.2688	-	-	12	3	-
16	6.0934213	1,15	0.0000	-	0.2414	0.2414	0.2437	-	-	-	-	-
			1.4719	0.0134				-	-	12	3	-
	6.1056214	16	1.4266	0.0000	0.3342	0.3495	0.3495	-	-	12	4	-
17	6.3886098	1,16	0.0000	-	0.3175	0.3175	0.3175	-	-	-	-	-
			1.5042	0.0139				-	-	12	4	-
	6.3889747	1,16	0.0000	0.0195	0.2426	0.2426	0.3619	-	-	-	-	-
			1.5042	0.0000				-	-	12	4	-
18	6.6788303	1,17	0.0000	-	0.1791	0.1791	0.1823	-	-	-	-	-
			1.5353	0.0012				-	-	12	5	-
	6.6974417	18	1.4941	0.0352	0.2416	0.2416	0.3803	-	2	8	8	-
19	6.9641459	1,18	0.0000	-	0.2221	0.2221	0.3532	-	-	-	-	-
			1.5654	0.0122				-	2	8	8	-
	6.9878240	19	1.5261	0.0405	0.0227	0.2542	0.3329	-	-	12	7	-
20	7.2471808	1,19	0.0002	-	0.0345	0.2372	0.3101	-	-	-	-	-
			1.5946	0.0176				-	-	12	7	-
	7.2514451	2,18	0.5400	0.0504	0.1052	0.1593	0.2511	-	-	-	-	-
			1.6285	0.1090				-	2	8	8	-
21	7.5223777	1,20	0.0000	-	0.1869	0.1869	0.4160	-	-	-	-	-
			1.6226	0.0108				-	-	12	8	-
	7.5270457	2,19	0.5403	0.0621	0.1475	0.2144	0.2345	-	-	-	-	-
			1.6557	0.1041				-	-	12	7	-
22	7.7954689	1,21	0.0007	-	0.0712	0.0870	0.1565	-	-	-	-	-
			1.6499	0.0182				-	1	10	10	-
	7.7964445	2,20	0.5321	0.0007	0.0094	0.0845	0.2349	-	-	-	-	-
			1.6821	0.1052				-	-	12	8	-
23	8.0635754	2,21	0.5302	0.0000	0.0389	0.0627	0.1642	-	-	-	-	-
			1.7077	0.0927				-	-	12	9	-
	8.0635791	2,21	0.5303	0.0385	0.0901	0.0901	0.1692	-	-	-	-	-
			1.7077	0.1076				-	1	10	10	-
24	8.3268028	2,22	0.5260	0.0130	0.0842	0.1271	0.2047	-	-	-	-	-
			1.7326	0.0808				-	-	12	10	-
	8.3272196	2,22	0.5263	0.0000	0.0331	0.1201	0.1572	-	-	-	-	-
			1.7327	0.0854				-	-	12	10	-
25	8.5883607	2,23	0.5262	0.0000	0.1138	0.1138	0.2948	-	-	-	-	-
			1.7570	0.0978				-	-	12	11	-
	8.5889178	3,22	0.6958	0.0000	0.2054	0.2200	0.2200	-	-	-	-	-
			1.7849	0.1226				-	-	12	10	-
26	8.8442362	2,24	0.5241	0.0000	0.1934	0.1964	0.1964	-	-	-	-	-
			1.7805	0.0575				-	-	12	12	-
	8.8459235	3,23	0.6931	0.0195	0.1214	0.2303	0.2364	-	-	-	-	-
			1.8081	0.1219				-	-	12	11	-
27	9.0973346	3,24	0.6898	0.0166	0.0632	0.1058	0.2364	-	-	-	-	-
			1.8305	0.1045				-	-	12	12	-
	9.0974154	3,24	0.6895	0.0170	0.0683	0.1827	0.2391	-	-	-	-	-
			1.8305	0.0999				-	-	12	12	-
28	9.3483678	3,25	0.6889	0.0027	0.0765	0.1710	0.2133	-	-	-	-	-
			1.8525	0.1150				-	-	12	13	-
	9.3483829	3,25	0.6889	0.0215	0.1162	0.1361	0.2040	-	-	-	-	-
			1.8525	0.1289				-	-	12	13	-
29	9.5954351	4,25	0.7987	0.0268	0.1203	0.1684	0.2458	4	-	-	-	-
			1.8992	0.1110				-	-	12	13	-
	9.5957698	3,26	0.6872	0.0055	0.0435	0.1723	0.1923	-	-	-	-	-
			1.8740	0.0964				-	-	12	14	-

Table 0.1 – Continued

N	E	conf.	r	$\Delta(r)$	f_1	f_2	f_3	N(3)	N(4)	N(5)	N(6)	N(7)
30	9.8389647	4,26	0.7961	0.0311	0.0559	0.1627	0.1825	4	-	-	-	-
			1.9198	0.1109				-	-	12	14	-
	9.8395917	3,27	0.6841	0.0037	0.1424	0.1549	0.2055	-	-	-	-	-
			1.8950	0.1052				-	-	12	15	-
31	10.0795110	4,27	0.7926	0.0124	0.1114	0.1742	0.1847	4	-	-	-	-
			1.9399	0.1098				-	-	12	15	-
	10.0795174	4,27	0.7927	0.0208	0.0959	0.1931	0.1978	4	-	-	-	-
			1.9399	0.1165				-	-	12	15	-
32	10.3186788	4,28	0.7935	0.0000	0.2282	0.2282	0.2282	4	-	-	-	-
			1.9596	0.0882				-	-	12	16	-
	10.3190407	4,28	0.7912	0.0025	0.0908	0.1390	0.1828	4	-	-	-	-
			1.9597	0.1232				-	-	12	16	-
33	10.5565871	4,29	0.7914	0.0215	0.1059	0.1059	0.1714	4	-	-	-	-
			1.9791	0.1304				-	-	12	17	-
	10.5566443	4,29	0.7908	0.0092	0.0625	0.0997	0.1105	4	-	-	-	-
			1.9791	0.1208				-	-	12	17	-
34	10.7908419	4,30	0.7901	0.0000	0.0505	0.1399	0.1589	4	-	-	-	-
			1.9980	0.1052				-	-	12	18	-
	10.7914888	5,29	0.8867	0.0677	0.0303	0.1531	0.1568	2	3	-	-	-
			2.0200	0.1253				-	-	12	17	-
35	11.0227310	5,30	0.8859	0.0821	0.0413	0.1399	0.1672	2	3	-	-	-
			2.0381	0.1467				-	-	12	18	-
	11.0227585	5,30	0.8849	0.0820	0.0582	0.0719	0.0872	2	3	-	-	-
			2.0383	0.1448				-	-	12	18	-
36	11.2519226	6,30	0.9582	0.0000	0.0882	0.0882	0.2117	-	6	-	-	-
			2.0775	0.1018				-	-	12	18	-
	11.2519406	6,30	0.9576	0.0197	0.0748	0.0816	0.1126	-	6	-	-	-
			2.0775	0.1020				-	-	12	18	-
37	11.4787472	6,31	0.9585	0.0324	0.2319	0.2334	0.2334	-	6	-	-	-
			2.0947	0.1150				-	-	12	19	-
	11.4789060	6,31	0.9571	0.0480	0.0905	0.1492	0.2089	-	6	-	-	-
			2.0948	0.1228				-	-	12	19	-
38	11.7029516	6,32	0.9549	0.0000	0.1089	0.1490	0.1490	-	6	-	-	-
			2.1119	0.1166				-	-	12	20	-
	11.7029615	6,32	0.9546	0.0000	0.1070	0.1070	0.1070	-	6	-	-	-
			2.1119	0.0903				-	-	12	20	-
39	11.9283228	6,33	0.9549	0.0348	0.0621	0.1103	0.1316	-	6	-	-	-
			2.1289	0.1186				-	-	13	19	1
	11.9283233	6,33	0.9553	0.0387	0.0838	0.1437	0.1514	-	6	-	-	
			2.1288	0.1041				-	-	13	19	1
40	12.1501629	6,34	0.9547	0.0253	0.0812	0.1198	0.1450	-	6	-	-	-
			2.1453	0.1282				-	-	12	22	-
	12.1513063	7,33	1.0280	0.1387	0.1032	0.1362	0.1663	-	5	2	-	-
			2.1641	0.1124				-	-	12	21	-
41	12.3707915	6,35	0.9538	0.0178	0.0751	0.0929	0.1339	-	6	-	-	-
			2.1618	0.1222				-	-	12	23	-
	12.3708003	6,35	0.9538	0.0095	0.0458	0.0954	0.1453	-	6	-	-	-
			2.1618	0.1276				-	-	12	23	-
42	12.5891393	7,35	1.0260	0.1218	0.1071	0.1321	0.1577	-	5	2	-	-
			2.1961	0.1298				-	-	12	23	-
	12.5891687	7,35	1.0264	0.1280	0.0601	0.1383	0.1617	-	5	2	-	-
			2.1961	0.1393				-	-	12	23	-
43	12.8055452	7,36	1.0252	0.0985	0.0498	0.1312	0.1877	-	5	2	-	-
			2.2119	0.1171				-	-	12	24	-
	12.8056408	7,36	1.0250	0.0903	0.1145	0.1300	0.1969	-	5	2	-	-
			2.2119	0.1261				-	-	12	24	-
44	13.0200779	8,36	1.0845	0.0370	0.1116	0.1178	0.1310	-	4	4	-	-
			2.2454	0.1386				-	-	12	24	-
	13.0200965	8,36	1.0848	0.0083	0.0529	0.1265	0.1412	-	4	4	-	-
			2.2454	0.1302				-	-	12	24	-

Table 0.1 – Continued

N	E	conf.	r	$\Delta(r)$	f_1	f_2	f_3	N(3)	N(4)	N(5)	N(6)	N(7)
45	13.2329012	8,37	1.0845	0.0851	0.0758	0.1030	0.1208	-	4	4	-	-
			2.2603	0.1240				-	-	12	25	-
	13.2330752	8,37	1.0842	0.0472	0.1234	0.1454	0.1675	-	4	4	-	-
			2.2604	0.1555				-	-	12	25	-
46	13.4446015	8,38	1.0842	0.0826	0.0131	0.1450	0.1803	-	4	4	-	-
			2.2751	0.1129				-	-	12	26	-
	13.4446625	8,38	1.0833	0.0554	0.0649	0.1418	0.1447	-	4	4	-	-
			2.2752	0.1694				-	-	12	26	-
47	13.6544585	9,38	1.1391	0.1064	0.1185	0.1987	0.2025	-	3	6	-	-
			2.3066	0.1061				-	-	12	26	-
	13.6544883	9,38	1.1380	0.0960	0.0441	0.1211	0.1443	-	3	6	-	-
			2.3067	0.1277				-	-	12	26	-
48	13.8627620	9,39	1.1379	0.0892	0.1156	0.1582	0.1682	-	3	6	-	-
			2.3210	0.1235				-	-	12	27	-
	13.8629342	9,39	1.1372	0.0055	0.1039	0.1165	0.1165	-	3	6	-	-
			2.3212	0.1094				-	-	12	27	-
49	14.0699199	9,40	1.1371	0.0840	0.1137	0.1292	0.1552	-	3	6	-	-
			2.3351	0.1277				-	-	12	28	-
	14.0701384	9,40	1.1364	0.0457	0.0651	0.0651	0.0983	-	3	6	-	-
			2.3352	0.1305				-	-	12	28	-
50	14.2757285	9,41	1.1372	0.0529	0.1438	0.1438	0.2186	-	3	6	-	-
			2.3490	0.1302				-	-	12	29	-
	14.2759561	10,40	1.1876	0.1061	0.0891	0.0925	0.0989	-	2	8	-	-
			2.3652	0.1101				-	-	12	28	-
51	14.4801010	10,41	1.1877	0.0859	0.0676	0.0910	0.2202	-	2	8	-	-
			2.3788	0.1292				-	-	12	29	-
	14.4807038	9,42	1.1363	0.0654	0.0759	0.1018	0.1526	-	3	6	-	-
			2.3629	0.1382				-	-	12	30	-
52	14.6831926	10,42	1.1875	0.0787	0.0140	0.1687	0.2052	-	2	8	-	-
			2.3922	0.1268				-	-	12	30	-
	14.6833601	10,42	1.1871	0.0747	0.0535	0.0851	0.1067	-	2	8	-	-
			2.3923	0.1269				-	-	12	30	-
53	14.8852839	10,43	1.1872	0.0824	0.0945	0.1074	0.1163	-	2	8	-	-
			2.4055	0.1520				-	-	12	31	-
	14.8852982	10,43	1.1872	0.0820	0.0689	0.1106	0.1510	-	2	8	-	-
			2.4055	0.1286				-	-	12	31	-
54	15.0857028	10,44	1.1872	0.0581	0.1393	0.1393	0.1671	-	2	8	-	-
			2.4186	0.1061				-	-	12	32	-
	15.0857248	10,44	1.1867	0.0620	0.0187	0.1361	0.1384	-	2	8	-	-
			2.4186	0.1485				-	-	12	32	-
55	15.2847026	12,43	1.2773	0.0250	0.0456	0.0456	0.1197	-	-	12	-	-
			2.4618	0.1086				-	-	12	31	-
	15.2851700	11,44	1.2356	0.1654	0.1349	0.1446	0.1660	-	2	8	1	-
			2.4465	0.1624				-	-	12	32	-
56	15.4821444	12,44	1.2770	0.0193	0.0879	0.0879	0.1185	-	-	12	-	
			2.4743	0.1110				-	-	12	32	-
	15.4834142	1,12,43	0.0407	-	0.0462	0.0462	0.0778	-	-	-	-	-
			1.3786	0.0463				-	-	12	-	-
			2.4878	0.1372				-	-	12	31	-
57	15.6793502	12,45	1.2763	0.0210	0.0622	0.1012	0.1334	-	-	12	-	-
			2.4869	0.1110				-	-	12	33	-
	15.6794160	12,45	1.2759	0.0031	0.0757	0.0757	0.1089	-	-	12	-	-
			2.4869	0.0953				-	-	12	33	-
58	15.8754062	1,12,45	0.0052	-	0.0661	0.0828	0.1215	-	-	-	-	-
			1.3765	0.0150				-	-	12	-	-
			2.5126	0.1406				-	-	12	33	-
	15.8754397	12,46	1.2766	0.0000	0.2012	0.2012	0.2012	-	-	12	-	-
			2.4992	0.0932				-	-	12	34	-

Table 0.1 – Continued

N	E	conf.	r	$\Delta(r)$	f_1	f_2	f_3	N(3)	N(4)	N(5)	N(6)	N(7)
59	16.0701034	1,12,46	0.0000	-	0.1928	0.1928	0.1928	-	-	-	-	-
			1.3764	0.0000				-	-	12	-	-
			2.5247	0.1217				-	-	12	34	-
	16.0701563	1,12,46	0.0168	-	0.0722	0.0722	0.1448	-	-	-	-	-
			1.3771	0.0197				-	-	12	-	-
			2.5246	0.1294				-	-	15	28	3
60	16.2637073	12,48	1.2755	0.0094	0.1154	0.1202	0.1202	-	-	12	-	
			2.5236	0.1007				-	-	12	36	-
	16.2639715	1,12,47	0.0036	-	0.0719	0.0934	0.1105	-	-	-	-	-
			1.3764	0.0197				-	-	12	-	-
			2.5368	0.1294				-	-	12	35	-
61	16.4558128	1,12,48	0.0041	-	0.0899	0.1262	0.1262	-	-	-	-	-
			1.3751	0.0063				-	-	12	-	-
			2.5488	0.1264				-	-	12	36	-
	16.4558710	1,12,48	0.0000	-	0.0628	0.0628	0.0628	-	-	-	-	-
			1.3752	0.0000				-	-	12	-	-
			2.5489	0.1046				-	-	12	36	-
62	16.6475197	1,13,48	0.0164	-	0.0308	0.1233	0.1538	-	-	-	-	-
			1.4134	0.0953				-	1	10	2	-
			2.5738	0.1612				-	-	12	36	-
	16.6475207	1,13,48	0.0249	-	0.0623	0.0981	0.1401	-	-	-	-	-
			1.4133	0.0715				-	1	10	2	-
			2.5739	0.1509				-	-	12	36	-
63	16.8376940	1,14,48	0.0047	-	0.0633	0.0949	0.0993	-	-	-	-	-
			1.4473	0.0762				-	-	12	2	
			2.5988	0.1408				-	-	12	36	-
	16.8376973	1,14,48	0.0037	-	0.0138	0.0897	0.1014	-	-	-	-	-
			1.4473	0.0742				-	-	12	2	-
			2.5988	0.1311				-	-	12	36	-
64	17.0272889	1,14,49	0.0019	-	0.1435	0.1435	0.1633	-	-	-	-	-
			1.4478	0.0758				-	-	12	2	-
			2.6101	0.1233				-	-	12	37	-
	17.0273485	1,14,49	0.0071	-	0.1001	0.1336	0.1504	-	-	-	-	-
			1.4475	0.0725				-	-	12	2	-
			2.6101	0.1266				-	-	12	37	-
65	17.2153608	1,14,50	0.0000	-	0.1842	0.1947	0.1947	-	-	-	-	-
			1.4477	0.0517				-	-	12	2	-
			2.6212	0.1197				-	-	12	38	-
	17.2154915	1,14,50	0.0026	-	0.0648	0.1149	0.1625	-	-	-	-	-
			1.4470	0.0784				-	-	12	2	-
			2.6215	0.1381				-	-	12	38	-
66	17.4028913	1,15,50	0.0059	-	0.1165	0.1246	0.1499	-	-	-	-	-
			1.4805	0.0846				-	-	12	3	-
			2.6453	0.1339				-	-	12	38	-
	17.4028985	1,15,50	0.0042	-	0.0667	0.1156	0.1299	-	-	-	-	-
			1.4804	0.0680				-	-	12	3	-
			2.6453	0.1289				-	-	12	38	-
67	17.5893474	1,15,51	0.0046	-	0.1210	0.1384	0.1594	-	-	-	-	-
			1.4803	0.0724				-	-	12	3	-
			2.6563	0.1436				-	-	12	39	-
	17.5893617	1,15,51	0.0027	-	0.0809	0.0963	0.1458	-	-	-	-	-
			1.4802	0.0708				-	-	12	3	-
			2.6564	0.1412				-	-	12	39	-
68	17.7748744	1,16,51	0.0034	-	0.1446	0.1446	0.1748	-	-	-	-	-
			1.5123	0.0756				-	-	12	4	-
			2.6797	0.1201				-	-	12	39	-
	17.7750173	1,16,51	0.0155	-	0.1070	0.1310	0.1567	-	-	-	-	-
			1.5123	0.0957				-	-	12	4	-
			2.6797	0.1260				-	-	12	39	-

Table 0.1 – Continued

N	E	conf.	r	$\Delta(r)$	f_1	f_2	f_3	N(3)	N(4)	N(5)	N(6)	N(7)
69	17.9594322	1,16,52	0.0010	-	0.1491	0.1768	0.1768	-	-	-	-	-
			1.5126	0.0968				-	-	12	4	-
			2.6903	0.1043				-	-	12	40	-
	17.9594876	1,16,52	0.0000	-	0.1329	0.1329	0.1329	-	-	-	-	-
			1.5130	0.0836				-	-	12	4	-
			2.6902	0.1055				-	-	12	40	-
70	18.1433383	1,16,53	0.0023	-	0.1333	0.1487	0.1622	-	-	-	-	-
			1.5119	0.0885				-	-	12	4	-
			2.7010	0.1228				-	-	12	41	-
	18.1433927	1,16,53	0.0057	-	0.0821	0.1361	0.1694	-	-	-	-	-
			1.5120	0.0928				-	-	12	4	-
			2.7010	0.1340				-	-	12	41	-
71	18.3262819	1,16,54	0.0084	-	0.1102	0.1590	0.1800	-	-	-	-	-
			1.5118	0.0791				-	-	12	4	-
			2.7116	0.1316				-	-	12	42	-
	18.3263270	1,16,54	0.0030	-	0.0962	0.1450	0.1653	-	-	-	-	-
			1.5115	0.0843				-	-	12	4	-
			2.7117	0.1371				-	-	12	42	-
72	18.5084443	1,17,54	0.0059	-	0.1167	0.1293	0.1315	-	-	-	-	-
			1.5423	0.0744				-	-	12	5	-
			2.7342	0.1505				-	-	12	42	-
	18.5084666	1,17,54	0.0073	-	0.0918	0.1218	0.1560	-	-	-	-	-
			1.5424	0.0797				-	-	12	5	-
			2.7342	0.1548				-	-	12	42	-
73	18.6897294	1,17,55	0.0047	-	0.0965	0.1287	0.1432	-	-	-	-	-
			1.5422	0.0724				-	1	10	6	-
			2.7445	0.1434				-	-	12	43	-
	18.6897341	1,17,55	0.0031	-	0.1061	0.1432	0.1773	-	-	-	-	-
			1.5420	0.0741				-	-	12	5	-
			2.7445	0.1568				-	-	12	43	-
74	18.8701679	1,17,56	0.0088	-	0.0998	0.1439	0.1635	-	-	-	-	-
			1.5423	0.0640				-	2	8	7	-
			2.7546	0.1681				-	-	12	44	-
	18.8701690	1,17,56	0.0051	-	0.0698	0.1325	0.1501	-	-	-	-	-
			1.5421	0.0625				-	-	12	5	-
			2.7547	0.1790				-	-	12	44	-
75	19.0497421	1,18,56	0.0055	-	0.1108	0.1154	0.1461	-	-	-	-	-
			1.5717	0.1016				-	2	8	8	-
			2.7765	0.1401				-	-	12	44	-
	19.0497889	1,18,56	0.0058	-	0.0913	0.1288	0.1521	-	-	-	-	-
			1.5716	0.1007				-	2	8	8	-
			2.7765	0.1426				-	-	12	44	-
76	19.2286002	1,18,57	0.0000	-	0.0975	0.0975	0.1649	-	-	-	-	-
			1.5714	0.0562				-	-	12	6	-
			2.7865	0.1149				-	-	12	45	-
	19.2286011	1,18,57	0.0031	-	0.0628	0.1374	0.1574	-	-	-	-	-
			1.5717	0.0803				-	2	8	8	-
			2.7864	0.1317				-	-	12	45	-
77	19.4068165	1,18,58	0.0033	-	0.0693	0.1191	0.1454	-	-	-	-	-
			1.5714	0.0971				-	2	8	8	-
			2.7964	0.1390				-	-	12	46	-
	19.4068274	1,18,58	0.0056	-	0.0895	0.1175	0.1353	-	-	-	-	-
			1.5717	0.0958				-	-	12	6	-
			2.7964	0.1518				-	-	12	46	-
78	19.5841752	1,18,59	0.0046	-	0.0987	0.1108	0.1475	-	-	-	-	-
			1.5715	0.0732				-	-	12	6	-
			2.8063	0.1385				-	-	12	47	-
	19.5842034	1,18,59	0.0061	-	0.0972	0.1330	0.1460	-	-	-	-	-
			1.5714	0.0793				-	-	12	6	-
			2.8063	0.1373				-	-	12	47	-

Table 0.1 – Continued

N	E	conf.	r	$\Delta(r)$	f_1	f_2	f_3	N(3)	N(4)	N(5)	N(6)	N(7)
79	19.7607999	1,18,60	0.0049	-	0.0641	0.1102	0.1913	-	-	-	-	-
			1.5709	0.0885				-	2	8	8	-
			2.8161	0.1549				-	-	12	48	-
	19.7608055	1,18,60	0.0013	-	0.0781	0.1348	0.1540	-	-	-	-	-
			1.5710	0.0830				-	2	8	8	-
			2.8161	0.1511				-	-	12	48	-
80	19.9366899	1,19,60	0.0031	-	0.0930	0.1310	0.1580	-	-	-	-	-
			1.6002	0.1195				-	-	12	7	-
			2.8369	0.1429				-	-	12	48	-
	19.9366954	1,20,59	0.0049	-	0.0628	0.0883	0.1355	-	-	-	-	-
			1.6276	0.1198				-	-	12	8	-
			2.8481	0.1447				-	-	12	47	-
81	20.1115924	1,20,60	0.0064	-	0.0727	0.0945	0.1006	-	-	-	-	-
			1.6271	0.1021				-	-	12	8	-
			2.8577	0.1372				-	-	12	48	-
	20.1116078	1,20,60	0.0014	-	0.0522	0.1064	0.1124	-	-	-	-	-
			1.6272	0.1176				-	-	12	8	-
			2.8576	0.1262				-	-	12	48	-
82	20.2861031	1,20,61	0.0050	-	0.0420	0.0987	0.1113	-	-	-	-	-
			1.6274	0.1081				-	-	12	8	-
			2.8671	0.1464				-	-	12	49	-
	20.2861622	2,20,60	0.5468	0.0000	0.0699	0.0930	0.1130	-	-	-	-	-
			1.6883	0.1829				-	-	12	8	-
			2.8773	0.1626				-	-	12	48	-
83	20.4598342	2,20,61	0.5447	0.0629	0.0891	0.0971	0.1153	-	-	-	-	-
			1.6886	0.1873				-	-	12	8	-
			2.8866	0.2084				-	-	12	49	-
	20.4598388	2,20,61	0.5457	0.0333	0.0931	0.0993	0.1445	-	-	-	-	-
			1.6887	0.1799				-	-	12	8	-
			2.8865	0.2000				-	-	13	47	1
84	20.6327589	2,21,61	0.5426	0.0047	0.0674	0.0913	0.1289	-	-	-	-	-
			1.7140	0.2477				-	1	10	10	-
			2.9064	0.1758				-	-	12	49	-
	20.6327815	2,21,61	0.5410	0.0353	0.0671	0.1014	0.1031	-	-	-	-	-
			1.7137	0.2052				-	1	10	10	-
			2.9065	0.1568				-	-	12	49	-
85	20.8049075	2,21,62	0.5422	0.0306	0.1124	0.1194	0.1385	-	-	-	-	-
			1.7135	0.2091				-	1	10	10	-
			2.9156	0.1594				-	-	12	50	-
	20.8049198	2,21,62	0.5417	0.0125	0.0962	0.1161	0.1351	-	-	-	-	-
			1.7136	0.2168				-	1	10	10	-
			2.9156	0.1507				-	-	12	50	-
86	20.9765178	2,21,63	0.5403	0.0136	0.0478	0.1128	0.1571	-	-	-	-	-
			1.7138	0.2117				-	-	12	9	-
			2.9247	0.1898				-	-	12	51	-
	20.9765313	2,21,63	0.5407	0.0017	0.0482	0.0972	0.1177	-	-	-	-	-
			1.7137	0.2423				-	1	10	10	-
			2.9247	0.1681				-	-	12	51	-
87	21.1473848	2,22,63	0.5386	0.0063	0.0804	0.1240	0.1480	-	-	-	-	-
			1.7380	0.2213				-	-	12	10	-
			2.9442	0.1553				-	-	13	49	1
	21.1474046	2,22,63	0.5376	0.0097	0.0743	0.0968	0.1314	-	-	-	-	-
			1.7378	0.1895				-	-	12	10	-
			2.9442	0.1573				-	-	12	51	-
88	21.3176820	2,22,64	0.5385	0.0081	0.0267	0.1186	0.1367	-	-	-	-	-
			1.7378	0.1826				-	-	12	10	-
			2.9532	0.1602				-	-	12	52	-
	21.3176867	2,22,64	0.5380	0.0000	0.0414	0.1045	0.1146	-	-	-	-	-
			1.7377	0.1946				-	-	12	10	-
			2.9532	0.1176				-	-	12	52	-

Table 0.1 – Continued

N	E	conf.	r	$\Delta(r)$	f_1	f_2	f_3	N(3)	N(4)	N(5)	N(6)	N(7)
89	21.4873691	2,22,65	0.5375	0.0000	0.0990	0.1089	0.1292	-	-	-	-	-
			1.7378	0.1552				-	-	12	10	-
			2.9621	0.1380				-	-	12	53	-
	21.4874019	2,22,65	0.5376	0.012	0.0708	0.1113	0.1208	-	-	-	-	-
			1.7376	0.1962				-	-	12	10	-
			2.9620	0.1646				-	-	12	53	-
90	21.6564037	2,22,66	0.5359	0.0000	0.0791	0.1085	0.1109	-	-	-	-	-
			1.7376	0.1955				-	-	12	10	-
			2.9709	0.1657				-	-	14	50	2
	21.6564542	2,22,66	0.5369	0.0036	0.0674	0.1020	0.1338	-	-	-	-	-
			1.7374	0.2154				-	-	12	10	-
			2.9709	0.1621				-	-	12	54	-
91	21.8248231	3,22,66	0.7050	0.0079	0.1106	0.1150	0.1297	-	-	-	-	-
			1.7916	0.2288				-	-	12	10	-
			2.9891	0.1871				-	-	13	52	1
	21.8248255	2,22,67	0.5363	0.0182	0.0658	0.1152	0.1428	-	-	-	-	-
			1.7373	0.1602				-	-	12	10	-
			2.9797	0.1671				-	-	12	55	-
92	21.9925417	3,22,67	0.7052	0.0304	0.0693	0.1242	0.1369	-	-	-	-	-
			1.7911	0.2386				-	-	12	10	-
			2.9979	0.1984				-	-	12	55	-
	21.9925442	3,22,67	0.7052	0.0264	0.0784	0.1496	0.1600	-	-	-	-	-
			1.7911	0.2187				-	-	12	10	-
			2.9979	0.1873				-	-	12	55	-
93	22.1594897	3,24,66	0.7019	0.0226	0.0269	0.0968	0.1271	-	-	-	-	-
			1.8361	0.2716				-	-	12	12	-
			3.0260	0.1530				-	-	12	54	-
	22.1595122	3,24,66	0.7012	0.0388	0.0585	0.0639	0.0900	-	-	-	-	-
			1.8361	0.2707				-	-	12	12	-
			3.0260	0.1764				-	-	12	54	-
94	22.3258413	3,24,67	0.7001	0.0340	0.0346	0.0906	0.1039	-	-	-	-	-
			1.8356	0.1973				-	-	12	12	-
			3.0347	0.1696				-	-	12	55	-
	22.3258448	3,24,67	0.7006	0.0263	0.0898	0.0970	0.1104	-	-	-	-	-
			1.8354	0.1904				-	-	12	12	-
			3.0347	0.1622				-	-	12	55	-
95	22.4918782	4,24,67	0.8089	0.0487	0.0493	0.0944	0.1360	4	-	-	-	-
			1.8848	0.2173				-	-	12	12	-
			3.0522	0.1774				-	-	12	55	-
	22.4918953	4,24,67	0.8090	0.0320	0.0807	0.1119	0.1269	4	-	-	-	-
			1.8846	0.2324				-	-	12	12	-
			3.0523	0.1737				-	-	12	55	-
96	22.6572706	4,24,68	0.8083	0.0572	0.0221	0.0868	0.1205	4	-	-	-	-
			1.8846	0.2237				-	-	12	12	-
			3.0606	0.1854				-	-	12	56	-
	22.6573098	4,24,68	0.8103	0.0277	0.0814	0.1188	0.1338	4	-	-	-	-
			1.8848	0.2344				-	-	12	12	-
			3.0605	0.1997				-	-	12	56	-
97	22.8220322	4,24,69	0.8095	0.0517	0.0736	0.1016	0.1401	4	-	-	-	-
			1.8849	0.2134				-	-	12	12	-
			3.0687	0.2059				-	-	14	53	2
	22.8220678	4,24,69	0.8088	0.0527	0.1019	0.1244	0.1471	4	-	-	-	-
			1.8847	0.2268				-	-	12	12	-
			3.0689	0.1757				-	-	12	57	-

Table 0.1 – Continued

N	**E**	**conf.**	**r**	$\Delta(r)$	f_1	f_2	f_3	**N(3)**	**N(4)**	**N(5)**	**N(6)**	**N(7)**
98	22.9861991	4,25,69	0.8081	0.0560	0.0706	0.0706	0.0815	4	-	-	-	-
			1.9055	0.2482				-	-	12	13	-
			3.0864	0.1388				-	-	12	57	-
	22.9862098	4,25,69	0.8078	0.0401	0.0881	0.1184	0.1520	4	-	-	-	-
			1.9058	0.2468				-	-	12	13	-
			3.0863	0.1562				-	-	12	57	-
99	23.1497580	4,25,70	0.8071	0.0581	0.1012	0.1152	0.1281	4	-	-	-	-
			1.9056	0.2477				-	-	12	13	-
			3.0945	0.2070				-	-	12	58	-
	23.1497869	4,25,70	0.8064	0.0276	0.0623	0.1007	0.1264	4	-	-	-	-
			1.9056	0.2638				-	-	12	13	-
			3.0945	0.1858				-	-	13	56	1
100	23.3127593	4,26,70	0.8055	0.0530	0.0710	0.1105	0.1235	4	-	-	-	-
			1.9259	0.3221				-	-	12	14	-
			3.1117	0.2120				-	-	14	54	2
	23.3127595	4,26,70	0.8056	0.0523	0.0946	0.1060	0.1223	4	-	-	-	-
			1.9254	0.2559				-	-	12	14	-
			3.1119	0.2079				-	-	12	58	-

References

1. E. P. Wigner, Phys. Rev. **46**, 1002 (1934).
2. V. M. Bedanov and F. M. Peeters, Phys. Rev. B **49**, 2667 (1994).
3. J. A. Goree and R. L. Merlino, Physics Today, **57**, 32 (2004).
4. G. S. Selwyn, J. Singh, and R. S. Bennett, J. Vac. Sci. Technol. **A7**, 2758 (1989).
5. S. Hachisu, Y. Kobayashi, and A. Kose, J. Colloid Interf. Sci. **42**, 342 (1973).
6. P. N. Pusey and W. van Megen, Nature (London) **320**, 340 (1986).
7. W. K. Kegel and A. van Blaaderen, Science **287**, 290 (2000).
8. K. N. Pham, A. M. Puertas, J. Bergenholtz, S. U. Egelhaaf, A. Moussaïd, P. N. Pusey, A. B. Schofield, M. E. Cates, M. Fuchs, and W. C. K. Poon, Science **296**, 104 (2002).
9. S. Ichimaru, Rev. Mod. Phys. **54**, 1017 (1982).
10. L. Bonsall and A. A. Maradudin, Phys. Rev. B **15**, 1959 (1977).
11. S. Hamaguchi, R. Farouki, and D. H. E. Dubin, Phys. Rev. E **56**, 4671 (1997).

12. J. H. Chu and Lin I, Phys. Rev. Lett. **72**, 4009 (1994).

13. W.-T. Juan, Z.-H. Huang, J.-W. Hsu, Y.-J. Lai, and L. I, Phys. Rev. E **58**, R6947 (1998).

14. MICROPARTICLES GMBH, Rudower Chaussee 5, 12484 Berlin.

15. A. Melzer, M. Klindworth, and A. Piel, Phys. Rev. Lett. **87**, 115002 (2001).

16. V. A. Schweigert and F. M. Peeters, Phys. Rev. B **51**, 7700 (1995).

17. A. P. Nefedov, G. E. Morfill, V. E. Fortov, H. M. Thomas, H. Rothermel, T. Hagl, A. V. Ivlev, M. Zuzic, B. A. Klumov, A. M. Lipaev, V. I. Molotkov, O. F. Petrov, Y. P. Gidzenko, S. K. Krikalev, W. Shepherd, A. I. Ivanov, M. Roth, H. Binnenbruck, J. A. Goree, and Y. P. Semenov, New J. Phys. **5**, 33.1 (2003).

18. O. Arp, D. Block, M. Klindworth, and A. Piel, Phys. Plasmas **12**, 122102 (2005).

19. R. W. Hasse and V. V. Avilov, Phys. Rev. A **44**, 4506 (1991).

20. M. Drewsen, C. Brodersen, L. Hornekaer, J. S. Hangst, and J. P. Schiffer, Phys. Rev. Lett. **81**, 2878 (1998).

21. M. Bonitz, D. Block, O. Arp, V. Golubnychiy, H. Baumgartner, P. Ludwig, A. Piel, and A. Filinov, Phys. Rev. Lett. **96**, 075001 (2006).

22. A. Melzer, Phys. Rev. E **67**, 016411 (2003).

23. H. Rothermel, T. Hagl, G. E. Morfill, M. H. Thoma, and H. M. Thomas, Phys. Rev. Lett. **89**, 175001 (2002).

24. O. Arp, D. Block, and A. Piel, Phys. Rev. Lett. **93**, 165004 (2004).

25. M. Saint Jean, C. Even, and C. Guthmann, Europhys. Lett. **55**, 45 (2001).

26. G. Coupier, C. Guthmann, Y. Noat, and M. S. Jean, Phys. Rev. E **71**, 046105 (2005).

27. Ying-Ju Lai and Lin I, Phys. Rev. E **60**, 4743 (1999).

28. L. J. Campbell and R. M. Ziff, Phys. Rev. B, **20**, 1886 (1979).

29. F. Bolton and U. Rössler, Supperlatt. Microstruct. **13**, 139 (1993).

30. M. Saint Jean and C. Guthmann, J. Phys.: Condens. Matter **14**, 13653 (2002).

31. L. R. E. Cabral and F. M. Peeters, Phys. Rev. B **70** 214522 (2004).

32. P. Galatola, G. Coupier, M. Saint Jean, J. -B. Fournier, and C. Guthmann, Eur. Phys. J. B **50** 549 (2006).

33. L. Hornekær, N. Kjærgaard, A. M. Thommesen, and M. Drewsen, Phys. Rev. Lett. **86**, 1994 (2001).

34. W. Paul and H. Steinwedel, Zeitschrift für Naturforschung, **8A**, 448 (1953).

35. W. Paul, Agewandte Chemie - International Edition **29**, 739 (1990).

36. M. Drewsen, I. Jensen, J. Lindballe, N. Nissen, R. Martinussen, A. Mortensen, P. Staanum, and D. Voigt, Int. J. Mass Spectrometry **229**, 83 (2003).

37. M. Drewsen, A. Brøner, Phys. Rev. A **62**, 045401 (2001).

38. R. F. Wuerker, H. Shelkton, R. V. Langmuir, J. Appl. Phys. **30**, 342 (1959).

39. I. Chakraborty, Quantum Dots: A survey of the properties of artificial atoms, Elsevier North-Holland (1999).

40. R. C. Ashoori, Nature (London) **379**, 413 (1996).

41. G. W. Bryant, Phys. Rev. Lett. **59**, 1140 (1987).

42. B. Szafran, S. Bednarek, and J. Adamowski, Phys. Rev. B **67**, 045311 (2003).

43. I. V. Grigorieva, W. Escoffier, J. Richardson, L. Y. Vinnikov, S. Dubonos, and V. Oboznov, Phys. Rev. Lett. **96**, 077005 (2006).

44. M. Kong, PhD thesis, University of Antwerp, 2004.

45. G. Berdiyorov, PhD thesis, University of Antwerp, 2007.

46. P. Leiderer, W. Ebner, and V. B. Shikin, Surf. Sci. **113** 405 (1982).

47. C. C. Grimes and G. Adams, Phys. Rev. Lett. **42**, 795 (1979).

48. M. A. Kastner, Phys. Today **46**, 24 (1993).

49. S. Tarucha, D. G. Austing, T. Honda, R. J. V. der Hage, and L. P. Kouwenhoven, Phys. Rev. Lett. **77**, 3613 (1996).

50. H. Drexler, D. Leonard, W. Hansen, J. P. Kotthaus, and P. M. Petroff, Phys. Rev. Lett. **73** 2252 (1994).

51. B. Partoens, PhD thesis, University of Antwerp, 2000.

52. N. Metropolis, A. W. Rosenbluth, M. N. Rosenbluth, A. M. Teller, and E. Teller, J. Chem. Phys. **21**, 1087 (1953).

53. K. E. Atkinson, An Introduction to Numerical Analysis, 2nd edition, John Wiley & Sons, New York, 1989.

54. V. M. Bedanov, G. V. Gadiyak, and Y. E. Lozovik, Phys. Lett. **109A**, 289 (1985).

55. L. Verlet, Phys. Rev. **159**, 98 (1967); *ibid.* Phys. Rev. **165**, 201 (1967).

56. H. C. Andersen, J. Chem. Phys. **72**, 23848 (1980).

57. W. Feller, An Introduction to Probability Theory and Its Applications, Vol. I. Wiley, New York, 1957.

58. M. Golosovsky, Y. Saado, and D. Davidov, Phys. Rev. E **65**, 061405 (2002).

59. G. B. Hess, Phys. Rev. **161**, 189 (1967); D. Stauffer and A. L. Fetter, *ibid.* **168**, 156 (1968).

60. Y. Pearl, Appl. Phys. Lett. **5**, 65 (1964).

61. A. I. Buzdin and J. P. Brison, Phys. Lett. A **196**, 267 (1994).

62. B. Partoens and P. S. Deo, Phys. Rev. B **69**, 245415 (2004).

70. L. Cândido, J. P. Rino, N. Studart, and F. M. Peeters, J. Phys.: Condens. Matter **10**, 11627 (1998).

64. J. P. Schiffer, Phys. Rev. Lett. **70**, 818 (1993).

65. F. M. Peeters, Phys. Rev. B **42**, R1486 (1990).

66. G. Blatter, M. V. Feigel'man, V. B. Geshkenbein, A. I. Larkin, and V. M. Vinokur, Rev. Mod. Phys. **66**, 1125 (1994).

67. A. K. Geim, I. V. Grigorieva, S. V. Dubonos, J. G. S. Lok, J. C. Maan, A. E. Filippov, and F. M. Peeters, Nature (London) **390**, 259 (1997).

68. R. S. Crandall and R. Williams, Phys. Lett. A **34**, 404 (1971).

69. S. W. S. Apolinario, B. Partoens, and F. M. Peeters, Phys. Rev. E **72**, 046122 (2005).

70. L. Cândido, J. P. Rino, N. Studart, and F. M. Peeters, J. Phys.: Condens. Matter **10**, 11627 (1998).

71. A. P. Young, Phys. Rev. B **19**, 1855 (1979).

72. D. R. Nelson and B. I. Halperin, Phys. Rev. B **19**, 2457 (1979).

73. J. M. Kosterlitz and D. J. Thouless, J. Phys. C **6**, 1181 (1973).

74. D. R. Nelson and B. I. Halperin, Phys. Rev. B **19**, 2457 (1979).

75. A. H. Marcus and S. A. Rice, Phys. Rev. E **55**, 637 (1997).

76. K. J. Strandburg, Rev. Mod. Phys. **60**, 161 (1988).

77. F. M. Peeters, V. A. Schweigert, and V. M. Bedanov, Physica B **212**, 237 (1995).

78. Yu. E. Lozovik and V. A. Mandelshtam, Phys. Lett. A, **145**, 269 (1990).

79. B. Partoens and F. M. Peeters, J. Phys.: Condens. Matter **9**, 5383 (1997).

80. E. Y. Andrei, G. Deville, D. C. Glattli, F.I.B. Williams, E. Paris, and B. Etienne, Phys. Rev. Lett. **60**, 2765 (1988).

81. Y. Kondo, J. S. Korhonen, M. Krusius, V. V. Dmitriev, E. V. Thuneberg, and G. E. Volovik, Phys. Rev. Lett. **68**, 3331 (1992).

82. W. M. Itano, J. J. Bollinger, J. N. Tan, B. Jelenković, X. -P. Huang, and D. J. Wineland, Science **279**, 686 (1998).

83. O. Arp, D. Block, A. Piel, and A. Melzer, Phys. Rev. Lett. **93**, 165004 (2004).

84. T. Pohl, T. Pattard, and J. M. Rost, Phys. Rev. Lett. **92**, 155003 (2004).

85. T. Killian, Nature (London) **429**, 815 (2004).

86. A. Rahman and J. P. Schiffer, Phys. Rev. Lett. **57**, 1133 (1986).

87. R. W. Hasse and J. P. Schiffer, Ann. Phys. (Berlin) **203**, 419 (1990).

88. J. P. Schiffer, Phys. Rev. Lett. **70**, 818 (1993).

89. J. P. Schiffer, Phys. Rev. Lett. **88**, 205003 (2002).

90. D. H. E. Dubin and T. M. O′Neil, Phys. Rev. Lett. **60**, 511 (1988).

91. S. L. Gilbert, J. J. Bollinger, and D. J. Wineland, Phys. Rev. Lett. **60**, 2022 (1988).

92. F. Diedrich, E. Peik, J. M. Chen, W. Quint, and H. Walther, Phys. Rev. Lett. **59**, 2931 (1987).

93. H. Löwen, Phys. Rep. **237**, 249 (1994).

94. M. Kong, B. Partoens, and F. M. Peeters, New Journal of Physics **5**, 23 (2003).

95. J. P. Schiffer, J. Phys. B: At. Mol. Opt. Phys. **36**, 511 (2003).

96. R. Rafac, J. P. Schiffer, J. S. Hangst, D. H. E. Dubin, and D. J. Wales, Proc. Natl. Acad. Sci. USA **88**, 483 (1991).

97. O. Arp, D. Block, M. Bonitz, H. Fehske, V. Golubnychiy, S. Kosse, P. Ludwig, A. Melzer, and A. Piel, Journal of Physics: Conference Series **11**, 234 (2005).

98. P. Ludwig, S. Kosse, and M. Bonitz, Phys. Rev. E. **71**, 046403 (2005).

99. H. W. Kroto, J. R. Heath, S. C. Obrien, R. F. Curl, and R. E. Smalley, Nature (London) **318**, 162 (1985).

100. M. F. Jarrold, Nature (London) **407**, 26 (2000).

101. A. Pérez-Garrido, M. J. W. Dodgson, and M. A. Moore, Phys. Rev. B **56**, 3640 (1996).

102. J. J. Thomson, Phil. Mag. **7**, 237 (1904).

103. P. Leiderer, Z. Phys. B **98**, 303 (1995).

104. C. J. Marzec and L. A. Day, Biophys. Jour. **65**, 2559 (1993).

105. U. B. Sleytr, M. Sára, D. Pum, and B. Schuster, Prog. Surf. Sci. **68**, 231 (2001).

106. D. Pum, P. Messner, and U. B. Sleytr, J. Bacteriology **173**, 6865 (1991).

107. D. H. E. Dubin and J. P. Schiffer, Phys. Rev. E **53**, 5249 (1996).

108. S. Earnshaw, Trans. Cambridge Philos. Soc. **7**, 97 (1842).

109. T. E. Sheridan, Phys. Rev. E **72**, 026405 (2005).

110. K. Tsuruta and S. Ichimaru, Rhys. Rev. A **48**, 1339 (1993).

111. P. Buffat and J. P. Borel, Phys. Rev. A **13**, 2287 (1976).

112. S. W. Apolinario, B. Partoens, and F. M. Peeters, New J. Phys. **9**, 283 (2007).

113. B. G. A. Brito, J. N. T. Rabelo, and L. Cândido, Phys. Lett. A **353**, 70 (2006).

114. V. A. Schweigert and F. M. Peeters, J. Phys.: Condens. Matter **10**, 2417 (1998).

115. W. P. Ferreira, B. Partoens, F. M. Peeters, and G. A. Farias, Phys. Rev. E **71**, 021501 (2005).

116. B. Partoens, V. A. Schweigert, F. M. Peeters, Phys. Rev. Lett. **79**, 3990 (1997).

117. L. Cândido, J. P. Rino, N. Studart, and F. M. Peeters, J. Phys.: Condens. Matter **10**, 11627 (1998).

118. V. Golubnychiy, H. Baumgartner, M. Bonitz, A. Filinov, and H. Fehske, J. Phys. A **39**, 4527 (2006).

119. J. E. Hug, F. van Swol, and C. F. Zukoski, Langmuir **11**, 111 (1995).

120. S. Neser, T. Palberg, C. Blechinger, and P. Leiderer, Prog. Colloid Polym. Sci. **104**, 194 (1997).

121. A. Melzer, A. Homann, and A. Piel, Phys. Rev. E **53**, 2757 (1996).

122. H. Thomas and G. E. Morfill, Nature (London) **379**, 806 (1996).

123. L. I, W. -T. Juan, C. -H. Chiang, and J. H. Chu, Science **272**, 1626 (1996).

124. A. Piel and A. Melzer, Plasma Phys. Control. Fusion **44**, R1 (2002).

125. W.-T. Juan, Z.-H. Huang, J.-W. Hsu, Y.-J. Lai, and L. I, Phys. Rev. E **58**, R6947 (1998).

126. M. Klindworth, A. Melzer, A. Piel, and V. A. Schweigert, Phys. Rev. B **61**, 8404 (2000).

127. G. E. Morfill, H. M. Thomas, U. Konopka, H. Rothermel, M. Zuzic, A. Ivlev, and J. Goree, Phys. Rev. Lett. **83**, 1598 (1999).

128. M. Klindworth, A. Piel, and A. Melzer, Phys. Rev. Lett. **93**, 195002 (2004).

129. M. Klindworth, O. Arp, and A. Piel, J. Phys. D: Appl. Phys. **39**, 1095 (2006).

130. M. Bonitz, D. Block, O. Arp, V. Golubnychiy, H. Baumgartner, P. Ludwig, A. Piel, and A. Filinov, Phys. Rev. Lett. **96**, 075001 (2006).

131. V. Golubnychiy, H. Baumgartner, M. Bonitz, A. Filinov, and H. Fehske, J. Phys. A: Math. Gen. **39** 4527 (2006).

132. S. W. S. Apolinario and F. M. Peeters, Phys. Rev. E. **76** 031107 (2007).

133. S. W. S. Apolinario, B. Partoens, and F. M. Peeters, Phys. Rev. E **74**, 031107 (2006).

134. G. Piacente, I. V. Schweigert, J. J. Betouras, and F. M. Peeters, Phys. Rev. B **69**, 045324 (2004).

135. Y. G. Cornelissens, B. Partoens, and F. M. Peeters, Physica E **8**, 314 (2000).

136. Minghui Kong, B. Partoens, A. Matulis and F. M. Peeters, Phys. Rev. E **69**, 036412 (2004).

137. D. M. Tomecka, B. Partoens, and F. M. Peeters, Phys. Rev. E **71**, 062401 (2005).

138. S. W. S. Apolinario, B. Partoens, and F. M. Peeters, Phys. Rev. B **77**, 035321 (2008).

Curriculum Vitae

Sérgio Apolinário
Born on April 02, 1977
in Olinda / Brazil

June 2004 - May 2008: Doctorate in physics, Condensed Matter Theory group, Physics Department, University of Antwerpen, Belgium.

March 2002 - March 2004: Master in Physics, Universidade Federal de Pernambuco, Recife, Brazil.

March 1997 - November 2001: Bachelor in Physics, Universidade Federal de Pernambuco, Recife, Brazil.

Promotor: Prof. dr. F. M. Peeters
Co-promotor: Prof. dr. B. Partoens

List of publications

1. S. W. S. Apolinario, B. Partoens, and F. M. Peeters, *Structure and spectrum of anisotropically confined two-dimensional clusters with logarithmic interaction*, Phys. Rev. E **72**, 046122 (2005).

2. S. W. S. Apolinario, B. Partoens, and F. M. Peeters, *Inhomogeneous melting in anisotropically confined two-dimensional clusters*, Phys. Rev. E **74**, 031107 (2006).

3. S. W. Apolinario, B. Partoens, and F. M. Peeters, *Structural and dynamical aspects of small three-dimensional spherical Coulomb clusters*, New J. Phys. **9**, 283 (2007).

4. S. W. S. Apolinario and F. M. Peeters, *Melting transitions in isotropically confined three-dimensional small Coulomb clusters*, Phys. Rev. E. **76** 031107 (2007).

5. S. W. S. Apolinario, B. Partoens, and F. M. Peeters, *Multiple rings in a 3D anisotropic Wigner crystal: structural and dynamical properties*, Phys. Rev. B **77**, 035321 (2008).

6. S. W. S. Apolinario and F. M. Peeters, *Melting of anisotropically confined Coulomb balls*, submitted.